Manipulation of Nano-rods and Biomolecules with Insulator-based Dielectrophoresis

by

Mohammad Towshif Rabbani

A Dissertation Presented in Partial Fulfillment
of the Requirements for the Degree
Doctor of Philosophy

Approved June 2022 by the
Graduate Supervisory Committee:

Alexandra Ros, Chair
Nicholas Stephanopoulos
Daniel Buttry

ARIZONA STATE UNIVERSITY

August 2022

ABSTRACT

Microfluidics has enabled many biological and biochemical applications such as high-throughput drug testing or point-of-care diagnostics. Dielectrophoresis (DEP) has recently achieved prominence as a powerful microfluidic technique for nanoparticle separation. Novel electric field-assisted insulator-based dielectrophoresis (iDEP) microfluidic devices have been employed to fractionate rod-shaped nanoparticles like Single-walled carbon nanotubes (SWNTs) and manipulate biomolecules like Deoxyribonucleic acid (DNA) and proteins. This dissertation involves the development of traditional as well as 3D-printed iDEP devices for the manipulation of nm-to-μm scale analytes. First, novel iDEP microfluidic constriction-based sorting devices were developed to introduce inhomogeneous electric field gradients to fractionate SWNTs by length. SWNTs possess length-specific optical and electrical properties, expanding their potential applications for future nanoscale devices. Standard synthesis procedures yield SWNTs in large-length polydispersity and chirality. Thus, an iDEP-based fractionation tool for desired lengths of SWNTs may be beneficial. This dissertation presents the first study of DEP characterization and fractionation of SWNTs using an iDEP microfluidic device. Using this iDEP constriction sorter device, two different length distributions of SWNTs were sorted with a sorting efficiency of >90%. This study provides the fundamentals of fractionating SWNTs by length, which can help separate and purify SWNTs for future nanoscale-based applications. Manipulation of nm-scale analytes requires achieving high electric field gradients in an iDEP microfluidic device, posing one of the significant challenges for DEP applications. Introducing nm-sized constrictions in an iDEP device can help generate a higher electric field gradient. However, this requires cumbersome and

expensive fabrication methods. In recent years, 3D printing has drawn tremendous attention in microfluidics, alleviating complications associated with complex fabrication methods. A high-resolution 3D-printed iDEP device was developed and fabricated for iDEP-based manipulation of analytes. A completely 3D-printed device with 2 μm post-gaps was realized, and fluorescent polystyrene (PS) beads, λ-DNA, and phycocyanin protein trapping were demonstrated. Furthermore, a nm-resolution 3D-printed iDEP device was successfully printed. In the future, these high-resolution 3D-printed devices may lead to exploring DEP characteristics of nanoscale analytes like single protein molecules and viruses. The electric field-assisted unique fractionation phenomena in microfluidic platforms will become a critical solution for nanoparticle separation and manipulating biomolecules.

DEDICATION

To my mother (Jahanara Begum) and my wife (Jumana Hoque), without their sacrifice and support, it would not be possible for me to come this far.

ACKNOWLEDGMENTS

First, I would like to express my gratitude to my mentor, Dr. Alexandra Ros, for her guidance and support throughout my Ph.D. period. Thanks for putting her faith in me and giving me the various research opportunities in the lab that encouraged me to be a better scientist. The guidance and wisdom she has provided me over the last six years have motivated me to think scientifically and push further than my limit. Additionally, I would like to thank my oral exam and graduate advisory committee members, Dr. Daniel Buttry, Dr. Nicholas Stephanopoulos, and Dr. Mark Hayes, for their excellent advice about graduate research and being a professional.

I am very grateful to all of my collaborators who enormously contributed to developing my projects during my Ph.D. I thank Dr. Christoph Schmidt for allowing me to work in his lab in Göttingen, Germany, and his constructive research idea helped me to finish my single-walled carbon nanotube dielectrophoresis project in time. I want to thank the following researchers for their priceless contributions to various projects: Dr. Rober Ros for allowing me to use the atomic force microscope, Dr. Mukul Sonker for providing the design idea of the 3D-DEP project and all of the experimental support, Dr. Jorvani Cruz for helping me to design the 3D-printed devices, Diandra Doppler for collaborating with me in the co-flow project and all of the experimental help, and all of BioXFEL team members for their support during the experiments. I thank all the collaborators I worked with for the thoughtful discussions and the learning I got from each of you.

Special thank goes to my family for supporting me through all these years apart. I want to express my gratitude to my mother, who lived 8000 miles away from me but still encouraged me all these years. I feel deeply grateful to my wife for her sacrifice and

unconditional support; without her, I would not be able to overcome my difficult times during my Ph.D. Also, thank you to all my friends for supporting and motivating me. I also want to thank all my lab mates. I appreciate the friendly and supportive environment created in and outside the lab.

This thesis is an outcome not just of my work but contributions of the many people without whom it would not be possible for me to come this far. Finally, I would like to thank everyone who helped me finish my dissertation on time.

TABLE OF CONTENTS

Page

CHAPTER Page

CHAPTER Page

CHAPTER Page

LIST OF TABLES

LIST OF FIGURES

Figure Page

1. INTRODUCTION

Over the last decades, considerable progress has been made in microfluidics-based lab-on-a-chip (LOC) devices. Microfluidics is a technology developed to engineer the behavior of fluids and analytes in a channel with dimensions of tens of micrometers. It is a technology offering numerous advantages over conventional analysis techniques and developed to manipulate fluids and samples in channels with dimensions of a millimeter to a micro- or nanometer-sized environment. The advantages include low cost, high resolution, and small volumes of samples required for the analytical devices.[1] It has immense potential in biological, chemical, and medical research. Micro-electromechanical systems (MEMS) have offered extremely miniaturized analytical tools with high sensitivity. The operation of these MEMS devices can be fully automated and programmable allowing high throughput and reducing the requirement for manual labor.[2-4]

Particle manipulation using a microfluidics device is crucial due to the broad industry and laboratory research applications. Generally, particle manipulation includes sorting, separation, fractionation, focusing, trapping, and pre-concentration. Particle separation is an essential sample processing step in the biological and medical fields. Current separation methods using a microfluidic device can be categorized as active and passive types. An external force is incorporated in an active separation method, whereas the passive separation method depends on the designed channel geometries and internal forces.[5] Active separation methods include electrophoresis, dielectrophoresis, flow cytometry, acoustophoresis, and optical forces.[6, 7]

In recent years, dielectrophoresis (DEP) has become a powerful tool for nanoparticle and biomolecules separations. The term dielectrophoresis was coined by Pohl in 1970, which refers to the motion of a polarizable particle caused by a spatially non-uniform electric field.[8] DEP has been reported to separate, pattern, manipulate, characterize, sort, and capture targets such as cells [9-18], biomolecules [19-25], bacteria [26, 27], proteins [28-32], viruses [33], etc. DEP has gained attention as a manipulation tool for SWNTs due to its potential for separation, purification, and non-destructive assembly of SWNTs according to their electrical properties.[34-36]The interest in SWNTs and their exploitation through various applications has increased in the past few decades due to their unique optical, thermal, chemical, and electronic properties.[37-40] Carbon nanotubes are hollow cylinders formed by carbon atoms exhibiting lengths ranging from nanometers to several centimeters and diameters in the range of nanometers.[41] They can be described as wrapped-up graphene sheets, whereas the chirality determines the wrapping direction. The optical and electrical properties of SWNTs are determined by their unique chirality.[41-43] From the discovery of CNTs by Iijima and Ichihashi,[44] researchers have studied this new form of carbon due to its excellent electrical, mechanical, optical, and thermal properties.[45] Depending on their chirality, CNTs may be semiconducting or metallic; thus, nanometer-scale carbon materials have gained tremendous attraction in semiconductors.[46, 47] These unique properties of CNTs open the door for a new composite for high-performance building blocks of future nanoscale devices, including field emission displays,[38] biological transporters or sensors,[48, 49] Schottky-type transistors,[50] high-capacity hydrogen storage media,[51] lithium-ion batteries, fuel cells,[52] logic circuits,[53] and many others.

Applications of SWNTs require uniform and predictable properties of SWNTs, and researchers have been exploring strategies for preparing CNT samples with well-defined lengths, chiralities, diameters, and electronic properties.[41] Various techniques have been reported for the purification, separation, and sample preparation of CNTs.[54, 55] Size-exclusion chromatography,[56] ultracentrifugations,[43] electrophoresis, and ion-exchange[57] are the most popular techniques. However, some of these methods require specific wrapping agents to suspend the CNTs, limiting large-scale applications due to the cost, stability, and availability of wrapping agents.

DEP describes the phenomenon of a force experienced by a dielectric particle when it is subjected to a non-uniform electric field. The DEP force scales up with particle size, the medium and particle conductivity ratio, and the electric field gradient. A stronger electric field is often required to manipulate nanoparticles or smaller biomolecules, i.e., proteins, DNA, or viruses, which is difficult to achieve with conventional fabrication techniques. Recently, 3D printing has been successfully implemented in microfluidics due to several advantages over conventional fabrication processes. 3D printing offers rapid prototyping, high reproducibility, and truly 3-dimensional geometries that cannot be realized with conventional fabrication techniques. There are several approaches to 3D printing, and among those, the two-photon polymerization (2PP) process offers unique capabilities with unprecedented resolution compared to a standard polymer 3D printing technology such as stereolithography. For various iDEP applications, higher electric field gradients are required, and 2PP 3D printing can be employed to create nanometer-resolution constrictions and gaps to achieve orders of magnitudes higher electric fields.

This dissertation describes the application and development of multiple microfluidic devices to manipulate single-walled carbon nanotubes (SWNTs) and biomolecules using dielectrophoresis (DEP). The main objective of this dissertation is to address the challenges in fractionation and purification of SWNTs by lengths using DEP and to introduce a high-resolution 3D-printed microfluidic device to manipulate biomolecules. The dissertation is organized into 7 chapters. Chapter 2 briefly discusses the fabrication methods used to make the microfluidic devices to fractionate and manipulate SWNTs. Also, the transport phenomena in a microenvironment and migration behaviors under electric fields are discussed. In addition, the structure, properties, and synthesis process of SWNTs are discussed in chapter 2. Chapter 3 includes a detailed study of SWNTs DEP and the DEP applications of SWNTs. Chapter 4 explores the DEP properties of SWNTs in the low-frequency regime (<1kHz). This study was carried out in a PDMS microfluidic device that contains an array of circular posts. A qualitative study using a numerical model is presented, confirming the trapping positions of the SWNTs in the microfluidic device. This was further demonstrated experimentally with SWNTs and visualized with near-infrared microscopy. Chapter 5 continues with the DEP-based fractionation and purification of the SWNTs by lengths using a PDMS microfluidic sorter device.

Chapter 6 describes this dissertation's second major theme, the manipulation of biomolecules in a high-resolution 3D-printed device. Lastly, a summary and conclusion of the thesis are given in chapter 7.

2. BACKGROUND AND THEORY

2.1 Transport Phenomena in the Microenvironment

Microfluidics uses microscale (up to 100 μm) structures to manipulate a small amount of fluid (nL to pL volume).[1, 58, 59] Microfluidic platforms can manipulate nano- and microscale particles and biomolecules e.g., DNA, RNA, proteins, and cells. Microfluidics offers manipulation of analytes in a microenvironment and avoids sample dilution. Understanding the governing physics and principles of the flow phenomena at the microscale is vital. This section reviews some of the physics of microfluidics and microfluidic flow.

2.1.1. Navier-Stokes Equation

The Navier-Stokes equations govern linear momentum for fluid motions of a Newtonian fluid, and the velocity of an incompressible fluid can be derived from the following equation:

$$\rho\left(\frac{d\boldsymbol{u}}{dt} + (\boldsymbol{u}\cdot\nabla)\boldsymbol{u}\right) = -\nabla p + \mu\nabla^2\boldsymbol{u} + \boldsymbol{F_v} \qquad (2.1)$$

where $\boldsymbol{u}$ is the fluid velocity vector, ρ is the density, p is the pressure, μ is the fluid dynamic viscosity and $\boldsymbol{F_v}$ is an external acceleration force. This equation is based on the simplified conservation laws of momentum and mass, considering density and viscosity are constant over space and time. The right-hand side of Eq (2.1) includes all associated forces such as pressure, viscous, Brownian, gravitational, external acceleration, and electric force acting on the fluid.[60] The left-hand side of Eq (2.1) corresponds to the inertial forces. The nonlinear term $\left((\boldsymbol{u}\cdot\nabla)\boldsymbol{u} = 0\right)$ can be eliminated in the simplified shape of the fluid channel, and Eq (2.1) can be simplified as:[61]

$$\rho\left(\frac{d\boldsymbol{u}}{dt}\right) = -\nabla p + \mu\nabla^2\boldsymbol{u} + \boldsymbol{F_v} \quad (2.2)$$

2.1.2. Reynolds Number and Péclet Number

The flow pattern in a microfluidic device can be predicted using the Reynolds number (R) .[58, 62] It is a dimensionless number representing a property of fluids indicative of their mechanical behavior in dynamic conditions. The Reynolds number represents the relationship between the inertial forces and viscous forces in a system and can be described as:[61]

$$R = \frac{\rho u L}{\mu} \quad (2.3)$$

where ρ is the fluid density, u is the fluid velocity, L is the characteristic length, and μ is the viscosity. In microfluidics, most inertial effects are negligible, yielding laminar flow when Re is generally small ($R \leq 1$). A laminar flow is a flow of liquid streamlines flowing parallel without perturbations. A large Reynolds ($R \geq 2000$) number represents fluids with turbulent flow profiles that increasingly mix stochastically. In turbulent flow conditions, flow profiles cannot be predicted accurately.[63]

In addition to the Reynolds number, the mass transport of a fluid is described by the Péclet number (P_e) which can be defined as:

$$P_e = \frac{uL}{D} \quad (2.5)$$

here, D is the diffusion coefficient. Equation 2.5 represents the diffusive transport of molecules in the fluid.[59] Small P_e defines situations where slow mixing occurs due to diffusion in the microsystem. Diffusion defines the migration of ions and molecules due to Brownian motion. The diffusion coefficient is represented by the Stokes-Einstein equation:[64]

$$D = (K_b \mathrm{T})/(6\pi\mu \mathrm{r}) \quad (2.6)$$

where K_b is the Boltzmann constant, r is the particle's radius, and T is the temperature.

2.2 Background on Electrokinetic Phenomena

Reuss conducted the first observation of electrokinetic phenomena in 1809;[65] however, the first theoretical developments of electrokinetic transport were reported by Helmholtz and Smoluchowski.[66, 67] Dukhin and Derjaguin summarized the follow-up developments of these early works, and since then, considerable attention has been conferred on electrokinetic phenomena.[68] Electrokinetics applies an electric field to induce electrostatic forces on polarizable or charged liquids and suspended particles. Applying this electric field induces the motion of the fluids and particles. The general classification of electrokinetic phenomena consists of electroosmosis, electrophoresis, and dielectrophoresis. The following sections will discuss a brief discussion and accompanying background on electrokinetic transport phenomena.

2.2.1. The Electric Double Layer

A solid surface is in contact with ionic aqueous solutions tends to gain surface charges. When the surface makes contact with an electrolyte solution, it attracts the opposite ions towards it, namely counter-ions, and repels the similar charges away from it called co-ions. For example, Polydimethylsiloxane (PDMS) is widely used to fabricate microfluidic devices. After plasma treatment, PDMS has negative charges on its surface due to the deprotonation of the silanol groups in an aqueous solution.[69] Thus, an electric double layer (EDL) is formed due to the surface charge of ions near the microchannel surface.[70] The liquid layer surrounding the channel exists in two parts: a thin layer of counter-ions tightly bound to the solid surface, known as the Stern layer, and an outer region where ions are

less firmly attached, known as the diffuse layer. The thickness of the Stern layer is typically one or two times the diameter of the counter-ions, and across the Stern layer, the electric potential is assumed to drop linearly.[71] There is a boundary within the diffuse layer, and any ions within the diffuse layer move with the particle in the liquid. This boundary is called the slipping plane. Between the particle surface and the dispersing liquid, a potential exists. This potential varies according to the distance from the particle surface, and the potential at the slipping plane is known as zeta potential (ζ).

In summary, the EDL comprises the immobile Stern and diffuse layer. A schematic of the EDL is shown in Figure 2.1. It can be seen that the EDL is formed at the interface of a negatively charged surface and the surrounding liquid. In a plasma-treated PDMS microchannel, the cations in the Stern layer are immediately adjacent to the negatively charged wall. Cations are immobilized due to the strong electrostatic interaction with the wall's surface. Because the counter-ion number exceeds co-ions close to the surface of the microchannel, this EDL locally exhibits a net charge counteracting the surface charge. Due to the Boltzman distribution of counter-ions within the EDL, the net electric potential in the fluid is non-zero. For an infinite slab, the electrical potential Ψ can be defined as:[72]

$$\Psi(x) = \zeta e^{\frac{-x}{\lambda_D}} \tag{2.7}$$

where x is the coordinate normal to the plane, λ_D is the thickness of the EDL known as Debye length, λ_D. The latter is expressed mathematically as:[72]

$$\lambda_D = \sqrt{\frac{\varepsilon K_B T}{2z^2 e^2 C_0 N_A}} \tag{2.8}$$

where ε, K_B and T are the permittivity of fluid, Boltzman constant, and absolute temperature. C_0 refers to the bulk counter-ion concentration and N_A denotes the Avogadro's

number. The valence of the counter-ions species is given by "z" and e is the charge of an electrode. The Debye length usually ranges from a few nanometers to a few hundred nanometers.[72]

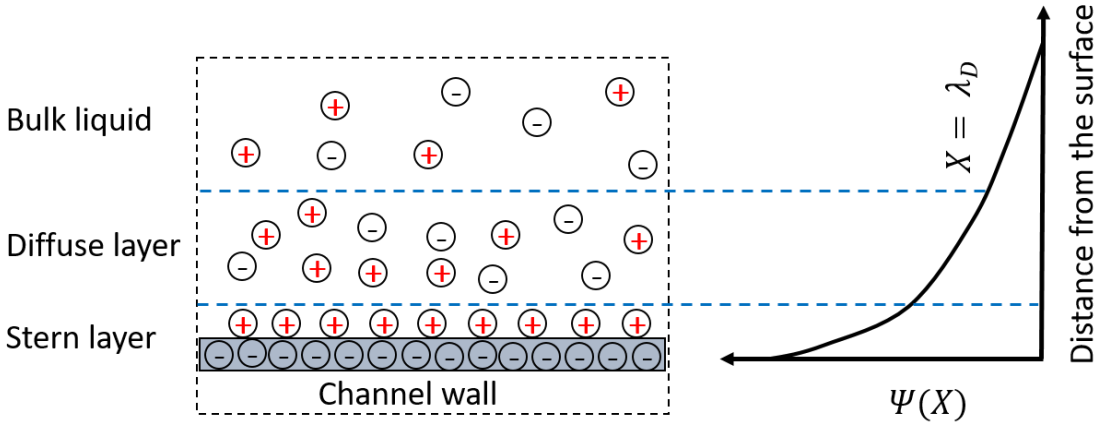

Figure 2.1: Schematic of an EDL formed adjacent to a negatively charged surface. The EDL is formed at the interface of the charged surface and liquid, and the grey area presents the negatively charged surface. The Stern layer is adjacent to the negatively charged wall, and due to the strong electrostatic interaction with the wall's surface, the cations are immobilized in the Stern layer. Just beyond the immobilized layer, the diffuse layer is formed.

2.2.1. Electroosmosis

The excessive counter-ions within the EDL migrate toward the oppositely charged electrode dragging the viscous fluid with them when an external field is applied.[73, 74] In the presence of a surface charge, a flow motion is induced when an electric field is applied known as electroosmotic flow (EOF). This bulk fluid motion shows a uniform flow profile and drops to zero at the liquid-solid interface as shown in Figure 2.2. The electroosmotic velocity can be defined as:

$$\mu_{EOF} = \frac{\varepsilon_m \zeta}{\eta} \tag{2.9}$$

where, ε_m, and η are the medium permittivity, and viscosity of the fluid, respectively. The electroosmotic velocity ($\boldsymbol{v}_{EOF}$) can be expressed as:[75]

$$\boldsymbol{v}_{EOF} = \mu_{EOF}\boldsymbol{E} \tag{2.10}$$

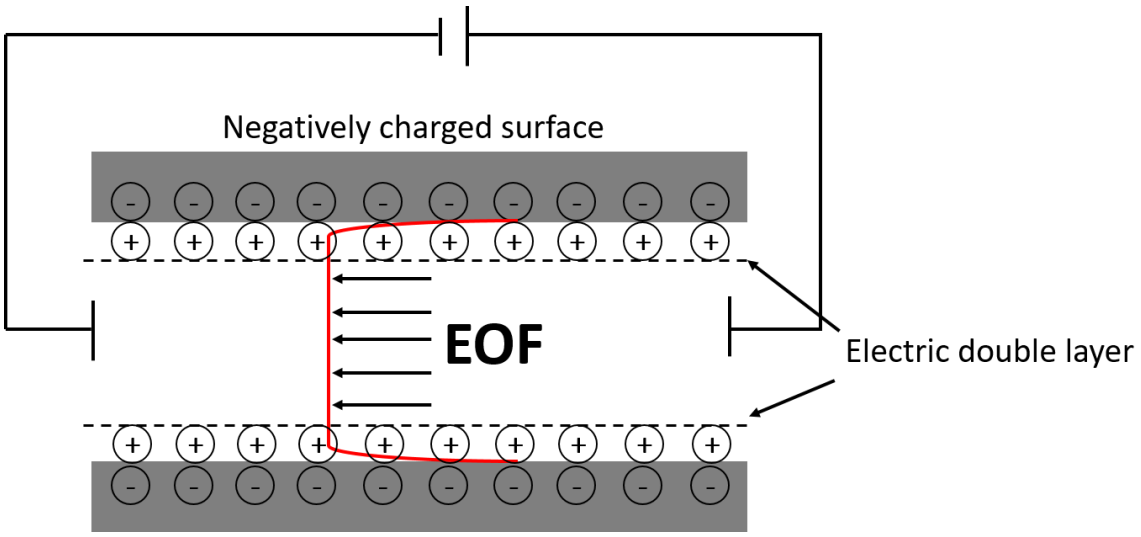

Figure 2.2: Schematic of EOF in a channel with a uniform negative surface charge. The velocity of EOF is uniform throughout the cross-section of the channel and drops to zero at the channel interface.

2.2.3. Electrophoresis

Electrophoresis (EP) refers to the movement of a charged particle in a fluid upon applying an electric field.[76-78] Figure 2.3 represents the schematic of electrophoresis in a microchannel.

The direction of particle movement or rate in the electric field depends on the electric charge and size of the particles. If the charge of the particle is q, the electrophoretic force F_{ep} can be defined as:

$$\boldsymbol{F}_{ep} = q\boldsymbol{E} \tag{2.11}$$

The drag force, F_D acting on a spherical particle based on stokes drag law is defined as:[32]

$$\boldsymbol{F}_D = 6\pi\eta r\boldsymbol{u} \tag{2.12}$$

where u is the particle mobility, and r is the particle radius. The EP velocity, v_{EP}, can be derived when F_{ep} is balanced with F_D and can be expressed as:

$$6\pi\eta r(\boldsymbol{u} - \boldsymbol{v}_{EP}) = q\boldsymbol{E} \tag{2.13}$$

The EP mobility can thus be defined as:[79]

$$\mu_{EP} = \frac{\boldsymbol{v}_{EP}}{\boldsymbol{E}} = \frac{q}{6\pi\eta r} \tag{2.14}$$

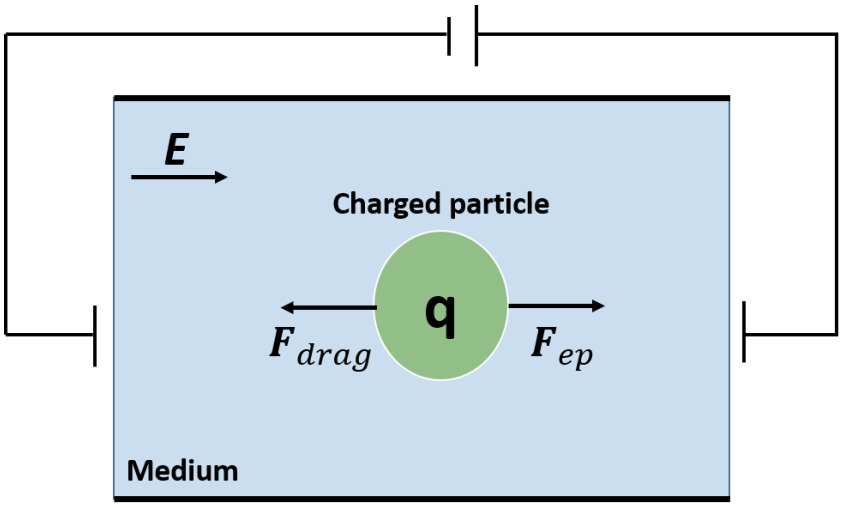

Figure 2.3: Schematic of electrophoresis. The charged particle migrates relatively to the medium upon applying an electric field.

2.2.4. Dielectrophoresis

2.2.4.1. Dielectrophoresis Theory

The term dielectrophoresis (DEP) was first introduced by Pohl in 1970 and referred to the motion of a polarizable particle by a spatially non-uniform electric field.[80] DEP is governed by the difference in dielectric properties of the aqueous medium and suspended particles. A common approach to explaining the DEP force acting on a polarizable particle is based on the model of a homogeneous sphere, as shown in Figure 2.4. The DEP force depends on the dielectric constant of the suspended particles and their surrounding media and is proportional to the third power of the particle size. The DEP force acting on a spherical particle suspended in a medium can be expressed as follows:[81]

$$\boldsymbol{F}_{DEP} = 2\pi r^3 \varepsilon_m Re(CM) \boldsymbol{\nabla E}^2 \quad (2.15)$$

where, ε_m is medium permittivity, r is the particle's radius, and $\boldsymbol{\nabla E}$ is the electric field gradient. The term $Re(CM)$ refers to the real part of the Clausius-Mossotti (CM) factor described by:[82]

$$CM = \frac{\varepsilon_p^* - \varepsilon_m^*}{(\varepsilon_p^* + 2\varepsilon_m^*)} \quad (2.16)$$

where, ε_p^* and ε_m^* denote the frequency-dependent permittivity of the particle and medium, respectively. The complex permittivity of the medium and the particle in equation 2.16 are given by: $\varepsilon_p^* = \varepsilon_p - i\frac{\sigma_p}{\omega}$, $\varepsilon_m^* = \varepsilon_m - i\frac{\sigma_m}{\omega}$, where σ_p, σ_m and ω denote the particle conductivity, medium conductivity, and frequency, respectively, and $i = \sqrt{-1}$. Depending on the sign of the $Re(CM)$ factor, the DEP force could be positive DEP (pDEP) or negative DEP (nDEP). Particles move toward the regions with a higher electric field, showing pDEP when the particle's permittivity is higher than the medium with $Re(CM)$>0. In contrast, particles show nDEP when the particle permittivity is lower than the suspended medium. In the nDEP case, particles are repulsed from the higher electric field and move toward the lower electric field region.

At high frequencies ($\omega \to \infty$), $\boldsymbol{F}_{DEP}$ is typically governed by the permittivity of the particle and medium as the dielectric current dominates.[21] In contrast, $\boldsymbol{F}_{DEP}$ is governed by the conductivity of the particle and medium as the current is dominated by conduction of free charges at lower frequencies ($\omega \to 0$), including DC conditions.[21] Figure 2.4a illustrates the pDEP scenario when $\varepsilon_p > \varepsilon_m$ with the particle attracted to the higher electric field. In contrast, Figure 2.4b shows particles moving to the lower electric field, showing nDEP with $\sigma_p < \sigma_m$.

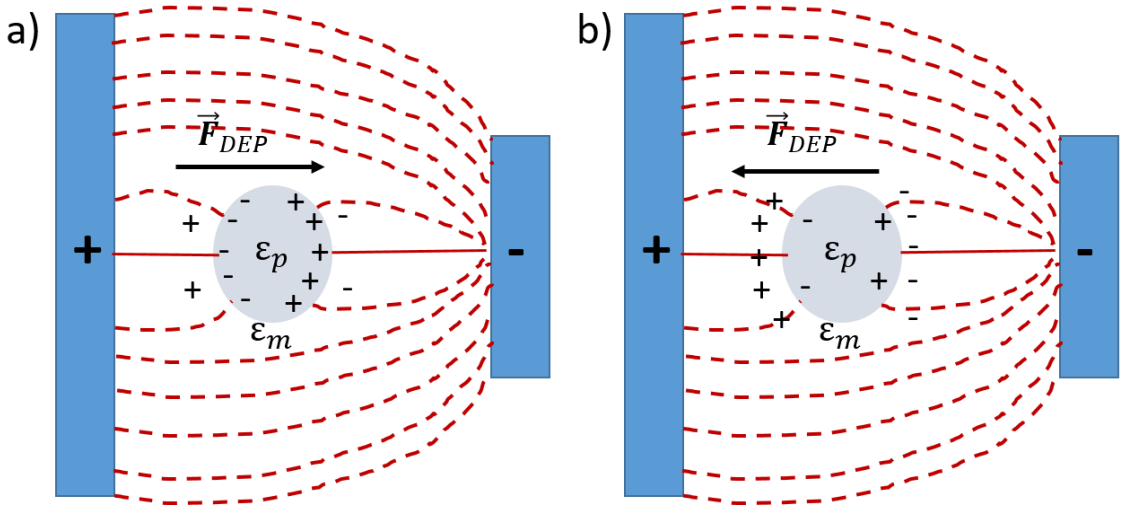

Figure 2.4: Schematic representation of DEP of a spherical particle in a non-uniform electric field. (a) The particle with higher conductivity than the medium migrates to the higher electric field, showing pDEP. (b) The particle moves to the lower electric field, showing nDEP, with $\varepsilon_p < \varepsilon_m$.

Depending on the particle's shape and the number of shells, the DEP force acting on the particle could differ.[83] In most cases, the biological particles are composed of multi-shell structures, and their DEP properties cannot be explained with the conventional homogeneous spherical DEP model.[81] For example, typical biological species, *i.e.*, exosomes, bacteria, liposomes, or endosomes, are described with a single shell model, where a thin membrane shell surrounds their spherical core. Due to the thin outer membrane with a radius r_2 the DEP force is modified as follows:[81]

$$\boldsymbol{F}_{DEP} = 2\pi {r_2}^3 \varepsilon_m Re(CM) \boldsymbol{\nabla} \boldsymbol{E}^2 \tag{2.17}$$

$$\mathrm{CM} = \left(\frac{\mathcal{E}^*_{eff} - \mathcal{E}^*_m}{\mathcal{E}^*_{eff} + 2\mathcal{E}^*_m} \right) \tag{2.18}$$

where $\mathcal{E}^*_{eff}$ is the effective complex permittivity of the particle. If the inner radius of the particle is r_1, then $\mathcal{E}^*_{eff}$ can be expressed as:[81, 84]

$$\varepsilon^*_{eff} = \varepsilon^*_s \frac{\left(\frac{r_2}{r_1}\right)^3 + 2\frac{\varepsilon^*_p - \varepsilon^*_s}{\varepsilon^*_p + 2\varepsilon^*_s}}{\left(\frac{r_2}{r_1}\right)^3 - \frac{\varepsilon^*_p - \varepsilon^*_s}{\varepsilon^*_p + 2\varepsilon^*_s}} \quad (2.19)$$

For biological species consisting of multi-shells, the DEP force can be explained with the multi-shell theory proposed by Irimajiri *et al*.[85] If r_1 is the radius of the core and r_{N+1} is the radius of the outer shell, and N is the number of shells, the DEP force can be expressed as:[86, 87]

$$\boldsymbol{F}_{DEP} = 2\pi {r_N}^3 \varepsilon_m Re(CM) \boldsymbol{\nabla} \boldsymbol{E}^2 \quad (2.20)$$

$$\varepsilon^*_{eff} = \varepsilon^*_{N+1} \frac{\left(\frac{r_{N+1}}{r_N}\right)^3 + 2\frac{\varepsilon^*_{N-1\,eff} - \varepsilon^*_{N+1}}{\varepsilon^*_{N-1\,eff} - 2\varepsilon^*_{N+1}}}{\left(\frac{r_{N+1}}{r_N}\right)^3 - \frac{\varepsilon^*_{N-1\,eff} - \varepsilon^*_{N+1}}{\varepsilon^*_{N-1\,eff} - 2\varepsilon^*_{N+1}}} \quad (2.21)$$

Furthermore, the CM function can be expressed as:[32, 86]

$$CM = \frac{(\varepsilon^*_p - \varepsilon^*_m)(\varepsilon^*_{p_{eff}} + 2\varepsilon^*_m) + \frac{(\sigma^*_{p_{eff}} - \sigma^*_m)(\sigma^*_{p_{eff}} + 2^*\sigma m)}{\omega^2}}{\left(\varepsilon^*_{p_{eff}} + 2\varepsilon^*_m\right)^2 + \left(\frac{(\sigma^*_{p_{eff}} - 2\sigma^*_m)}{\omega}\right)^2} \quad (2.22)$$

where, $\varepsilon^*_{p_{eff}}$ and $\sigma^*_{p_{eff}}$ denote the complex effective permittivity and conductivity of the simplified model, respectively. The DEP force acting on a particle could differ due to the heterogeneity in shape, size, or a combination of both.

2.2.4.2. Dielectrophoresis of DNA

Dielectrophoresis has been used to manipulate various biomolecules ranging from nanometer-sized proteins over tens to a few hundred nanometer-sized DNA molecules.[24, 88, 89] Several groups have reported the DNA polarization study, but it is still not fully understood.[90-94] DEP has been commonly used to manipulate, concentrate, separate, and analyze DNA molecules.[23, 93, 95, 96] The DEP force acting on a DNA molecule results from the electric field to the charge induced in the DNA and can be expressed as:

$$F_{DEP} = \alpha(\boldsymbol{E} \cdot \boldsymbol{\nabla})\boldsymbol{E} \tag{2.23}$$

where α is the polarizability of the DNA fragment. In solution, the λ-DNA attracts counterions, as shown in Figure 2.5. The polarizability of DNA in an electrolyte solution can be expressed as having charges on the DNA backbone and in the double layer around it when an external electric field is applied. The induced dipole $p = \alpha\boldsymbol{E}$will be parallel to the electric field, assuming that the charge relaxation frequency, $\omega_c = \sigma/\varepsilon$ is larger than the frequencies of the external electric field. Moreover, under these assumptions, it can be assumed that the polarization process is lossless as it occurs in the phase with the external electric field, and α can be modeled as a scalar, real-valued quantity.[23] The electric field, $\boldsymbol{E}$ can be generated in various ways as discussed later of this section. For insulator-based DEP, $\vec{E}$ can be generated by an AC or DC signal or a combination of both. For the time-periodic driving potential, the time-averaged DEP force is obtained by replacing the $\vec{E}$ with its RMS value and can be expressed as:

$$\boldsymbol{F}_{DEP} = \alpha(\boldsymbol{E}_{rms} \cdot \boldsymbol{\nabla})\boldsymbol{E}_{rms} \tag{2.24}$$

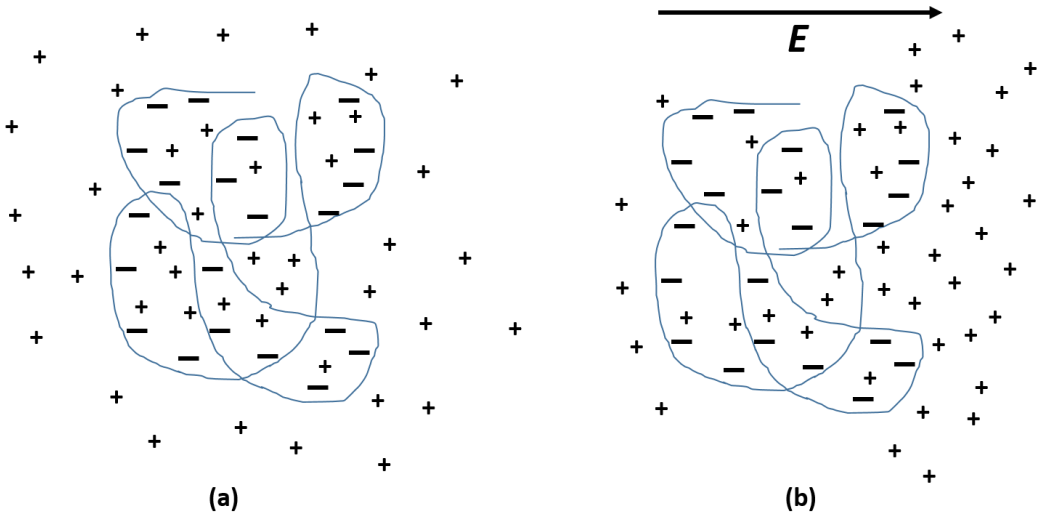

Figure 2.5: Schematic of λ-DNA DEP. a) A negatively charged λ-DNA (not to scale) attracts counterions (mostly cations). b) When an electric field is applied, the cations shifted in the direction of the applied electric field, leaving the negative ions on the DNA backbone.

2.2.4.3. Dielectrophoresis of Protein

Over a few decades, a considerable amount of work on protein DEP has been reported.[29, 97-99] However, the experimental observations for proteins disagree with the predicted DEP forces, and the classical theory does not apply to proteins and other biomolecules on the nanometer length.[99-101] Microscopic details can not be ignored on the nanometer length scale, and the assumptions used in the classical DEP theory using $Re(CM)$ factor arguably fail to describe the situation for proteins. The classical DEP theory fails to consider the permanent dipole moments. For example, the assumption in classical DEP theory based on a spherical model considers that the sphere carries no net charge. An additional potential term is considered if it carries a uniformly distributed surface charge, but the total dipole moment remains unaltered. However, macromolecules like proteins can not be considered colloidal or solid spherical particles. Proteins are polypeptides and form a particular tertiary structure. Due to the spatial arrangements of polarizable groups

originating from polarizable bonds in the polypeptide backbone, a dipole arises in most proteins. Proteins possess a permanent dipole moment that interacts with water dipoles of hydration and shows other physicochemical behavior at the molecular scale.[98, 102, 103] Protein dipole moment also depends on the solvent-protein interaction.[104] The ion distribution in the EDL can influence protein DEP response polarization.[86] Specific motifs such as α-helices, or polar groups of the amino acid side chains contribute to the overall protein permanent dipole with a magnitude of a few hundred Debye.[105-109]

Several groups have reported the DEP manipulation of globular proteins using a smaller applied field gradient (within the rage of $10^{12}\ V^2/m^3 - 10^{14}\ V^2/m^3$).[102, 110, 111] Sometimes, it appears too small to overcome the thermal (Brownian) force acting on protein molecules.[102, 110, 111] To address this situation, an empirical model has been proposed that considers the protein's intrinsic, permanent, dipole moment.[110] To amplify the $Re(CM)$ factor in the classical DEP force equation, an empirical factor $(\kappa + 2)$ was introduced, and the DEP force is then expressed as:

$$\boldsymbol{F}_{DEP} = (3/2)\Omega_0 \varepsilon_m (\kappa + 2)\boldsymbol{\nabla E}^2 \tag{2.25}$$

where Ω_0 is the volume of the protein, and κ is the dielectric susceptibility. For macroscopic particles, κ=1 is used. For molecular-(micro)-and macro scale, the empirical relationship was proposed as:

$$CM_{micro} = (\kappa + 2)CM_{macro} \tag{2.26}$$

This empirical theory represents that the macroscopic $Re(CM)$ factor employed in the current DEP theory is similar to but not the same as the molecular $Re(CM)$ factor explained by the classical DEP theory.[112] Matyushov and co-workers recently reported an evolving theory of protein DEP in solution.[98, 113] According to their study, the

dielectrophoretic susceptibility (κ) is many orders of magnitude higher than the $Re(CM)$ factor predicted by the classical DEP theory. In the classical DEP theory, the DEP force scales with the $Re(CM)$ factor restricted to -0.5< $Re(CM)$<1. In contrast, by using molecular dynamics (MD) simulation, Matyushov reported that for small globular proteins, the susceptibility value lies in the range of $10^3 - 10^4$.[113] By using the molecular dynamics (MD) simulation, the values for the dipole moment and cavity field susceptibility χ_c are derived by Matyushov and co-workers.[114, 115] The molecular surface of the protein and its immediate waters of hydration were considered as the relevant boundary conditions in the MD simulation. Finally, the DEP force acting on a solvated protein derived by Matyushov was expressed as:

$$\boldsymbol{F}_{DEP=} \frac{3\varepsilon_0\Omega_0}{2\varepsilon_s} K\boldsymbol{\nabla E}^2 \tag{2.27}$$

where K is the DEP constant and ε_s represents the dipolar response of the entire protein. pDEP and nDEP correspond for $K > 0$ and $K < 0$, respectively.

In conclusion, the protein DEP theory is still evolving and not fully understood. The classical DEP theory explains that the DEP theory works well for a spherical shape and size particle without having a permanent dipole moment. However, this theory does not apply to biomolecules with a permanent dipole moment. The DEP force of globular protein in the solution is dominated by the protein dipole moment. It has been reported that the $\nabla\boldsymbol{E}^2$ estimated by the classical DEP theory is 3 orders of magnitude lower than the experimental value. An empirical theory has been introduced to address this situation, and a correction factor $(\kappa + 2)$ is introduced to amplify the classical DEP force. Experimentally, several groups have reported $(\kappa + 2)$ values for different proteins.[111] In

recent years, Matyushov *et al.*, reported the evolving theory of protein in solution. By using MD simulations, they predicted the DEP constant for a small globular protein in the range of $10^3 - 10^4$. Their theoretical suggestions mirror the empirical-based findings of different groups, as reported previously.

2.2.5. Technical Realization Platform for DEP

Dielectrophoresis can be evoked once electric field inhomogeneities are apparent. The electric fields and gradients in the microfluidic device can be introduced with the fabrication of microelectrodes or with insulating geometries. With advances in microfabrication techniques, two major techniques have been adopted to generate high electric fields and gradients for dielectrophoretic applications. The first way to generate these electric fields is by introducing a microelectrode in the microfluidic device, commonly known as electrode-based DEP (eDEP).[116] In this technique, the microelectrodes are typically fabricated in a microfluidic platform to generate a non-uniform electric field and positioned inside the microfluidic channels. The strength of the generated electric field can be tuned with different shapes and structures of the microelectrodes. In an eDEP system, the particles experience a large electric field near the microelectrode. The electrodes are positioned inside the microchannel, making direct contact with the medium and analytes. However, the fabrication process of the electrodes is complex and can be accomplished by various methods, including thin film deposition using different metals, photolithography, and etching techniques. eDEP allows the investigation of analytes in the kHz to MHz regime. Even though a high magnitude of DEP forces can be introduced in eDEP devices on the application of low voltages, it has several drawbacks, including fouling effects, Joule heating, and electrolysis.

The second way to introduce the electric field in a microfluidic device is by introducing non-conducting insulating constrictions in the microchannel. In this case, the constrictions are surrounded by a conductive medium, and electrical potentials are applied via electrodes immersed in reservoirs. This method is known as insulator-based DEP (iDEP).[117] Compared to iDEP, eDEP offers strong local electric field gradients by applying small potentials, but the fabrication of eDEP microdevices is often more complicated than iDEP devices. In addition, due to chemical reactions, eDEP devices often suffer from the limitation of the potential electrode fouling in the zone of particle manipulation.. Though iDEP offers many advantages, the main limitation of iDEP refers to challenging access to the high-frequency regime and much higher applied potential difference needed to achieve equivalent electric field magnitudes compared to eDEP. In recent years, a third way to generate an electric field in the microdevice has been demonstrated without contact between the sample fluid and the electrodes.[118] This method is known as contactless DEP (cDEP), where the main channel is separated from the electrodes by thin insulating materials (e.g. PDMS). The capacitive properties of the insulating materials provide the non-uniform electric field required to generate the DEP force. This method eliminates the possibility of sample contamination, reduces fouling effects, Joule heating, and reduces gas bubble formation.[119] The performance of cDEP depends on the thickness and capacitive property of membrane barrier material. Most of the iDEP and cDEP devices are fabricated using photolithography and soft lithography that will be discussed in the following section.

2.3. Photolithography and Soft Lithography

Various methods are used to fabricate microfluidic devices and design the necessary channel and features.[120] Photolithography is a widely used fabrication method to fabricate microfluidic devices. Photolithography is carried out for microscale patterns and structures for fabricating templates for PDMS -based devices. In this technique, a photoreactive polymer mix is deposited on a silicon substrate and illuminated with a UV light source using a photomask containing the device design. A typical wavelength between 300 nm to 450 nm is used in optical lithography. In this section, the optical lithographic method will be discussed.[64]

Figure 2.6 represents the significant steps included in a standard photolithography method. Using computer-aided design (CAD) software, an object with precision geometry is drawn. Next, the photomask is produced using an electron beam on a glass substrate (e.g., soda-lime, borosilicate, or quartz). The precision of the photomask is generally on the order of a micrometer.[64] A thin layer of photosensitive material commonly known as photoresist is deposited on the silicon substrate as shown in Figure 2.6a. Two types of photoresists are used depending on the photochemistry required: positive and negative. During the exposure step, the photoresist polymerizes in a negative photoresist, and a developer removes the unexposed photoresist. SU-8 is a commonly used negative tone photoresist used in a photolithography process. The thickness of the photoresist is controlled by using a spin coater. After the spinning step, a soft bake on a hot plate is performed to evaporate the moisture from the photoresist. Next, this spin-coated photoresist on the substrate is used for pattern transfer using mask alignment and a UV exposure system. The mask is placed on top of the mask holder, the substrate is aligned accordingly, and the wafer is exposed to

UV radiation, as shown in Figure 2.6b. After the exposure step, another baking step is repeated to increase the photochemical reaction rate. After baking, the undeveloped photoresist is removed using a commercial organic developer. Additionally, a post-exposure bake is used to evaporate any leftover developer and helps increase the adhesion of polymerized photoresist on the silicon substrate.

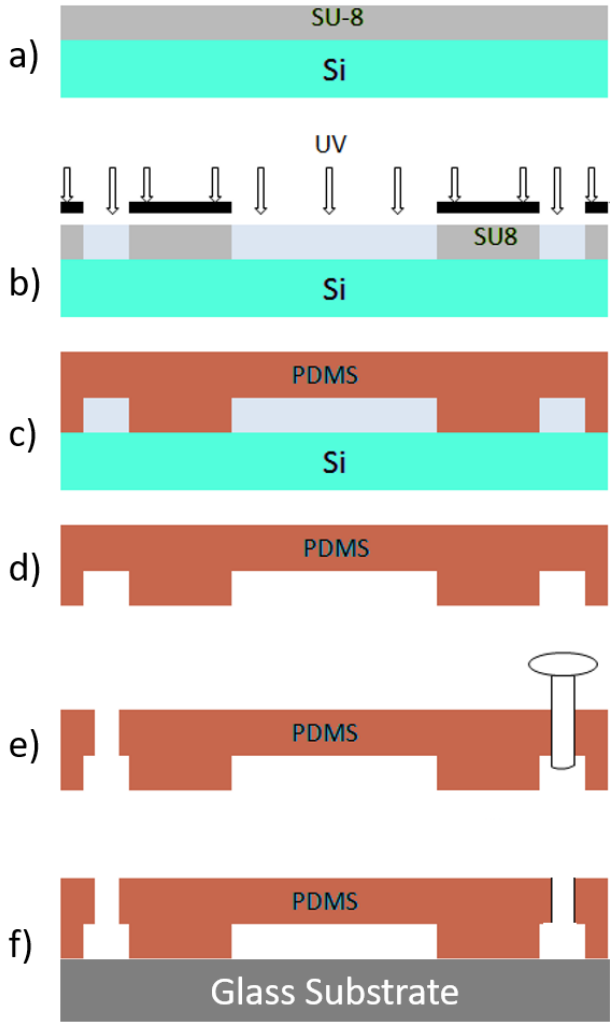

Figure 2.6: Schematic of a photolithography process. (a) coating of negative photoresist SU-8 on a Si wafer. (b) Exposing UV radiation through the mask to transfer the pattern to the photoresist on the substrate. (c) The casting of PDMS on the Si substrate. (d) PDMS peeled out from the wafer. (e) Inlet/outlets are created using a hollow needle. (f) Finally, the PDMS device is attached to the glass substrate.

Soft lithography is a method to replicate the polymer-based mold for microfluidic devices.[121] In soft lithography, the previously fabricated template transfers the device design to an elastomeric material like PDMS. PDMS contains an organic -(Si-O)- backbone and organic methyl group attached to silicon.[122] The liquid mixture of PDMS with curing agent becomes solid by crosslinking via hydrosilylation reaction between vinyl and hydrosilane (Si-H) groups. A mixture of a catalyst (curing agent) and a polymer are poured on a mold and cured in replica modeling, as shown in Figure 2.6c. After pouring PDMS on the patterned substrate, PDMS is degassed and baked for 2-3 h in an oven. After baking, PDMS is peeled off from the substrate, as shown in Figure 2.6d. A biopsy punch is used to cut out the device's inlets and outlets, as shown in Figure 2.6e. Finally, the device is bonded with a glass slide using oxygen plasma.

2.4. Two-photon Polymerization (2PP)

The microfluidics community has widely exploited recent advancements in 3D printing techniques. The fabrication of a 3D object can be achieved in a single process from computer-aided design using a 3D printer. This technique offers fast prototyping, and in addition, true 3D structures can be realized that cannot be achieved in a conventional microfluidic fabrication technique. Stereolithography (SL), extrusion printing, fused deposition modeling (FDM), and inkjet printing are currently used in 3D printing techniques.[123] Among the several approaches of 3D printing techniques, the two-photon polymerization (2PP) process offers unique capabilities with unprecedented resolution compared to a standard polymer 3D printing technology such as stereolithography. In 2PP, two photons are consecutively absorbed by a photosensitizing chromophore when an ultra-

short pulsed near-infrared laser is closely focused on the polymer material, followed by the chain reaction polymerization.[124]

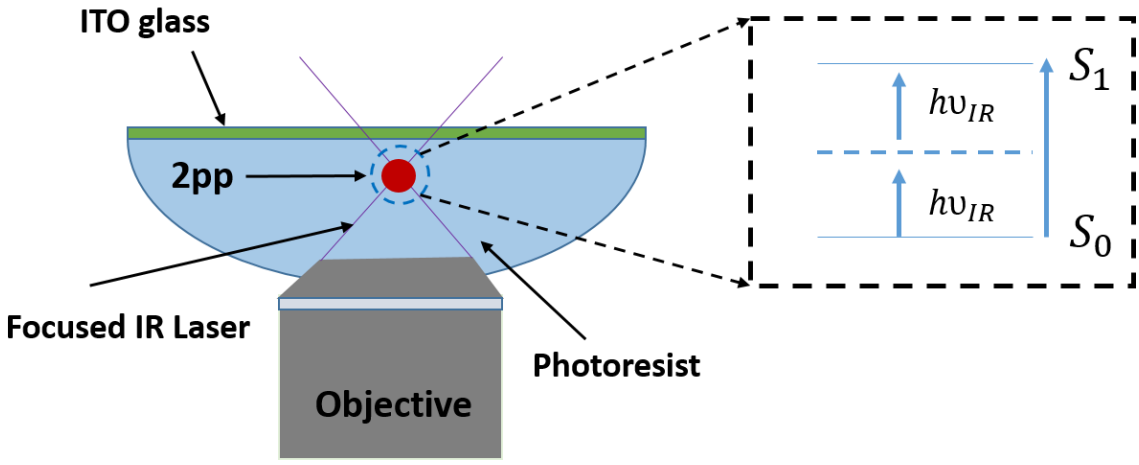

Figure 2.7: Schematic of the dip-in 2PP process. In 2PP, the first absorbed photon excites to a virtual intermediate state, followed by a second photon absorbed during the short lifetime (~10^{-15}s) of this virtual state. The red dot in the photoresist indicates the smallest area where the highly confined beam meets.

Figure 2.7 represents a dip-in liquid lithography 2PP mode. As shown in Figure 2.7, the first absorbed photon excites a single electron to a virtual state and a second photon excites this absorbed electron in the virtual state simultaneously during a short lifetime ($10^{-15}s$). Enough energy can be provided to reach the excitation band of the electron for a photochemical reaction from the 2PP absorption process.[125] A 3D laser writing is implemented by scanning a stage, and 780 nm photons are focused using a high-density objective to a small focal point known as a voxel.[123] In this focal point, a high probability of two photons being absorbed consecutively for the 2PP process, resulting in the photochemical reaction of the photo-initiator and photoresist at a wavelength of 390 nm. 2PP enables high spatial resolution of complex 3D structure design since the probability of a low two-photon absorption outside the focused point is very low. 2PP offers a direct

printing method to fabricate nano- or micro-structures without a mask. In this process, 3D structures can be fabricated with a resolution down to 100 nm using various materials (e.g., ceramics, metals, polymers, and hybrid materials) in a single step. .[126-128]

2.5. Structure, Properties, and Synthesis of Carbon Nanotubes

Due to CNTs' unique chemical, optical, thermal, and electronic properties, the interest in CNTs and their exploitation through various applications has increased in the past few decades. [37-40] Carbon nanotubes are hollow cylinders formed by carbon atoms exhibiting diameters in the range of nanometers and lengths ranging from nanometers to several centimeters.[41] CNTs are wrapped-up graphene sheets, whereas the wrapping direction determines a unique chirality. They form spontaneously and efficiently under well-defined conditions, either as single-walled carbon nanotubes (SWNT) or multi-walled carbon nanotubes (MWNT). CNTs exhibit unique optical and electrical properties of CNTs determined by their chirality.[41-43] CNTs are considered attractive materials in various areas of electronics, including lithium-ion batteries, field emission displays [38], biological transporters or sensors [48, 49], Schottky-type transistors [50], fuel cells [52], high-capacity hydrogen storage media [51], logic circuits [53], and many others.

Iijima and Ichihashi first discovered CNTs; researchers have studied this new form of carbon due to its excellent electrical, mechanical, optical, and thermal properties.[45] CNTs are categorized in semiconducting or metallic types depending on their chirality, and these nanometer-scale carbon materials have gained tremendous attraction in semiconductors.[46, 47] The applications of CNTs often require uniform and predictable properties, and researchers have been exploring strategies for preparing CNT samples with well-defined

diameters, lengths, chiralities, and electronic properties. [41] This section will include the structure, characteristics, and synthesis procedures of CNTs.

2.5.1. Structure

In CNTs, a 2-D sheet of carbon atoms (graphene) is arranged in a hexagonal array where each carbon atom is bonded to three nearest neighbors.[129] Depending on the graphene sheet's rolling process, the properties of CNTs on its atomic arrangement and electronic properties are determined. CNTs tend to attract each other due to strong van der Waals forces, providing an opportunity to develop high conductivity and ultra-high-strength materials. MWNTs are composed of concentrically arranged SWNTs, as shown in Figure 2.8a. The diameter of SWNTs varies from ~0.4 nm to 3 nm, whereas for MWNTs, diameters can range from ~1.4 nm up to 100 nm.[130, 131]

The atomic structure of CNTs is defined by the chiral angle θ and the chiral vector $\boldsymbol{C_h}$. Figure 2.8b represents a schematic diagram showing how a sheet of carbon is rolled to form a cylindrically shaped SWNT. The chiral vector can be represented as:

$$\boldsymbol{C}_h = n\boldsymbol{a}_1 + m\boldsymbol{a}_2 \tag{2.28}$$

where, $\boldsymbol{a}_1$, $\boldsymbol{a}_2$ are unit vectors, and the indices n and m are integers corresponding to the number of unit vectors along with the two directions of the hexagonal lattice, as shown in Figure 2.8b. For a chiral angle of 0° and 30° are referred to as zig-zag and armchair type CNTs. The illustration of an armchair and zig-zag nanotube, respectively, is shown in Figures 2.8c and 2.8d. Figure 2.8c and 2.8d represent Armchair nanotubes with a chiral vector of (n,n), i.e., $n = m$, whereas zig-zag SWNTs are rolled-up in (n,0) or m=0 configuration. The material properties of CNTs are defined by their chirality. For example,

zig-zag nanotubes behave as semiconductors, whereas the unique chirality of the armchair nanotubes determines their conducting properties.[132]

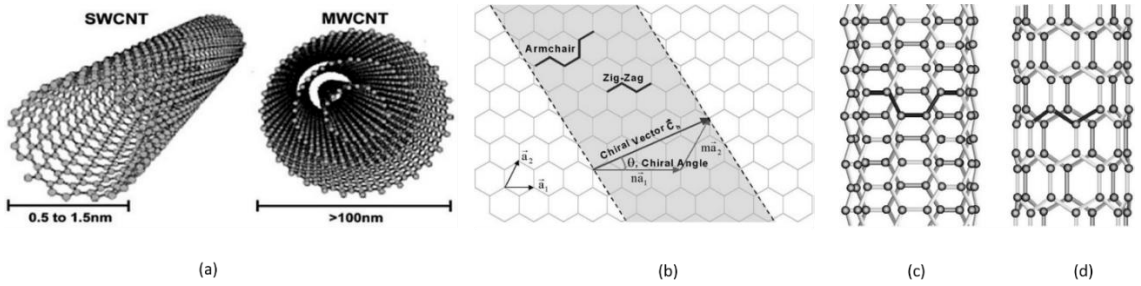

Figure 2.8: Structure of CNTs. (a) Schematic representation of SWNT and MWNT with typical size scales (adapted and reprinted with permission from Ribeiro et al., copyright (2017), SciELO Analytics[133]); (b) Diagram showing how a sheet of graphene is rolled up to form a carbon nanotube. Here C_h and θ denote the chiral vector and chiral angle, respectively; (c) Illustration of the atomic structure of an armchair and (d) a zig-zag nanotube. Note the thick black lines in each SWNT to emphasize the difference. (adapted and reprinted with permission from Thostenson et al., copyright (2001), Elsevier [129]).

2.5.2. Properties

2.5.2.1. Electrical properties

CNTs can exhibit metallic or semiconducting properties due to their unique structure and chirality. Their electronic structure can be explained with a two-dimensional unrolled graphene plane where periodic boundary conditions can be applied in the transverse direction, and translational symmetry exists in the direction of the fiber. As reviewed elsewhere, within a reasonable approximation with the present tight-binding model in the zone folding scheme, the rolled CNTs can be studied. The electrical properties of CNTs can be defined based on their chirality with the zone-folding approach. The electronic structure of CNTs can be characterized using equation 2.23, where n and m define the chiral vector of CNTs and the chiral indices. The electronic properties of CNTs can be defined by $n - m = 3i$, where i is an integer. For $n - m = 3i$, SWNTs are defined

as metallic, and those for which $n - m \neq 3i$ are semiconducting.[46] There is no band gap between conduction and valance band, which makes them metallic when $n = m$ is met (i.e. armchair CNTs). There is a band gap on the order of few tens of meV to hundreds of meV between the conduction and valence band for the zigzag CNTs (m = 0), resulting in semiconducting properties.[134-137] Additionally, the diameter of the SWNT is inversely proportional to the bandgap.[137] SWNTs exhibit field-effect transistor (FET) behavior at room temperature and use nanoelectronic devices, including transistors and logic gates.[136, 138-142] Carbon nanotubes with semiconducting properties could be useful in building nanoscale transistors for integrated circuits in future electronic devices.[37, 39, 134, 143] CVD techniques are used to synthesize the armchair CNTs, and they have electrical properties similar to metal [137] and current flows when a potential difference is applied to the two ends of an armchair nanotube. Armchair CNTs are often used as electrical wires and have higher conductivity than copper. Armchair CNTs can replace the metal for patterning narrower connector lines in nanoelectronic devices and integrated circuits. Theoretical calculations revealed that electrons in CNTs could travel micrometer range distances without scattering at room temperature.[144]

The permittivity of the metallic SWNTs is typically assumed to be >4000[145] with conductivities in the range of 10^2 to 10^6 S/m.[146, 147] Metallic MWNTs may also exhibit large permittivities typically in the range of 10^2 to 10^4,[148, 149] and conductivities in the order of 10^2 to 10^8 S/m.[150-153]. In contrast, semiconducting SWNTs have vastly reduced dielectric constants (<5, for example, estimated by their bandgap energies[132]), which leads to different dielectrophoretic behavior. Krupke *et al.*[154] and others[35, 145] reported semiconducting SWNT with less pronounced conducting properties without doping agents

or gate bias[145] can acquire conductive properties governed by surface charges. Conductivity values reported for the surface conduction mechanism range from about 0.01 S/m to a few S/m [145, 154-156]. The conduction mechanism becomes dependent on the type of derivatization strategy since the suspension of SWNTs is typically achieved through surface derivatization. Therefore, the intrinsic and surface conduction mechanisms give rise to a rich, frequency-dependent dielectrophoretic response of CNTs, which will be described in detail in chapter 3.

2.5.2.2. Surface Functionalization

The chemical functionalization and modification of CNTs are essential aspects of the research on CNT-based materials.[157] The modification of CNTs can be divided into two categories. The first category includes non-covalent bonding between CNT and functional molecules.[158, 159] Such non-covalent modification may be mediated by π-stacking interactions and achieved by the physical adsorption of wrapping agents to the surface of CNTs. Examples of wrapping agents include biomolecules (such as proteins, peptides, and DNA),[155, 160] polymers,[161, 162] and surfactants.[163, 164] The main advantage of non-covalent modification is that it typically has no influence on their intrinsic electrical properties and does not significantly influence the sidewall properties of CNTs. However, if charged species are non-covalently attached to CNTs, they may induce surface conductivity, significantly influencing the dielectrophoretic properties of semiconducting SWNTs.

The second modification is the covalent bonding between CNTs and reactive molecules, where strong bonds are established between the CNT and functionalization agent. The advantage of this method includes the often high reactivity of the functionalization agents, which offers controllable and efficient surface modification. Several researchers have

reported successful functionalization of CNTs.[165-168] Among the reported methods, esterification and amidation of nanotube-bound carboxylic acids are widely used as functionalization of CNTs[169] Covalent attachment alters their electronic structure resulting change in the intrinsic conductivity of CNTs. For example, Bekyarova *et al.* studied networks of SWNTs functionalized with octadecylamine (ODA).[170] The reported conductivity of ODA-functionalized SWNTs was two orders of magnitude lower than the non-functionalized SWNTs. Such changes in the intrinsic conductivity of CNTs may influence the DEP behavior of functionalized SWNTs.

2.5.3. Synthesis

High-quality nanotube materials are required for fundamental and technological applications. High quality refers to the absence of chemical and structural defects in CNTs. Various techniques have been developed in the past for producing SWNTs and MWNTs. Industrial applications of nanotubes still require developing synthesis techniques for the large-scale production of defect-free CNTs. Several synthesis techniques have been reported and developed for fabricating CNT structures and are further reviewed elsewhere.[171-173] Chemical vapor deposition (CVD) techniques,[174, 175] the arc-discharge,[174, 176]and laser-ablation methods [174] are mostly used for synthesizing CNTs. The main challenge in nanotube synthesis remains the large-scale production of CNTs with selective production and high quality at a low cost. The following sections briefly discuss the three primary methods commonly used for CNT synthesis.

2.5.3.1. Arc-discharge Method

A new type of carbon structure consisting of hexagonal-shaped nanotubes synthesized with the arc discharge was first reported by Iijima in 1991.[44] Two high purity

graphite rods as the anode and cathode are used during the synthesis procedure for nanotubes by arc-discharge evaporation. An electrical potential difference is applied until a stable arc is achieved in a helium atmosphere between these rods. The anode is consumed during the synthesis process, and material is deposited on the cathode. The deposited material forms a needle consisting of a softer fibrous inner core containing nanotubes, other carbon particles, and an outer shell of fused materials. The generated needles consisted of graphite sheet coaxial tubes revealed by transmission electron microscopy (TEM), later termed MWNTs. Ebbesen and Ajayan *et al*. reported a large-scale synthesis method of MWNTs by a variation of the standard arc-discharge technique.[177] Under helium atmosphere with a sufficiently significant potential difference applied between two thin graphite rods and pressure of ~500 Torr, a yield of ~75% MWNTs relative to the starting graphite material was reported. The synthesized MWNTs had a diameter between 2-20 nm and lengths extending to several micrometers.

In 1993, Iijima and Icchihashi *et al*.,[178] and Bethune *et al*.[179] reported the synthesis procedure of single-walled carbon nanotubes almost simultaneously. The electrodes are doped with small amounts of metallic catalysts in an arc discharge gas chamber filled with methane and argon gas mixture.[141, 178, 180, 181] Later on, by an arc discharge technique under a helium atmosphere, large quantities (> 1 g) of SWNTs were generated by Journet *et al*.[182] The authors concluded that unique growth rendering high yields mainly depends on the kinetics of carbon condensation in a non-equilibrium situation.

2.5.3.2. Laser Ablation Method

A laser ablation technique was used to achieve the initial synthesis of fullerenes. This technique has also been implemented to synthesize SWNTs over the years. The

synthesis of SWNTs by laser ablation of graphite rods with small amounts of Ni and Co was first reported in 1996 by Smalley and co-workers.[183, 184] Their synthesis process consists of a graphite rod containing a 50:50 catalyst mixture of Co and Ni yielding >70% SWNTs instead of fullerenes. X-ray diffraction and TEM showed that the synthesized nanotubes formed bundles with a length of tens to hundreds of microns and uniform in diameters (5-20 nm). In this method, metal catalyzes the production of SWNTs, but side products are formed containing a substantial fraction of nanoscale impurities which are difficult to separate from CNTs. Liu *et al*. proposed a procedure to purify the as-grown nanotube from the produced side products.[185] The net yield of the purified CNTs based on this method was increased by 20% by weight.

2.5.3.2. Catalytic Growth

The arc-discharge and laser ablation methods are limited in the amount of sample they can produce in contrast to the size of the carbon source. Additionally, subsequent purification steps are required to separate CNTs from undesirable by-products. Due to these limitations, new gas-phase synthesis techniques referred to as chemical vapor deposition (CVD) were developed. CNTs are formed by decomposing a carbon-containing gas in the reaction chamber using a mixture of nitrogen, ethylene, and acetylene. In 1993 Yacaman *et al*.[186] and in1994 Ivanov *et al*.[187, 188] first attempted synthesizing MWNTs with CVD techniques, which have been improved and optimized since then. The carbon source is continually replaced by gaseous compounds resulting in high purity nanotubes minimizing purification steps. Further development of this approach, the high-pressure conversion of carbon monoxide (HiPco), is now widely used and commercialized by Carbon

Nanotechnology Inc (Houston, Tx) for high-scale high-purity production. A summary of different synthesis

techniques is enlisted in Table 2.1.

Table 2.1: Summary of different synthesis processes of CNTs

Method	Arc discharge	Laser ablation	Catalytic growth
Conditions	Low-pressure gas (mostly helium)	Argon gas at 1200°C	Atmospheric pressure at 700-900°C
Carbon source	Graphite	Graphite	Hydrocarbon
Yield	32-91% [182]	>70% [183]	Up to 100% [135]
SWNT	Short length and diameter ≤ 1.4 nm [182]	Short length and diameter 1-2 nm [184]	Long SWNTs and diameter ≤ 4 nm [186]
MWNT	Short tubes with diameters up to 20 nm [178]	Long tubes with a diameter of 5 -20 nm [184]	Long tubes with a diameter ≤ 240 nm [186]
Cost	$$$	$$$	$

3. DIELETROPHORESIS THEORY AND APPLICATIONS OF SINGLE-WALLED CARBON NANOTUBES

3.1 Dielectrophoresis Theory

A force is induced on the particle when a dielectric particle is subjected to a non-uniform electric field.[189] This phenomenon is referred to as dielectrophoresis (DEP) force. The direction of this force depends on the polarizability of the surrounding medium and the polarizability of the particle. The DEP force is called positive DEP (pDEP) when the particle experiences a force and is attracted to the higher electric field. Negative DEP (nDEP) corresponds to the particle's movement towards the lower electric field regions. The DEP force experienced by the polarized particle can be expressed as: [189]

$$\boldsymbol{F}_{DEP} = (\boldsymbol{p} \cdot \boldsymbol{\nabla})\boldsymbol{E} \tag{3.1}$$

where $\boldsymbol{p}$ is the induced dipole moment and $\boldsymbol{E}$ is the electric field. The polarized particles exhibit frequency-dependent behavior in an AC electric field. The DEP behavior of CNTs is determined by their permittivity and conductivity and that of the surrounding medium. CNTs are cylindrical-shaped particles as long, thin rods and experience a force due to the induced dipole moment when placed in a non-uniform electric field.[190] The underlying DEP force exerted on the nanotube is proportional to the CNT length.[191] If the viscous and damping force is neglected and taking into account the ohmic losses of the interface between the CNT and medium, the time-averaged DEP force acting on the cylindrical-shaped nanotube aligned with the field is expressed as [189, 192]:

$$\boldsymbol{F}_{DEP} = \frac{\pi r^2 l}{6} \varepsilon_m Re(CM) \boldsymbol{\nabla} \boldsymbol{E}^2 \tag{3.2}$$

where r and l are the radius and length of the nanotube, ε_m is the medium permittivity, and $Re(CM)$ is the real part of the Clausius-Mossotti *(CM)* factor. Based on equation 3.2, the DEP force experienced by the CNT is proportional to the Clausius-Mossotti factor [35, 154, 193-195]. The electrical polarizability of the CNT is described by the Clausius-Mossotti factor and can be expressed as:

$$Re(CM) = \frac{\varepsilon_p^* - \varepsilon_m^*}{\varepsilon_m^* + (\varepsilon_p^* - \varepsilon_m^*)L} \tag{3.3}$$

where ε_m^* and ε_p^* are defined as complex permittivity of the medium and the particle, respectively, as described in chapter 2, equation 2.16, section 2.2.4.. The depolarization factor L is approximated by [194]:

$$L = \frac{4r^2 * (\ln\left(\frac{l}{r}\right) - 1)}{l^2} \tag{3.4}$$

As $Re(CM)$ depends on the geometry of the particles, and because of the high aspect ratio and consequently very small depolarization factor of most CNTs, Dimanki *et al*. expressed their $Re(CM)$ as:[146]

$$Re(CM) = \frac{\varepsilon_p^* - \varepsilon_m^*}{\varepsilon_m^*} \tag{3.5}$$

The DEP behavior of CNTs is frequency-dependent, allowing tuning of the DEP behavior based on the applied frequency. The permittivity mainly governs the DEP behavior of CNT at sufficiently high frequency (typically MHz and above). It was reported that metallic SWNT has a much larger relative permittivity of $\varepsilon_p > 4000$ while semiconducting SWNT exhibit a relative permittivity, $\varepsilon_p < 5$.[134, 196] It has been reported that metallic SWNTs experience pDEP due to the large ε_p of metallic CNTs surmounting that of most suspension media.[134] For semiconducting SWNTs, ε_p is much smaller, thus

both pDEP and nDEP characteristics have been observed. semiconducting SWNTs may show negative DEP based on their low permittivity at high frequency; however, in an intermediate frequency range, both conductivity and permittivity give rise to a complex dielectrophoretic response. The dielectrophoretic response may be governed by surface conduction in the case of suspended nanotubes at low frequency, as further detailed below. Figure 3.1a demonstrates $Re(CM)$ in the range $10^2 \leq f \leq 10^{10}$ Hz to illustrate the frequency-dependent variation of $Re(CM)$ for semiconducting SWNTs. A SWNT length of 1 μm is assumed, resulting in a depolarization factor of $L = 10^{-5}$ and the SWNTs are considered to be suspended in an aqueous solution due to surfactant wrapping, which also induces a surface charge. The initially positive $Re(CM)$ decreases at above ~10 MHz and above a frequency of $\sim 10^8$ Hz, it drops beyond the crossover frequency (where $Re(CM) = 0$) to negative values indicating nDEP. Note that $Re(CM)$ is positive in this frequency range resulting in pDEP due to the high permittivity of metallic SWNTs. This differing DEP behavior of metallic and semiconducting SWNTs at high frequency (typically > 10 MHz) is a major tool to separate SWNTs and distinguish them, discussed below with various applications later in this chapter.

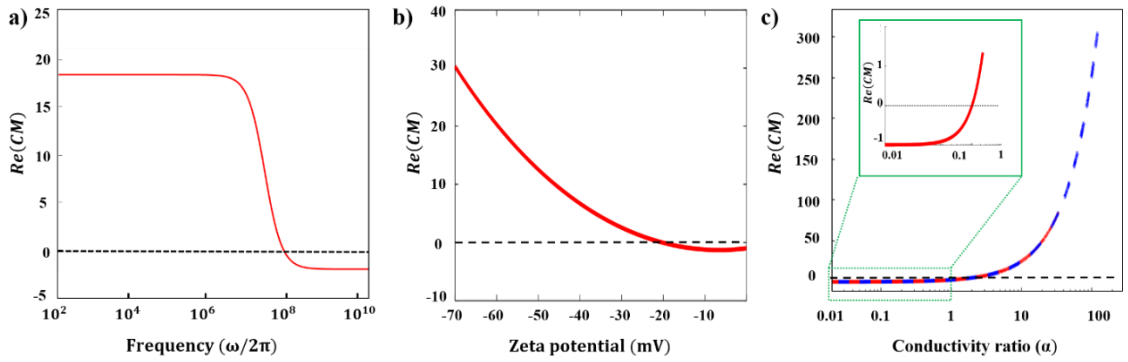

Figure 3.1: Calculated $Re(CM)$ in dependence of frequency, conductivity ratio, and ζ: (a) Variation of $Re(CM)$ with frequency for semiconducting SWNT with parameters ε_p=5 and $\sigma_p = 2.94\ \mathrm{S/m}$ in a medium with σ_m= 0.15 S/m. The particle conductivity for SWNTs wrapped with the surfactant NaDOC. Note that in an intermediate frequency regime, the initially positive $Re(CM)$ drops to negative values. For more details, see text; (b) Dependency of $Re(CM)$ on ζ for NaDOC wrapped semiconducting SWNTs. The dashed line represents $Re(CM)$ =0. Note that $Re(CM)$ changes sign from positive to negative. (c) Calculated $Re(CM)$ vs conductivity ratio at 1000 Hz. The red line indicates semiconducting, NaDOC-wrapped SWNTs. The Black dashed line represents $Re(CM)$=0 and the inset shows that $Re(CM)$ is negative if the conductivity ratio is below 1 (Figure is adapted and reprinted with permission from Rabbani et al., copyright (2020), Electrophoresis.[197])

The frequency-dependent DEP behavior of semiconducting SWNTs is more complex than that of metallic SWNTs.[198] Numerous experimental studies demonstrated that surface conductance contributions dictate the dielectrophoretic behavior at a low and intermediate frequency. One such detailed experimental study of SWNT DEP was reported by Kim *et al.*[35] pDEP was consistently observed at 10 MHz regardless of the surfactant type employed for metallic SWNTs with large ε_p. However, for semiconducting either pDEP or nDEP was observed for small ε_p. Kim *et al.* [35] linked this to the conductivity ratio, $\alpha = \frac{\sigma_p}{\sigma_m}$, and determined that semiconducting SWNTs exhibit pDEP for α >1.19 and nDEP for α < 1.19 at 10 MHz. They further investigated the crossover frequency for semiconducting SWNT and demonstrated a strong dependence on α. This study reveals

that whether semiconducting SWNTs demonstrate pDEP or nDEP at intermediate frequency is determined by the the interplay of conductivity and permittivity.

In recent years, the low-frequency dielectrophoretic response of CNTs has been investigated in more detail, while the high-frequency behavior of CNTs was probed and experimentally demonstrated early on. In the low-frequency regime, the conductivities of the particle and the medium govern the DEP response of CNTs. At low frequency, equation 3.3 can then be expressed as:

$$Re(CM) = \frac{\sigma_p - \sigma_m}{\sigma_m} = -1 + \alpha \tag{3.7}$$

where α is the conductivity ratio, as defined previously. Contributions from their intrinsic conductivity determine the conductivity of the CNTs, σ_{int}, but also by the conductivity arising due to surface charges implied through the adsorption of highly charged wrapping agents or surface functionalization of the CNTs. This is particularly important for semiconducting SWNTs, where the intrinsic conductivity may be neglected.[145] To prevent aggregation and allow further manipulation and specific applications, the wrapping of SWNTs with suitable agents is practiced to suspend them individually in a solvent. the solvent conductivity σ_m is determined by the ionic strength and the solvent is an aqueous solution. As wrapping agents, detergents, polyelectrolytes, or biomolecules such as DNA have been employed. Surface conductance effects can be expressed through the particle conductivity σ_P defined as:[199]

$$\sigma_P = \sigma_{int} + {}^{2\,\lambda_s}/_{a} \tag{3.8}$$

where λ_s is the surface conductance and a is the diameter of a SWNT. The total surface conductance can be modeled from two components: a conductance due to the movement

of charges in the diffuse layer, $\lambda_{s,d}$, and a second due to the movement of charges in the Stern layer, $\lambda_{s,s}$. The SWNT conductivity can be tuned with the surfactants used for wrapping and dispersion in liquid media. The total surface conductance can be expressed as [193]:

$$\lambda_s = \lambda_{s,d} + \lambda_{s,s} \tag{3.9}$$

with

$$\frac{\lambda_{s,d}}{\lambda_{s,s}} = 0.56 \tag{3.10}$$

The diffuse layer conductance is dependent on the Zeta potential (ζ) and can be expressed as [193, 200]:

$$\lambda_{s,d} = \frac{4q^2cz^2}{k_BT\beta}\left[D_+\left(e^{\frac{-zq\zeta}{2k_BT}}-1\right)\left(1+\frac{3m_+}{z^2}\right)+D_-\left(e^{\frac{zq\zeta}{2k_BT}}-1\right)\left(1+\frac{3m_-}{z^2}\right)\right] \tag{3.11}$$

here, q is the charge of an electron, D is the diffusion constant, k_B is the Boltzman constant, m is the ion mobility, β is the reciprocal Debye length, η is the viscosity of the solution, z is the valence of the ion, and c is the ion concentration.

Equations 3.8-3.11, now allow an assessment of $Re(CM)$ based on equation 3.7. The DEP behavior of semiconducting SWNTs depends mainly on the magnitude of the diffuse and Stern layer conductance with a given medium conductivity. As the latter two are governed by ζ of the SWNTs, the DEP phenomenon may be predicted through the measurement of ζ or tuned through an adequate choice of wrapping agents, wrapping conditions, or other surface functionalization. Figure 3.1b demonstrates how variations in ζ may affect $Re(CM)$. With decreasing ζ, $Re(CM)$ drops and eventually reaches negative values, implying a non-frequency dependent crossover from positive to negative DEP.

Recently Rabbani *et al.*[155, 201] reported variations in ζ for sodium deoxycholate (NaDOC) and ssDNA wrapped SWNTs. Using a probe sonicator, they subjected the SWNT with surfactant for various times. Improved wrapping of SWNT leading to a higher ζ was observed for longer sonication times. In contrast, short sonication times resulted in reduced ζ. positive DEP for the well-suspended SWNTs with as the $Re(CM)$ resulted in a positive value of 18.6. $Re(CM)$ of -0.8 was predicted based on the ζ assessment for less well-suspended SWNTs. The well-suspended SWNTs demonstrated pDEP, and the SWNTs exhibiting small ζ demonstrated nDEP, and the corresponding DEP behavior was confirmed with DEP trapping experiments. This low frequency-dependent DEP behavior is summarized in Figure 3.1c, where $Re(CM)$ is plotted in relation to the conductivity ratio, α at 1 kHz. Based on equation 3.7, a change from pDEP to nDEP occurs $Re(CM)$ drops below zero for $\alpha < 1$. Rabbani *et al.* [155] could confirm this behavior with their study on semiconducting SWNT DEP at low frequency.

Finally, we note that the surface conductivity of semiconducting SWNTs can also explain their DEP properties at an intermediate frequency, where the $Re(CM)$ is governed by both permittivity and conductivity. The dependence on surface charge for metallic and semiconducting SWNTs was investigated by Hong *et al.*[145] A switch from pDEP to nDEP was observed when the surface charge of SWNTs was considerably reduced, i.e. when α dropped below a critical value. The surface charge of SWNTs plays an important role in controlling the conductivity ratio was reported by Kang *et al.*[202] and Krupke *et al.*[134] which can switch the SWNT DEP behavior. Kang *et al.* [202], for example, reported that anionic sodium dodecyl sulfate (SDS) and cationic cetyltrimethylammonium bromide (CTAB) wrapped SWNTs displayed high negative (-49.8 mV) and positive (56.8 mV) ζ,

respectively, resulting in pDEP for both metallic and semiconducting SWNTs. On the other hand, a small α was found for nonionic Pluronic-wrapped SWNTs exhibiting a smaller negative ζ (-11.5 mV). A switch from pDEP to nDEP was observed for semiconducting SWNTs under these wrapping conditions. Notably, a switch from pDEP to nDEP for semiconducting SWNTs dispersed in alcohol medium was reported by Lai et al. [147]. Semiconducting SWNT experiences nDEP when the frequency is >10 MHz and undergoes pDEP in the low frequency range (<1 MHz).

3.2. Technical Realization Platforms for DEP Manipulation of SWNTs

Dielectrophoresis can be evoked once electric field inhomogeneities are apparent. Several technical platforms have been realized for the DEP manipulation of CNTs and are briefly discussed below. The reader is also referred to excellent comprehensive reviews related to the state-of-the-art dielectrophoresis techniques.[15, 17, 21] DEP at high frequency was initially suggested as a potential sorting technique of CNTs according to their electrical size and properties.[35, 145] Metallic CNTs were separated from the semiconducting one using DEP by Kang *et al.*[198] due to their differences in DEP behavior, as outlined above. one needs to introduce high electric fields and gradients in the microfluidic device to manipulate CNTs with dielectrophoresis, which can be introduced with the fabrication of microelectrodes or with insulating geometries. Two primary techniques have been adopted to generate high gradients and electric fields for dielectrophoretic manipulation of CNTs with advances in microfabrication techniques.[20, 119, 203] Pohl *et al.*, introduced the first approach called electrode-based DEP (eDEP).[204, 205] In this technique, the microelectrodes are positioned inside the microfluidic channels and typically fabricated in a microfluidic platform to generate a non-uniform electric field.[206] This approach offers analytes to

experience high DEP forces near the microelectrodes. The electrodes make direct contact with the medium and analytes. However, the fabrication process of the electrodes is complex and can be accomplished by various methods, including photolithography, thin film deposition using different metals, and etching techniques.[11, 207, 208] The micro-electrodes can be pairs of electrodes at a close distance, interdigitated electrodes,[209] arrays of electrodes, or quadruple.[210] eDEP allows the investigation of CNTs in the kHz to MHz regime. Even though a high magnitude of DEP forces can be introduced in eDEP devices on the application of low voltages, it has several drawbacks including fouling effects, joule heating, and electrolysis.

A newer approach to generate high electric field gradients in micro-devices is electrodeless DEP, also known as insulator-based DEP (iDEP). iDEP has shown potential in many applications, including chemical, biomedical assessments, bioanalysis, etc.[211] Dielectric obstacles are introduced in the microfluidic channel to generate the inhomogeneous electric field.[29] The iDEP devices are fabricated with photolithography and soft lithography techniques offering low-cost fabrication and biocompatible platforms, an advantage over eDEP platforms. iDEP devices avoid chemical electrode reactions that often occur in eDEP.[28, 212] Low-frequency DEP behavior of the analytes can be examined with iDEP techniques.[17] Due to its transparency, flexibility, biocompatibility, and high insulation properties, Polydimethylsiloxane (PDMS) is widely used as the fabrication material of iDEP devices. Though iDEP offers many advantages, the main limitation of iDEP refers to challenging access to the high-frequency regime and much higher applied potential difference needed to achieve equivalent electric field magnitudes compared to eDEP.[213]

Over the past few decades, the manipulation of CNTs under non-uniform electric fields with DEP microdevices has been explored. Understanding the DEP behavior of CNTs has led to applications of DEP like fractionation, enrichment, trapping, and deflection using different device designs and geometries. SWNTs have been manipulated with iDEP and eDEP mechanisms in the past few decades and are discussed in the sections below.

3.3. SWNT DEP Application

SWNTs have gained much attention for their unique electrical, mechanical, conductive, optical, and dielectric properties. They can be used for biosensors, microelectronics, and reinforced polymer nanocomposites.[157, 214, 215] Initial interest in DEP studies on SWNTs was mainly stimulated by the need for alignment over specific electrodes and geometric structures. Further studies include the demonstration of patterning of SWNTs on surfaces and self-assembly. Alignment of SWNTs is required in most sensing applications of SWNTs and is further summarized later in this section. A controlled self-alignment and assembly of suspended SWNT can be achieved through DEP, resulting in reproducible, well-defined structural arrangements of CNTs for device applications. The following section discusses the studies related to the sensing, self-assembly, and purification reported in the past 15 years for SWNT applications, also enlisted in Table 3.1.

Table 3.1: Selected SWNT DEP applications.

Application	Biological Applications Reported	pDEP/nDEP	Frequency Range	References
Alignment	No	pDEP	5 MHz	Banerjee *et al*. [216]
Alignment	No	pDEP	3-80 MHz	Blatt *et al*. [217] and Banerjee *et al*. [218]
Alignment	No	pDEP	10 MHz	Li *et al*. [219]
Alignment	No	pDEP	10 MHz	Makaram *et al*. [220]
Tunable Array	No	pDEP	51 kHz - 5 MHz	Shekhar *et al*. [221]
Field-effect transistor	No	pDEP	1 MHz	Stokes *etal*. [222, 223]
Field-effect transistor	No	pDEP	5 - 100 MHz	Zhang *et al*. [224]
Transistors	No	pDEP	5 MHz	Kim *et al*. [225]
Transistors	No	pDEP	300 kHz	Taeger *et al*. [226]
Transistors	No	pDEP	50 kHz - 5 MHz	Dong *et al*. [227]
Assembly	No	pDEP	10 MHz	Makaram *et al*. [220]
Assembly	No	pDEP	10 MHz	Burg *et al*. [228]
Assembly	No	pDEP	5 MHz	Seo *et al*. [229]
Assembly	No	pDEP	10-70 MHz	Krupke *et al*. [230]

Assembly	No	pDEP	200 kHz - 15 MHz	Pathangi *et al.* [231]
Assembly	No	both	1 kHz and 5 MHz	Sorgenfrei *et al.* [232]
Assembly	No	pDEP	5MHz	Li *et al.* [233]
Assembly	No	pDEP	100-300 kHz	Vijayaraghavan *et al.* [234, 235]
Assembly	No	pDEP	500 kHz	Zheng *et al.* [236]
Assembly	No	pDEP	10 MHz	Kumatani *et al.* [237]
Assembly	Yes	pDEP	60 Hz	Srivastava *et al.* [238]
Assembly	Yes	pDEP	1 MHz	Kim *et al.* [239]
Separation	No	pDEP	5 MHz	Chen *et al.* [240]
Separation	No	both	10kHz-10MHz	Dimaki *et al.* [146]
Separation	No	both	10 - 50 MHz	Shin *et al.* [241]
Separation	No	pDEP	3-50 KHz	Lutz *et al.* [242]
Separation	No	Both	10 MHz	Krupke *et al.* [134]
Separation	No	Both	1-3 MHz	Peng *et al.* [55]
Separation	No	Both	>10 MHz	Lai *et al.* [147]
Separation	No	pDEP	10 MHz	Padmaraj *et al.* [243]
Separation	No	pDEP	1 MHz	Mendes *et al.* [244]
Separation	No	pDEP	100 kHz	Lee *et al.* [245]
Separation	No	both	1-15 MHz	Mureau *et al.* [246]

NO_2 Gas sensor	No	pDEP	100 kHz	Suehiro *et al*. [247]
H_2 Gas sensor	No	pDEP	100 kHz	Suehiro *et al*. [248]
NH_3 gas sensor	No	both	1 MHz	Lucci *et al*. [249]
pH sensor	No	pDEP	5 MHz	Li *et al*. [250]
Sensor	Yes	both	>100 kHz	Zhou *et al*. [251]
Immunosensor	Yes	pDEP	200 kHz	Singh *et al*. [252]
Deposition	No	pDEP	3 MHz	Ericson *et al*. [253]
Deposition	No	pDEP	2 MHz	Tang *et al*. [254]
Trapping	No	both	1000 Hz	Rabbani *et al*. [155]

3.3.1. Alignment, Self-assembly, and Patterning

DEP represents an excellent tool for manipulating SWNTs, aligning a single SWNT, and allowing accurate spatial positioning and electrode gaps. Selective patterning-based applications and self-assembly using DEP for SWNTs have also been used. Banerjee *et al*. reported that Precise positioning and alignment of SWNTs in a device architecture using DEP.[216, 218] The SWNTs were aligned between two electrodes without any bending due to local electric field hotspots induced by the metal posts in the presence of patterned metal post arrays. A CNT network is composed of randomly oriented semiconducting, and SWNTs aligned with metallic SWNTs were reported by Blatt *et al*.[217] It was reported that semiconducting SWNTs are randomly oriented at high field frequency, while metallic SWNTs were well aligned, and their preferential direction was parallel to the electric field lines. A successful dispersion and large scale-parallel assembly of surface-synthesized SWNTs was reported by Burg *et al*.[228] CVD synthesized SWNTs, and dielectrophoretic

deposition was used to bridge straight, individual, and long SWNTs between two electrodes as shown in Figure 3.2a. A similar approach was reported by Li *et al*.[219], where SWNTs suspended in isopropyl alcohol (IPA) were deposited between two cross-structured electrodes using DEP. Zhang *et al*. reported the deposition of individual semiconducting type SWNTs onto predefined electrodes using DEP.[224] Semiconducting SWNTs suspended in the aqueous sodium dodecyl sulfate (SDS) solution were deposited onto predefined electrodes using DEP at 100 MHz. Specially designed multigap nanoelectrodes to separate and assemble semiconducting and metallic SWNTs were used by Chen *et al*.[240] The gold electrode array exhibited excellent thermal sensitivity with low-power consumption. The sensitivity of their device is dependent on the number of gaps: more gaps lead to higher sensitivity. Metallic SWNTs are subject to the most significant DEP force in the outermost electrode gaps, and enrichment of metallic SWNTs was observed. Accumulating the aligned semiconducting type SWNTs increased in the innermost electrodes where DEP force is lowest.

In the past, SWNTs have also been manipulated using DEP via self-assembly and selective patterning-based applications. Lu *et al.* reported a theoretical study of the assembly of SWNTs using.[255] The influence of electrode type, thermal noise, and electrode voltage on the DEP assembly of SWNTs was analyzed. They used a comb and a parallel electrode to assemble SWNTs using DEP forces. Simulation results showed that the competition decided the array distribution of SWNTs between the strength of the AC electric field and thermal noise. Their experimental result reveals that the comb electrode has a better position control of SWNTs than the parallel electrode. Makaram *et al*. reported a hybrid top-down fabrication with the bottom-up assembly of SWNTs based on three-

dimensional interconnects.[220] When a voltage was applied, SWNTs were assembled on a 3D platform using DEP at room temperature. The scanning electron microscopy revealed a uniform assembly of SWNTs on the electrodes. The effect of the applied electric field frequency in different medium conductivities on the DEP deposition of SWNTs was studied by Naieni *et al*.[256] Their study indicates that CNT deposition remained unaffected by frequency in high conductivity medium. However, for low conductivity media, a change in frequency can alter the rate of CNT deposition around the electrodes. A reproducible and controlled mass production of SWNT bundles using DEP was reported by Seo *et al*.[229] Gold electrodes were fabricated using microfabrication techniques, and SWNTs were aligned between two electrodes following the electric field lines. To achieve controlled alignment of SWNTs between a pair of electrodes using DEP, a similar concept was also reported by Krupke *et al.* [230], Pathangi *et al.* [231], and Dong *et al.*[227] Similar microfluidic devices for well-directed and precise assembly of SWNTs via DEP were also reported by multiple research groups.[221, 232-235, 257, 258] A self-limiting direct assembly of individual SWNTs using DEP on a pair of electrodes was reported recently by Zheng *et al*.[236] DEP methods are unsuitable for large-scale design as disordered SWNTs usually are produced. They used a substrate-bent configuration to overcome this problem and introduced deep gaps at the center of electrode pair arrays. Their fabrication process does not require any chemical modifications of the substrate or SWNTs and is fully compatible with current microfabrication technologies. The optimum condition for deposition was found for $\frac{\varepsilon_p}{\varepsilon_m}$ =100 considering other parameters, such as frequency, electrode space, and applied potential difference are constant. The alignment and self-assembly of CNTs using DEP can be used on a laboratory scale to fabricate many devices with identical SWNT sources,

thereby allowing statistical studies such as on SWNT piezoelectricity or sensing applications.[259, 260]

3.3.2. Sensing-based Applications

Considerable attention for different SWNT-based sensor applications since they have higher selectivity, higher thermal and chemical stability, and faster electrical response for sensing applications. Suehiro *et al*. introduced and fabricated an SWNT gas sensor by DEP on metallic electrodes made of Al, Pd, or Cr.[247, 261] The Al/SWNT sensor resistance increased and showed the highest sensitivity when exposed to NO_2 gas. At room temperature, sub-ppm levels of NO_2 gas could be detected in a few tens of seconds. Later on, the authors also detected H2 gas using an SWNT/Pd gas sensor.[248] The sensor detected 0.052% H_2 in the air at 90°C, and DEP methods were used to fabricate the interface between catalytic palladium (Pd) and SWNT. Lucci *et al*. demonstrated an efficient gas sensor for NH_3 detection using dielectrophoretically aligned SWNTs.[249] Stokes *et al*. demonstrated the fabrication of SWNT-FETs with local Al bottom gates through DEP.[222] Their method offers a convenient way to assemble the gated SWNT-FET devices from the solution. In their technique, the local-gated device offers fast switching behavior due to the channel-controlled mechanism due to the thin local Al gate, and high-temperature growth of SWNTs is not required. Later on, the same group reported the improved device performance of individual SWNT FETs assembled from a commercial surfactant-free solution by DEP.[223] The device showed an on-state conductance up to 6 μS and field-effect mobility up to 1380 cm^2/V s, which was close to the theoretical limit. Kim *et al*. [225] and Taeger *et al*. also reported a similar approach for fabricating SWNT-FET.[226] Li *et al*. characterized and developed a high-performance pH sensor using DEP-aligned SWNTs,

and teeth-shaped electrodes.[250] A linear relationship between pH in the range of 5-9 and normalized resistance was observed highly repeatably. Figure 3.2b shows the SEM image of the aligned SWNTs via DEP and the structure of the sensor. Mureau *et al*. reported an alternative approach to study the accurate measurement of DEP collection of SWNTs using a combination of dielectrophoresis and impedance spectroscopy.[246] Later on, an efficient way to fabricate SWNT-based AFM probes with controlled length and orientation using DEP was demonstrated by Tang *et al*.[254] The fabricated probe could be used to image structures with a large aspect ratio and had a longer lifetime compared to the etched silicon tips.

3.3.3. Separation and Purification

The applicability of SWNTs is often limited due to the various sizes and types of SWNTs, generally synthesized in a polydisperse mixture. Purification and separation of SWNTs are also essential for patterning, self-assembly, and biosensor applications.[262, 263] The electrical frequency-dependent DEP characteristics of SWNTs based on their chirality show promising potential for sorting and separating SWNTs.[264] CNTs can be of a semiconducting or metallic type based on chirality and structure, and different applications of SWNT require either semiconducting or metallic types. It is important to separate metallic SWNTs from the semiconducting types to improve the device performance. Thus, several studies have reported separating SWNTs according to their electrical properties.

A theoretical study to separate metallic SWNTs from semiconducting types was reported by Baik and co-workers.[265] According to their theoretical study, it was found that the DEP behavior of semiconducting SWNTs is primarily dependent on the conductivity ratio σ. By using different wraping agents, the conductivity ratio can be tuned. Mendes *et*

al. reported a theoretical study to separate metallic SWNTs from semiconducting types using DEP.[244] This study showed that 99% sorting efficiency could be achieved by operating in a region where the semiconducting SWNTs are only partially oriented, and metallic SWNTs are completely oriented with the electric field. The efficient manipulation of SWNTs using an optically driven platform was demonstrated by Lee *et al.*[245] By using a photoconductive layer made of amorphous silicon within the developed platform, and a non-uniform electric field was generated. This photoconductive layer, when optically illuminated, spatially acted as virtual electrodes and generated an inhomogeneous electric field that can effectively manipulate SWNTs. The mechanism of translational motion of SWNTs in nematic liquid crystal medium driven by pDEP was demonstrated by Srivastava *et al.*[238] His study showed the amplitude of the translational motion of CNTs inversely proportional to the frequency and is directly proportional to the applied electric field.

Using DEP experimentally, Krupke et al. developed a method to separate metallic SWNTs from semiconducting.[134] Metallic SWNTs were trapped in the microelectrode array, leaving semiconducting tubes in the solvent, SWNTs accumulated on the electrode via DEP, as shown in Figure 3.2c. The separation of metallic and semiconducting SWNTs was observed using dielectrophoresis field flow fractionation reported by Peng *et al.*[55] Additionally, the enrichment of semiconducting SWNTs with band gaps and various diameters was also observed. Lutz et al. reported an earlier attempt to separate metallic SWNTs from semiconducting SWNTs using a macroscopic electrode system.[242] The separation of SWNTs according to their electrical properties with a similar approach using eDEP was recently reported by Kang *et al.*[198] and Lai *et al.*[147] Using nanoscale gap electrodes, Padmaraj *et al.* [243] reported selective alignment inducing separation of SWNTs.

CNTs were separated according to their electrical properties by selective deposition as metallic and semiconducting CNTs aligned parallel or orthogonal to the electric field.

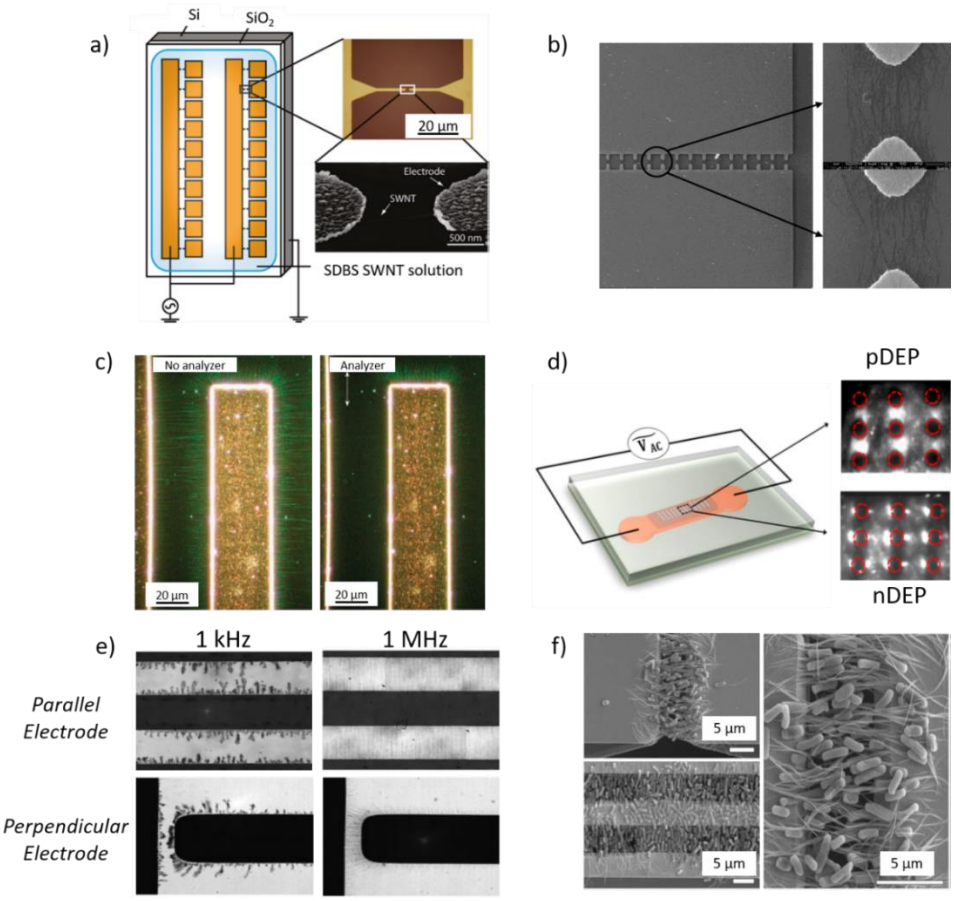

Figure 3.2: Selected DEP manipulation devices for SWNTs. (a) Example of SWNT patterning: (left) The electrical connection and device scheme used for the deposition of individual SWNTs; (right, top) The optical microscope image shows an electrode pair, and (right, bottom) the SEM image shows the successful DEP deposition of 2µm long SWNTs on the electrodes. (b) Example for dielectrophoretically assembled SWNTs: SEM image of the teeth like sensor structures and dielectrophoretically aligned SWNTs at 5 MHz with an applied voltage of 10 V. SWNTs are deposited in between electrode pairs where the electric field is highest. (c) Dark-field micrograph of deposited SWNTs via dielectrophoresis. Because of strong Rayleigh scattering in the green wavelength range, the deposited SWNTs appear green. The homogeneity of the nanotube alignment can be visualized by inserting a polarization filter. When this analyzer was placed perpendicular to the deposited electrodes (right) the scattered light is not visible over large area.
(d) Selective trapping of NaDOC coated SWNTs between insulating posts in an iDEP device. Trapping occurred between the two posts when 1000 V/cm was applied at 1000 Hz. Dependent on ζ of wrapped SWNTs, pDEP or nDEP can be observed. (e) SWNTs self-assembly at microelectrodes under different frequency conditions: The left column

represents the assembly of SWNTs at 1 kHz, and the right column represents the assembly of SWNTs at 1MHz at SWNT concentration of 0.2 mg/mL. The top two frames show parallel electrodes with 100 μm in width with 100 μm separation. The bottom two images represent perpendicular electrodes of 106 μm width and 50 μm separation. At low frequency (1 kHz), SWNT self-assembly was confined to a thin boundary near the electrodes (left column). When the frequency was increased to 1 MHz, SWNTs formed thin uniform wires that bridged the gap (right column). (f) SEM image of E. coli attached SWNT films using DEP: The top left image shows the entire configuration and the left image is the magnified view of the gap between the two electrodes. Bacteria are trapped between electrodes when a frequency of 1 MHz and a voltage of 7 Vpp are applied. (Figure is adapted and reprinted with permission from Rabbani et al., copyright (2020), Electrophoresis[197])

According to their DEP properties, Shin et al.[241] reported a continuous fractionation method for metallic and semiconducting SWNTs. DEP forces were generated by using an H-shaped microfluidic device with integrated electrodes. The metallic SWNT experienced a higher magnitude of DEP force than semiconducting SWNTs in the applied frequency range, and high purity metallic SWNTs were continuously extracted from a mixture. The semiconducting SWNTs remained in the original fluid stream while the higher DEP force deflected metallic SWNTs from the fluid stream. Dimaki and co-workers previously reported a similar concept of aligning SWNTs.[146] This study suggests both metallic and semiconducting type SWNTs experience pDEP for frequency <200 MHz; however, they can be separated due to a difference in the magnitude of experienced DEP force. Rabbani et al. recently reported continuous fractionation of SWNTs by length using an insulator-based dielectrophoresis constriction sorter.[266] A sorting efficiency of up to 95% in specific outlets was observed for SWNTs with a length of ≥1μm and nDEP corresponding to short sonication times, small ζ. For the pDEP case, under the same flow conditions and applied potential differences, SWNTs with lengths of ≤300nm were sorted into the center outlet with an efficiency of ~90%. This study provided a numerical model and experimental

fundamentals of fractionating SWNTs by length, which will be useful for the separation and purification of SWNTs for future applications.

3.3.4. Surface Functionalization and Biological Applications

SWNTs can exhibit variation in their DEP properties based on the surface modifications. Due to van der Waals interactions, CNTs often tend to aggregate and bundle, which hampers the potential technological application of CNTs. The surface modification of CNTs can prevent such effects, as discussed in section 2.5.2.2. Briefly, the functionalization of SWNTs can be accomplished by the attachment of organic and inorganic moieties to their tubular structure. The functionalization can improve the chemical compatibility and suspension properties of SWNT that are required in their nanomaterial and technological applications. Covalent and noncovalent functionalization strategies are mainly used for the surface modification of SWNTs.[267] To enhance the dispersion of SWNTs in the target medium, covalent functionalization is commonly used. The chemical modification with carboxylic groups on the surface of SWNTs can improve the adhesion or wetting characteristics and reduces agglomeration.[268] The noncovalent functionalization of SWNTs is based on molecular interactions via different adsorption forces. The noncovalent functionalization by adsorption can be achieved by biopolymers using surfactants, small aromatic molecules, or polymer wrapping. Surfactants often functionalize CNTs, but biomolecules such as peptides, proteins, and nucleic acids have also been employed.[268-270]

Baik and co-workers studied the effect of sidewall functionalization on the DEP mobility of SWNTs.[265] a high degree of alignment was observed for both metallic and semiconducting SWNTs deposited across a microelectrode gap when SWNTs were

dispersed in an aqueous solution of 1 wt% dodecyl sulfate. When SWNTs were functionalized using diazonium salts, fewer nanotubes were deposited between two electrodes. The sidewall functionalization might sterically impede ion mobility on the surface and decrease the intrinsic conductivity of the metallic SWNTs, thereby reversing the sign of $Re(CM)$. Recently Rabbani *et al.* provided an example of low frequency DEP of SWNTs.[155, 201] selective trapping of surfactant and ssDNA wrapped SWNTs was observed in a post array iDEP device. Figure 3.2d represents the pDEP or nDEP properties of SWNTs. The variation in DEP behavior could be linked to Zeta potential and thus SWNT conductivity differences of the wrapped SWNTs.

Improved capturing of targets like bacteria, microbes, etc., has been achieved recently using SWNTs. Zhou *et al.* reported the detection of bacterial cells and microparticles with SWNTs.[251] SWNT were self-assembled in branches at low frequency (< 1 kHz). Figure 3.2e represents self-assembled SWNTs to form thin uniform wires bridged between electrodes when the frequency increases to 1 MHz. The SWNT assembly was confined in a thin layer near the electrode boundary. pDEP-based trapping of the complexes at a high frequency (>1 MHz) has also been used to detect and capture bacteria and microparticles by using the high polarizability of SWNTs. Singh *et al.* reported the detection of influenza virus with a sensitive, label-free, and selective electrical immunosensor using dielectrophoretically deposited SWNTs.[252] The immunosensor detected one plaque-forming unit per sample unit volume (PFU/mL) of the influenza virus from the mixture with MS2 bacteriophages. Kim *et al.* reported Immobilization of Escherichia coli (E. *coli*) cells and their DEP trapping in a microfluidic setup using

SWNTs.[239] The captured bacteria on the formed SWNT film can be tuned by varying the electric field and cell density, as shown in Figure 3.2f.

4. SINGLE-WALLED CARBON NANOTUBES PROBED WITH INSULATOR-BASED DIELECTROPHORESIS

4.1 Abstract

Single-walled carbon nanotubes (SWNTs) offer unique electrical and optical properties. Common synthesis processes yield SWNTs with large length polydispersity (several tens of nanometers up to centimeters) and heterogeneous electrical and optical properties. Applications often require suitable selection and purification. Dielectrophoresis is one manipulation method for separating SWNTs based on dielectric properties and geometry. Here, we present a study of surfactant and ssDNA wrapped SWNTs suspended in aqueous solutions manipulated by insulator-based dielectrophoresis (iDEP). This method allows us to manipulate SWNTs with the help of arrays of insulating posts in a microfluidic device around which electric field gradients are created by the application of an electric potential to the extremities of the device. Semiconducting SWNTs were imaged during dielectrophoretic manipulation with fluorescence microscopy making use of their fluorescence emission in the near IR. We demonstrate SWNT trapping at low-frequency alternating-current (AC) electric fields with applied potentials not exceeding 1000 V. Interestingly, suspended SWNTs showed both positive and negative dielectrophoresis, which we attribute to their Zeta potential and the suspension properties. Such behavior agrees with common theoretical models for nanoparticle dielectrophoresis. We also show that the measured Zeta potential and suspension properties are in excellent agreement with a numerical model predicting the trapping locations in the iDEP device. This study is fundamental for the future application of low frequency AC iDEP for technological applications of SWNTs.

4.2. Introduction

Single-walled carbon nanotubes (SWNTs) possess unique electronic, mechanical, optical and structural properties which can be exploited for future nanoscale applications.[37, 271-275] Their use in nanoscale electronics ranges from field-effect-Schottky-type transistors,[37, 275, 276] nanometer sized semiconducting devices, probes,[277] data storage or field emission sensors[272] to biological transporters and biosensors.[48] SWNTs have also been exploited as mechanical sensors in living cells thanks to their unique fluorescence properties including superb photostability[278, 279] and fluorescence emission in the IR range[280-282] where autofluorescence in biological samples is minimal.

Typically, SWNTs are produced in processes yielding mixtures with broadly dispersed diameters, lengths (from 10 nm up to 1 cm)[283] and chirality. Chirality is important to determine electrical and optical properties of SWNTs.[284, 285] Producing SWNTs with defined lengths or chiralities has not been achieved. One of the most successful fabrication methods is the high-pressure carbon monoxide (HiPco) process, yielding SWNTs in diameters of ~ 1 nm, lengths from several tens of nm to a few micrometers and preferred, but not unique chirality.[286, 287] In addition, SWNTs form adducts and bundles through van der Waals forces[282] during fabrication. Applications of SWNTs thus require overcoming the challenges related to post-synthesis separation steps.

Various separation methods of SWNTs have been reported according to their electronic type,[54, 288] and these separated nanotubes can be used in future electronic device components.[289] In applications requiring SWNTs in aqueous solutions, they must be suspended using a surfactant or wrapping agent, influencing their surface charge and Zeta potential. Sorting of suspended SWNTs has been attempted with ion-exchange [57] and size-

exclusion chromatography.[290] The combination of the two has even allowed the separation of similar-sized diameter SWNTs by chirality.[291] The method is, however not generally applicable to samples with large variations in diameters or chirality. Ultracentrifugation, including density gradient methods, has been used for sorting, yielding small amounts that can be employed for selected applications.[292] In addition, the unique chemical reactivity of ends or side walls of SWNTs has been exploited for sorting as well as to selectively break down non-desired species in SWNT mixtures through etching approaches.[293] Sorting of SWNTs can also be carried out in direct current electric fields via electrophoresis employing sieving matrices.[294, 295]

An alternative electrical separation method for SWNTs is dielectrophoresis. Alternating current dielectrophoresis (AC DEP) has gained attention as a potential technique for sorting carbon nanotubes according to their electrical properties.[145, 273, 296, 297] When a cylindrical nanotube is placed in a non-uniform electric field, it will experience a force due to the induced dipole moment.[273, 298] Depending on the polarization properties of the nanoparticles and the surrounding medium, particles can be manipulated or trapped using DEP. Particles experiencing positive DEP (pDEP) drift towards the regions of largest electric field strength, while the underlying dielectrophoretic force is proportional to the carbon nanotube length.[299] The dielectrophoretic force strongly depends on the frequency of the electric field and the frequency-dependent electrical properties of particles. The frequency dependence is manifested in the Clausius-Mossotti factor, which may have complex frequency behavior. Thus, the DEP behavior of SWNTs can be tuned with the applied frequency. It has been reported that metallic nanotubes always experience pDEP due to their large dielectric constant.[273] Depending on the electric field frequency and

particle surface conductivity, semiconducting SWNTs can show either positive or negative DEP.[145, 285, 296] Therefore, DEP has been used to separate metallic from semiconducting SWNTs.[273, 300] The transport and trapping properties of DEP can also be employed as a means to control large-scale or even single SWNT deposition for electronic applications.[301, 302]Inhomogeneous electric fields for AC DEP can be generated in two different ways: (i) by introducing microelectrodes in a sample chamber, or (ii) by constructing topological structures between macroelectrodes.[303] Electrode-based DEP (eDEP) is an established method where μm-sized electrodes are patterned on a substrate. These electrodes can be quadruple electrodes,[304] pairs of electrodes at close distance,[305] or interdigitated electrodes.[299] With eDEP, high frequencies can be reached, and the DEP response of nanoparticles can be investigated in the kHz to MHz regime. The other, newer approach is insulator based DEP (iDEP) where different dielectric obstacles are introduced in a microfluidic channel producing inhomogeneous electric fields when an electrical potential is applied between the access ports of the microfluidic device.[29] With an iDEP device, DC and low-frequency DEP behavior of particles can be examined.[117] iDEP devices avoid chemical electrode reactions that can occur in eDEP applications, fabrication steps are facilitated and the electric field gradient can be generated along the entire depth of microfluidic devices.[28, 306]

iDEP at low frequencies < 1kHz as an alternative approach to manipulating SWNTs has not been used. At low frequencies, the DEP of nanoparticles is mainly governed by their conductivity and that of the surrounding medium[307, 308] (see theory section for more detail) and critically depends on the wrapping agent used to suspend the SWNTs.[145] We here report on the DEP characteristics of SWNTs using an insulator-based microfluidic

system. We have studied the dielectrophoretic behavior of SWNTs wrapped with single-stranded DNA (ssDNA) or with sodium deoxycholate (NaDOC) at frequencies up to 1 kHz. The resultant DEP trapping behavior of semiconducting SWNTs was investigated by infrared fluorescence microscopy in an elastomer microfluidic channel. We correlate the observed dielectrophoretic behavior with differences in the Zeta potential, which, in turn, depends on the method used for the suspension of the investigated SWNTs.

4.3. Materials and Methods

4.3.1. Chemicals

SWNTs (batch number 189.2) were obtained from Rice University (TX, USA) through a materials transfer agreement. Sodium hydroxide (NaOH) was purchased from Merck KGaA (Germany), N-(2-hydroxyethyl) piperazine-N'-2-ethanesulfonic acid (HEPES), single-stranded DNA composed of 30 tyrosine bases (dT30), sodium deoxycholate (NaDOC) and Pluronic F-108 were purchased from Sigma-Aldrich (MO, USA). Muscovite Mica (V-5, sheet size 50×75 mm, thickness 0.15-0.21 mm) was purchased from Science Service (Germany) and (3-aminopropyl) triethoxysilane (APTES) was obtained from Sigma-Aldrich (MO, USA). Sylgard® silicone elastomer kit for polydimethylsiloxane (PDMS) was obtained from Dow Corning Corporation (MI, USA). Glass slides (40 mm×50 mm) were from Menzel GmbH and purchased through Thermo Scientific (Germany). Deionized (DI) water was produced using an Arium® 611 ultrapure water system from Sartorius (Germany).

4.3.2. Microchip Fabrication

The microfluidic chip layout was designed with AutoCAD and then patterned on a silicon wafer by standard photolithography. From this master wafer, a PDMS mold was

prepared via standard soft lithography procedures.[309] Briefly, liquid PDMS was mixed with PDMS curing agent in a ratio of 10:1 (w/w). The mixture was poured on the master wafer, degassed using a vacuum desiccator, and heated in an oven for 4 h at 80°C. The mold was subsequently removed from the master wafer, and 3 mm diameter reservoirs were punched manually by a puncher at the beginning and end of the post array portion of the corresponding microchannel. The PDMS mold was cut into slabs of appropriate size, and these slabs and glass slides were cleaned with isopropanol and distilled water, dried with a stream of nitrogen and baked on a hot plate at 90°C until completely dried. Both surfaces were activated with an oxygen plasma (PDC-001: Harrick Plasma cleaner/sterilizer, USA) at high power (18 W) for 30 s. After the plasma treatment, the PDMS slab was pressed against a glass slide to form a closed microchannel system and then placed on a hot plate at 90°C for 3-5 min. The chamber was then filled with DI water, washed several times with DI water by suction and then the surface was treated with Pluronic F108 (1% w/v) and incubated overnight prior to use as described previously.[310] With surface treatment particles can experience strong DEP force and can be immobilized towards the dielectric obstacles, even at higher medium conductivity.[307, 308] As F180 and SWNTs both are negatively charged, coating surface with F108 prevent the SWNTs sticking with surface during the experiment.

The PDMS channel was 1.5 cm long with a post array section integrated over ~1 cm as shown in Figure 4.1c. The posts had a diameter of 10 µm, the row distance was also 10 µm and the post to post distance in one row was 5 µm.

4.3.3. SWNT Sample Preparation

SWNTs were solubilized by wrapping with either surfactant (NaDOC) or single-stranded DNA (dT30). NaDOC (1% w/v) was dissolved in 10 mM HEPES buffer at pH 7. A glass scintillation vial was cleaned with ethanol and dried with a stream of nitrogen. Then, ~2 mg SWNTs were carefully transferred to the clean vial with a spatula, and 2 ml of NaDOC solution was added. The vial was placed in a bucket with ice and sonicated with a 2 mm Microtip sonicator (Sonics & Material INC, Danbury, CT, USA) at 20 kHz and 20 W. Two types of NaDOC coated SWNT samples were prepared. Sample A was prepared by 20 min sonication, and sample B was prepared by 60 min sonication. After sonication, the SWNT suspension was transferred to an Eppendorf vial and centrifuged (Sigma 1-14 centrifuge, Germany) at 14000 rpm for 15 min. After centrifugation, the pellet was discarded, and the supernatant was collected to be used in experiments and stored at 4°C. For ssDNA wrapping of SWNTs, DI water was added at a 1:1 (w/w) ratio to dry ssDNA to yield about 0.5 mL of 1 mg/mL concentration. The vial was centrifuged at low spin speed for a few seconds and vortexed for a few seconds repeatedly for approx. 5 min to ensure homogeneous solubilizing of ssDNA. In the next step, ~1 mg SWNTs was transferred to a clean glass scintillation vial, and DNA solution was added to the SWNTs. Then the sample was sonicated at 20 kHz and 20 W for 90 min as described above. After sonication, the sample was ultra-centrifuged (Optima™ Ultracentrifuge 28000 rpm, Beckman Coulter, Germany) for 90 min at 4°C. After centrifugation, the supernatant was collected and stored at 4°C prior to experiments. Surface charge was measured with a Zetasizer Nano ZS instrument (Malvern, USA). Five trials were made, and the average Zeta potential value determined. An Orion-3 Star conductivity meter from Thermo

Scientific (Germany) was used to measure medium conductivity. The conductivity meter was calibrated with a standard NaCl solution (conductivity of 0.1413 S/cm and 692 ppm).

4.3.4. SWNT Imaging

SWNTs were imaged as previously reported.[48] Briefly, a sample rich in fluorescent (6,5) carbon nanotubes with an excitation maximum of 567 nm and emission maximum of 975 nm were used in this work. SWNTs were excited by a 561 nm DPSS laser (500 mW cw; Cobolt Jive™; Cobolt). A neutral density filter (NDC-50C-4M, Thorlabs) served to adjust the intensity of the beam. The laser beam was directed into the back aperture of a high-NA objective (Zeiss, alpha Plan-Apochromat, 100x, NA = 1.46). Fluorescence light was collected through the same objective and passed through a dichroic beam splitter (630 DCXR; AHF Analysentechnik), further filtered using a 900 nm long-pass filter (F47-900; AHF Analysentechnik) and focused on a short-wave infrared (SWIR) camera with an InGaAs detector (XEVA-SHS-1.7-320 TE-1, Xenics). Images of SWNTs were recorded with 100 ms exposure times. Data analysis was performed with ImageJ software. Five trapping regions were chosen from a representative image in each case, and pixel intensities were extracted, averaged, and normalized with the largest intensity in each case. Origin 8.5 software was used for plotting the normalized data with associated error bars at the different applied potentials.

4.3.5. Atomic Force Microscopy

Atomic force microscopy (AFM) was used to determine lengths and diameters of the SWNTs. The SWNT suspensions were incubated on mica surfaces (Grade V1, Ted Pella, Inc. USA) for 15 min, washed with DI water and dried. A Nanotec AFM instrument

(Nanotec, Spain) was used for imaging SWNTs in tapping mode. SWNT length was measured for about 100 nanotubes for each sample.

4.3.6. Computation of Electric Field

A section of the microfluidic device matching the post array geometry was drawn in COMSOL Multiphysics version 5.2a. Domains for the microchannel material and solvent were assigned and material properties chosen according to pre-defined parameters in COMSOL for PDMS and water. The electric field within the designed geometry was solved by choosing a stationary study with the Electric Current module. It solves Maxwell's current equation with appropriate boundary selection with the posts and side walls considered electrical insulators. The inlet boundary was considered the input of the electric potential and a positive potential was applied. The outlet boundary was grounded. The current density was solved by calculating the electric field intensity with this module.

4.4. Theory

Following the literature, we briefly describe the DEP force on a single walled carbon nanotube. When a cylindrical solid particle is placed in a non-uniform DC electric field, it experiences a dielectric force as described in equation 3.2, section 3.1, chapter 3.In the case of a hollow tube, the geometry factor will be replaced by $\pi l\delta(2r-\delta)$ with the wall thickness δ. The real part of equation 3.2 can be represented as:

$$Re(CM)=\frac{-(1+L){\sigma_m}^2+\sigma_p\sigma_m+\varepsilon_m(\varepsilon_p-\varepsilon_m)\omega^2+L\left({\sigma_p}^2-{(\varepsilon_m-\varepsilon_p)}^2\omega^2\right)}{(1+L)^2{\sigma_m}^2+2L(1+L)\sigma_p\sigma_m+{\varepsilon_m}^2\omega^2+2\varepsilon_m(\varepsilon_m-\varepsilon_p)L\omega^2+L^2\left({\sigma_p}^2+{(\varepsilon_m-\varepsilon_p)}^2\omega^2\right)} \quad (4.1)$$

For $\rightarrow 0$, $Re(CM)$ becomes:

$$Re(CM)=\frac{-(1+L){\sigma_m}^2+\sigma_p\sigma_m+L{\sigma_p}^2}{(1+L)^2{\sigma_m}^2+2L(1+L)\sigma_p\sigma_m+L^2{\sigma_p}^2} \quad (4.2)$$

The Clausius-Mossotti factor for SWNTs can be estimated based on intrinsic parameters. The relative permittivity for metallic and semiconducting SWNTs was reported as 4000 and 5, respectively.[145, 273] For nanoparticles, it has been shown that the effective particle conductivity consists of the intrinsic conductivity and of surface conductivity near the particle. It was reported that the radius of sodium dodecyl sulfate-suspended SWNTs is approximately 2.7 nm because a double layer is formed around the radial direction of the nanotubes.[145] This value was used for the particle conductivity calculation in this study. The internal conductivity of semiconducting SWNTs can be taken as approximately zero because of the large band gap.[145] The surface conductance λ_s is the sum of the diffuse layer conductance, $\lambda_{s,d}$, and the Stern layer conductance, $\lambda_{s,s}$, where the ratio of diffuse layer conductance and Stern layer conductance has been reported as 0.56.[311] The diffuse layer conductance can be calculated from the Zeta potential, ζ, of SWNTs and the properties of the electrolyte, using the following equations[145, 312]

$$\lambda_{s,d} = \frac{4q^2nz^2}{k_BT\beta}\left[D_+\left(e^{\frac{-zq\zeta}{2k_BT}}-1\right)\left(1+\frac{3m_+}{z^2}\right) + D_-\left(e^{\frac{zq\zeta}{2k_BT}}-1\right)\left(1+\frac{3m_-}{z^2}\right)\right] \tag{4.3}$$

with

$$\beta = \sqrt{\frac{2q^2z^2n}{\varepsilon k_BT}} \tag{4.4}$$

and

$$m_{\pm} = \frac{2}{3}\frac{\varepsilon}{D_{\pm}\eta}\left(\frac{k_B T}{q}\right)^2 \quad (4.5)$$

here, $\lambda_{s,d}$ is the diffuse layer conductance, q is the charge of an electron, D is the diffusion constant, k_B is the Boltzman constant, m is the contribution from electroosmotic transport, β is the reciprocal Debye length, η is the viscosity of the solution, z is the valence of the ion, and n is the ion concentration. The surface conductivity can be obtained from the Zeta potential, which was assessed experimentally in this study (see Table 1). The effective particle conductivity can then be calculated using equation 4.3-4.5, the surface conductivity λ_s $(= \lambda_{s,d} + \lambda_{s,s})$ and Eq. 6. Note that this calculation accounts for an ideally suspended SWNT with no interactions with other particles or aggregation. Parameters used were q = 1.60×10^{-19} C, n = 2.05×10^{25} m^{-3} for NaDOC wrapped SWNTs (n = 5.5×10^{23} m^{-3} for ssDNA wrapped SWNTs), z = 1, k_B = 1.38×10^{-23} J K^{-1}, T = 297 K, D_+ = 1.334×10^{-9} m^2 s^{-1}, D_- = 1.334×10^{-9} m^2 s^{-1}, η = 0.890×10^{-3} K g m^{-1} s^{-1} (for water) as well as the permittivity of water $\varepsilon = 80\ \varepsilon_0$ with ε_0 = 8.854×10^{-12} F m^{-1}.

4.5. Results and Discussions

For this study, SWNTs were solubilized by wrapping with the surfactant NaDOC or with dT30 single-stranded DNA, and their iDEP behavior was studied in a microfluidic device. Figure 4.1a-b shows AFM images of NaDOC- and DNA-wrapped SWNTs together with schematic drawings of wrapping. AFM imaging revealed a height of 1.52 ± 0.6 nm for NaDOC-coated SWNTs and an average length of 1050 ± 610 nm. For SWNTs wrapped with ssDNA, an average height of 1.33 ± 0.64 nm was found as well as an average length of 1100 ± 550 nm. A PDMS microfluidic chip was used to test the DEP behavior in trapping experiments as shown in Figure 4.1c. Figure 4.1d represents the numerically calculated

electric field in the circular post array in a representative section of the device. We present iDEP trapping results for two NaDOC-wrapped SWNT samples differing in the sonication time during suspension and one ssDNA-wrapped SWNT sample, as listed in Table 4.1. All results presented below relate to semiconducting SWNTs observed through their infrared fluorescence upon excitation with a 561nm laser. Metallic SWNTs do not fluoresce and are not probed with our method.

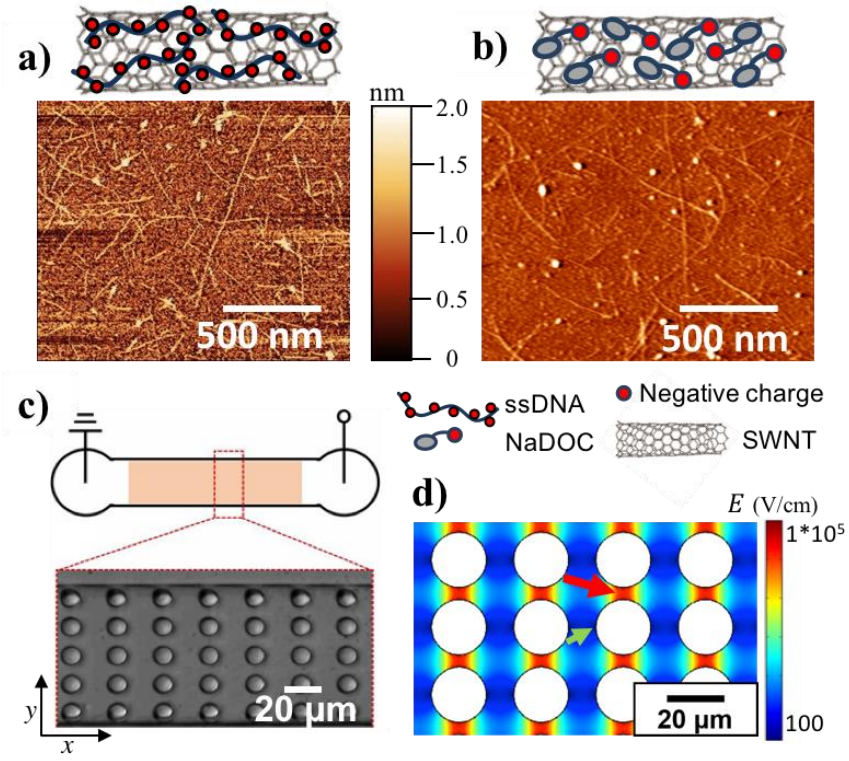

Figure 4.1: SWNT characterization and microfluidic device scheme: a) Schematic drawing of ssDNA-wrapped SWNT and AFM image of ssDNA-suspended single SWNTs. b) Schematic drawing of NaDOC-wrapped SWNT and AFM image of NaDOC-suspended single SWNTs. c) Schematic of microfluidic device employed for iDEP and bright field microscopy image of a section of the post array. d) Electric field distribution as obtained from a COMSOL model in a section of the post array at an applied electric potential of 1000V across the 1.5cm long microchannel. The green arrow (small) points towards the region with the lowest electric field and the red arrow (large) points at the region with the highest electric field. (Figure is adapted and reprinted with permission from Rabbani et al., copyright (2017), Anal. Chem.[355])

4.5.1. Prediction of iDEP Trapping Regions for SWNTs

Depending on the sign of $Re(CM)$, nDEP or pDEP particle trapping may occur. Since SWNT DEP trapping behavior at low frequency has not been reported previously, we developed a numerical model to predict the trapping locations of SWNTs in an iDEP microfluidic device with COMSOL Multiphysics 5.2a. The model accounts for the device geometry, applied potentials scaled to the device section modeled, resulting electric field as well as electric field gradients, and diffusion properties of the particles and allows to track the particle positions due to DEP forces in a time dependent study. Particles are released at specific positions within a post array section and their migration can be traced over time. Figure 4.2a shows the result of a study for the nDEP and pDEP case. SWNTs released in between two post rows and subject to DEP forces according to a negative $Re(CM)$ accumulate in the regions between two post rows of different rows, as shown in Figure 4.2a. These locations correspond to the lowest electric field regions, as indicated by the gray scale surface plot in Figure 4.2a. In contrast, Figure 4.2b represents the pDEP trapping behavior of SWNTs when a positive $Re(CM)$ is assumed. In this case, SWNTs are trapped between the two posts in the same row, where the strength of electric field is highest. Thus, the pDEP trapping regions differ distinctively from the nDEP trapping regions. Note that the model parameters were adapted to reflect the case of sample A (nDEP) and sample B (pDEP) for NaDOC-wrapped SWNTs, as experimentally investigated below. Details of the numerical model and supplementary movies showing the migration of SWNTs to the final trapping positions are available as supplementary information.

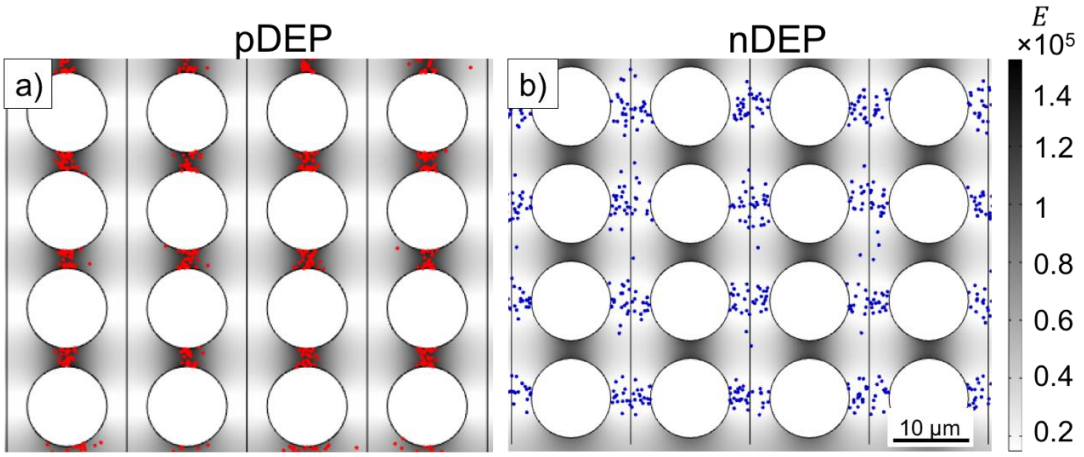

Figure 4.2: Predicted trapping positions of SWNTs subject to iDEP: a) SWNT trapping position predicted with the numerical model for $Re(CM) > 0$. The applied potential to this 200µm long channel section was adapted reflecting the case of 1000V applied over a 1.5cm. The image shows the end position of xxx SWNTs (shown as red dots) released from each vertical line. SWNTs experienced pDEP and accumulated between two posts in the same raw where the highest electric field strength was. b) SWNT (shown as blue dots) trapping position predicted with the numerical model for $Re(CM) < 0$. The applied potential is same as in a). The image shows the end position of xxx SWNTs released from each vertical line. SWNTs experienced nDEP and accumulate between two rows, where the electric field strength is lowest. The grey scale surface plot in a) and b) indicated electric field strength. (Figure is adapted and reprinted with permission from Rabbani et al., copyright (2017), Anal. Chem.[355])

4.5.2. Experimental Observation of SWNT iDEP

Next, the iDEP trapping behavior of two NaDOC-wrapped SWNT samples was studied. Applied frequencies ranged between 0 and 1000 Hz and potentials between 0 and 1000 V across a channel of 1.5cm length. Figure 4.3a shows an image of a microchannel filled with NaDOC-suspended SWNTs without an externally applied potential. SWNTs were evenly distributed around the posts in the channel. Figure 4.3b-c represents Sample A's trapping behaviorA probed at frequencies of 70 Hz and 700 Hz with an applied potential of 1000 V over the 1.5cm ong microfluidic channel. Figure 4.3b shows that NaDOC-wrapped SWNTs were trapped at the left and right side of a post at 70 Hz in x-

direction. These positions correspond to the lowest electric field strength in the post array as apparent from comparing with Figure 4.1d and the electric field suface plot also shown in Figure 4.2a. It is also apparent that the trapping positions correspond to those resultant from the numerical model assuming nDEP for SWNTs as demonstrated in Figure 4.2a indicating excellent agreement between experiment and numerical model. The observed trapping positions also correspond to those previously observed for polystyrene beads exhibiting nDEP.[46] At 700 Hz, NaDOC-suspended SWNTs showed the same nDEP trapping behavior (Figure 4.3c). The trapping behavior was investigated at frequencies up to 1000 Hz (data not shown), with the trapping positions not changing in the post array. This indicates that the DEP behavior is not frequency dependent in the range tested.

We also note that some nanotubes were not trapped. We attribute this to the large length distribution (approx. 400-1600 nm) of suspended SWNTs after the sonication process. Smaller SWNTs do not experience large enough DEP forces to be trapped. In addition, a residual flow can be caused by hydrostatic pressure differences or electroosmotic forces due to a DC voltage offset preventing smaller SWNTs from being trapped.

Next, the DEP behavior of Sample B was investigated (Figure 4.3d) which was prepared with 60 min sonication time. We note that the location of DEP trapping in the post array changed and was now consistent with pDEP, i.e. SWNTs accumulated at the regions with the highest field strength. These trapping regions coincide well with the regions predicted by the numerical model, indicating excellent agreement between experiment and model. However, the change from nDEP for Sample A to pDEP for Sample B is unexpected and will be further examined below.

In addition, the iDEP trapping behavior was studied for various applied potentials by analyzing the fluorescence intensity in the corresponding trapping regions. The fluorescence intensity is indicative of SWNT concentration due to iDEP trapping. As shown in Figure 4.3e-f, for both Sample A and Sample B, above a threshold potential of 300 V accumulation in the pDEP or nDEP trapping regions occurs. In addition, a plateau is reached in both cases upon which no significant increase in the concentration of SWNTs in the trapping regions is observed. This can be explained by the accumulation of all SWNTs experiencing a sufficiently large DEP force.

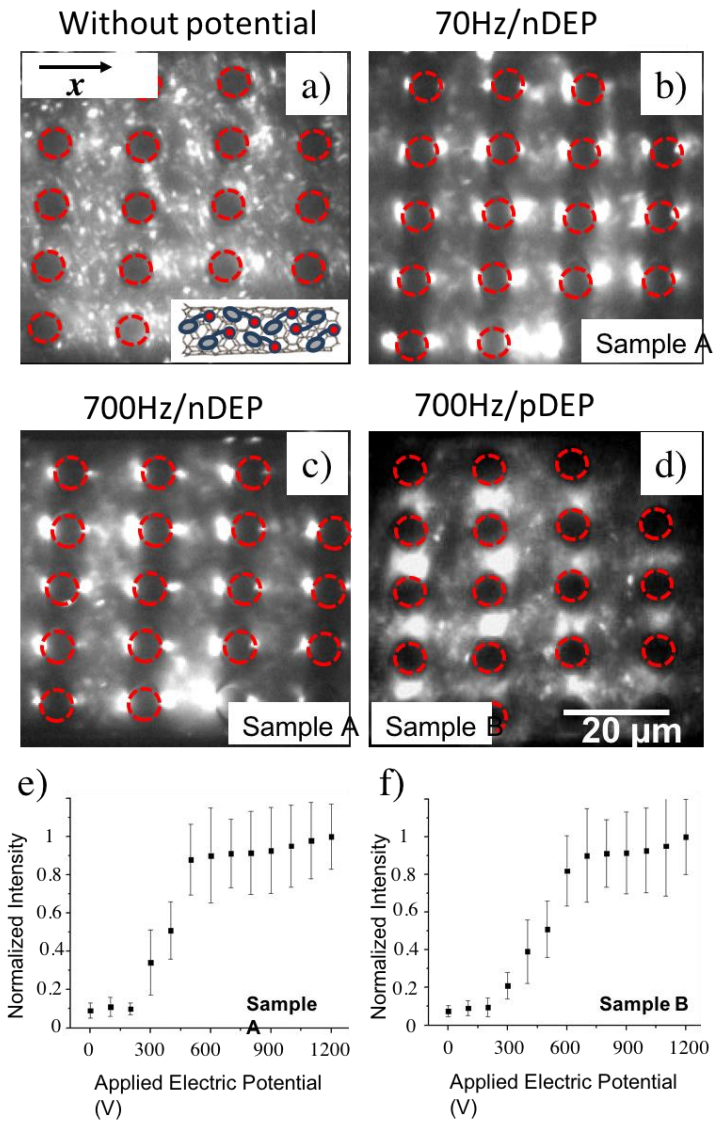

Figure 4.3: DEP trapping of NaDOC-wrapped SWNTs: IR fluorescence imaging of NaDOC-wrapped SWNTs subject to DEP trapping: a) Without potential, no trapping was observed. b) A potential of 1000 V was applied over the entire microchannel of 1.5 cm length at 70 Hz (external field direction horizontal) for Sample A (20 min sonication). SWNTs accumulated in the regions of lowest electric field strength consistent with nDEP. c) Same as b) but at 700 Hz and Sample A. SWNTs still accumulate in the regions of lowest electric field strength consistent with nDEP. d) For Sample B, SWNTs (60 min sonication) accumulated in the regions of highest electric field strength consistent with pDEP. Scale bar: 20 µm for a)-d). e) Normalized fluorescence intensity indicative of DEP trapping vs applied electric potential for sample A in the regions where nDEP occurs. f) similar to e) but with sample B for pDEP trapping regions. (Figure is adapted and reprinted with permission from Rabbani et al., copyright (2017), Anal. Chem.[355])

Figure 4.4a shows the trapping behavior of ssDNA-wrapped SWNTs, which were suspended similarly to Sample B by tip sonication for 90 min. At 700 Hz and 1000V applied over the 1.5cm long channel, the SWNTs accumulated in the regions of highest electric field strength in between posts, consistent with pDEP. We note that, similarly to the NaDOC-wrapped SWNTs, some ssDNA-wrapped SWNTs were not trapped. The pDEP trapping behavior for ssDNA wrapped SWNTs coincides with Sample B of the NaDOC wrapped SWNTs. The potential origin for the variations in DEP behavior of SWNTs at low frequencies probed in this study will be given in the next section. Figure 4.4b shows the trapping behavior of ssDNA wrapped SWNTs at varying applied potentials from 0V to 1200V. No trapping was observed below 300V. Above this potential, SWNTs accumulate due to iDEP trapping, whereas a plateau is reached above 600V. We also attribute this to trapping of all available SWNTs for which the DEP trapping force is large enough. Other smaller SWNTs for which the trapping threshold is not reached, are not trapped and are still observed in regions of lower electric fields.

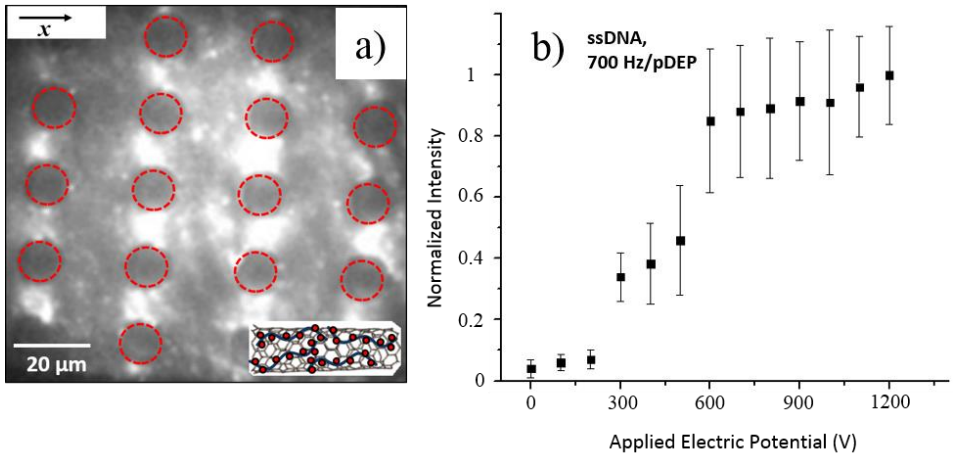

Figure 4.4: DEP trapping of ssDNA-wrapped SWNTs: IR fluorescence imaging of ssDNA-wrapped SWNTs subject to DEP trapping: At 700 Hz and 1000V applied over the entire microchannel of 1.5 cm length, ssDNA-wrapped SWNTs accumulated in the regions of highest electric field strength, consistent with pDEP. Scale bar: 20 µm, external field

direction horizontal, along the x-direction. b) Normalized fluorescence intensity indicative of DEP trapping vs applied electric potential for ssDNA-wrapped SWNTs in the regions where pDEP occurs. The onset of trapping is observed around 300V and above 600V the fluorescence intensity plateaus. (Figure is adapted and reprinted with permission from Rabbani et al., copyright (2017), Anal. Chem.[355])

4.6. Origin of Low-Frequency DEP Behavior of Suspended SWNT Species

In the low-frequency regime, the DEP behavior of nanoparticles is governed by their conductivities and that of the medium. The magnitude of $Re(CM)$ is thus expected to be independent of the applied frequency in the range investigated in this work. Our experimental observations are in agreement, since all SWNT preparations tested showed frequency-independent iDEP trapping behavior in the range probed (0-1000 Hz). Moreover, we observed nDEP or pDEP behavior dependent on how samples were suspended. For NaDOC-suspended SWNTs, the type of DEP behavior was dependent on the sonication time (Samples A and B). In the following we discuss possible factors giving rise to this difference in DEP behavior.

According to established models, $Re(CM)$ of semiconducting SWNTs is governed by the effective particle conductivity, which is dominantly determined by the double layer contributions arising from Stern layer and diffuse layer conductance. The latter depend on the Zeta potential of the charged nanoparticle suspended in an electrolyte. It is well documented in the literature, that the Zeta potential of SWNTs varies for different surfactants and surfactant concentrations. [313, 314] We thus independently measured the Zeta potential of the SWNTs prepared in the different manners . Table 4.1 lists the experimentally determined Zeta potentials for all samples for which the DEP behavior was studied as well as some cases at even lower sonication time.

Sample B, subjected to a longer sonication time, showed a Zeta potential of ζ = -58.6±1.8 mV, which is in reasonable agreement with the literature, considering variations in sonication time and power as well as aqueous solution additives (in our case HEPES buffer).[314] Sample A with a shorter sonication duration resulted in ζ = -20.2±1.1 mV, about one third of the value of Sample B. Moreover, shorter sonication times of 5 and 10 min resulted in Zeta potentials slightly lower than -20.2 mV. We attribute this large difference in Zeta potential to a less dense wrapping of the SWNTs with the surfactant in Sample A, C and D. High Zeta potentials typically indicate a good stability of dispersed particles due to electrostatic repulsion between suspended particles whereas lower Zeta potentials are typically an indication for a higher tendency of aggregation of dispersed particles.[314] A Zeta potential of only -20 mV could therefore signify lower stability of the nanotube suspension and a tendency to aggregate. Our findings are consistent with a report by Mahbubul *et al.*[315] who have shown a direct correlation of the Zeta potential with sonication time for aluminum oxide nanoparticles suspended in aqueous solutions and the observation by Zaib *et al.*,[316] where carbon nanotubes increase their electrophoretic mobility and thus Zeta potential with longer sonication times.

Table 4.1: Zeta potential, σ_m , σ_p, conductivity ratio and Clausius Mossotti factor for suspended SWNTs.

Sample	**Sonication Time (min)**	**Zeta potential (mV)**	$\boldsymbol{\sigma_p}$ **(S/m)**	$\boldsymbol{\sigma_m}$ **(S/m)**	**Conductivity ratio (γ)**	$\boldsymbol{Re(CM)}$
NaDOC (Sample C)	5	-18.6±1.7	0.03	0.15	0.2	-0.8
NaDOC (Sample D)	10	-19.4±1.4	0.12	0.15	0.8	-0.2
NaDOC (Sample A)	20	-20.2±1.1	0.14	0.15	0.93	-0.07
NaDOC (Sample B)	60	-58.6±1.8	2.94	0.15	19.6	18.6
ssDNA	90	-60.7±2.0	0.53	0.04	13.25	12.3

The measured Zeta potentials can now be linked to the observed DEP trapping. In the low-frequency regime, the $Re(CM)$ can be simplified as a conductivity ratio of the medium and particle as mentioned in equation .3.7 in chapter 3. We define the conductivity ratio γ as $\frac{\sigma_p}{\sigma_m}$. For $\gamma < 1$, nDEP is prevalent since $Re(CM) < 0$, whereas for $\gamma > 1$, $Re(CM)$ is positive resulting in pDEP. Figure 4.4a shows the dependence of $Re(CM)$ on γ indicating that the sign of the Clausius-Mossotti factor critically depends on the medium used to suspend the SWNTs and the nanotube's surface conductivity.

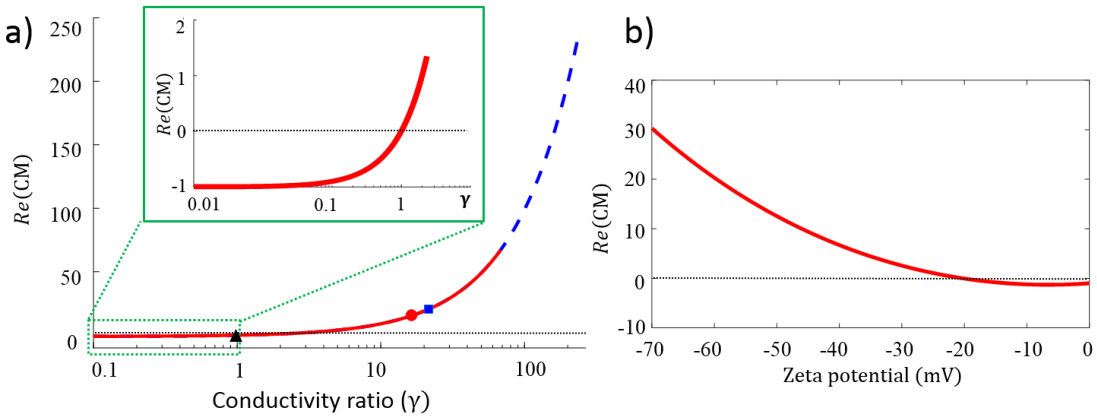

Figure 4.5: Calculated Re(CM) in dependence of γ and Zeta potential: a) Calculated Re(CM) vs. $\gamma(=\frac{\sigma_p}{\sigma_m})$ in the low-frequency regime, calculated for a frequency of 700 Hz. The red lines show curves for semiconducting NaDOC-wrapped SWNT and the (blue) dashed line for semiconducting ssDNA-wrapped SWNTs. Note that both curves coincide in the low frequency regime as Re(CM) is only governed by the conductivity ratios. The black dashed line indicates $\mathrm{Re(CM)} = 0$. The black triangle, blue square and red circle indicate the values for sample A, sample B, and ssDNA-wrapped SWNTs, respectively. The inset in a) corresponds to a zoom in for low values of $\gamma < 1$, where negative Re(CM) prevails. b) Dependency of Re(CM) on Zeta potential for NaDOC suspended SWNTs. The dashed line indicates $\mathrm{Re(CM)} = 0$. It is apparent that Re(CM) changes sign from positive to negative at low Zeta potential (< 21 mV). (Figure is adapted and reprinted with permission from Rabbani et al., copyright (2017), Anal. Chem.[355])

Next, we examine the conductivity ratio γ in the different experimental conditions. For a given SWNT suspension, σ_m is defined by the solution employed during the suspension process and can be assessed experimentally through conductivity measurement. The particle conductivity is governed by the surface conductivity, which in turn is defined via the diffuse layer and Stern layer conductance as described in the Theory section. Based on the experimentally determined Zeta potentials, the diffuse layer conductance $\lambda_{s,d}$ can be calculated, yielding σ_p according to equation 4.3. Table 1 lists the calculated conductivity ratio for the SWNT samples. The calculated particle conductivity was 0.14 S/m for NaDOC wrapped SWNTs for Sample A, 2.94 S/m for Sample B, and 0.53 S/m for

DNA wrapped SWNTs. The medium conductivity was also determined experimentally and found to be 0.15 S/m for both NaDOC-wrapped samples and 0.04 S/m for ssDNA-wrapped SWNTs, respectively.

Figure 4.5a shows the dependence of $Re(CM)$ on the conductivity ratio γ and the Zeta potential, with the symbols corresponding to SWNT samples studied experimentally. For NaDOC-wrapped Sample B, $Re(CM)$ is positive with a value of 18.6 corresponding to γ of 19.6. For DNA-wrapped SWNTs, γ is 13.25 with a corresponding $Re(CM)$ of 12.3. This calculation matches the experimentally observed trapping behavior of NaDOC-coated SWNTs (Sample B) and ssDNA-wrapped SWNTs where pDEP was observed. The numerical study underlines this experimental observation since the trapping regions match in both model and experiment.

We further examined the relationship between Zeta potential and $Re(CM)$ for the NaDOC-wrapped SWNTs. When ζ drops, the Clausius-Mossotti factor decreases and eventually becomes negative, leading to nDEP (Figure 5b). This occurs below a value of -21 mV. Note that the measured Zeta potential of Sample A is within the region where the $Re(CM)$ drops below zero (corresponding to ζ < -21 mV) and that of Sample B in the range where a positive $Re(CM)$ is expected according to Figure 5b. We thus conclude that the SWNT dielectrophoretic behavior is dependent on the Zeta potential, which in turn is determined by the suspension quality, i.e. sonication duration. This conclusion is in agreement with reports by Kang *et al.* who observed a relation between the dielectrophoretic behavior of surfactant suspended SWNTs with the type of surfactant and concomitant changes in the Zeta potential.[202] Similar observations were also recently made with biological cells. Tang et al. reported that the dielectrophoretic behavior of yeast cells

changes through the surface interaction with surfactants such as sodium dodecyl sulfate.[317] Our observations for the SWNT samples subject to short sonication times (20 min and below) also agree with the commonly accepted "zipping mechanism" responsible for SWNT suspension with surfactants.[318, 319] Sonication is needed to "unzip" bundle ends of SWNTs followed by adsorption of the charged surfactant and eventually leads to full unzipping and release of individual SWNTs. At small sonication times, this process is not fully finalized leading to a large distribution of species, including a variation of large bundles, individual long SWNTs as well as smaller individual SWNTs. Based on this mechanism we can also explain why sample A exhibiting a small negative Zeta potential leading to a very small negative $Re(CM)$ can be trapped at similar potentials as compared to sample B. Since bundles and long SWNTs are predominant in sample A, trapping occurs above 300V similar to shorter well dispersed SWNTs exhibiting a larger Zeta potential since the DEP forces are increased due to an overall larger geometry. In summary, the observed pDEP trapping of NaDOC-suspended (Sample B) and ssDNA-wrapped SWNTs is in agreement with the observed Zeta potentials, dielectrophohoretic models relating the Zeta potential of nanoparticles to the Clausius–Mossotti factor and suspension behavior of individual SWNTs. The nDEP behavior observed in experiments for NaDOC-suspended SWNTs prepared with shorter sonication time coincides with a smaller Zeta potential of not ideally suspended SWNTs and correspondingly negative $Re(CM)$.

4.7. Conclusion

We have studied the DEP properties of semiconducting SWNTs in the low frequency regime (<1 kHz) with insulator-based dielectrophoresis, a frequency range not previously investigated with SWNTs. The study was carried out in PDMS microfluidic

devices where the semiconducting SWNTs could be visualized with near infrared microscopy. As predicted by established models, the observed DEP trapping behavior was frequency independent. We could show, however, that the sign of the Clausius-Mossotti factor can switch, depending on the Zeta potential and the corresponding suspension properties of the nanotubes. Well suspended NaDOC-and ssDNA-wrapped SWNTs exhibited pDEP, which is in accordance with the measured Zeta potential and related positive $Re(CM)$. In contrast, less densely NaDOC-wrapped SWNTs exhibited lower Zeta potential and demonstrated nDEP. The experimental observations were in excellent agreement to a numerical study. Our work shows that carbon nanotubes can be effectively manipulated and even trapped with iDEP in low frequency AC electric fields and suggests that poorly suspended constituents may be effectively removed in DEP sorters exploiting the variations in pDEP and nDEP. Moreover, the DEP response can be tuned by the surfactant properties and suspension quality, which may in turn be exploited for optimization of purification and separation of carbon nanotubes based on DEP or alignment and positioning of SWNTs.[52] In addition, the near IR microscopy imaging of DEP of semiconducting SWNT allows the observation of DEP trapping and migration directly in a microfluidic device without the need for post-DEP analysis involving Raman spectroscopy or nanoscale imaging techniques following tedious recovery procedures.

5. LENGTH-SELECTIVE DIELETROPHORETIC MANIPULATION OF SINGLE-WALLED CARBON NANOTUBES

5.1. Abstract

Single-walled carbon nanotubes (SWNTs) possess unique physical, optical, and electrical properties with great potential for future nanoscale device applications. Common synthesis procedures yield SWNTs with large length polydispersity and varying chirality. Electrical and optical applications of SWNTs often require specific lengths, but the preparation of SWNTs with the desired length is still challenging. Insulator-based dielectrophoresis (iDEP) integrated into a microfluidic device has the potential to separate SWNTs by length. Semiconducting SWNTs of varying length suspended with sodium deoxycholate (NaDOC) show unique dielectrophoretic properties at low-frequencies (<1 kHz) that were exploited here using an iDEP-based microfluidic constriction sorter device for length-based sorting. Specific migration directions in the constriction sorter were induced for long SWNTs (≥1000 nm) with negative dielectrophoretic properties compared to short (≤300 nm) SWNTs with positive dielectrophoretic properties. We report continuous fractionation conditions for length-based iDEP migration of SWNTs, and we characterize the dynamics of migration of SWNTs in the microdevice using a finite element model. Based on the length and dielectrophoretic characteristics, sorting efficiencies for long and short SWNTs recovered from separate channels of the constriction sorter amounted to >90% and were in excellent agreement with a numerical model for the sorting process.

5.2. Introduction

Applications of single-walled carbon nanotubes (SWNTs) in nanotechnology require the understanding of their unique mechanical, electrical, optical, and structural properties.[37, 39, 40, 134, 320, 321] Metallic SWNTs are promising for the field of nanoscale electronics[37, 50, 289, 321], while semiconducting SWNTs can open the door for field-effect Schottky-type transistor applications,[48, 50] nanometer size devices,[322] biological transporters, and biosensors.[37, 322] Due to their high photostability[323, 324] and unique fluorescence emission in the IR range,[280, 325, 326] where autofluorescence in a biological sample is minimal, SWNTs are also employed as mechanical sensors in living cells. Their structural and chemical properties have also led to applications as atomic force microscopy (AFM) probes.[327-329]

An important factor for SWNT applications is their length. For example, Wang *et al.* demonstrated the direct correlation of SWNT and multi-wall carbon nanotube (MWNT) length with electrical and thermal conductivities.[330] In addition, SWNT-based field-effect transistors have the potential to replace silicon technologies. The length of SWNTs has a strong impact on the performance of such transistors.[331] Recent studies also show that the mechanical, thermal, electrical and electromagnetic properties of MWNT-based epoxy resins depend on carbon nanotube length.[332] Wan *et al.* demonstrated that SWNT length is important for reinforcing nano-composites, since their length both affects the Young's modulus as well as the load transfer between SWNTs and matrix.[333] Similarly, a study by Shokreich *et al.*[334] revealed that the improvement in the Young's modulus of SWNT-composites is negligible for SWNT length smaller than 100 nm and that only SWNTs with lengths above 1000 nm reinforce the polymer matrix significantly. Furthermore, Wang *et*

al. used CNTs as an electrode material in Li-ion batteries and catalyst support in fuel cells.[335] Their study revealed the short CNTs (<300 nm) provide better electrochemical performance during charging and discharging than longer CNTs. It was also reported that the reversible capacities of long CNTs were half of those of short carbon nanotubes.[336] In addition, the charge-transfer resistance of long CNTs was much higher than those of short carbon nanotubes. [336] Furthermore, Cheng *et al.* demonstrated that the toxicity of functionalized MWNTs in zebrafish embryos *in vivo* is influenced by nanotube length.[337] SWNT cytotoxicity studies revealed that the degree of functionalization is responsible for the cytotoxic response of cells in a cell culture which also depends on the length of SWNTs.[338] Therefore, depending on the particular nanotube-based application and to achieve green chemistry with SWNTs, length characterization and control is required.

Despite the importance of length in SWNT applications, current synthesis methods cannot control length. The most common synthesis processes produce mixtures of both metallic and semiconducting SWNTs with varying chirality, a range of diameters (from ~1 nm to ~2 nm),[339, 340] and large variations in length (from 10 nm up to >1 cm). [41, 285, 288] The high-pressure carbon monoxide (HiPCO) process for example is a common fabrication method yielding SWNTs in diameters of ~1 nm and lengths from several nanometers to several micrometers, containing more than 50 chirality types.[285, 286, 288, 341] The samples may thus show broadly varying electrical and optical properties, determined by the variations in chirality.[42, 265] In addition, SWNTs also form adducts and bundles held together by van der Waals forces, leading to a large variety of adduct species.[326] An alternative synthesis strategy uses a focused ion beam, but this approach is expensive and has small throughput.[342] Producing SWNTs with specific lengths or chirality at high yield is still

challenging. Post-synthesis processing methods are therefore required to yield pure SWNT fractions.

Several separation methods of SWNTs have been reported in recent years that take advantage of distinct electronic properties.[54, 288] Ultracentrifugation using density gradient methods has been developed to purify SWNTs and sort them by size.[43] This method, however, is based on specific DNA oligomers used to wrap the SWNTs. This limits large scale applications due to cost and oligomer availability.[43] Furthermore, DNA-wrapped SWNTs have limited stability in aqueous density gradients, and stripping the DNA wrapping agent after separation could not be achieved. Ion exchange[57] and size-exclusion chromatography[56] have also been used as length sorting tools, and a combination of these two has been reported for separation of SWNTs by chirality with similar diameters.[343] These separation techniques also require wrapping SWNTs with DNA with similar problems with stability, cost, and unwrapping. Electrophoresis using DC electric fields has also been used as a separation tool for SWNTs based on their diameter. This is more a diagnostic than a production method since recovery from gels is cumbersome.[258, 294] Importantly, all these methods do not offer separation of SWNTs in a continuous manner. Thus, a versatile fractionation or separation approach for SWNTs by length is still lacking. Dielectrophoresis (DEP) has in recent years achieved prominence as a powerful tool for nanoparticle separation.[21, 31, 263, 344, 345] DEP has been used to capture proteins,[346] nucleic acids,[347] as well as other biomolecules,[10, 33, 116, 119, 348-354] and also carbon nanotubes as we [355] and others reported previously[41, 54, 55, 117, 134, 145, 202, 356, 357]. Dielectrophoresis has also been employed to sort SWNTs according to their dielectric properties.[145] Insulator-based DEP (iDEP) has garnered attention due to several advantages among the devices that can

produce inhomogeneous electric field gradients.[358-360] In an iDEP-based microfluidic system, when an electrical potential is applied across the channel, inhomogeneous electric field gradients are produced by the insulating geometries or constrictions introduced in the channel.[29] iDEP offers several advantages such as simple fabrication and low cost using well established soft lithography techniques, avoiding electrode reactions within the devices. The electric field gradient can be generated along with the entire depth of the device. Typically, iDEP is used to examine DC and low-frequency DEP behavior of particles.[28, 117, 306]

Studying single SWNT properties requires suspending them in solvents and in many cases, aqueous media are preferred. However, due to strong van der Waals interactions SWNTs often aggregate in aqueous solutions. Thus, SWNTs must be suspended using surfactants or biomolecular wrapping agents. Successful suspension of SWNTs was reported with anionic surfactants such as sodium deoxycholate (NaDOC) or sodium dodecyl sulfate (SDS), cationic surfactants such as cetyltrimethylammonium bromide (CTAB), ssDNA, among others.[35, 202, 355] The suspension of SWNTs with different surfactants or biomolecules will eventually influence their surface charge and Zeta potential (ζ).[145, 202, 258, 296, 355] Previously, we reported that at low frequencies (<1 kHz), the DEP behavior of NaDOC suspended SWNTs mainly depends on the conductivity of the particle and the surrounding medium which, in turn, is determined by the Zeta potential induced by surfactant wrapping. In this low-frequency regime, $Re(CM)$ reduces to an expression for the particle and medium conductivity, σ_p and σ_m respectively, such that $Re(CM) = -1 + \frac{\sigma_p}{\sigma_m}$.[201, 285, 355] Here, we exploit this unique DEP behavior at low

frequencies to induce size-selective iDEP migration of SWNTs and exploit it for fractionation of SWNTs by length.

5.3. Materials and Methods

5.3.1. Chemicals

SWNTs were obtained from Rice University (Houston, TX, USA) through a materials transfer agreement (MTA). Sodium deoxycholate (NaDOC) for the suspension of SWNTs, N-(2-hydroxyethyl) piperazine-N'-2-ethanesulfonic acid (HEPES) and Pluronic F-108 were purchased from Sigma-Aldrich (MO, USA), sodium hydroxide (NaOH) was purchased from Merck KGaA (Darmstadt, Germany). The SYLGARD 184 silicone elastomer kit for polydimethylsiloxane (PDMS) for microdevice fabrication was obtained from Dow Corning Corporation (Midland, MI, USA). Glass slides (48mm×60mm) for device assembly were purchased from Electron Microscopy Sciences (Hatfield, PA, USA). Deionized (DI) water was produced with an Arium 611 ultrapure water system from Sartorius (Göttingen, Germany). For atomic force microscopy imaging, Muscovite Mica (V-1, sheet size 25×25mm, thickness 0.15-0.21mm) was purchased from Ted Pella, Inc (Redding, CA, USA) and (3-aminopropyl) triethoxysilane (APTES) was obtained from Sigma-Aldrich (Hamburg, Germany). **A MalvernZetasizer Nano ZS instrument (Westborough, MA, USA) was used** for surface charge measurements. **Medium conductivity was measured by a Thermo Scientific Orion 3-star conductivity meter (Waltham, MA, USA).**

5.3.2. Microdevice Fabrication

Microfluidic constriction sorter devices were fabricated with soft lithography techniques as previously reported.[361] Briefly, the microfluidic chip layout and channel

structures were designed using AutoCAD software (Autodesk, San Rafael, CA, USA) which was used to construct a chrome photomask (Photo Sciences, Inc., Torrance, CA, USA). The pattern was transferred to a 4-inch silicon master wafer using SU-8 negative photoresist (Microchem, Westborough, MA, USA). Then, the PDMS elastomer base was mixed with curing agent at a 10:1 ratio (w/w), poured over the master wafer, degassed for 30 min and the PDMS cast was cured in an oven for 4h at 80°C. The cast was subsequently peeled off the master wafer, reservoirs were punched manually with a punch, with a 1.5 mm diameter at the inlets and 3 mm diameter at the outlets for fluidic access. The PDMS cast was cut into appropriate pieces, and these slabs and microscope glass slides were cleaned with isopropanol and distilled water in an ultrasonic bath for 2 min, dried with nitrogen, and baked on a hot plate for 30 s at 90 °C. The PDMS slab and glass slides were then treated with oxygen plasma in a plasma cleaner oven (PDC-001: Harrick Plasma cleaner/sterilizer, USA) at high RF (18 W) for 30 s. Both surfaces were then brought into contact, and the device was irreversibly bonded with the glass slide to create fluid channels. The channels were washed several times with distilled water, and then the surface was treated with Pluronic F-108 (1% w/v) and incubated overnight, as previously described.[310] The assembled PDMS microfluidic chip had an overall length of 5 mm with a 30 μm wide constriction region; the inlet channel was 100 μm wide and all outlets were 20 μm wide as shown in Figure 5.1. All channels were ~20 μm high.

5.3.3. SWNT Sample Preparation

SWNTs used for the experiments were suspended with the surfactant NaDOC. NaDOC was dissolved at a concentration of 1% (w/v) in 10 mM HEPES buffer (pH 7.2) containing 1% (w/v) F108. About 1 mg of SWNTs were carefully transferred into a clean

glass scintillation vial with a spatula and 1 mL NaDOC solution was added. To wrap and solubilize SWNTs, they were sonicated at 20 kHz at 10W using a 2 mm microtip sonicator (Sonics & Material INC, Danbury, CT, USA). Two types of NaDOC-coated samples were prepared with different sonication times. To obtain short SWNTs (sample A), the solution was sonicated for 60 min. After sonication, the sample was centrifuged for 10 min at 14800 rpm. After centrifugation, the supernatant was collected for the experiments. This sample was diluted at a ratio of 10:1 with HEPES buffer containing F108. To obtain long SWNTs (sample B), the solution was sonicated for 10 s. After sonication, the SWNT suspension was transferred to an Eppendorf cup and centrifuged (Sigma 1-14 centrifuge, Germany) at 2000 rpm for 10 min. All samples were stored at 4°C prior to the experiments.

5.3.4. Detection of SWNTs

The imaging setup for the SWNTs of (6,5) chirality used for this experiment was described previously.[355] SWNT fluorescence was excited with a 561 nm solid-state laser (500 mW cw, Cobolt Jive, Cobolt) coupled through a neutral density filter (NDC-50C-4M, Thorlabs) which was used to adjust the intensity of the laser. The laser beam was directed into a high-NA objective (CFI plan-Apo IR, 60X, Nikon, Japan) and the same objective was used to collect the fluorescence light through a dichroic beam splitter (630 DCXR; AHF Analysentechnik). After the beam splitter, the fluorescence light was further filtered through a 900 nm long-pass filter (F47-900; AHF, Analysentechnik). SWNTs were imaged with an InGaAs infrared camera (XEVS-SHS-1.7-320 TE-1, Xenics). Images were captured at a 100 ms frame rate, and data analysis was performed with Micromanager software (ImageJ, version 1.52a, NIH, USA).

5.3.5. SWNT Sorting and Size Characterization

To characterize length distributions of SWNTs in samples A and B and in the fractionated samples, dynamic light scattering (DLS) was carried out with a Zetasizer Nano ZS instrument (Malvern, USA). During the sorting experiments, flow rates were maintained at 25 µL/h with a syringe pump (HA1100, Instech, USA), while a potential of 350V was applied at a frequency of 1000 Hz. After ~3 h of sorting at optimized potential and frequency, ~20 µL SWNT sample was accumulated from the center outlet and then diluted to 1 mL with sample buffer for DLS. In addition, atomic force microscopy (AFM) was used to image SWNTs. Briefly, mica (Grade V1, 25 mm*25 mm, Tedpella, USA) was treated with APTES and a drop of the respective SWNT sample was incubated on the mica surface for 5 min. After incubation, the mica surface was cleaned with DI water and dried for the AFM measurements. A Cypher S AFM (Asylum Research, USA) was used for SWNT imaging using tapping mode in the air with a Si tip with spring constant 42 N/m and a resonance frequency of 300 kHz (AC160 TS C2, Olympus, Düsseldorf, Germany). About 35-40 nanotubes were measured for each sample to determine the average length. Further, sample A and B were mixed and a similar fractionation experiment performed as described above. The mixed SWNT sample was prepared by adding 500 µL each of sample A and sample B in an Eppendorf tube. The mixed sample was introduced into the microdevice through the inlet reservoir with a flow rate of 25 µL/h and subjected to fractionation at 1000 Hz and with an applied potential of 350 V. To determine the separation resolution R, we quantified the fluorescence intensity along a curved line spanning the start of the outlet channels with Image G (version 1.52a, fit the data with a Gaussian in Origin software (OriginPro 2017version 94E) and calculated R according to

$R = 1.18 * \frac{x_A - x_B}{w_A + w_B}$, where x_A and x_B are the peak maxima and w_A and w_B correspond to the full width at half maximum, respectively.[362]

5.4. Results and Discussion

We studied the migration of SWNTs wrapped with sodium deoxycholate (NaDOC) in a continuous-flow iDEP microfluidic constriction sorter. Figure 5.1a depicts the microfluidic sorter consisting of an inlet channel, a constriction, and five outlet channels (with 2 denoted *S1* and 2 denoted *S2* for sides, and one denoted *C* for center). Bulk fluid transport through the sorter was induced by external pressure. The unique geometry of the constriction was responsible for creating localized electric field nonuniformities near the constriction and the outlet channels *via* the electrical potential applied between the inlet and outlet reservoirs. Due to the non-uniform electric field, the resulting DEP forces deflect particles based on their length and surfactant wrapping properties into different outlets (see Figure 5.1b,c). The electric field maximum is located in the center outlet channel and the minimum in the side outlet channels. The migration behavior of semiconducting SWNTs was experimentally investigated by infrared fluorescence microscopy as detailed in the methods section and numerically modeled as outlined in the supporting information.

5.4.1. SWNT Sample Characterization

As previously shown,[355] SWNT suspensions prepared with long sonication times (> 60 min) contained short SWNTs with high Zeta potential, exhibiting pDEP ($Re(CM) > 0$). In contrast, short sonication times resulted in SWNTs with lower Zeta potential but increased lengths displaying nDEP ($Re(CM) < 0$). Two samples were prepared accordingly using different sonication times, primarily containing short (sample A) and long (sample B) SWNTs. The length distribution of samples A and B, as well as the Zeta potential, was

investigated with dynamic light scattering (DLS) and atomic force microscopy (AFM) imaging as summarized in Table 1. AFM and DLS measurements showed the average SWNT length in sample A to be 366.9±16.8 and 324.5±16.6 nm, respectively. For sample B, the average length was determined as 1145.7±435.0 nm with AFM and 932.3±34.0 nm with DLS.

Table 5.1. ζ and average lengths data for sample A and sample B

Separation type	**Parameter**	**Measuring modality**	**Sample A**	**Sample B**
Before fractionation	ζ (mV)	DLS	-49.7±1.3	-19.8±1.7
	Length (nm)	DLS	324.5±16.6	932.3±34.0
	Length (nm)	AFM	366.9±16.8	1145.7±435.0
After fractionation (side outlets)	ζ (mV)	DLS	-23.6±4.5	-10.7±1.7
	Length (nm)	DLS	506.2±26.3	1245.3±239.1
	Length(nm)	AFM	581.0±253.0	1462.2±412.8
After fractionation (center outlet)	ζ (mV)	DLS	-51.3±0.7	-51.8±4.0
	Length (nm)	DLS	278.8±4.5	309.0±24.8
	Length (nm)	AFM	288.8±139.3	449.2±139.3

5.4.2. Prediction of iDEP Separation of SWNTs

Based on the size distribution in the two samples and varying Zeta potentials, the expected migration behavior of SWNTs is non-trivial. We therefore first conducted a numerical study to predict the SWNT migration in the constriction sorter (as detailed in the

supplementary information). SWNT lengths from 50-2000 nm were studied with the numerical model, spanning the size range explored experimentally in samples A and B. Figure 5.1b shows a snapshot image obtained from the numerical simulation after passage through the constriction for ~300 nm long SWNTs with pDEP properties ($Re(CM)$ = 13.44). From the inlet, 100 particles were released, and a majority of them were found in the center channel (see Table SB_1 for details). Figure 5.1c shows the migration of 1000 nm long SWNTs with $Re(CM)$ = -1.18. In this case, SWNTs were sorted with a preference into the side outlets where the electric field strength is lowest, which is expected for nanotubes with nDEP ($Re(CM) < 0$). This example demonstrates that short SWNTs with pDEP properties can be sorted from large SWNTs with nDEP into different outlets.

Figure 5.1b (higher particle count in the center channel) and Figure 5.1c (higher particle count in side channel) show distinct migration preference into different outlets for the two selected SWNT species exhibiting variations in length and DEP properties. To quantify the preference of migration, the recovery efficiency, $\%E_S$, was calculated based on particle counts found in each outlet channel:

$$\%E_{S1} = \frac{N_{S1}}{N_{S1}+N_{S2}+N_C} \tag{5.1}$$

where, N_{S1}, N_{S2} and N_C are the number of particles found in the two side 1 outlets, two side 2 outlets, and the center outlet. Similarly, the efficiencies of side outlet 2 ($\%E_{S2}$) and center ($\%E_C$) outlets were obtained. For the two cases shown in Figure 5.1 b and 5.1c, the recovery efficiency resulted in 83.9% in the case of 1000 nm SWNTs with nDEP for the sum of S1 and S2 outlets, and in 83.1% for the 300nm SWNTs exhibiting pDEP in the center outlet (see Supporting InformationTable S1).

The numerical model allows to investigate $\%E$ for monodisperse SWNTs. To carefully map the migration behavior over a broad range of length distribution of surfactant wrapped SWNTs originating from the suspension and wrapping process, [355, 363] we studied $\%E$ of various SWNT lengths ranging from 50 nm up to 2000 nm with the numerical model, as summarized in the supporting information and Table SB_1. We studied both nDEP and pDEP properties for each SWNT length to account for well-wrapped (pDEP and high ζ) as well as such SWNT species exhibiting nDEP resulting from uncomplete wrapping and low ζ. The numerical study revealed that the sorting efficiencies in the center outlet increased for decreasing the length of SWNTs in the case of pDEP. For long SWNTs with nDEP properties, this trend is significantly different. The longer the SWNT species the stronger their preferred migration to the side outlets (with preference in the S2 side outlets).

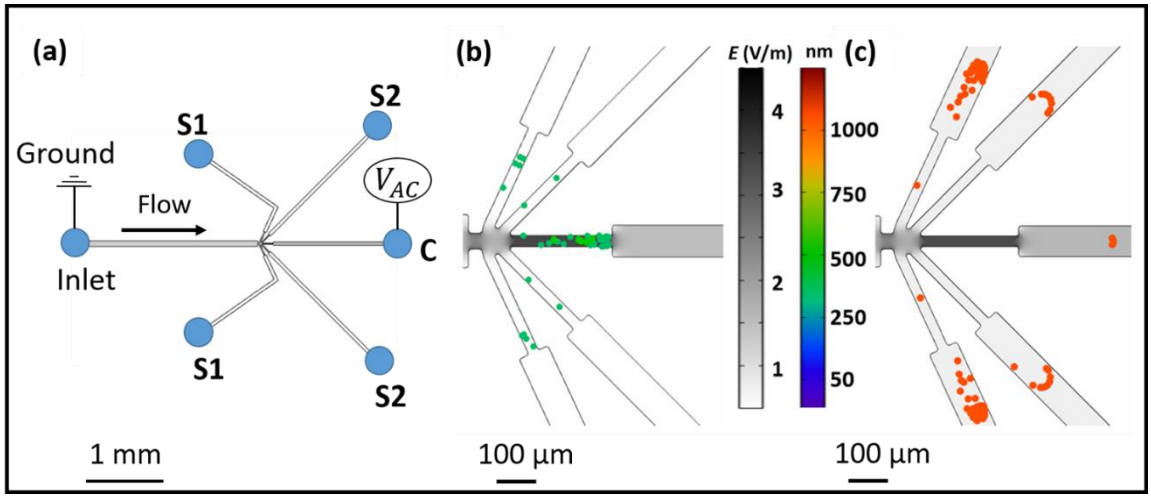

Figure 5.1: Design and basic operation of the iDEP sorting device: (a) Schematics of the iDEP sorter: The suspended SWNT sample was introduced via the inlet reservoir and channel. The sample flowed through the channel toward a constriction region leading to five outlet branches which are labeled as S_1 and S_2 for the two side outlets and C for the center outlet. (b) Representative snapshot of particle position obtained from the numerical study as outlined in the supplementary information showing that small (300nm) SWNT particles exhibiting pDEP migrate to the center outlet after migrating through the

constriction and when released in the inlet channel (see also supporting movie SB_1). (c) Similarly to b), long (1000 nm) SWNTs exhibiting nDEP migrate preferentially to the side outlets (see also supporting movie SB_2). This behavior indicates that smaller SWNTs can be collected in the center channel (C) and long SWNTs in the side channels (S_1 and S_2). (Figure is adapted and reprinted with permission from Rabbani et al., copyright (2020), Anal. Chem.[266])

5.4.3. Prediction of iDEP Separation of SWNTs

Based on this analysis, a recovery efficiency ~90.2% can theoretically be achieved for SWNT of 50 nm length with pDEP causing preferred migration into the center outlet. SWNTs of the same size with nDEP properties, however, did not show a preferential sorting efficiency. In contrast, for 2000 nm long SWNT with nDEP properties, a $\%E$ of ~92.9% can be achieved due to preferred migration into the four side channels combined. Table SB_1 demonstrates the general trend, in which longer SWNTs with nDEP properties (resultant from lower ζ) preferentially migrate into the side channels and can be sorted from larger SWNTs with pDEP properties (resultant from higher ζ). Note that experimentally, we expect improved wrapping properties, higher Zeta potentials and therefore pDEP for the shorter SWNTs, since shorter SWNTs result from longer sonication and suspension times, as further detailed below. The converse holds for longer SWNTs. [355]

To test this length-dependent migration behavior experimentally, a microfluidic constriction sorter was employed using a sample with a majority of short SWNTs (sample A) and one with longer SWNTs (sample B). SWNTs were introduced into the microdevice through the inlet reservoir with a syringe pump at a flow rate of 25 µL/h. Figure B.1 in the Appendix B, shows an image of a microchannel filled with NaDOC wrapped SWNTs without an externally applied potential. In this case, SWNTs were distributed evenly in the microchannel. Next, DEP-based migration was induced by varying the applied potentials

at a flow rate of 25 µL/h. No preferred migration into any outlet channel was observed below 300 V, in agreement with previous studies.[355] Fractionation behavior was investigated with a frequency of 1000 Hz and an applied potential of 350 V where DEP forces were sufficiently high.

To characterize the length distribution in samples A and B, AFM imaging and DLS were used before and after the DEP migration experiments. We also characterized ζ for each sample before and after the sorting experiment. At low frequencies, the sign of $Re(CM)$ of semiconducting SWNTs is governed by the conductivity of the medium and the particle. While the particle conductivity is dominantly determined by the double layer contributions arising from the Stern layer and diffuse layer conductance,[202] it is also dependent on the Zeta potential of the charged particle suspended in an electrolyte. Therefore, the Zeta potential has an impact on the Clausius Mossotti factor and DEP properties of SWNTs, as shown previously.[145, 202, 355] For sample A (short SWNTs), the Zeta potential was measured to be -49.7±1.3 mV prior to sorting, which is in agreement with the previous reports.[355, 364] For sample B (long SWNTs), the Zeta potential was measured as -19.8±1.7 mV (see also Table 1).

Both samples were subjected to fractionation in the constriction sorter, while the sorting behavior was monitored with near-infrared fluorescence microscopy. Figure 5.2a shows the fractionation behavior of sample A as observed during the sorting experiment, demonstrating that the majority of SWNTs migrated to the center channel, where the electric field strength was highest. This migration behavior corresponds to that predicted by the numerical model for the pDEP case for SWNT lengths ≤300 nm as demonstrated in Figure 5.1b. Figure 5.2b represents the normalized intensity in the different outlets,

demonstrating that maximum intensity was observed in the center outlet and that the short SWNTs migrated into the center outlet. Figure 5.2c shows an AFM image of NaDOC-wrapped SWNTs collected from the center outlet after 3 h of fractionation. AFM imaging revealed an average length of 288.8±139.3 nm. Consistent with this result, the DLS measurement gave an average SWNT length of 278.8±4.5 nm and ζ of -51.3±0.7 mV for the center outlet fraction. The average length after fractionation is thus slightly reduced compared to sample A before fractionation, and the Zeta potential is slightly increased. The side outlet fractions from the same fractionation experiment were combined and analyzed. Both AFM (581.0±253.0 nm) and DLS (506.2±26.3 nm) indicated a larger average length than the starting sample A, and the Zeta potential of -23.6±4.5 mV was considerably reduced. We attribute this outcome to the fact that the sorter was capable of fractionating the somewhat polydisperse sample A. In addition we note, that this sorting behavior is in excellent agreement with the numerical results. Table 1 lists average lengths and ζ values for the original and fractionated samples. We note that length distributions of SWNTs analyzed by AFM and DLS are in good agreement with, although slightly higher average lengths are obtained with AFM measurements. We attribute this difference to the length weighting inherent to the DLS technique and to a systematic bias in the SWNT length determination via AFM, which was also reported by Fagan *et al.*[365] The latter may result from undercounting of overlapped SWNTs and preferential deposition on the surface prior to AFM imaging. However, a significance test confirmed that the two methods do not differ ($p = 0.05$).

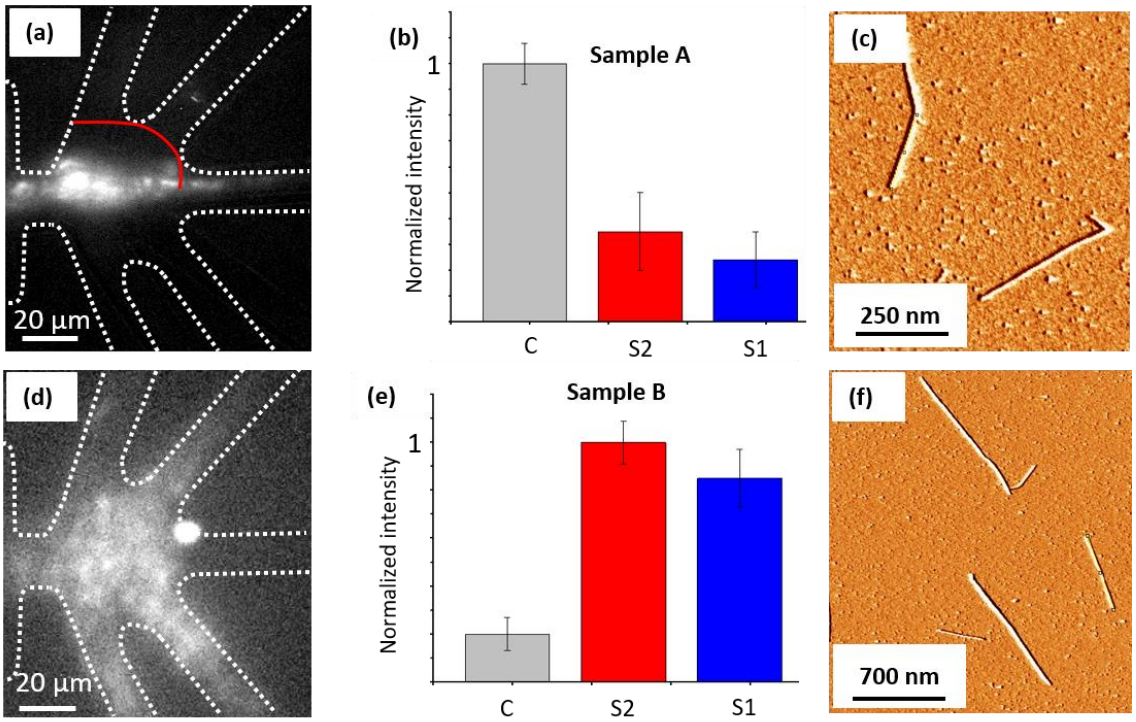

Figure 5.2: DEP fractionation of NaDOC wrapp*ed SWNTs and characterization.* a) NIR fluorescence image of short SWNTs in the constriction sorter (at 1kHz Hz and 350 V). Short SWNTs concentrate in the regions of highest electric field strength located in the center outlet channel indicative of pDEP. The red line indicates the location at which the SWNT fluorescence intensity was analyzed for determining the separation resolution as *further outlined in Figure a.* b) Normalized fluorescence intensity of (a) for all outlet channels demonstrating higher analyte conce*ntration in the center outlet.* c) Representative AFM image of fractionated NaDOC wrapped SWNTs collected from the center *outlet after sorting sample A.* d) NIR fluorescence image of sample B (at 1kHz Hz and 350 V) during sorting. Long SWNTs concentrate in the regions of lowest electric field strength in the side outlets indictive of nDEP. e) Normalized fluorescence intensity of (d) for all outlet channels demonstrating higher analyte conc*entration in the side outlets.* f) Representative AFM image of fractionated NaDOC wrapped SWNTs collected from the side outlet after sorting sample B. (Figure is adapted and reprinted with permission from Rabbani et al., copyright (2020), Anal. Chem.[266])

Next, the fractionation behavior of sample B (long SWNTs) prepared with shorter sonication time was investigated. Long SWNTs suspended by 10s sonication have a lower Zeta potential and showed nDEP characteristics in agreement with previous reports.[355] In the sorting experiment, they preferably migrated to the low electric field regions in the side

outlets, shown in Figure 5.2d. This observation was confirmed by the fluorescence intensity quantification, where the most intensity was found in the side outlets as shown in Figure 5.2e. In agreement with the preferred migration of longer SWNTs with nDEP behavior into the side outlets, AFM analysis resulted in an average length of 1462.2±412.8 nm. DLS characterization confirmed the preferred migration of long SWNTs into the side outlets and showed an average length of 1245.3±239.1 nm and ζ of -10.7±1.2 mV. The much smaller fluorescence intensity observed in the center outlet channel is attributed to smaller SWNTs with pDEP behavior migrating to the center channel, which was also confirmed by the length analysis of the fraction collected in the center outlet after sorting. Both DLS and AFM characterization revealed a shorter average length (see Table 1). This result is again in agreement with the numerical model for SWNTs ≥1000 nm and nDEP.

The dependence of the DEP response on ζ can be explained with the variations in surface conductance induced through the quality of the surfactant wrapping. While longer SWNTs exhibit smaller ζ, the shorter SWNTs, subjected to more rigorous sonication and longer wrapping times show high ζ. As previously outlined by us and others,[201, 202, 265, 355] the Zeta potential influences the SWNT surface conduction, since it determines the magnitude of the diffuse layer conductance, $\lambda_{s,d}$, as well as the Stern layer conductance, $\lambda_{s,s}$, which both sum up to the surface conductance, λ_s. The surface conductance can be used to describe the SWNT conductivity, via $\sigma_P = 2\,\lambda_s a^{-1}$,[366] where a is the radius, and intrinsic conductivity is neglected.[145, 202, 355, 357] A lower Zeta potential then leads to lower λ_s and consequently lower σ_P. Since σ_P governs the dielectrophoretic response of SWNTs at a given σ_m via the $Re(CM) = -1 + \frac{\sigma_p}{\sigma_m}$.

To further characterize the resolution of the SWNT separation, we analyzed the intensity of SWNTs from samples A and B at a location close to the constriction, right before the start of the three types of outlet channels. For this purpose, we conducted a spatial intensity analysis along the line indicated in red in Figure 5.2a. The intensity distributions along this line are shown in Figure 5.3, which allow for the calculation of R between sample A and B. From this analysis, the spatial separation resolution along this line resulted in 1.39. Finally, we conducted a fractionation experiment of the entire size range, by combining sample A and B. Figure B.2a-c in the Appendix B, show representative AFM images of SWNTs for the mixture, and the fractions pertaining to side outlets and center outlet. The AFM analysis revealed an average length of 1372.3±251.6 nm in the side outlets and an average length of 366.2±221.2 nm in the center outlet. This is in very good agreement with the migration experiments carried out for the individual samples A and B, as demonstrated in Table 1 and confirmed the working principle of the SWNT fractionation approach based on DEP at low frequency.

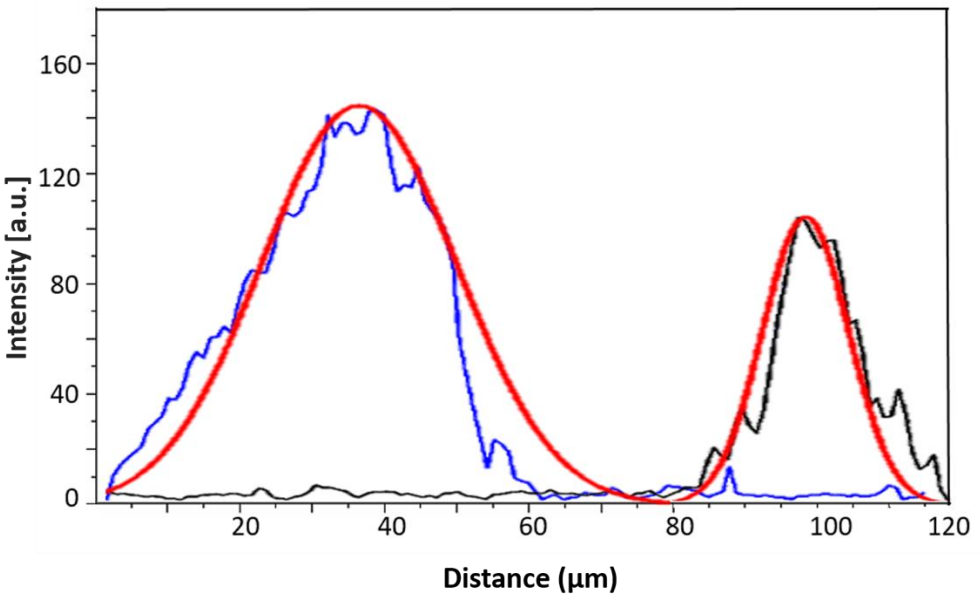

Figure 5.3: Fluorescence intensity of SWNTs for sample A (black) and B (blue) as obtained experimentally by analyzing the intensity along the line indicated in Figure 5.2a. The red curve indicates the Gaussian fit for each peak, resulting in R = 1.39. (Figure is adapted and reprinted with permission from Rabbani et al., copyright (2020), Anal. Chem.[266])

5.5. Conclusion

In summary, we conducted a study of SWNT fractionation based on the length and DEP properties using an insulator-based dielectrophoresis constriction sorter. We present a numerical model that predicts recovery efficiencies up to ~90% in selected outlets of a constriction sorter based on SWNT length and DEP properties. Experimentally, two samples differing in lengths and DEP properties showed migration behavior matching the numerical model. Long SWNTs with small Zeta potentials exhibited nDEP and migrated preferably into the side outlets of the sorter. In contrast, small SWNTs with high negative Zeta potentials were fractionated into the center channel. We demonstrate that the variations in Zeta potential caused by surfactant wrapping and sonication time can be conveniently exploited to fractionate SWNTs by DEP. The resultant resolution for the two

length distributions assessed experimentally was almost at baseline resolution demonstrating a good separation quality. We note that a similar iDEP constriction sorter was previously used for size-based fractionation of protein crystals[367, 368], organelles[369], and nucleic acids[306], demonstrating that this fractionation concept has a broad application range for various analytes. In addition, the employed constriction sorter is capable of sorting SWNTs in continuous mode which is advantageous for technological applications in which larger quantities of SWNTs are required. Future optimization of the geometry of the device as well as the electrical driving parameters could further improve the length selectivity of this fractionation approach.

6. HIGH-RESOLUTION 3D-PRINTED INSULATOR-BASED DIELECTROPHORESIS DEVICES FOR BIOMOLECULAR MANIPULATION

6.1. Abstract

The advancement of Microfluidics has enabled a wide range of biochemical and biological applications, such as high-throughput drug testing or point-of-care diagnostics, to name a few. Implementing insulator-based dielectrophoresis (iDEP) in microfluidic systems has provided a new dimension for the precise manipulation of biomolecules. DEP is based on the movement of polarizable particles in a non-uniform electric field. Despite the advancements in iDEP, it has been hampered due to often cumbersome and expensive fabrication methods. However, in recent years, 3D printing has drawn tremendous attention in microfluidics, alleviating several issues with cleanroom-based fabrication. Two-photon polymerization (2PP) is a novel 3D printing technique that offers unique capabilities with unprecedented resolution compared to standard polymer 3D printing technologies such as stereolithography. This technique can create nanometer-resolution gaps that induce high electric field gradients required for various iDEP applications. Here, we report the first iDEP-based manipulation of biomolecules, namely λ-DNA and phycocyanin, with high-resolution 3D-printed microfluidic devices. iDEP microfluidic devices with different post geometries were printed and developed with a gap resolution down to 2 μm. For λ-DNA and phycocyanin, positive DEP (pDEP)-based trapping was observed. A numerical model was developed to estimate the DEP trapping force and polarizability of protein. Our numerical models were in excellent agreement with experimentally observed trapping conditions. Furthermore, sub-micron spatial resolution was achieved down to 800 nm. This 3D printing technology may offer great potential for prototyping novel iDEP microdevices

due to its greater adaptability for design upgrades, with scope for further improvement in resolution down to a few hundred nanometers, opening the opportunity to explore iDEP-based applications for various biomolecules in the future.

6.2. Introduction

Microfluidics is a science that offers precise fluid control and rapid sample processing due to the high surface-to-volume ratio.[2, 3] Microfluidics offers superior advantages over conventional macro-scale platforms, *e.g.*, flow cytometry, centrifugation, etc.[370] Several technologies have already been proposed and developed to manipulate particles in microfluidic systems. In recent years, insulator-based dielectrophoresis (iDEP) has gained attraction due to the precise manipulation of biomolecules and nanoparticles. In an iDEP-based microfluidic device, insulating geometries of constrictions are introduced in the channel to generate the inhomogeneous electric field gradients in the device.[29]

The DEP force scales with $\boldsymbol{\nabla E^2}$ and the volume of the particles. Thus, to manipulate the smaller size particles, i.e., nanoparticles, proteins, or viruses, higher $\boldsymbol{\nabla E^2}$ is often required. In recent years, iDEP microfluidics has provided a new dimension for precisely manipulating bioparticles and biomolecules. Using iDEP includes less fouling of electrodes, minimal gas formation due to less electrolysis, and simpler device fabrication.

In the presence of electric field gradients, DEP's selectivity stems from the biomolecules' polarizability. A theoretical framework to describe the polarizability mechanism has been reported previously for biological particles such as cells, viruses, and organelles.[194] For example, DEP responses for cells can be described with a shell model, which assigns different permittivities in each layer of the shell structures.[20, 21, 116] However, theoretical models for DNA and proteins are comparatively less developed and still under

debate. The polarizability of biomolecules is not easily accessible, and various strategies have been reported to determine it. For DNA, the polarization is mainly caused by the surrounding ion cloud on the negatively charged backbone.[371] For proteins, the polarization mechanism for DEP transport is still not fully understood. Since extremely high electric field gradients are required to manipulate nm-sized proteins, the DEP manipulation of proteins has posed many challenges for microfluidic devices. Researchers have reported a variety of formats and conditions to manipulate proteins using DEP with $\boldsymbol{\nabla E^2}$ ranging from $10^{12} v^2/m^3$ $10^{21} v^2/m^3$.[31, 97, 102, 113, 372, 373] One way to generate high $\boldsymbol{\nabla E^2}$ is by applying higher electrical potentials, which can induce Joule heating and instability of the sample mixture. Another way to increase to $\boldsymbol{\nabla E^2}$ is by creating nm-sized gaps/constrictions in the microfluidic device. Several groups have reported smaller constrictions in the past to generate high electric fields using electron beam lithography or focused ion beam milling.[99, 374-376] However, these fabrication procedures are not often suitable due to cumbersome and expensive fabrication methods, requiring highly skilled personnel and sophisticated instruments in cleanroom facilities.

In recent years, three-dimensional printing (3D printing) has gained attention in the field of microfluidics for its rapid prototyping capabilities.[377] 3D printing is also known as additive manufacturing or a layer-by-layer manufacturing method. 3D printing has several advantages over conventional microfluidic devices.[378-380] Conventional microfluidic devices are commonly fabricated using thermoplastics,[381, 382] elastomers,[383, 384] paper,[385, 386] *etc*. Polydimethylsiloxane (PDMS) is one of the most commonly used fabrication materials for iDEP devices due to its elastic and insulating properties.[15, 20, 387] Creating nm-sized features using photolithography often requires more cumbersome fabrication steps

than traditional μm-resolution rapid prototyping. 3D printing alleviates several issues with cleanroom-based fabrication and offers rapid prototyping. Due to advances in the field, 3D-printed microfluidic devices have been widely used in several areas such as chemistry,[388] biology,[389] organ printing,[390, 391] immuno-affinity, and solid-phase extraction,[392] among others. Depending on the printing principles, the commercial 3D printing methods are classified into different categories, including extrusion-based,[393, 394] paper cutting,[395] photo-curing,[396-398] photo-melting,[399, 400] and inkjet-based 3D printing.[401, 402] Recently, an alternative 3D printing approach named two-photon polymerization (2PP gained attention due to its high-resolution printing capability.[403] In a typical 2PP fabrication process, a photosensitive material absorbs two photons consecutively to initiate a polymerization reaction. The photosensitive materials are mostly negative-tone photoresists, and the polymerization occurs from the crosslinking of soluble monomers in the photoresist. Due to the high spatial resolution enabled by the 2PP technique nm-gap constrictions and posts can be successfully integrated with such 3D-printed devices to exhibit high electric field density required to manipulate nm-scale analytes.

Here, to the best of our knowledge, we present the first report on using a high-resolution iDEP microfluidic device fabricated by a 2PP polymerization technique to dielectrophoretically manipulate biomolecules in a low-frequency regime. The iDEP characteristics of model polystyrene beads were studied using the 3D-printed device matching the same post geometries and gaps reported previously.[203] The iDEP characterization of PS beads using the 3D-printed device was cross-matched with previous studies. Furthermore, the iDEP characterization of λ-DNA and phycocyanin protein were studied using the assembled 3D-printed microdevice.

6.3. Experimental Section

6.3.1. Material and Chemicals

0.87-μm-diameter (FP-0852-2) polystyrene beads exhibiting negative surface charges were purchased from Spherotech (Lake Forest, IL, USA). Genomic Lambda phage dsDNA (λ-DNA, 48.5 kbp) and microscope glass slides (Cover glass, No.1 Thickness, 35 x 50 mm and 24 x 40 mm) were purchased from Thermo Fisher Scientific (Waltham, MA, USA). BOBO-3 intercalating dye for fluorescent labeling of λ-DNA was obtained from Life Technologies (Carlsbad, CA, USA). SYLGARD® 184 silicone elastomer kit for polydimethylsiloxane (PDMS) was obtained from Dow Corning Corporation (Midland, MI, USA). 4-(2-hydroxyethyl)piperazine-1-ethanesulfonic acid (HEPES), poly(ethylene glycol)-block-poly(propylene glycol)-block-poly(ethylene glycol) (Pluronic® F108), sodium hydroxide (NaOH), Dimethyl sulfoxide (DMSO), and sucrose were purchased from Sigma-Aldrich (St. Louis, MO, USA). Deionized (DI) water was obtained from an Elga water purification system (Woodridge, USA). Platinum wire was purchased from Alfa Aesar (Ward Hill, MA, USA).

6.3.2. 3D-printed Device Fabrication

The device layout and channel structure were designed in AutoCAD software (Autodesk, San Rafael, CA, USA) and imported into the DeScribe software of the Nanoscribe GT instrument (Nanoscribe GmbH, Germany). Meso Scale protocol was used to print sub 5μm resolution iDEP device structures with IP-S photoresist (Nanoscribe GmbH, Germany) using a 25x objective. A small drop of IP-S was deposited on the indium tin oxide-coated boroaluminosilicate glass slide, and the designed 3D structure was printed using two-photon polymerization of IP-S. The initial device design consisted of an array

with circular post arrays, and the final length was ~4.8 mm; the reservoir diameter was 900 µm with a height of 400 µm. The post array channel length was 2.6 mm with a height of 100 µm resulting in a total fluid volume of ~75 µL. The horizontal post-gaps were kept at 5 µm, whereas the vertical post gaps varied from 5 µm down to 2 µm. The sub-µm resolution was achieved using an IP-Dip photoresist[404, 405] (Nanoscribe GmbH, Germany) in Dip-in Liquid mode with a 63x objective. After printing, the devices were developed by one or more cycles of 5 min sonication followed by 1h on a shaker in SU-8 developer (Microchem, USA). The developed devices were rinsed with isopropyl alcohol until complete development was observed by visual inspection with an optical stereomicroscope. The devices were flood exposed for 30 min with UV radiation using a Thor Labs UV curing system before fluorescence imaging experiments to improve device robustness and decrease background fluorescence. A thin layer of PDMS slab was prepared by mixing PDMS elastomer with curing agent at a 10:1 ratio (w/w), poured on a Petri dish, and degassed for 30 min. The PDMS was cured in an oven for 2h at ~80° C, and the cured cast was subsequently peeled off the Petri dish and cut into small pieces. The PDMS slab and No.1 thickness glass slides were treated with oxygen plasma in a plasma cleaner oven (PDC-001, Harrick Plasma cleaner/sterilizer, USA) at high RF (18 W) for 2 min. The PDMS slab was irreversibly bonded with the glass slide by bringing them into contact. Finally, the developed 3D-printed device was glued using epoxy glue to the PDMS slab (as shown in Figure 6.1a). After assembly, the device was filled with buffer solution (1 mM F108, 10 mM HEPES, pH adjusted to 7.4 by NaOH) by capillary action, and the device was stored in a 100% humid environment for overnight coating of the surface with F108. Finally, Pt electrodes were inserted in the inlet and outlets, and an AC potential was applied

through the electrodes using a high voltage amplifier (AMT 3B20, Matsusada Precision, Inc.) during experiments.

6.3.3. Experimental Setup, Imaging, and Data Analysis

All experiments were performed using the final iteration of the 3D-printed microfluidic device schematically shown in Figure 6.1b. The printed microdevices were secured on the stage, and fluorescence images were acquired with an inverted microscope (IX71, Olympus, Center Valley, PA, USA) equipped with a 100 W mercury burner (U-RFL-T, Olympus, Center Valley, PA, 54 USA). The images were viewed with 20x objectives. For the 0.87 μm bead sample, fluorescence was collected with a filter set containing a 470/40 nm excitation filter, dichroic T495LP, and 525/50 emission filter from Semrock (Henrietta, NY, USA). For the λ-DNA sample, fluorescence was collected with a filter set containing a 607/36 nm excitation filter and a 670/30 nm emission filter from Semrock (Henrietta, NY, USA). A filter set containing 470/40 nm excitation filter and 525/50 nm emission filters (Semrock, USA) was used to capture the fluorescence of the polystyrene beads and phycocyanin sample. Images were captured using a monochromatic QuantEM:512SC CCD camera (Photometrics, Tucson, AZ, USA) and Micro-Manager software (version 1.4.9, Vale Lab, UCSF, CA, USA). Exposure time was set to either 10 ms or 50 ms for these experiments. Pt electrodes were inserted into the inlet and outlet reservoirs and connected to an AC power supply using a high voltage amplifier (AMT-3B20, Matsusada Precision Inc.) via micro clamps (Labsmith, Livermore, CA, USA). The AC signal was produced using a USB 6343 DAQ device (USB X series, National instrument, Tx, USA) and programmed by LabVIEW 2014, version 14.0. Recorded videos and images were processed by ImageJ software (version 1.53, NIH).[406]

6.3.4. Sample Preparation

The bead suspension was prepared by diluting 1µL stock bead suspension from the manufacturer in 100µL DI water. The sample was sonicated for 15 mins, and then 10 µL bead solution was diluted in 500µL sample buffer (1 mM F108, 10 mM HEPES, pH adjusted to 7.4 by NaOH). λ-DNA was diluted to 2.1 ng/µL in 5 mM phosphate buffer at pH 7.6, corresponding to the final DNA concentration of 600 pM. The λ-DNA analytes were labeled with BOBO-3 intercalating dye at a 1:10 molar ratio of dye molecules to DNA base pairs. The recovered labeled DNA was added to a 100 µL buffer. The final buffer contained 10 mM HEPES at pH 7.4, 1 mM Pluronic F108 block copolymer, 100 mM sucrose and 0.2% v/v β-mercaptoethanol. To prepare the protein sample, a 10µL C-phycocyanin protein sample (M_w 242 kDa) was diluted with 100µL buffer solution 10 mM HEPES at pH 7.4, and 1 mM Pluronic F108 block copolymer corresponding final protein concentration to 5 mg/mL. The protein sample was sonicated for 5 mins before the experiment.

6.4. Numerical Modeling

Numerical modeling was performed with COMSOL Multiphysics 6.0 to predict the trapping regions for the pDEP and nDEP cases. A section of the printed microfluidic device matching the post array geometry was drawn in COMSOL. The material properties were chosen according to pre-defined parameters for water as a medium, and medium conductivity was adjusted to 0.03 S/m. A potential was applied matching the electric field in the experiment scaled to the channel section at the extremities of the channel section. The Electric Current module was used to compute the electric field distribution within the

section. Maxwell's current equation was used to study the electric field distribution, which was defined as:

$$J = \sigma E \tag{6.1}$$
$$E = -\nabla V \tag{6.2}$$

Where J is the current density, σ is the medium conductivity, E is the electric field, and V is the potential. The post walls and side walls were selected as an insulator. The potential was applied to the inlet boundary, and the outlet was kept grounded. Next, the Particle Tracing for Fluid Flow module was used with a time-dependent solver to trace trajectories and trapping behavior of the analytes. In this module, the Brownian force (F_b), drag force (F_D), and DEP (F_{DEP}) force accounted for the total force acting on the analytes. The electrophoretic force (F_{EP}) and electroosmotic flow (EOF) was neglected in this model as they do not contribute considerably to particle transport in the low-frequency regime. With the time-dependent solver, the particle trajectories were computed with the following equation:

$$\frac{d(m_p \boldsymbol{v})}{dt} = \boldsymbol{F}_t \tag{6.3}$$

where F_t is defined as the total force, $m_{p,}$ and v are the mass and velocity of the analyte, respectively, which can also be expressed as:

$$\boldsymbol{F}_t = \boldsymbol{F}_b + \boldsymbol{F}_D + \boldsymbol{F}_{dep} \tag{6.4}$$

The Brownian force is defined as:

$$\boldsymbol{F}_b = \sqrt{\frac{12\pi k_B \mu T r_p}{\Delta t}} \tag{6.5}$$

where r_p is the radius of the analyte, μ is the viscosity, T is temperature and k_B is the Boltzman constant. In this model, the drag force was computed with the following equations:

$$\boldsymbol{F}_D = \frac{1}{\beta} m_p(\boldsymbol{u} - \boldsymbol{v}) \tag{6.6}$$

$$\beta = \frac{\rho_p {d_p}^2}{18\mu} \tag{6.7}$$

where m_p, ρ_p and d_p are the mass, density, and diameter of the particle, β is the velocity response time, and μ is the viscosity. u and v are fluid velocity and particle velocity, respectively. The DEP force acting on a biomolecule can be expressed by its polarizability. In COMSOL, this DEP force acting on a biomolecule was coupled using a user-defined force function. Furthermore, the DEP force was defined as:

$$\boldsymbol{F}_{DEP} = \frac{1}{2}\alpha \boldsymbol{\nabla} \boldsymbol{E}^2 \tag{6.8}$$

where α is defined as the polarizability of biomolecules.

In this simulation, for PS beads, $\boldsymbol{F}_b$, $\boldsymbol{F}_D$ and $\boldsymbol{F}_{DEP}$ were considered. Considering PS beads as spherical particles, the DEP force equation of PS beads was expressed with equation 2.15, as mentioned in section 2.2.4.1 in chapter 2, with $Re(CM)$ = -0.5. For λ-DNA and phycocyanin, only $\boldsymbol{F}_b$, and $\boldsymbol{F}_{DEP}$ were considered during the simulation. For λ-DNA and phycocyanin, $\boldsymbol{F}_b$ was estimated by COMSOL using equation 6.5. Using DLS, the radius of the λ-DNA and phycocyanin was approximated as 720 nm and 3.5 nm, respectively, based on the hydrodynamic diameter measured. An $\alpha = 3.3 * 10^{-29}\ Fm^2$ was used for λ-DNA in the numerical model, as reported previously, to account for $\boldsymbol{F}_{DEP}$.[89] The α of a protein was unknown and estimated using the numerical model.

At first, experimentally, the minimum potentials required to trap the biomolecules with DEP were determined. Based on these experimental observations, the $\boldsymbol{\nabla} \boldsymbol{E}^2$ was calculated using the numerical model. Next, the α value was varied until trapping was observed in the numerical model. Different α values of proteins were used in the simulation as mentioned

in Table 6.1 as indicated by α_1 to α_5. Finally, DEP trapping was observed for a value of $\alpha_{phycocyanin} = 3.5 * 10^{-31}\text{Fm}^2$. The radius of PS beads, λ-DNA, and phycocyanin, the diffusion coefficient of phycocyanin, the polarizability value of λ-DNA, and phycocyanin used in this numerical model also can be found in Table 6.1, listed below.

Table 6.1: Parameters used in the numerical modeling

Variable	Value	Unit
Temperature	298	K
Density of water	997	kg/m^3
Dynamic viscosity of water	0.89	cP
PS conductivity ($\varepsilon_{\text{PS bedas}}$)	0	S/m
$\text{Re}(\text{CM}_{\text{PS}})$	-0.5	N/A
Radius of PS beads	0.87	μm
Radius of λ-DNA	720	nm
Radius of phycocyanin	3.5	nm
Diffusion coefficient of phycocyanin	$6.9 * 10^{-11}$	m^2/s
Polarizability of phycocyanin (α_1)	$2.0 * 10^{-34}$	Fm^2
Polarizability of phycocyanin (α_2)	$4.0 * 10^{-32}$	Fm^2
Polarizability of phycocyanin (α_3)	$1.0 * 10^{-31}$	Fm^2
Polarizability of phycocyanin (α_4)	$2.0 * 10^{-31}$	Fm^2
Polarizability of phycocyanin (α_5)	$3.0 * 10^{-31}$	Fm^2
Polarizability (α_λDNA)	$3.3 * 10^{-29}$	Fm^2
Polarizability (α_phycocyanin)	$3.5 * 10^{-31}$	Fm^2

6.5. Results and Discussion

iDEP-based separation devices use the insulating nature of the fabrication material to generate non-uniformity in the electric fields required for inducing a DEP force. Here, we use 3D printing to exploit the insulating nature of cured photoresists to enable iDEP-based particle manipulation. Additionally, this study was designed to characterize high-resolution 3D-printed devices with nm to low μm post-gaps enabling high electric field gradients required for iDEP-based manipulation of nm-scale bioanalytics, especially proteins. Briefly, high-resolution 3D printing enabled by 2PP was used to print devices

with arrays of different post-shape and gaps to generate large electric fields and allow the manipulation of PS beads, DNA, and proteins were demonstrated.

Figure 6.1a represents the schematic of the experimental setup showing the printed device mounted on a thin layer of a PDMS slab attached to a glass slide for fluorescence imaging. Figure 6.1b represents a schematic of the designed iDEP device. The zoomed-in image of Figure 6.1b shows a scanning electron microscopy (SEM) image of the printed post area. The SEM image revealed that the posts area was well developed with a gap resolution down to 2 µm.

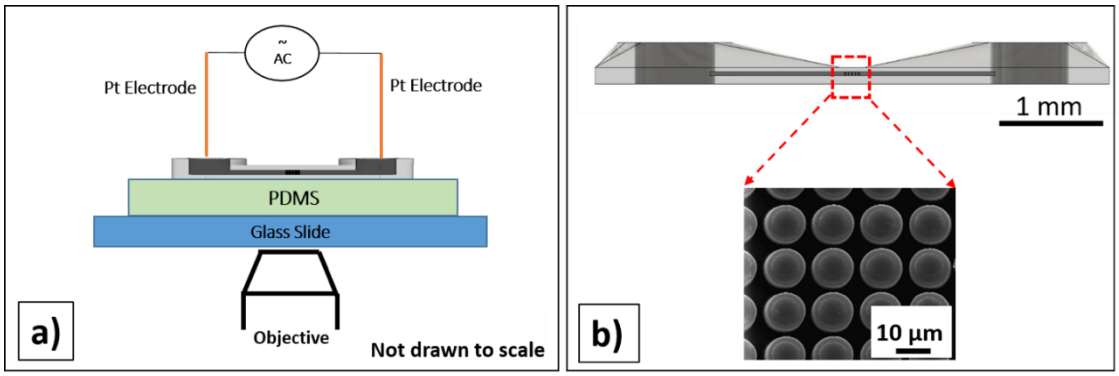

Figure 6.1: Experimental setup and device design: a) Schematic of the experimental setup of the 3D-DEP experiment. The device was printed with an IP-S photoresist with a 2PP technique, and the final length of the device is ~4.8mm. The 3D-printed device was mounted on a thin layer of PDMS slab attached to a glass slide. b) a) Schematic (top) of 3D-printed microfluidic device employed for iDEP studies of biomolecules. The zoomed-in image (bottom) represents the scanning electron micrograph of the post region. The maximum resolution was achieved down to 2 µm.

Previously, several research groups have reported an increase $\boldsymbol{\nabla E^2}$ with decreasing the gap size between two constrictions.[374, 407, 408] Here, we further explore the improvement in electric field magnitude based on defined post gaps ranging from 5 µm down to 500 nm using a numerical model. Figure 6.2 represents the numerically calculated $\boldsymbol{\nabla E^2}$ in the circular post array in a representative section of the device. Figure 6.2a represents the

distribution of $\boldsymbol{\nabla E^2}$ in a post array with a horizontal and vertical post-gap of 5 µm. For an applied electric field of 500 V/cm, $\boldsymbol{\nabla E^2} = 3.8 * 10^{15}\ \mathrm{V^2/m^3}$ was computed. The $\boldsymbol{\nabla E^2}$ increased by ~10 folds when the post-gap decreased from 5 µm to 500 nm, as represented in Figure 6.2b. Figure 6.2c represents the variation in $\boldsymbol{\nabla E^2}$ with incremental post-gaps up to 5 µm. From the figure, it was shown that the $\boldsymbol{\nabla E^2}$ increased when the gap between the two posts decreased.

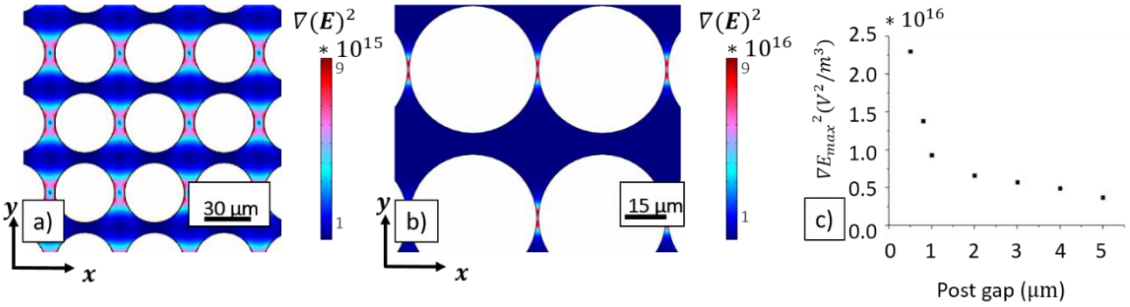

Figure 6.2: Variation in $\boldsymbol{\nabla E^2}$ with different post gaps. a) Computed distribution of gradient of $\boldsymbol{\nabla E^2}$ in a post array at an applied electric field of 700 V/cm. The gap between the two circular posts is 5 µm resulted $\boldsymbol{\nabla E^2} = 3.8 * 10^{15}\ \mathrm{V^2/m^3}$ b) Computed distribution of gradient of $\boldsymbol{\nabla E^2}$in a post array at an applied electric field of 700 V/cm. $\boldsymbol{\nabla E^2}$ increased by ~10 folds when the post gaps are 500 nm. c) Electric field gradients predicted for various post-gap sizes ranging from 5 µm to 500 nm.

6.5.1. iDEP Trapping Observations by Numerical Modelling

Depending on the sign of the $Re(CM)$, two major types of DEP-based analyte trapping phenomena (nDEP and pDEP) may occur. We developed a numerical model using a user-defined DEP force function to predict the α of a protein using COMSOL Multiphysics 6.0. The developed model includes the device geometry, material properties, applied potential scaled to the printed device section, the resulting electric field, electric field gradients, and boundary conditions, allowing one to track the analytes' positions in the microdevice due to the DEP force in a time-dependent manner. The migration of the analytes was traced

over time after releasing from the horizontal lines between the two post rows, as shown in Figure 6.3, and their migration was traced over time. Figure 6.3 represents the pDEP and nDEP trapping for PS beads, λ-DNA, and phycocyanin. PS beads were released between the two post rows and experienced nDEP forces consistent with $Re(CM)$ = -0.5, as reported previously.[203] Figure 6.3a represents the nDEP trapping of the PS beads, which was expected as $Re(CM)$ = -0.5 was used in the simulation. Upon application of the electric field at 700 V/cm, PS beads migrate to the region where the electric field is lowest, confirming the nDEP characteristics of PS beads. Figure 6.3a shows an accumulation in the region between the two posts where the electric field is lowest. These trapping conditions are in agreement with previous reports.[203, 409]

Figure 6.3b represents the pDEP trapping behavior of the λ-DNA. A user-defined DEP force function was introduced in the model allowing to employ of the polarizability, α, to account for their DEP force, see also equation 6.8. An α value of $3.3 * 10^{-29}\ Fm^2$ was used for λ-DNA in the numerical model, as reported previously.[89] With an application of 600 V/cm, the λ-DNA is trapped between the two posts of the same row where the strength of the electric field is highest. By using the numerical model, the estimated DEP force has a magnitude of $10^{-13}N$. Previously, Yokokawa *et al.* reported DEP trapping of λ-DNA (48.5 kbp) using a quadrupole electrode-based microfluidic device.[410] Experimentally, they reported a DEP force of $10^{-13}N$ is required to trap the λ-DNA with an applied potential of 2.5 V and a frequency of 1 kHz. Using a theoretical model, they also estimated the DEP force on the order of $10^{-12}N$. Regtmeier *et al.*, also reported pDEP trapping of λ-DNA (48.5 kbp) using an iDEP device with rectangular posts with a post-gap of 2.3 μm. Their experimental result reveals that pDEP trapping was for λ-DNA over a frequency range of

30 Hz- 200 Hz. Their result matches with the frequency range of 50 Hz - 1 kHz, for which trapping was observed as reported by Chou *et al*.[89] Our experimental observation was in excellent agreement with the observation reported previously.

The DEP force of a protein depends on its polarizability. However, the polarizability of proteins is not easily accessible. If the DEP trapping force for a protein and $\boldsymbol{\nabla E^2}$ is known, a protein's polarizability can be estimated using equation 6.8. Previously, Hölzel *et al*. reported pDEP trapping of R-phycoerythrin.[209] The size and molecular weight of R-phycoerythrin (240 kDa) is similar to phycocyanin (242 kDa). By using a pair of nanoelectrodes with an electrode gap of 500 nm, pDEP trapping was observed. Experimentally, with a frequency of 0.1 MHz and an applied potential of 10 V, the DEP trapping force was estimated as 0.1 pN. An α value of $2.0 * 10^{-34}\ Fm^2$ was estimated from the reported DEP force and $\boldsymbol{\nabla E^2}$ reported by Hölzel *et al.* Experimentally, pDEP of phycocyanin was observed using the 3D-printed device as described in section 6.4.2. An electric field of 450 V/cm was applied, and proteins accumulated between the two horizontal posts (2 µm gap), showing pDEP where the electric field strength was maximum. By using the numerical model, $\boldsymbol{\nabla E^2}$ was calculated when 450 V/cm was applied in the iDEP device. The DEP force equation for biomolecules as stated in the equation 6.8 was used as a user-defined force equation in COMSOL and α was varied until DEP trapping was observed. From the numerical model, the polarizability and DEP trapping force were estimated as $3.5 * 10^{-31}\ Fm^2$ and 0.012 pN, respectively. The estimated DEP trapping force was 1 order of magnitude lower than the estimated value by Hölzel *et al.* Our simulation observation and DEP trapping conditions of proteins were similar but not the

same as previous reports.[111, 209, 411] Several factors could potentially be responsible for this and will be discussed in the next section.

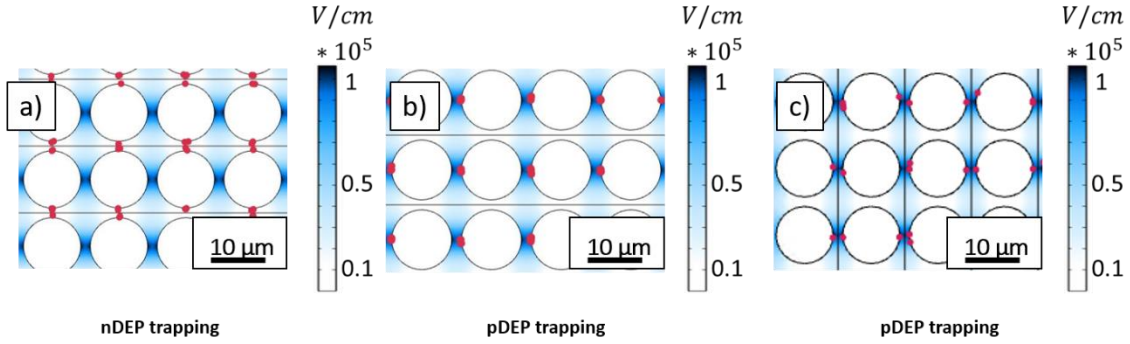

Figure 6.3. Numerical Modeling of DEP behavior for multiple analytes. a) Confirmation of trapping positions of Polystyrene beads subjected to iDEP trapping in two different post geometries. An nDEP response was predicted by the model. b) Prediction of trapping positions of λ-DNA subjected to iDEP trapping in two different post geometries. Trapping positions predicted by numerical modeling for $\alpha = 3.33 * 10^{-29}$ Fm^2. 100 particles were released from the horizontal lines drawn between the column of posts, and λ-DNA experienced pDEP and accumulated between two columns of posts where the electric field strength is highest, also represented by the color bar. c) pDEP trapping of phycocyanin protein using $\alpha = 3.5 * 10^{-31}$ Fm^2.

6.5.2. Experimental Observation of iDEP Characteristics

The iDEP trapping of PS beads, λ-DNA, and phycocyanin was also studied experimentally using the 3D-printed microdevice. The applied potentials ranged between 0 and 1000 V/cm across the device was studied during the experiment. To show the potential of 3D-printed iDEP devices, a variety of post-array geometries and gaps were realized and DEP manipulation was demonstrated for analytes previously characterized using traditional iDEP devices. First, an iDEP ratchet post array device was printed matching the same post geometries and post gaps as reported previously.[203] With this particular geometry, a ratchet-based migration mechanism of 0.87 µm PS beads using a PDMS iDEP ratchet device was reported by Kim *et al*.[203] The mechanism involves nDEP trapping of the PS beads which was observed when 800V was applied over 1 cm of the

channel with a frequency of 10 kHz. Similar experiments were conducted here with the 3D-printed ratchet device using the same buffer and DEP conditions. Figure C.1 in Appendix C, shows an image of nDEP trapping of PS beads trapped in the microdevice (y-direction) associated with elliptical post arrays with an applied potential of 800 V/cm and a frequency of 10 kHz. These positions correspond to the lowest electric field region compared to Figure C.1. The nDEP trapping observation shows an excellent agreement matching the trapping conditions with those reported previously by Kim *et al*.[203]

Next, the DEP behavior of λ-DNA was investigated experimentally in a 3D-printed microdevice with an array of circular posts. With a minimum applied potential of 600 V/cm and 1000 Hz, λ-DNA was trapped in the regions with higher electric field strength, as shown in Figure 6.4a. We note that the location of DEP trapping in the post array changed from what was observed for the PS bead trapping locations, indicating pDEP trapping of the λ-DNA. These trapping regions coincide well with the regions predicted by the numerical model. The iDEP trapping behavior for λ-DNA was studied under various applied potentials, and Figure 6.4b indicates the fluorescent intensity at a different applied potential. Above a threshold potential of 300V/cm, the accumulation of λ-DNA starts to occur in the pDEP trapping regions. A plateau was reached with an applied potential of 600 V/cm or above. The experimentally observed pDEP trapping for λ-DNA is in excellent agreement with the numerical model (Figure 6.3b).

Next, iDEP manipulation of phycocyanin protein was studied with the 3D-printed device. Figure 6.4c shows the trapping behavior of phycocyanin. At 1000Hz and 450 V/cm applied on the entire device, the phycocyanin accumulated in the highest electric field regions, exhibiting pDEP. By adjusting the estimated α value in the numerical model, our

experimental observation of pDEP trapping of phycocyanin shows an excellent agreement with the numerical model, as shown in Figure 6.3c. Figure 6.4d shows the trapping behavior of phycocyanin protein at varying applied potentials from 0 to 900 V/cm in the device. No trapping was observed below 150 V/cm. Above 150 V/cm, the phycocyanin starts to accumulate, showing pDEP trapping behavior, and a plateau was reached above 400 V/cm. Previously, Hölzel *et al.* reported pDEP trapping of R-phycoerythrin requiring a trapping force of 0.1 pN.

Using a numerical model and the iDEP trapping conditions of phycocyanin, we estimated that a trapping force of 0.012 pN is required to trap the protein in the printed iDEP device. Our estimated DEP force is 1 order magnitude lower than the trapping force estimated by Hölzel *et al.* Several experimental factors could potentially contribute to the overall DEP force during the experiments. R-phycoerythrin was considered for the numerical model due to its size and molecular weight proximity to phycocyanin. These two proteins could potentially have different permanent dipole moment and dielectric susceptibilities that can influence the overall required DEP trapping force. Additionally, A hydrodynamic flow in the printed device was noticed, potentially contributing to the overall DEP force or may result in inconsistent trapping around the posts. Second, we attribute that the proteins might be aggregated, and instead of trapping a single protein molecule between the posts, we might have manipulated the aggregated protein samples. These aggregated proteins may exhibit a larger effective radius than a single protein. Since the DEP force depends on the particle radius, a lower DEP force would be required to trap these aggregated protein molecules. Furthermore, the protein DEP is dominated by the permanent dipole of the protein and the solvent-protein interaction.[104] The DEP response of the protein is also

influenced by the ion distribution in the EDL. As reported previously, the dielectrophoretic susceptibility of proteins also differs for different proteins.[111] In conclusion, as two different proteins are being compared here and considering experimental errors, the required DEP trapping force of phycocyanin potentially could be different from the DEP trapping forces to trap proteins with similar sizes as reported previously.[209]

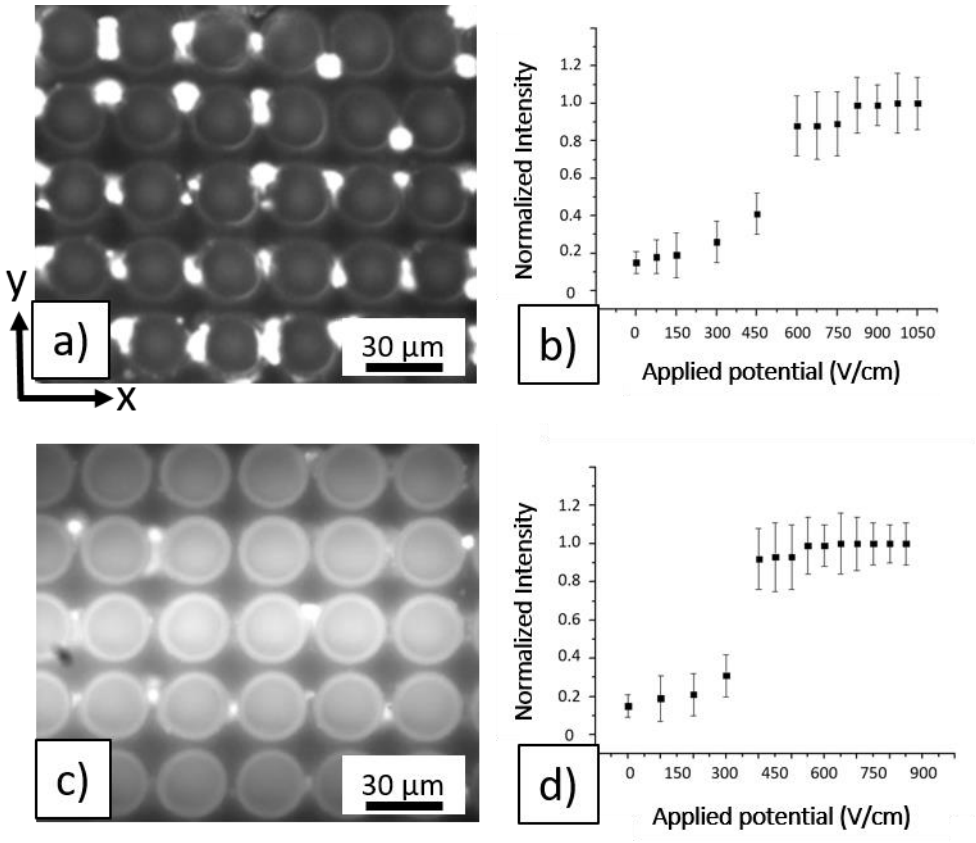

Figure 6.4: Experimental results: (a) At 500Hz (700V/cm), λ-DNA (48.5 kbp) labeled with BOBO-3 (100 pM) shows pDEP as trapping occurs in the regions of the high electric field gradient. (b) Normalized fluorescence intensity is indicative of iDEP trapping vs applied electric potential for λ-DNA. (c) At 100Hz and 600V/cm, Phycocyanin experiences pDEP as trapping occurs in the high electric field gradient regions. (d) Normalized fluorescence intensity is indicative of iDEP trapping vs applied electric potential for phycocyanin. Above 550 V/cm, fluorescence intensity reaches a plateau.

6.5.3. Nanometer-Resolution 3D-Printed Devices for Nano-Scale Analytes

To expand the analyte profile that can be manipulated on such devices in the future, the post gaps are required to be in the nanometer range to produce the required high electric field gradients. Therefore, our next attempts were towards increasing the resolution of these devices. We employed the IP-Dip photoresist and small-feature printing protocols to achieve such spatial resolution.[404, 405] Due to this design's micrometer-sized channels and nano-scale gaps, the development step (removal of unpolymerized photoresist) poses a challenge. Therefore, we designed an open face post array device to assess printing parameters and resolution. After optimizing printing parameters such as laser power, scan speed, etc., an open face post-array device with post gaps down to 800 nm was successfully printed and developed as shown in Figure 6.5. These devices can be covered with a PDMS slab to enclose a channel for DEP applications. Further design and printing parameter characterization are underway to improve the post-gap resolution and develop a completely enclosed 3D-printed device to manipulate nano-scale analytes in the future.

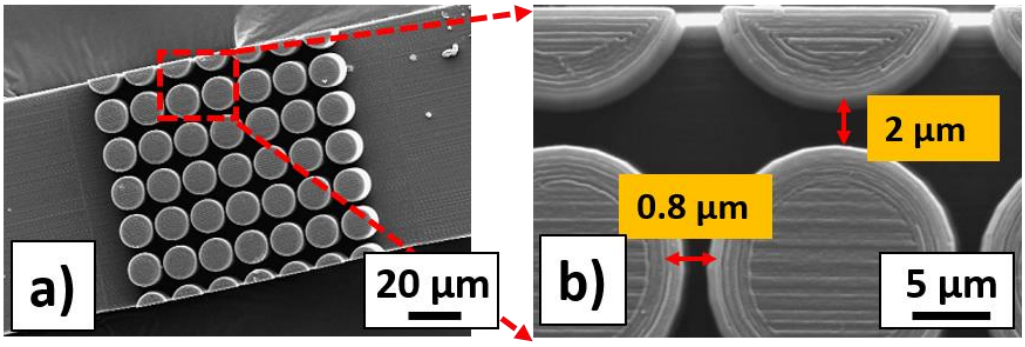

Figure 6.5: Nanometer resolution 3D-printed iDEP devices using IP-Dip photoresist for manipulation of nano-scale analytes.

6.6. Conclusion

3D printing technologies have been widely accepted and employed in many areas of biological and analytical applications. The field of microfluidics has also been impacted by 3D printing due to its rapid prototyping abilities. New iterations of microfluidic devices and applications involving 3D printing are being reported every year, especially in the field of microfluidics. Here, to the best of our knowledge, we report the first completely 3D-printed devices for iDEP based manipulation of analytes. As discussed above, we successfully 3D printed devices with post gaps down to 2 μm and demonstrated the first-ever reported[412] iDEP-based pDEP and nDEP trapping for PS beads, phycocyanin, and λ-DNA in a completely 3D printed microfluidic device. Various post geometries were 3D printed in an enclosed device to reproducibly trap PS beads and biomolecules (phycocyanin and λ-DNA). Additionally, numerical models were developed and studied to predict electric field gradients ($\boldsymbol{\nabla E^2}$) for various post-gaps. The numerical model predicted a ~10 fold increase in $\boldsymbol{\nabla E^2}$ when the post-gap was reduced from 5 μm to 500 nm. Furthermore, trapping behavior for different analytes like PS beads, λ-DNA, and phycocyanin was also predicted and verified experimentally. The experimental observations for the trapping behavior of the above-mentioned analytes were found to be in excellent agreement with the numerical model. Currently, nanometer resolution devices are being developed that may lead to exploring DEP characteristics of nanoscale analytes like single protein molecules and viruses in the future.

7. SUMMARY AND CONCLUSION

Throughout this dissertation, several microfluidic platforms were demonstrated using the electric field-driven migration behavior of the polarizable particle. This dissertation focuses on two main objectives: Fractionating SWNTs by length using an iDEP microfluidic device and introducing a high-resolution 3D printed iDEP microfluidic device to manipulate biomolecules.

In the first part of the work, a novel fractionation and purification of SWNTs by length was demonstrated using an iDEP microfluidic sorter device. The DEP properties of semiconducting type SWNTs were studied in the low-frequency regime (<1 kHz) that has not been previously investigated. A PDMS microfluidic device consisting of circular post arrays was used for this study. Due to the excellent fluorescence properties of semiconducting (6,5) SWNTs in the IR range, near-infrared microscopy was used to visualize the SWNTs. Two different wrapping agents were used during this study named NaDOC and ssDNA, to prevent the aggregation of SWNTs in the aqueous media. According to this study, the DEP properties of SWNTs strongly depend on the ζ and the corresponding suspension properties of the SWNTs. The estimated ζ for well-suspended SWNTs was higher, yielding shorter SWNTs, whereas less densely wrapped SWNTs yielded a longer length with a lower ζ. The conductivity of the medium and SWNTs was estimated to predict the sign of $Re(CM)$. According to this study, well suspended NaDOC and ssDNA-wrapped SWNTs exhibited pDEP. In contrast, less densely NaDOC and ssDNA-wrapped SWNTs showed nDEP. A numerical model was developed to predict the trapping location of SWNTs in the iDEP device. Experimentally, the well-suspended SWNTs accumulated in the post array device showed pDEP, where electric field strength

was highest. Less densely wrapped SWNTs showed nDEP and accumulated in the region where electric field strength was lowest. The experimental observations were in excellent agreement with the numerical modeling. Both numerical modeling and experimental study indicated that the DEP characteristics of SWNTs were frequency independent within the range of 0-1000 Hz. This work suggested that SWNTs can be effectively manipulated in the low-frequency AC electric field and indicated that SWNTs could be fractionated using their different characteristics.

Next, in chapter 5, SWNTs fractionation based on the length and DEP properties experiments was conducted using an iDEP constriction sorter device. First, a numerical model was developed to predict the recovery efficiencies of various lengths of SWNTs based on their DEP properties. The numerical model revealed that a recovery efficiency of up to ~90% in selected outlets of the sorter device could be achieved. Experimentally, two samples differing in length and DEP properties showed different migration behavior. Long SWNTs with small ζ, experienced nDEP and migrated in the side outlets where electric field strength was lowest. In contrast, short SWNTs with high ζ experienced pDEP and migrated to the center channel. This migration behavior was in excellent agreement with the numerical model. The resultant resolutions for the two different length distribution were almost at baseline resolution and showed a good separation quality. The fabricated iDEP constriction sorter device could sort SWNTs in continuous mode, which is advantageous for technological applications where purified and larger quantities of SWNTs are required.

The second theme of the dissertation was to develop and fabricate a high-resolution 3D printed iDEP microfluidic device to manipulate biomolecules, as discussed in chapter 6. Insulator-based dielectrophoresis (iDEP) is a non-destructive approach to manipulating

biomolecules in a non-uniform electric field that has provided a new dimension for precisely manipulating biomolecules. The implementation of iDEP in microfluidic systems has provided a new dimension for the precise manipulation of biomolecules. A higher DEP force is often required to manipulate smaller biomolecules or nanoparticles. One way to achieve this high DEP force is by generating a higher electric field, which is often not easy to access using the standard fabrication procedures. However, in recent years, 3D printing has drawn tremendous attention in microfluidics, alleviating complications associated with cleanroom-based device fabrication. 2PP polymerization is a novel 3D printing technique that allows printing nanometer resolution to generate high electric fields in iDEP applications. In this work, two high-resolution 3D printed iDEP devices were printed using 2PP techniques to manipulate biomolecules. The printed iDEP device includes an array of posts with different geometries. The first device was printed with a photoresist named IP-S, and a resolution down to 2 μm was achieved. iDEP trapping of biomolecules, namely phycocyanin protein and λ-DNA, was successfully achieved and agreed with theoretical predictions. Using a user-defined DEP force equation, a numerical model was developed to confirm the trapping location in the iDEP device. The numerical model was in excellent agreement with the experimental observation. The second iDEP microfluidic device was printed in Dip-in Liquid mode using a photoresist named as IP-Dip. A resolution down to 800 nm was achieved and confirmed with the SEM imaging. This study provides insight into a novel approach to high-resolution 3D printed microfluidic devices that generate higher electric fields to manipulate smaller biomolecules and nanoparticles.

In conclusion, various microfluidic devices were successfully designed, fabricated, and demonstrated experimentally to fractionate and manipulate analytes such as SWNTs,

protein, and λ-DNA with the aid of electric fields. The fabricated iDEP devices coupled with electric fields can fractionate and purify SWNTs in a continuous manner. The high-resolution 3D printed device creates nanometer-resolution constrictions that can induce higher electric field gradients required for iDEP applications of nanoscale analytes. This 3D printing technology may offer great potential for prototyping novel iDEP microdevices due to its greater adaptability for design upgrades compared to conventionally microfabricated iDEP devices.

REFERENCES

1. Whitesides, G. M., The origins and the future of microfluidics. *Nature* **2006,** *442* (7101), 368-373.

2. Teh, S.-Y.; Lin, R.; Hung, L.-H.; Lee, A. P., Droplet microfluidics. *Lab on a Chip* **2008,** *8* (2), 198-220.

3. Seemann, R.; Brinkmann, M.; Pfohl, T.; Herminghaus, S., Droplet based microfluidics. *Reports on progress in physics* **2011,** *75* (1), 016601.

4. Sackmann, E. K.; Fulton, A. L.; Beebe, D. J., The present and future role of microfluidics in biomedical research. *Nature* **2014,** *507* (7491), 181-189.

5. McGrath, J. S.; Quist, J.; Seddon, J. R.; Lai, S. C.; Lemay, S. G.; Bridle, H. L., Deformability assessment of waterborne protozoa using a microfluidic-enabled force microscopy Probe. *PloS one* **2016,** *11* (3), e0150438.

6. Jackson, E. L.; Lu, H., Advances in microfluidic cell separation and manipulation. *Current opinion in chemical engineering* **2013,** *2* (4), 398-404.

7. Bhagat, A. A. S.; Bow, H.; Hou, H. W.; Tan, S. J.; Han, J.; Lim, C. T., Microfluidics for cell separation. *Medical & biological engineering & computing* **2010,** *48* (10), 999-1014.

8. Pohl, H. A., Dielectrophoresis, a New Technique for Studying Cells and Organelles. *Am. Phys. Soc.* **1970,** *15*, 1362.

9. Demircan, Y.; Özgür, E.; Külah, H., Dielectrophoresis: Applications and future outlook in point of care. *Electrophoresis* **2013,** *34* (7), 1008-1027.

10. Gagnon, Z. R., Cellular dielectrophoresis: Applications to the characterization, manipulation, separation and patterning of cells. *Electrophoresis* **2011,** *32* (18), 2466-2487.

11. Khoshmanesh, K.; Nahavandi, S.; Baratchi, S.; Mitchell, A.; Kalantar-zadeh, K., Dielectrophoretic platforms for bio-microfluidic systems. *Biosens. Bioelectron.* **2011,** *26* (5), 1800-1814.

12. Li, M.; Li, W. H.; Zhang, J.; Alici, G.; Wen, W., A review of microfabrication techniques and dielectrophoretic microdevices for particle manipulation and separation. *J. Phys. D: Appl. Phys.* **2014,** *47* (6), 063001.

13. Markx, G. H., The use of electric fields in tissue engineering. *Organogenesis* **2008,** *4* (1), 11-17.

14. Nango, E.; Royant, A.; Kubo, M.; Nakane, T.; Wickstrand, C.; Kimura, T.; Tanaka, T.; Tono, K.; Song, C.; Tanaka, R.; Arima, T.; Yamashita, A.; Kobayashi, J.; Hosaka, T.; Mizohata, E.; Nogly, P.; Sugahara, M.; Nam, D.; Nomura, T.; Shimamura, T.; Im, D.; Fujiwara, T.; Yamanaka, Y.; Jeon, B.; Nishizawa, T.; Oda, K.; Fukuda, M.; Andersson, R.; Bath, P.; Dods, R.; Davidsson, J.; Matsuoka, S.; Kawatake, S.; Murata, M.; Nureki, O.; Owada, S.; Kameshima, T.; Hatsui, T.; Joti, Y.; Schertler, G.; Yabashi, M.; Bondar, A. N.; Standfuss, J.; Neutze, R.; Iwata, S., A three-dimensional movie of structural changes in bacteriorhodopsin. *Science* **2016,** *354* (6319), 1552-1557.

15. Martinez-Duarte, R., Microfabrication technologies in dielectrophoresis applications—A review. *Electrophoresis* **2012,** *33* (21), 3110-3132.

16. Md Ali, M. A.; Ostrikov, K.; Khalid, F. A.; Majlis, B. Y.; Kayani, A. A., Active bioparticle manipulation in microfluidic systems. *RSC Adv.* **2016,** *6* (114), 113066-113094.

17. Srivastava, S. K.; Gencoglu, A.; Minerick, A. R., DC insulator dielectrophoretic applications in microdevice technology: a review. *Anal. Bioanal. Chem.* **2011,** *399* (1), 301-321.

18. Zhang, C.; Khoshmanesh, K.; Mitchell, A.; Kalantar-zadeh, K., Dielectrophoresis for manipulation of micro/nano particles in microfluidic systems. *Anal. Bioanal. Chem.* **2010,** *396* (1), 401-420.

19. Lu, Y.; Liu, T.; Lamanda, A. C.; Sin, M. L. Y.; Gau, V.; Liao, J. C.; Wong, P. K., AC Electrokinetics of Physiological Fluids for Biomedical Applications. *J. Lab. Autom.* **2015,** *20* (6), 611-620.

20. Kim, D.; Sonker, M.; Ros, A., Dielectrophoresis: From Molecular to Micrometer-Scale Analytes. *Anal. Chem.* **2019,** *91* (1), 277-295.

21. Pethig, R., Review Article—Dielectrophoresis: Status of the theory, technology, and applications. *Biomicrofluidics* **2010,** *4* (2), 022811.

22. Qian, C.; Huang, H.; Chen, L.; Li, X.; Ge, Z.; Chen, T.; Yang, Z.; Sun, L., Dielectrophoresis for Bioparticle Manipulation. *Int. J. Mol. Sci.* **2014,** *15* (10), 18281-18309.

23. Viefhues, M.; Eichhorn, R., DNA dielectrophoresis: Theory and applications a review. *Electrophoresis* **2017,** *38* (11), 1483-1506.

24. Jubery, T. Z.; Srivastava, S. K.; Dutta, P., Dielectrophoretic separation of bioparticles in microdevices: A review. *Electrophoresis* **2014,** *35* (5), 691-713.

25. Kuzyk, A., Dielectrophoresis at the nanoscale. *Electrophoresis* **2011,** *32* (17), 2307-2313.

26. Fernandez, R. E.; Rohani, A.; Farmehini, V.; Swami, N. S., Review: Microbial analysis in dielectrophoretic microfluidic systems. *Anal. Chim. Acta* **2017,** *966*, 11-33.

27. Mobley, J.; Waters, K. R.; Miller, J. G., Finite-bandwidth effects on the causal prediction of ultrasonic attenuation of the power-law form. *J. Acoust. Soc. Am.* **2003,** *114* (5), 2782-2790.

28. Regtmeier, J.; Eichhorn, R.; Viefhues, M.; Bogunovic, L.; Anselmetti, D., Electrodeless dielectrophoresis for bioanalysis: Theory, devices and applications. *Electrophoresis* **2011,** *32* (17), 2253-2273.

29. Nakano, A.; Ros, A., Protein dielectrophoresis: Advances, challenges, and applications. *Electrophoresis* **2013,** *34* (7), 1085-1096.

30. Laux, E.-M.; Bier, F. F.; Hölzel, R., Electrode-based AC electrokinetics of proteins: A mini-review. *Bioelectrochemistry* **2018,** *120*, 76-82.

31. Lapizco-Encinas, B. H., On the recent developments of insulator-based dielectrophoresis: A review. *Electrophoresis* **2019,** *40* (3), 358-375.

32. Dash, S.; Mohanty, S., Dielectrophoretic separation of micron and submicron particles: A review. *Electrophoresis* **2014,** *35* (18), 2656-2672.

33. Ding, J.; Lawrence, R. M.; Jones, P. V.; Hogue, B. G.; Hayes, M. A., Concentration of Sindbis virus with optimized gradient insulator-based dielectrophoresis. *Analyst* **2016,** *141* (6), 1997-2008.

34. Purewal, M. S.; Hong, B. H.; Ravi, A.; Chandra, B.; Hone, J.; Kim, P., Scaling of Resistance and Electron Mean Free Path of Single-Walled Carbon Nanotubes. *Phys. Rev. Lett.* **2007,** *98* (18), 186808.

35. Kim, Y.; Hong, S.; Jung, S.; Strano, M. S.; Choi, J.; Baik, S., Dielectrophoresis of Surface Conductance Modulated Single-Walled Carbon Nanotubes Using Catanionic Surfactants. *J. Phys. Chem. B* **2006,** *110* (4), 1541-1545.

36. Oron-Carl, M.; Hennrich, F.; Kappes, M. M.; Löhneysen, H. v.; Krupke, R., On the Electron−Phonon Coupling of Individual Single-Walled Carbon Nanotubes. *Nano Lett.* **2005,** *5* (9), 1761-1767.

37. Tans, S. J.; Verschueren, A. R. M.; Dekker, C., Room-temperature transistor based on a single carbon nanotube. *Nature* **1998,** *393* (6680), 49-52.

38. Tománek, D.; Jorio, A.; Dresselhaus, M. S.; Dresselhaus, G., Introduction to the Important and Exciting Aspects of Carbon-Nanotube Science and Technology. In *Carbon Nanotubes: Advanced Topics in the Synthesis, Structure, Properties and Applications*, Jorio, A.; Dresselhaus, G.; Dresselhaus, M. S., Eds. Springer Berlin Heidelberg: Berlin, Heidelberg, 2008; pp 1-12.

39. Baughman, R. H.; Zakhidov, A. A.; de Heer, W. A., Carbon Nanotubes--the Route Toward Applications. *Science* **2002,** *297* (5582), 787-792.

40. Yao, Z.; Kane, C. L.; Dekker, C., High-Field Electrical Transport in Single-Wall Carbon Nanotubes. *Phys. Rev. Lett.* **2000,** *84* (13), 2941-2944.

41. Hersam, M. C., Progress towards monodisperse single-walled carbon nanotubes. *Nat. Nanotechnol.* **2008,** *3,* 387.

42. Nanot, S.; Hároz, E. H.; Kim, J.-H.; Hauge, R. H.; Kono, J., Optoelectronic Properties of Single-Wall Carbon Nanotubes. *Adv. Mater.* **2012,** *24* (36), 4977-4994.

43. Arnold, M. S.; Green, A. A.; Hulvat, J. F.; Stupp, S. I.; Hersam, M. C., Sorting carbon nanotubes by electronic structure using density differentiation. *Nat. Nanotechnol.* **2006,** *1* (1), 60-65.

44. Iijima, S., Helical microtubules of graphitic carbon. *Nature* **1991,** *354* (6348), 56-58.

45. Collins, P. G.; Zettl, A.; Bando, H.; Thess, A.; Smalley, R. E., Nanotube Nanodevice. *Science* **1997,** *278* (5335), 100-102.

46. Hamada, N.; Sawada, S.-i.; Oshiyama, A., New one-dimensional conductors: Graphitic microtubules. *Phys. Rev. Lett.* **1992,** *68* (10), 1579-1581.

47. Saito, S., Carbon Nanotubes for Next-Generation Electronics Devices. *Science* **1997,** *278* (5335), 77-78.

48. Fakhri, N.; Wessel, A. D.; Willms, C.; Pasquali, M.; Klopfenstein, D. R.; MacKintosh, F. C.; Schmidt, C. F., High-resolution mapping of intracellular fluctuations using carbon nanotubes. *Science* **2014,** *344* (6187), 1031-1035.

49. Cheng, Y.-H.; Moura, P. A. R.; Zhenglong, L.; Feng, L.; Arokiam, S.; Yang, J.; Hariharan, M.; Basuray, S., Effect of electrode configuration on the sensitivity of nucleic acid detection in a non-planar, flow-through, porous interdigitated electrode. *Biomicrofluidics* **2019,** *13* (6), 064118.

50. Wind, S. J.; Appenzeller, J.; Martel, R.; Derycke, V.; Avouris, P., Vertical scaling of carbon nanotube field-effect transistors using top gate electrodes. *Appl. Phys. Lett.* **2002,** *80* (20), 3817-3819.

51. Dillon, A. C., Storage of Hydrogen in Single-Walled Carbon Nanotubes. *Nature* **1997,** *386*, 377.

52. Che, G.; Lakshmi, B. B.; Fisher, E. R.; Martin, C. R., Carbon nanotubule membranes for electrochemical energy storage and production. *Nature* **1998,** *393* (6683), 346-349.

53. Collins, P. G.; Arnold, M. S.; Avouris, P., Engineering Carbon Nanotubes and Nanotube Circuits Using Electrical Breakdown. *Science* **2001,** *292* (5517), 706-709.

54. Komatsu, N.; Wang, F., A Comprehensive Review on Separation Methods and Techniques for Single-Walled Carbon Nanotubes. *Materials* **2010,** *3* (7), 3818-3844.

55. Peng, H.; Alvarez, N. T.; Kittrell, C.; Hauge, R. H.; Schmidt, H. K., Dielectrophoresis Field Flow Fractionation of Single-Walled Carbon Nanotubes. *J. Am. Chem. Soc.* **2006,** *128* (26), 8396-8397.

56. Huang, X.; McLean, R. S.; Zheng, M., High-Resolution Length Sorting and Purification of DNA-Wrapped Carbon Nanotubes by Size-Exclusion Chromatography. *Anal. Chem.* **2005,** *77* (19), 6225-6228.

57. Zheng, M.; Jagota, A.; Strano, M. S.; Santos, A. P.; Barone, P.; Chou, S. G.; Diner, B. A.; Dresselhaus, M. S.; Mclean, R. S.; Onoa, G. B.; Samsonidze, G. G.; Semke, E. D.; Usrey, M.; Walls, D. J., Structure-Based Carbon Nanotube Sorting by Sequence-Dependent DNA Assembly. *Science* **2003,** *302* (5650), 1545-1548.

58. Beebe, D. J.; Mensing, G. A.; Walker, G. M., Physics and applications of microfluidics in biology. *Annual review of biomedical engineering* **2002,** *4* (1), 261-286.

59. Convery, N.; Gadegaard, N., 30 years of microfluidics. *Micro and Nano Engineering* **2019,** *2*, 76-91.

60. Issadore, D.; Franke, T.; Brown, K. A.; Westervelt, R. M., A Microfluidic Microprocessor: Controlling Biomemetic Containers and Cells using Hybrid Integrated Circuit/Microfluidic Chips. *Lab on a Chip* **2010**.

61. Stone, H. A., Introduction to fluid dynamics for microfluidic flows. In *CMOS biotechnology*, Springer: 2007; pp 5-30.

62. Labeed, F. H.; Fatoyinbo, H. O., *Microfluidics in detection science: lab-on-a-chip technologies*. Royal Society of Chemistry: 2014.

63. Ostadfar, A., *Biofluid mechanics: Principles and applications*. Academic Press: 2016.

64. Tabeling, P., *Introduction to microfluidics*. Oxford University Press on Demand: 2005.

65. Reuss, F. F., Sur un nouvel effet de l'électricité galvanique. *Mem. Soc. Imp. Natur. Moscou* **1809,** *2*, 327-337.

66. von Smoluchowski, M., Contribution à la théorie de l'endosmose électrique et de quelques phénomènes corrélatifs. *Bull. Akad. Sci. Cracovie.* **1903,** *8*, 182-200.

67. Helmholtz, H. v., Studien über electrische Grenzschichten. *Annalen der Physik* **1879,** *243* (7), 337-382.

68. Dukhin, S., Non-equilibrium electric surface phenomena. *Advances in Colloid and Interface Science* **1993,** *44*, 1-134.

69. Tandon, V.; Bhagavatula, S. K.; Nelson, W. C.; Kirby, B. J., Zeta potential and electroosmotic mobility in microfluidic devices fabricated from hydrophobic polymers: 1. The origins of charge. *Electrophoresis* **2008,** *29* (5), 1092-1101.

70. Wilson, I. D., *Encyclopedia of separation science*. 2000.

71. Bruus, H., *Theoretical microfluidics*. Oxford university press: 2007; Vol. 18.

72. Kleinstreuer, C., *Microfluidics and nanofluidics: theory and selected applications*. John Wiley & Sons: 2013.

73. Qian, S.; Ai, Y., *Electrokinetic particle transport in micro-/nanofluidics: direct numerical simulation analysis*. CRC Press: 2012; Vol. 153.

74. Li, Y.; Jain, M.; Nandakumar, K. In *Numerical study of droplet formation inside a microfluidic flow-focusing device*, COMSOL Conference Proceeding, 2012.

75. Fernández-Abedul, M. T.; Álvarez-Martos, I.; García Alonso, F. J.; Costa-García, A., Improving the separation in microchip electrophoresis by surface modification. *Capillary Electrophoresis and Microchip Capillary Electrophoresis: Principles, Applications, and Limitations* **2013**, 95-125.

76. Monnig, C. A.; Kennedy, R. T., Capillary electrophoresis. *Analytical chemistry* **1994,** *66* (12), 280-314.

77. Baldessari, F.; Santiago, J. G., Electrophoresis in nanochannels: brief review and speculation. *Journal of Nanobiotechnology* **2006,** *4* (1), 1-6.

78. Breadmore, M. C., Capillary and microchip electrophoresis: challenging the common conceptions. *Journal of Chromatography A* **2012,** *1221*, 42-55.

79. Rodriguez, M. A.; Armstrong, D. W., Separation and analysis of colloidal/nano-particles including microorganisms by capillary electrophoresis: a fundamental review. *Journal of Chromatography B* **2004,** *800* (1-2), 7-25.

80. Pohl, H. A.; Crane, J. S., Dielectrophoresis of cells. *Biophysical journal* **1971,** *11* (9), 711-727.

81. Jones, T. B., *Electromechanics of particles*. Cambridge University Press: Cambridge [England] ;, 1995.

82. Pohl, H. A.; Crane, J. S., Dielectrophoretic force. *Journal of Theoretical Biology* **1972,** *37* (1), 1-13.

83. Benhal, P.; Quashie, D.; Kim, Y.; Ali, J., Insulator based dielectrophoresis: Micro, nano, and molecular scale biological applications. *Sensors* **2020,** *20* (18), 5095.

84. Huang, Y.; Holzel, R.; Pethig, R.; Wang, X.-B., Differences in the AC electrodynamics of viable and non-viable yeast cells determined through combined dielectrophoresis and electrorotation studies. *Physics in Medicine & Biology* **1992,** *37* (7), 1499.

85. Irimajiri, A.; Hanai, T.; Inouye, A., A dielectric theory of "multi-stratified shell" model with its application to a lymphoma cell. *Journal of theoretical biology* **1979,** *78* (2), 251-269.

86. Hughes, M. P., *Nanoelectromechanics in engineering and biology*. CRC press: 2018.

87. Pethig, R.; Menachery, A.; Pells, S.; De Sousa, P., Dielectrophoresis: a review of applications for stem cell research. *J Biomed Biotechnol* **2010,** *2010*, 182581.

88. Meighan, M. M.; Staton, S. J.; Hayes, M. A., Bioanalytical separations using electric field gradient techniques. *Electrophoresis* **2009,** *30* (5), 852-865.

89. Regtmeier, J.; Duong, T. T.; Eichhorn, R.; Anselmetti, D.; Ros, A., Dielectrophoretic manipulation of DNA: Separation and polarizability. *Analytical chemistry* **2007,** *79* (10), 3925-3932.

90. Bakewell, D. J.; Morgan, H., Dielectrophoresis of DNA: time-and frequency-dependent collections on microelectrodes. *IEEE transactions on nanobioscience* **2006,** *5* (1), 1-8.

91. Grandison, S.; Penfold, R.; Vanden-Broeck, J.-M., Monte Carlo simulation of an inhomogeneous dielectric continuum model for B-DNA. *Physical Chemistry Chemical Physics* **2005,** *7* (19), 3486-3495.

92. Ambia-Garrido, J.; Vainrub, A.; Pettitt, B. M., A model for structure and thermodynamics of ssDNA and dsDNA near a surface: A coarse grained approach. *Computer Physics Communications* **2010,** *181* (12), 2001-2007.

93. Parikesit, G. O.; Markesteijn, A. P.; Piciu, O. M.; Bossche, A.; Westerweel, J.; Young, I. T.; Garini, Y., Size-dependent trajectories of DNA macromolecules due to insulative dielectrophoresis in submicrometer-deep fluidic channels. *Biomicrofluidics* **2008,** *2* (2), 024103.

94. Rau, D. C.; Charney, E., Electric dichroism of DNA: Influence of the ionic environment on the electric polarizability. *Biophysical Chemistry* **1983,** *17* (1), 35-50.

95. Asbury, C. L.; Diercks, A. H.; Van Den Engh, G., Trapping of DNA by dielectrophoresis. *Electrophoresis* **2002,** *23* (16), 2658-2666.

96. Ghomian, T.; Jeong, H.; Pan, V.; Celik, K.; Alangari, M.; Ke, Y.; Hihath, J., High-Throughput Dielectrophoretic Trapping and Detection of DNA Origami. *Advanced Materials Interfaces* **2021,** *8* (5), 2001476.

97. Pethig, R., Protein Dielectrophoresis: A Tale of Two Clausius-Mossottis—Or Something Else? *Micromachines-Basel* **2022,** *13* (2), 261.

98. Seyedi, S. S.; Matyushov, D. V., Protein dielectrophoresis in solution. *The Journal of Physical Chemistry B* **2018,** *122* (39), 9119-9127.

99. Lapizco-Encinas, B. H.; Ozuna-Chacón, S.; Rito-Palomares, M., Protein manipulation with insulator-based dielectrophoresis and direct current electric fields. *Journal of Chromatography A* **2008,** *1206* (1), 45-51.

100. Liao, K. T.; Tsegaye, M.; Chaurey, V.; Chou, C. F.; Swami, N. S., Nano-constriction device for rapid protein preconcentration in physiological media through a balance of electrokinetic forces. *Electrophoresis* **2012,** *33* (13), 1958-1966.

101. Staton, S. J.; Jones, P. V.; Ku, G.; Gilman, S. D.; Kheterpal, I.; Hayes, M. A., Manipulation and capture of Aβ amyloid fibrils and monomers by DC insulator gradient dielectrophoresis (DC-iGDEP). *Analyst* **2012,** *137* (14), 3227-3229.

102. Hayes, M. A., Dielectrophoresis of proteins: Experimental data and evolving theory. *Analytical and bioanalytical chemistry* **2020,** *412* (16), 3801-3811.

103. Lapizco-Encinas, B. H., Microscale electrokinetic assessments of proteins employing insulating structures. *Current Opinion in Chemical Engineering* **2020,** *29*, 9-16.

104. Lapizco-Encinas, B. H.; Rito-Palomares, M., Dielectrophoresis for the manipulation of nanobioparticles. *Electrophoresis* **2007,** *28* (24), 4521-4538.

105. Pethig, R., Dielectric and electrical properties of biological materials. *Journal of Bioelectricity* **1985,** *4* (2), vii-ix.

106. Antosiewicz, J., Computation of the dipole moments of proteins. *Biophysical journal* **1995,** *69* (4), 1344-1354.

107. Oleinikova, A.; Sasisanker, P.; Weingärtner, H., What can really be learned from dielectric spectroscopy of protein solutions? A case study of ribonuclease A. *The Journal of Physical Chemistry B* **2004,** *108* (24), 8467-8474.

108. Sasisanker, P.; Oleinikova, A.; Weingärtner, H.; Ravindra, R.; Winter, R., Solvation properties and stability of ribonuclease A in normal and deuterated water studied by dielectric relaxation and differential scanning/pressure perturbation calorimetry. *Physical Chemistry Chemical Physics* **2004,** *6* (8), 1899-1905.

109. Takashima, S., Electric dipole moments of globular proteins: measurement and calculation with NMR and X-ray databases. *Journal of non-crystalline solids* **2002,** *305* (1-3), 303-310.

110. Pethig, R., Limitations of the Clausius-Mossotti function used in dielectrophoresis and electrical impedance studies of biomacromolecules. *Electrophoresis* **2019,** *40* (18-19), 2575-2583.

111. Hölzel, R.; Pethig, R., Protein dielectrophoresis: I. Status of experiments and an empirical theory. *Micromachines-Basel* **2020,** *11* (5), 533.

112. Dole, M., Debye's contribution to the theory of the viscosity of strong electrolytes. *The Journal of Physical Chemistry* **1984,** *88* (26), 6468-6469.

113. Heyden, M.; Matyushov, D. V., Dielectrophoresis of proteins in solution. *The Journal of Physical Chemistry B* **2020,** *124* (51), 11634-11647.

114. Matyushov, D. V., Electrostatic solvation and mobility in uniform and non-uniform electric fields: From simple ions to proteins. *Biomicrofluidics* **2019,** *13* (6), 064106.

115. Matyushov, D. V., Dipolar response of hydrated proteins. *The Journal of chemical physics* **2012,** *136* (8), 02B618.

116. Voldman, J., ELECTRICAL FORCES FOR MICROSCALE CELL MANIPULATION. *Annual Review of Biomedical Engineering* **2006,** *8* (1), 425-454.

117. Srivastava, S. K.; Gencoglu, A.; Minerick, A. R., DC insulator dielectrophoretic applications in microdevice technology: a review. *Analytical and Bioanalytical Chemistry* **2011,** *399* (1), 301-321.

118. Shafiee, H.; Caldwell, J. L.; Sano, M. B.; Davalos, R. V., Contactless dielectrophoresis: a new technique for cell manipulation. *Biomed. Microdevices* **2009,** *11* (5), 997.

119. Sonker, M.; Kim, D.; Egatz-Gomez, A.; Ros, A., Separation Phenomena in Tailored Micro- and Nanofluidic Environments. *Annu. Rev. Anal. Chem.* **2019,** *12* (1), null.

120. Gale, B. K.; Jafek, A. R.; Lambert, C. J.; Goenner, B. L.; Moghimifam, H.; Nze, U. C.; Kamarapu, S. K., A review of current methods in microfluidic device fabrication and future commercialization prospects. *Inventions* **2018,** *3* (3), 60.

121. Xia, Y.; Whitesides, G. M., Soft lithography. *Annual review of materials science* **1998,** *28* (1), 153-184.

122. Clarson, S.; Semlyen, J., In Siloxane Polymers; PTR Prentice Hall. *Inc.: Englewood Cliffs, New Jersey* **1993**.

123. Waheed, S.; Cabot, J. M.; Macdonald, N. P.; Lewis, T.; Guijt, R. M.; Paull, B.; Breadmore, M. C., 3D printed microfluidic devices: enablers and barriers. *Lab on a Chip* **2016,** *16* (11), 1993-2013.

124. Varadan, V. K., *Microstereolithography and other fabrication techniques for 3D MEMS*. Wiley-Blackwell: 2001.

125. Yazdi, A. A.; Popma, A.; Wong, W.; Nguyen, T.; Pan, Y.; Xu, J., 3D printing: an emerging tool for novel microfluidics and lab-on-a-chip applications. *Microfluid Nanofluid* **2016,** *20* (3), 1-18.

126. Park, S. H.; Yang, D. Y.; Lee, K. S., Two-photon stereolithography for realizing ultraprecise three-dimensional nano/microdevices. *Laser & Photonics Reviews* **2009,** *3* (1-2), 1-11.

127. Cumpston, B. H.; Ananthavel, S. P.; Barlow, S.; Dyer, D. L.; Ehrlich, J. E.; Erskine, L. L.; Heikal, A. A.; Kuebler, S. M.; Lee, I.-Y. S.; McCord-Maughon, D., Two-photon polymerization initiators for three-dimensional optical data storage and microfabrication. *Nature* **1999,** *398* (6722), 51-54.

128. Lee, K.-S.; Kim, R. H.; Yang, D.-Y.; Park, S. H., Advances in 3D nano/microfabrication using two-photon initiated polymerization. *Progress in Polymer Science* **2008,** *33* (6), 631-681.

129. Thostenson, E. T.; Ren, Z.; Chou, T.-W., Advances in the science and technology of carbon nanotubes and their composites: a review. *Compos. Sci. Technol.* **2001,** *61* (13), 1899-1912.

130. Tang, Z. K.; Zhang, L.; Wang, N.; Zhang, X. X.; Wen, G. H.; Li, G. D.; Wang, J. N.; Chan, C. T.; Sheng, P., Superconductivity in 4 Angstrom Single-Walled Carbon Nanotubes. *Science* **2001,** *292* (5526), 2462.

131. Ding, R. G.; Lu, G. Q.; Yan, Z. F.; Wilson, M. A., Recent Advances in the Preparation and Utilization of Carbon Nanotubes for Hydrogen Storage. *J. Nanosci. Nanotechnol.* **2001,** *1* (1), 7-29.

132. Dresselhaus, M. S.; Dresselhaus, G.; Eklund, P. C., Chapter 5 - Synthesis, Extraction, and Purification of Fullerenes. In *Science of Fullerenes and Carbon Nanotubes*, Dresselhaus, M. S.; Dresselhaus, G.; Eklund, P. C., Eds. Academic Press: San Diego, 1996; pp 110-142.

133. Ribeiro, B.; Botelho, E. C.; Costa, M. L.; Bandeira, C. F., Carbon nanotube buckypaper reinforced polymer composites: a review. *Polímeros* **2017,** *27*, 247-255.

134. Krupke, R.; Hennrich, F.; Löhneysen, H. v.; Kappes, M. M., Separation of Metallic from Semiconducting Single-Walled Carbon Nanotubes. *Science* **2003,** *301* (5631), 344-347.

135. Popov, V. N., Carbon nanotubes: properties and application. *Mater. Sci. Eng. R Rep.* **2004,** *43* (3), 61-102.

136. Zhou, C.; Kong, J.; Dai, H., Electrical measurements of individual semiconducting single-walled carbon nanotubes of various diameters. *Appl. Phys. Lett.* **2000,** *76* (12), 1597-1599.

137. Dai, H., Carbon Nanotubes: Synthesis, Integration, and Properties. *Acc. Chem. Res.* **2002,** *35* (12), 1035-1044.

138. Dekker, C., Carbon nanotubes as molecular quantum wires. *Phys. Today* **1999,** *52*, 22-28.

139. Martel, R.; Schmidt, T.; Shea, H. R.; Hertel, T.; Avouris, P., Single- and multi-wall carbon nanotube field-effect transistors. *Appl. Phys. Lett.* **1998,** *73* (17), 2447-2449.

140. Derycke, V.; Martel, R.; Appenzeller, J.; Avouris, P., Carbon Nanotube Inter- and Intramolecular Logic Gates. *Nano Lett.* **2001,** *1* (9), 453-456.

141. Bachtold, A.; Hadley, P.; Nakanishi, T.; Dekker, C., Logic Circuits with Carbon Nanotube Transistors. *Science* **2001,** *294* (5545), 1317.

142. Liu, X.; Lee, C.; Zhou, C.; Han, J., Carbon nanotube field-effect inverters. *Appl. Phys. Lett.* **2001,** *79* (20), 3329-3331.

143. Batra, N. M.; Ashokkumar, A. E.; Smajic, J.; Enyashin, A. N.; Deepak, F. L.; Costa, P. M. F. J., Morphological Phase Diagram of Gadolinium Iodide Encapsulated in Carbon Nanotubes. *J. Phys. Chem. C* **2018,** *122* (43), 24967-24976.

144. White, C. T.; Todorov, T. N., Carbon nanotubes as long ballistic conductors. *Nature* **1998,** *393* (6682), 240-242.

145. Hong, S.; Jung, S.; Choi, J.; Kim, Y.; Baik, S., Electrical Transport Characteristics of Surface-Conductance-Controlled, Dielectrophoretically Separated Single-Walled Carbon Nanotubes. *Langmuir* **2007,** *23* (9), 4749-4752.

146. Dimaki, M.; Bøggild, P., Dielectrophoresis of carbon nanotubes using microelectrodes: a numerical study. *Nanotechnology* **2004,** *15* (8), 1095-1102.

147. Lai, K. W. C.; Xi, N.; Wejinya, U. C., Automated process for selection of carbon nanotube by electronic property using dielectrophoretic manipulation. *J. Micro-Nano Mechatronics* **2008,** *4* (1), 37-48.

148. Prashantha, K.; Soulestin, J.; Lacrampe, M. F.; Krawczak, P.; Dupin, G.; Claes, M.; Tewari, A., Electrical and Dielectric Properties of Multi-Walled Carbon Nanotube Filled Polypropylene Nanocomposites. *Polym. Polym. Compos.* **2010,** *18* (9), 489-494.

149. Yue Wang; Zijian Cui; Dongying Zhu; Xianbin Zhang; Qian, L., Tailoring terahertz surface plasmon wave through free-standing multi-walled carbon nanotubes metasurface. *Opt. Express* **2018,** *26* (12), 15343-15352.

150. Grimes, C. A.; Dickey, E. C.; Mungle, C.; Ong, K. G.; Qian, D., Effect of purification of the electrical conductivity and complex permittivity of multiwall carbon nanotubes. *J. Appl. Phys.* **2001,** *90* (8), 4134-4137.

151. Moscatello, J.; Kayastha, V.; Ulmen, B.; Pandey, A.; Wu, S.; Singh, A.; Yap, Y. K., Surfactant-free dielectrophoretic deposition of multi-walled carbon nanotubes with tunable deposition density. *Carbon* **2010,** *48* (12), 3559-3569.

152. Dai, H.; Wong, E. W.; Lieber, C. M., Probing Electrical Transport in Nanomaterials: Conductivity of Individual Carbon Nanotubes. *Science* **1996,** *272* (5261), 523-526.

153. Ebbesen, T. W.; Lezec, H. J.; Hiura, H.; Bennett, J. W.; Ghaemi, H. F.; Thio, T., Electrical conductivity of individual carbon nanotubes. *Nature* **1996,** *382* (6586), 54-56.

154. Krupke, R.; Hennrich, F.; Kappes, M. M.; v. Löhneysen, H., Surface Conductance Induced Dielectrophoresis of Semiconducting Single-Walled Carbon Nanotubes. *Nano Lett.* **2004,** *4* (8), 1395-1399.

155. Rabbani, M. T.; Schmidt, C. F.; Ros, A., Single-Walled Carbon Nanotubes Probed with Insulator-Based Dielectrophoresis. *Anal. Chem.* **2017,** *89* (24), 13235-13244.

156. Zhang, Z.; Peng, J.; Zhang, H., Low-temperature resistance of individual single-walled carbon nanotubes: A theoretical estimation. *Appl. Phys. Lett.* **2001,** *79* (21), 3515-3517.

157. Spitalsky, Z.; Tasis, D.; Papagelis, K.; Galiotis, C., Carbon nanotube–polymer composites: Chemistry, processing, mechanical and electrical properties. *Prog. Polym. Sci.* **2010,** *35* (3), 357-401.

158. Star, A.; Stoddart, J. F.; Steuerman, D.; Diehl, M.; Boukai, A.; Wong, E. W.; Yang, X.; Chung, S.-W.; Choi, H.; Heath, J. R., Preparation and Properties of Polymer-Wrapped Single-Walled Carbon Nanotubes. *Angew. Chem. Int. Ed.* **2001,** *40* (9), 1721-1725.

159. Chen, R. J.; Zhang, Y.; Wang, D.; Dai, H., Noncovalent Sidewall Functionalization of Single-Walled Carbon Nanotubes for Protein Immobilization. *J. Am. Chem. Soc.* **2001,** *123* (16), 3838-3839.

160. Jagota, A.; Diner, B. A.; Boussaad, S.; Zheng, M., Carbon Nanotube—Biomolecule Interactions: Applications in Carbon Nanotube Separation and Biosensing. In *Applied Physics of Carbon Nanotubes: Fundamentals of Theory, Optics and Transport Devices*, Rotkin, S. V.; Subramoney, S., Eds. Springer Berlin Heidelberg: Berlin, Heidelberg, 2005; pp 253-271.

161. Satake, A.; Miyajima, Y.; Kobuke, Y., Porphyrin−Carbon Nanotube Composites Formed by Noncovalent Polymer Wrapping. *Chem. Mater.* **2005,** *17* (4), 716-724.

162. Liu, P., Modifications of carbon nanotubes with polymers. *Eur. Polym. J* **2005,** *41* (11), 2693-2703.

163. White, B.; Banerjee, S.; O'Brien, S.; Turro, N. J.; Herman, I. P., Zeta-Potential Measurements of Surfactant-Wrapped Individual Single-Walled Carbon Nanotubes. *J. Phys. Chem. C* **2007,** *111* (37), 13684-13690.

164. Oh, H.; Sim, J.; Ju, S.-Y., Binding Affinities and Thermodynamics of Noncovalent Functionalization of Carbon Nanotubes with Surfactants. *Langmuir* **2013,** *29* (35), 11154-11162.

165. Mickelson, E. T.; Chiang, I. W.; Zimmerman, J. L.; Boul, P. J.; Lozano, J.; Liu, J.; Smalley, R. E.; Hauge, R. H.; Margrave, J. L., Solvation of Fluorinated Single-Wall Carbon Nanotubes in Alcohol Solvents. *J. Phys. Chem. B* **1999,** *103* (21), 4318-4322.

166. Riggs, J. E.; Walker, D. B.; Carroll, D. L.; Sun, Y.-P., Optical Limiting Properties of Suspended and Solubilized Carbon Nanotubes. *J. Phys. Chem. B* **2000,** *104* (30), 7071-7076.

167. Niyogi, S.; Hu, H.; Hamon, M. A.; Bhowmik, P.; Zhao, B.; Rozenzhak, S. M.; Chen, J.; Itkis, M. E.; Meier, M. S.; Haddon, R. C., Chromatographic Purification of Soluble Single-Walled Carbon Nanotubes (s-SWNTs). *J. Am. Chem. Soc.* **2001,** *123* (4), 733-734.

168. Bahr, J. L.; Tour, J. M., Highly Functionalized Carbon Nanotubes Using in Situ Generated Diazonium Compounds. *Chem. Mater.* **2001,** *13* (11), 3823-3824.

169. Sun, Y.-P.; Fu, K.; Lin, Y.; Huang, W., Functionalized Carbon Nanotubes: Properties and Applications. *Acc. Chem. Res.* **2002,** *35* (12), 1096-1104.

170. Bekyarova, E.; Itkis, M. E.; Cabrera, N.; Zhao, B.; Yu, A.; Gao, J.; Haddon, R. C., Electronic Properties of Single-Walled Carbon Nanotube Networks. *J. Am. Chem. Soc.* **2005,** *127* (16), 5990-5995.

171. Eatemadi, A.; Daraee, H.; Karimkhanloo, H.; Kouhi, M.; Zarghami, N.; Akbarzadeh, A.; Abasi, M.; Hanifehpour, Y.; Joo, S. W., Carbon nanotubes: properties, synthesis, purification, and medical applications. *Nanoscale Res. Lett.* **2014,** *9* (1), 393.

172. Baddour, C. E.; Briens, C., Carbon Nanotube Synthesis: A Review. *Int. J. Chem. React. Eng.* **2005,** *3* (1).

173. Prasek, J.; Drbohlavova, J.; Chomoucka, J.; Hubalek, J.; Jasek, O.; Adam, V.; Kizek, R., Methods for carbon nanotubes synthesis—review. *J. Mater. Chem.* **2011,** *21* (40), 15872-15884.

174. Das, R.; Shahnavaz, Z.; Ali, M. E.; Islam, M. M.; Abd Hamid, S. B., Can We Optimize Arc Discharge and Laser Ablation for Well-Controlled Carbon Nanotube Synthesis? *Nanoscale Res. Lett.* **2016,** *11* (1), 510.

175. Danafar, F.; Fakhru'l-Razi, A.; Salleh, M. A. M.; Biak, D. R. A., Fluidized bed catalytic chemical vapor deposition synthesis of carbon nanotubes—A review. *Chem. Eng. J.* **2009,** *155* (1), 37-48.

176. Arora, N.; Sharma, N. N., Arc discharge synthesis of carbon nanotubes: Comprehensive review. *Diamond Relat. Mater.* **2014,** *50*, 135-150.

177. Ebbesen, T. W.; Ajayan, P. M., Large-scale synthesis of carbon nanotubes. *Nature* **1992,** *358* (6383), 220-222.

178. Iijima, S.; Ichihashi, T., Single-shell carbon nanotubes of 1-nm diameter. *Nature* **1993,** *363* (6430), 603-605.

179. Bethune, D. S.; Kiang, C. H.; de Vries, M. S.; Gorman, G.; Savoy, R.; Vazquez, J.; Beyers, R., Cobalt-catalysed growth of carbon nanotubes with single-atomic-layer walls. *Nature* **1993,** *363* (6430), 605-607.

180. Shi, Z.; Lian, Y.; Liao, F. H.; Zhou, X.; Gu, Z.; Zhang, Y.; Iijima, S.; Li, H.; Yue, K. T.; Zhang, S.-L., Large scale synthesis of single-wall carbon nanotubes by arc-discharge method. *J. Phys. Chem. Solids* **2000,** *61* (7), 1031-1036.

181. Saito, Y.; Nishikubo, K.; Kawabata, K.; Matsumoto, T., Carbon nanocapsules and single-layered nanotubes produced with platinum-group metals (Ru, Rh, Pd, Os, Ir, Pt) by arc discharge. *J. Appl. Phys* **1996,** *80* (5), 3062-3067.

182. Journet, C.; Maser, W. K.; Bernier, P.; Loiseau, A.; de la Chapelle, M. L.; Lefrant, S.; Deniard, P.; Lee, R.; Fischer, J. E., Large-scale production of single-walled carbon nanotubes by the electric-arc technique. *Nature* **1997,** *388* (6644), 756-758.

183. Rinzler, A. G.; Liu, J.; Dai, H.; Nikolaev, P.; Huffman, C. B.; Rodríguez-Macías, F. J.; Boul, P. J.; Lu, A. H.; Heymann, D.; Colbert, D. T.; Lee, R. S.; Fischer, J. E.; Rao, A. M.; Eklund, P. C.; Smalley, R. E., Large-scale purification of single-wall carbon nanotubes: process, product, and characterization. *App. Phys. A* **1998,** *67* (1), 29-37.

184. Zhang, Y.; Iijima, S., Formation of single-wall carbon nanotubes by laser ablation of fullerenes at low temperature. *Appl. Phys. Lett.* **1999,** *75* (20), 3087-3089.

185. Liu, J.; Rinzler, A. G.; Dai, H.; Hafner, J. H.; Bradley, R. K.; Boul, P. J.; Lu, A.; Iverson, T.; Shelimov, K.; Huffman, C. B.; Rodriguez-Macias, F.; Shon, Y.-S.;

Lee, T. R.; Colbert, D. T.; Smalley, R. E., Fullerene Pipes. *Science* **1998,** *280* (5367), 1253-1256.

186. José-Yacamán, M.; Miki-Yoshida, M.; Rendón, L.; Santiesteban, J. G., Catalytic growth of carbon microtubules with fullerene structure. *Appl. Phys. Lett.* **1993,** *62* (6), 657-659.

187. Ivanov, V.; Nagy, J. B.; Lambin, P.; Lucas, A.; Zhang, X. B.; Zhang, X. F.; Bernaerts, D.; Van Tendeloo, G.; Amelinckx, S.; Van Landuyt, J., The study of carbon nanotubules produced by catalytic method. *Chem. Phys. Lett.* **1994,** *223* (4), 329-335.

188. Amelinckx, S.; Zhang, X. B.; Bernaerts, D.; Zhang, X. F.; Ivanov, V.; Nagy, J. B., A Formation Mechanism for Catalytically Grown Helix-Shaped Graphite Nanotubes. *Science* **1994,** *265* (5172), 635-639.

189. Kim, J.-E.; Han, C.-S., Use of dielectrophoresis in the fabrication of an atomic force microscope tip with a carbon nanotube: a numerical analysis. *Nanotechnology* **2005,** *16* (10), 2245-2250.

190. Lei, U.; Lo, Y. J., Review of the theory of generalised dielectrophoresis. *IET Nanobiotechnol.* **2011,** *5* (3), 86-106.

191. Morgan, H.; Hughes, M. P.; Green, N. G., Separation of Submicron Bioparticles by Dielectrophoresis. *Biophys. J.* **1999,** *77* (1), 516-525.

192. Motayed, A.; He, M.; Davydov, A. V.; Melngailis, J.; Mohammad, S. N., Realization of reliable GaN nanowire transistors utilizing dielectrophoretic alignment technique. *J. Appl. Phys* **2006,** *100* (11), 114310.

193. Morgan, H.; Green, N. G., AC electrokinetics : colloids and nanoparticles. In *AC electrokinetics : colloids and nanoparticles*, Research Studies Press: Philadelphia, PA, 2003.

194. Jones, T. B., *Electromechanics of particles*. Cambridge University Press: Cambridge, 2005.

195. Green, N. G.; Morgan, H., Dielectrophoresis of Submicrometer Latex Spheres. 1. Experimental Results. *J. Phys. Chem. B* **1999,** *103* (1), 41-50.

196. Pichler, T.; Knupfer, M.; Golden, M. S.; Fink, J.; Rinzler, A.; Smalley, R. E., Localized and Delocalized Electronic States in Single-Wall Carbon Nanotubes. *Phys. Rev. Lett.* **1998,** *80* (21), 4729-4732.

197. Rabbani, M. T.; Sonker, M.; Ros, A., Carbon nanotube dielectrophoresis: Theory and applications. *Electrophoresis* **2020,** *41* (21-22), 1893-1914.

198. Kang, H.; Wang, B.; Hong, S.; Bae, J. J.; Kim, D.; Han, C.-s.; Lee, Y. H.; Baik, S., Dielectrophoretic separation of metallic arc-discharge single-walled carbon nanotubes in a microfluidic channel. *Synth. Met.* **2013,** *184*, 23-28.

199. O'Konski, C. T., ELECTRIC PROPERTIES OF MACROMOLECULES. V. THEORY OF IONIC POLARIZATION IN POLYELECTROLYTES. *J. Phys. Chem.* **1960,** *64* (5), 605-619.

200. Lyklema, J., Fundamentals of Interface and Colloid Science. *Academic Press: London* **1995,** *Vol 2*, chapter 4.

201. Rabbani, M. T.; Schmidt, C. F.; Ros, A. In *Towards separation of single walled carbon nanotubes with insulator-based dielectrophoresis*, 21st International Conference on Miniaturized Systems for Chemistry and Life Sciences, MicroTAS 2017, Chemical and Biological Microsystems Society: 2020; pp 1342-1343.

202. Kang, J.; Hong, S.; Kim, Y.; Baik, S., Controlling the Carbon Nanotube-to-Medium Conductivity Ratio for Dielectrophoretic Separation. *Langmuir* **2009,** *25* (21), 12471-12474.

203. Kim, D.; Luo, J.; Arriaga, E. A.; Ros, A., Deterministic Ratchet for Sub-micrometer (Bio)particle Separation. *Anal. Chem.* **2018,** *90* (7), 4370-4379.

204. Pohl, H. A., *Dielectrophoresis: The behavior of neutral matter in nonuniform electric fields (Cambridge Monographs on physics)*. Cambridge/New York: Cambridge University Press: 1978.

205. Pohl, H. A., The motion and precipitation of suspensoids in divergent electric fields. *J. Appl. Phys.* **1951,** *22* (7), 869-871.

206. Voldman, J., Electrical Forces for Microscale Cell Manipulation. *Annu. Rev. Biomed. Eng.* **2006,** *8*, 425-454.

207. Chan, J. Y.; Kayani, A. B. A.; Ali, M. A. M.; Kok, C. K.; Majlis, B. Y.; Hoe, S. L. L.; Marzuki, M.; Khoo, A. S.-B.; Ostrikov, K.; Rahman, M. A.; Sriram, S., Dielectrophoresis-based microfluidic platforms for cancer diagnostics. *Biomicrofluidics* **2018,** *12* (1), 011503.

208. Abd Rahman, N.; Ibrahim, F.; Yafouz, B., Dielectrophoresis for Biomedical Sciences Applications: A Review. *Sensors* **2017,** *17* (3), 449.

209. Hölzel, R.; Calander, N.; Chiragwandi, Z.; Willander, M.; Bier, F. F., Trapping Single Molecules by Dielectrophoresis. *Phys. Rev. Lett.* **2005,** *95* (12), 128102.

210. Jie, L.; Xiaorong, G.; Zhiguang, Z.; Shangkai, G.; Jinghao, Z. In *A new calibration method in 3D ultrasonic imaging system*, Proceedings of the 20th Annual International Conference of the IEEE Engineering in Medicine and Biology Society. Vol.20 Biomedical Engineering Towards the Year 2000 and Beyond (Cat. No.98CH36286), 1-1 Nov. 1998; 1998; pp 839-841 vol.2.

211. Lapizco-Encinas, B. H., On the recent developments of insulator-based dielectrophoresis: A review. *Electrophoresis* **2019,** *40* (3), 358-375.

212. Jones, P. V.; Salmon, G. L.; Ros, A., Continuous Separation of DNA Molecules by Size Using Insulator-Based Dielectrophoresis. *Anal. Chem.* **2017,** *89* (3), 1531-1539.

213. Hawkins, B. G.; Kirby, B. J., Electrothermal flow effects in insulating (electrodeless) dielectrophoresis systems. *Electrophoresis* **2010,** *31* (22), 3622-3633.

214. Coleman, J. N.; Khan, U.; Blau, W. J.; Gun'ko, Y. K., Small but strong: A review of the mechanical properties of carbon nanotube–polymer composites. *Carbon* **2006,** *44* (9), 1624-1652.

215. Wang, J., Carbon-Nanotube Based Electrochemical Biosensors: A Review. *Electroanalysis* **2005,** *17* (1), 7-14.

216. Banerjee, S.; White, B. E.; Huang, L.; Rego, B. J.; O'Brien, S.; Herman, I. P., Precise positioning of single-walled carbon nanotubes by ac dielectrophoresis. *J. Vac. Sci. Technol., B: Microelectron. Nanometer Struct.--Process., Meas., Phenom.* **2006,** *24* (6), 3173-3178.

217. Blatt, S.; Hennrich, F.; Löhneysen, H. v.; Kappes, M. M.; Vijayaraghavan, A.; Krupke, R., Influence of Structural and Dielectric Anisotropy on the Dielectrophoresis of Single-Walled Carbon Nanotubes. *Nano Lett.* **2007,** *7* (7), 1960-1966.

218. Banerjee, S.; White, B.; Huang, L.; Rego, B. J.; O'Brien, S.; Herman, I. P., Precise positioning of carbon nanotubes by ac dielectrophoresis using floating posts. *Appl. Phys. A* **2007,** *86* (4), 415-419.

219. Li, J.; Zhang, Q.; Peng, N.; Zhu, Q., Manipulation of carbon nanotubes using AC dielectrophoresis. *Appl. Phys. Lett.* **2005,** *86* (15), 153116.

220. Makaram, P.; Selvarasah, S.; Xiong, X.; Chen, C.-L.; Busnaina, A.; Khanduja, N.; Dokmeci, M. R., Three-dimensional assembly of single-walled carbon nanotube interconnects using dielectrophoresis. *Nanotechnology* **2007,** *18* (39), 395204.

221. Shekhar, S.; Stokes, P.; Khondaker, S. I., Ultrahigh Density Alignment of Carbon Nanotube Arrays by Dielectrophoresis. *ACS Nano* **2011,** *5* (3), 1739-1746.

222. Stokes, P.; Khondaker, S. I., Local-gated single-walled carbon nanotube field effect transistors assembled by AC dielectrophoresis. *Nanotechnology* **2008,** *19* (17), 175202.

223. Stokes, P.; Khondaker, S. I., High quality solution processed carbon nanotube transistors assembled by dielectrophoresis. *Appl. Phys. Lett.* **2010,** *96* (8), 083110.

224. Zhang, Z.-B.; Liu, X.-J.; Campbell, E. E. B.; Zhang, S.-L., Alternating current dielectrophoresis of carbon nanotubes. *J. Appl. Phys* **2005,** *98* (5), 056103.

225. Kim, S.; Xuan, Y.; Ye, P. D.; Mohammadi, S.; Lee, S. W., Single-walled carbon nanotube transistors fabricated by advanced alignment techniques utilizing CVD growth and dielectrophoresis. *Solid-State Electron.* **2008,** *52* (8), 1260-1263.

226. Taeger, S.; Sickert, D.; Atanasov, P.; Eckstein, G.; Mertig, M., Self-assembly of carbon nanotube field-effect transistors by ac-dielectrophoresis. *Phys. status solidi (b)* **2006,** *243* (13), 3355-3358.

227. Dong, L.; Chirayos, V.; Bush, J.; Jiao, J.; Dubin, V. M.; Chebian, R. V.; Ono, Y.; Conley, J. F.; Ulrich, B. D., Floating-Potential Dielectrophoresis-Controlled Fabrication of Single-Carbon-Nanotube Transistors and Their Electrical Properties. *J. Phys. Chem. B* **2005,** *109* (27), 13148-13153.

228. Burg, B. R.; Schneider, J.; Muoth, M.; Durrer, L.; Helbling, T.; Schirmer, N. C.; Schwamb, T.; Hierold, C.; Poulikakos, D., Aqueous Dispersion and Dielectrophoretic Assembly of Individual Surface-Synthesized Single-Walled Carbon Nanotubes. *Langmuir* **2009,** *25* (14), 7778-7782.

229. Seo, H.-W.; Han, C.-S.; Choi, D.-G.; Kim, K.-S.; Lee, Y.-H., Controlled assembly of single SWNTs bundle using dielectrophoresis. *Microelectron. Eng.* **2005,** *81* (1), 83-89.

230. Krupke, R.; Linden, S.; Rapp, M.; Hennrich, F., Thin Films of Metallic Carbon Nanotubes Prepared by Dielectrophoresis. *Adv. Mater.* **2006,** *18* (11), 1468-1470.

231. Pathangi, H.; Groeseneken, G.; Witvrouw, A., Dielectrophoretic assembly of suspended single-walled carbon nanotubes. *Microelectron. Eng.* **2012,** *98*, 218-221.

232. Sorgenfrei, S.; Meric, I.; Banerjee, S.; Akey, A.; Rosenblatt, S.; Herman, I. P.; Shepard, K. L., Controlled dielectrophoretic assembly of carbon nanotubes using real-time electrical detection. *Appl. Phys. Lett.* **2009,** *94* (5), 053105.

233. Li, P.; Xue, W., Selective Deposition and Alignment of Single-Walled Carbon Nanotubes Assisted by Dielectrophoresis: From Thin Films to Individual Nanotubes. *Nanoscale Res. Lett.* **2010,** *5* (6), 1072.

234. Vijayaraghavan, A.; Blatt, S.; Weissenberger, D.; Oron-Carl, M.; Hennrich, F.; Gerthsen, D.; Hahn, H.; Krupke, R., Ultra-Large-Scale Directed Assembly of Single-Walled Carbon Nanotube Devices. *Nano Lett.* **2007,** *7* (6), 1556-1560.

235. Vijayaraghavan, A.; Hennrich, F.; Stürzl, N.; Engel, M.; Ganzhorn, M.; Oron-Carl, M.; Marquardt, C. W.; Dehm, S.; Lebedkin, S.; Kappes, M. M.; Krupke, R., Toward Single-Chirality Carbon Nanotube Device Arrays. *ACS Nano* **2010,** *4* (5), 2748-2754.

236. Zheng, F.; Yang, X.; Wu, Y.; Zhou, Z.; Liu, Z., Large-scale directed assembly of single-walled carbon nanotube devices by alternating current coupling dielectrophoresis. *Carbon* **2017,** *124*, 693-699.

237. Kumatani, A.; Warburton, P. A., Characterization of the disaggregation state of single-walled carbon nanotube bundles by dielectrophoresis and Raman spectroscopy. *Appl. Phys. Lett.* **2008,** *92* (24), 243123.

238. Srivastava, A. K.; Jeong, S. J.; Lee, M.-H.; Lee, S. H.; Jeong, S. H.; Lee, Y. H., Dielectrophoresis force driven dynamics of carbon nanotubes in liquid crystal medium. *J. Appl. Phys* **2007,** *102* (4), 043503.

239. Kim, I.; An, T.; Choi, W.; Kim, C. S.; Cha, H. J.; Lim, G., Site-specific immobilization of microbes using carbon nanotubes and dielectrophoretic force for microfluidic applications. *RSC Adv.* **2014,** *4* (3), 1347-1351.

240. Chen, Z.; Wu, Z.; Tong, L.; Pan, H.; Liu, Z., Simultaneous Dielectrophoretic Separation and Assembly of Single-Walled Carbon Nanotubes on Multigap Nanoelectrodes and Their Thermal Sensing Properties. *Anal. Chem.* **2006,** *78* (23), 8069-8075.

241. Shin, D. H.; Kim, J.-E.; Shim, H. C.; Song, J.-W.; Yoon, J.-H.; Kim, J.; Jeong, S.; Kang, J.; Baik, S.; Han, C.-S., Continuous Extraction of Highly Pure Metallic Single-Walled Carbon Nanotubes in a Microfluidic Channel. *Nano Lett.* **2008,** *8* (12), 4380-4385.

242. Lutz, T.; Donovan, K. J., Macroscopic scale separation of metallic and semiconducting nanotubes by dielectrophoresis. *Carbon* **2005,** *43* (12), 2508-2513.

243. Padmaraj, D.; Zagozdzon-Wosik, W.; Xie, L. M.; Hadjiev, V. G.; Cherukuri, P.; Wosik, J., Parallel and orthogonalE-field alignment of single-walled carbon nanotubes by ac dielectrophoresis. *Nanotechnology* **2008,** *20* (3), 035201.

244. Mendes, M. J.; Schmidt, H. K.; Pasquali, M., Brownian Dynamics Simulations of Single-Wall Carbon Nanotube Separation by Type Using Dielectrophoresis. *J. Phys. Chem. B* **2008,** *112* (25), 7467-7477.

245. Lee, M.-W.; Lin, Y.-H.; Lee, G.-B., Manipulation and patterning of carbon nanotubes utilizing optically induced dielectrophoretic forces. *Microfluid. Nanofluid.* **2010,** *8* (5), 609-617.

246. Mureau, N.; Mendoza, E.; Silva, S. R. P.; Hoettges, K. F.; Hughes, M. P., In situ and real time determination of metallic and semiconducting single-walled carbon nanotubes in suspension via dielectrophoresis. *Appl. Phys. Lett.* **2006,** *88* (24), 243109.

247. Suehiro, J.; Zhou, G.; Imakiire, H.; Ding, W.; Hara, M., Controlled fabrication of carbon nanotube NO2 gas sensor using dielectrophoretic impedance measurement. *Sens. Actuators, B* **2005,** *108* (1), 398-403.

248. Suehiro, J.; Hidaka, S.-I.; Yamane, S.; Imasaka, K., Fabrication of interfaces between carbon nanotubes and catalytic palladium using dielectrophoresis and its application to hydrogen gas sensor. *Sens. Actuators, B* **2007,** *127* (2), 505-511.

249. Lucci, M.; Regoliosi, P.; Reale, A.; Di Carlo, A.; Orlanducci, S.; Tamburri, E.; Terranova, M. L.; Lugli, P.; Di Natale, C.; D'Amico, A.; Paolesse, R., Gas sensing using single wall carbon nanotubes ordered with dielectrophoresis. *Sens. Actuators, B* **2005,** *111-112*, 181-186.

250. Li, P.; Martin, C. M.; Yeung, K. K.; Xue, W., Dielectrophoresis Aligned Single-Walled Carbon Nanotubes as pH Sensors. *Biosensors* **2011,** *1* (1), 23-35.

251. Zhou, R.; Wang, P.; Chang, H.-C., Bacteria capture, concentration and detection by alternating current dielectrophoresis and self-assembly of dispersed single-wall carbon nanotubes. *Electrophoresis* **2006,** *27* (7), 1376-1385.

252. Singh, R.; Sharma, A.; Hong, S.; Jang, J., Electrical immunosensor based on dielectrophoretically-deposited carbon nanotubes for detection of influenza virus H1N1. *Analyst* **2014,** *139* (21), 5415-5421.

253. Ericson, L. M.; Pehrsson, P. E., Aggregation Effects on the Raman Spectroscopy of Dielectrophoretically Deposited Single-Walled Carbon Nanotubes. *J. Phys. Chem. B* **2005,** *109* (43), 20276-20280.

254. Tang, J., Rapid and Reproducible Fabrication of Carbon Nanotube AFM Probes by Dielectrophoresis. *Nano Lett.* **2005,** *5* (1), 11-14.

255. Lu, Y.; Chen, C.; Yang, L.; Zhang, Y., Theoretical Simulation on the Assembly of Carbon Nanotubes Between Electrodes by AC Dielectrophoresis. *Nanoscale Res. Lett.* **2008,** *4* (2), 157.

256. Kashefian Naieni, A.; Nojeh, A., Dielectrophoretic deposition of carbon nanotubes: The role of field frequency and its dependence on solution conductivity. *Microelectron. Eng.* **2014,** *114*, 26-30.

257. Sarker, B. K.; Shekhar, S.; Khondaker, S. I., Semiconducting Enriched Carbon Nanotube Aligned Arrays of Tunable Density and Their Electrical Transport Properties. *ACS Nano* **2011,** *5* (8), 6297-6305.

258. Heller, D. A.; Mayrhofer, R. M.; Baik, S.; Grinkova, Y. V.; Usrey, M. L.; Strano, M. S., Concomitant Length and Diameter Separation of Single-Walled Carbon Nanotubes. *J. Am. Chem. Soc.* **2004,** *126* (44), 14567-14573.

259. Zheng, F.; Zhou, Z.; Yang, X.; Tang, Y.; Wu, Y., Investigation on Strain-Sensing Suspended Single-Walled Carbon Nanotube Arrays. *IEEE T. Nanotechnol.* **2011,** *10* (4), 694-698.

260. Zheng, F.-z.; Zhou, Z.-y.; Yang, X.; Tang, Y.-k.; Wu, Y., Sorting single-walled carbon nanotubes by strain-based electrical burn-off. *Carbon* **2010,** *48* (8), 2169-2174.

261. Suehiro, J.; Imakiire, H.; Hidaka, S.-i.; Ding, W.; Zhou, G.; Imasaka, K.; Hara, M., Schottky-type response of carbon nanotube NO2 gas sensor fabricated onto aluminum electrodes by dielectrophoresis. *Sens. Actuators, B* **2006,** *114* (2), 943-949.

262. Burg, B. R.; Poulikakos, D., Large-scale integration of single-walled carbon nanotubes and graphene into sensors and devices using dielectrophoresis: A review. *J. Mater. Res.* **2011,** *26* (13), 1561-1571.

263. Çetin, B.; Li, D., Dielectrophoresis in microfluidics technology. *Electrophoresis* **2011,** *32* (18), 2410-2427.

264. Ghasemi, A.; Amiri, H.; Zare, H.; Masroor, M.; Hasanzadeh, A.; Beyzavi, A.; Aref, A. R.; Karimi, M.; Hamblin, M. R., Carbon nanotubes in microfluidic lab-on-a-chip technology: current trends and future perspectives. *Microfluid. Nanofluid.* **2017,** *21* (9), 151.

265. Baik, S.; Usrey, M.; Rotkina, L.; Strano, M., Using the Selective Functionalization of Metallic Single-Walled Carbon Nanotubes to Control Dielectrophoretic Mobility. *J. Phys. Chem. B* **2004,** *108* (40), 15560-15564.

266. Rabbani, M. T.; Schmidt, C. F.; Ros, A., Length-Selective Dielectrophoretic Manipulation of Single-Walled Carbon Nanotubes. *Anal. Chem.* **2020**.

267. Tobias, G.; Mendoza, E.; Ballesteros, B., Functionalization of Carbon Nanotubes. In *Encyclopedia of Nanotechnology*, Bhushan, B., Ed. Springer Netherlands: Dordrecht, 2012; pp 911-919.

268. Mallakpour, S.; Soltanian, S., Surface functionalization of carbon nanotubes: fabrication and applications. *RSC Adv.* **2016,** *6* (111), 109916-109935.

269. Mu, Q.; Liu, W.; Xing, Y.; Zhou, H.; Li, Z.; Zhang, Y.; Ji, L.; Wang, F.; Si, Z.; Zhang, B.; Yan, B., Protein Binding by Functionalized Multiwalled Carbon Nanotubes Is Governed by the Surface Chemistry of Both Parties and the Nanotube Diameter. *J. Phys. Chem. C* **2008,** *112* (9), 3300-3307.

270. Sheikholeslam, M.; Pritzker, M.; Chen, P., Dispersion of Multiwalled Carbon Nanotubes in Water Using Ionic-Complementary Peptides. *Langmuir* **2012,** *28* (34), 12550-12556.

271. *Carbon Nanotubes: Synthesis, Structure, Properties and Applications*. Springer-Verlag Berlin Heidelberg: 2001.

272. Baughman, R. H.; Zakhidov, A. A.; de Heer, W. A., Carbon nanotubes - the route toward applications. *Science* **2002,** *297* (5582), 787-792.

273. Krupke, R.; Hennrich, F.; v. Loehneisen, H.; Kappes, M. M., Separation of Metallic from Semiconducting Single-Walled Carbon Nanotubes. *Science* **2003,** *301*, 344-347

274. Yao, Z.; Kane, C. L.; Dekker, C., High-field electrical transport in single-wall carbon nanotubes. *Phys. Rev. Lett.* **2000,** *84* (13), 2941-2944.

275. McEuen, P. L., Single-wall carbon nanotubes. *Physics World* **2000,** *13* (6), 31-36.

276. Wind, S. J.; Appenzeller, J.; Martel, R.; Derycke, V.; Avouris, P., Vertical scaling of carbon nanotube field-effect transistors using top gate electrodes. *Appl. Phys. Lett.* **2002,** *80* (20), 3817-3819.

277. Li, J.; Papadopoulos, C.; Xu, J. M.; Moskovits, M., Highly-ordered carbon nanotube arrays for electronics applications. *Appl. Phys. Lett.* **1999,** *75* (3), 367-369.

278. Park, Y.; Yoo, J.; Lim, B.; Kwon, W.; Rhee, S. W., Improving the functionality of carbon nanodots: doping and surface functionalization. *J. Mater. Chem. A* **2016,** *4* (30), 11582-11603.

279. Boghossian, A. A.; Zhang, J. Q.; Barone, P. W.; Reuel, N. F.; Kim, J. H.; Heller, D. A.; Ahn, J. H.; Hilmer, A. J.; Rwei, A.; Arkalgud, J. R.; Zhang, C. T.; Strano, M. S., Near-Infrared Fluorescent Sensors based on Single-Walled Carbon Nanotubes for Life Sciences Applications. *Chemsuschem* **2011,** *4* (7), 848-863.

280. Cherukuri, T. K.; Tsyboulski, D. A.; Weisman, R. B., Length- and defect-dependent fluorescence efficiencies of individual single-walled carbon nanotubes. *ACS Nano* **2012,** *6* (1), 843-850.

281. Cherukuri, P.; Bachilo, S. M.; Litovsky, S. H.; Weisman, R. B., Near-infrared fluorescence microscopy of single-walled carbon nanotubes in phagocytic cells. *J. Am. Chem. Soc.* **2004,** *126* (48), 15638-15639.

282. O'Connell, M. J.; Bachilo, S. M.; Huffman, C. B.; Moore, V. C.; Strano, M. S.; Haroz, E. H.; Rialon, K. L.; Boul, P. J.; Noon, W. H.; Kittrell, C.; Ma, J. P.; Hauge, R. H.; Weisman, R. B.; Smalley, R. E., Band gap fluorescence from individual single-walled carbon nanotubes. *Science* **2002,** *297* (5581), 593-596.

283. Hersam, M. C., Progress towards monodisperse single-walled carbon nanotubes. *Nature Nanotechnol.* **2008,** *3* (7), 387-394.

284. Nanot, S.; Hároz, E. H.; Kim, J.-H.; Hauge, R. H., Optoelectronic properties of single-wall carbon nanotubes. *Adv. Mater. 24* (36), 4977-4994.

285. Baik, S.; Usrey, M.; Rotkina, L.; Strano, M., Using the Selective Functionalization of Metallic Single-Walled Carbon Nanotubes to Control Dielectrophoretic Mobility. *The Journal of Physical Chemistry B* **2004,** *108* (40), 15560-15564.

286. Duque, J. G.; Parra-Vasquez, A. N. G.; Behabtu, N.; Green, M. J.; Higginbotham, A. L.; Price, B. K.; Leonard, A. D.; Schmidt, H. K.; Lounis, B.; Tour, J. M.; Doorn, S. K.; Cognet, L.; Pasquali, M., Diameter-Dependent Solubility of Single-Walled Carbon Nanotubes. *ACS Nano* **2010,** *4* (6), 3063-3072.

287. Zhou, W.; Ooi, Y. H.; Russo, R.; Papanek, P.; Luzzi, D. E.; Fischer, J. E.; Bronikowski, M. J.; Willis, P. A.; Smalley, R. E., Structural characterization and diameter-dependent oxidative stability of single wall carbon nanotubes synthesized by the catalytic decomposition of CO. *Chem. Phys. Lett.* **2001,** *350* (1-2), 6-14.

288. Peng, H.; Alvarez, N. T.; Kittrell, C.; Hauge, R. H.; Schmidt, H. K., Dielectrophoresis Field Flow Fractionation of Single-Walled Carbon Nanotubes. *J. Am. Chem. Soc.* **2006,** *128* (26), 8396-8397.

289. Tanaka, T.; Jin, H.; Miyata, Y.; Fujii, S.; Suga, H.; Naitoh, Y.; Minari, T.; Miyadera, T.; Tsukagoshi, K.; Kataura, H., Simple and Scalable Gel-Based Separation of Metallic and Semiconducting Carbon Nanotubes. *Nano Letters* **2009,** *9* (4), 1497-1500.

290. Huang, X. Y.; McLean, R. S.; Zheng, M., High-resolution length sorting and purification of DNA-wrapped carbon nanotubes by size-exclusion chromatography. *Anal. Chem.* **2005,** *77* (19), 6225-6228.

291. Zheng, M.; Semke, E. D., Enrichment of single chirality carbon nanotubes. *J. Am. Chem. Soc.* **2007,** *129* (19), 6084-+.

292. Arnold, M. S.; Green, A. A.; Hulvat, J. F.; Stupp, S. I.; Hersam, M. C., Sorting carbon nanotubes by electronic structure using density differentiation. *Nature Nanotechnol.* **2006,** *1* (1), 60-65.

293. Zhang, G. Y.; Qi, P. F.; Wang, X. R.; Lu, Y. R.; Li, X. L.; Tu, R.; Bangsaruntip, S.; Mann, D.; Zhang, L.; Dai, H. J., Selective etching of metallic carbon nanotubes by gas-phase reaction. *Science* **2006,** *314* (5801), 974-977.

294. Vetcher, A. A.; Srinivasan, S.; Vetcher, I. A.; Abramov, S. M.; Kozlov, M.; Baughman, R. H.; Levene, S. D., Fractionation of SWNT/nucleic acid complexes by agarose gel electrophoresis. *Nanotechnology* **2006,** *17* (16), 4263-4269.

295. Heller, D. A.; Mayrhofer, R. M.; Baik, S.; Grinkova, Y. V.; Usrey, M. L.; Strano, M. S., Concomitant length and diameter separation of single-walled carbon nanotubes. *J. Am. Chem. Soc.* **2004,** *126* (44), 14567-14573.

296. Kim, Y.; Hong, S.; Jung, S.; Strano, M. S.; Choi, J.; Baik, S., Dielectrophoresis of Surface Conductance Modulated Single-Walled Carbon Nanotubes Using Catanionic Surfactants. *J. Phys. Chem. B* **2006,** *110* (4), 1541-1545.

297. Krupke, R.; Hennrich, F., Separation techniques for carbon nanotubes. *Adv. Eng. Mater.* **2005,** *7* (3), 111-116.

298. Lei, U.; Lo, Y. J., Review of the theory of generalised dielectrophoresis. *IET Nanobiotechnology* **2011,** *5* (3), 86-106.

299. Morgan, H.; Hughes, M. P.; Green, N. G., Separation of Submicron Bioparticles by Dielectrophoresis. *Biophys.J.* **1999,** *77*, 516-525.

300. Kang, H.; Wang, B.; Hong, S.; Bae, J. J.; Kim, D.; Han, C. S.; Lee, Y. H.; Baik, S., Dielectrophoretic separation of metallic arc-discharge single-walled carbon nanotubes in a microfluidic channel. *Synthetic Metals* **2013,** *184*, 23-28.

301. Burg, B. R.; Poulikakos, D., Large-scale integration of single-walled carbon nanotubes and graphene into sensors and devices using dielectrophoresis: A review. *J. Mater. Res.* **2011,** *26* (13), 1561-1571.

302. Xue, W.; Li, P., Dielectrophoretic Deposition and Alignment of Carbon Nanotubes. In *Carbon Nanotubes - Synthesis, Characterization, Applications*, Yellampalli, S., Ed. InTech: Rijeka, 2011; p Ch. 09.

303. Martinez-Duarte, R., Microfabrication technologies in dielectrophoresis applications-A review. *Electrophoresis* **2012,** *33* (21), 3110-3132.

304. Bakewell, D. J. G.; Hughes, M. P.; Milner, J. J.; Morgan, H., Dielectrophoretic Manipulation of Avidin and DNA. *Proc.20th Ann.Intern.Conf.IEEE Medicine and Biology Soc.* **1998,** *20*, 1079-1082.

305. Hoelzel, R.; Calander, N.; Chiragwandi, Z.; Willander, M.; Bier, F. F., Trapping Single Molecules by Dielectrophoresis. *Phys.Rev.Lett.* **2005,** *95*, 128102.

306. Jones, P. V.; Salmon, G. L.; Ros, A., Continuous Separation of DNA Molecules by Size Using Insulator-Based Dielectrophoresis. *Anal. Chem.* **2017,** *89* (3), 1531-1539.

307. Morgan, H.; Green, N. G., Dielectrophoretic manipulation of rod-shaped viral particles. *J. Electrostatics* **1997,** *42* (3), 279-293.

308. Jones, T. B., Basic theory of dielectrophoresis and electrorotation. *IEEE Eng. Med. Biol. Mag.* **2003,** *22* (6), 33-42.

309. Nakano, A.; Chao, T. C.; Camacho-Alanis, F.; Ros, A., Immunoglobulin G and bovine serum albumin streaming dielectrophoresis in a microfluidic device. *Electrophoresis* **2011,** *32* (17), 2314-22.

310. Hellmich, W.; Regtmeier, J.; Duong, T. T.; Ros, R.; Anselmetti, D.; Ros, A., Poly(oxyethylene) Based Surface Coatings for Poly(dimethylsiloxane) Microchannels. *Langmuir* **2005,** *21* (16), 7551-7557.

311. Ermolina, I.; Morgan, H., The electrokinetic properties of latex particles: comparison of electrophoresis and dielectrophoresis. *J. Colloid Interface Sci.* **2005,** *285* (1), 419-428.

312. Lyklema, J., *Fundamentals of interface and colloid science*. Academic Press: San Diego;London;, 1991; Vol. 1.

313. White, B.; Banerjee, S.; O'Brien, S.; Turro, N. J.; Herman, I. P., Zeta-potential measurements of surfactant-wrapped individual single-walled carbon nanotubes. *J. Phys. Chem. C* **2007,** *111* (37), 13684-13690.

314. Sun, Z.; Nicolosi, V.; Rickard, D.; Bergin, S. D.; Aherne, D.; Coleman, J. N., Quantitative evaluation of surfactant-stabilized single-walled carbon nanotubes: Dispersion quality and its correlation with zeta potential. *J. Phys. Chem. C* **2008,** *112* (29), 10692-10699.

315. Mahbubul, I. M.; Shahrul, I. M.; Khaleduzzaman, S. S.; Saidur, R.; Amalina, M. A.; Turgut, A., Experimental investigation on effect of ultrasonication duration on

colloidal dispersion and thermophysical properties of alumina-water nanofluid. *Int. J. Heat Mass Transf.* **2015,** *88*, 73-81.

316. Zaib, Q.; Khan, I. A.; Yoon, Y.; Flora, J. R. V.; Park, Y. G.; Saleh, N. B., Ultrasonication Study for Suspending Single-Walled Carbon Nanotubes in Water. *J. Nanosci. Nanotechnol.* **2012,** *12* (5), 3909-3917.

317. Tang, S.-Y.; Zhang, W.; Baratchi, S.; Nasabi, M.; Kalantar-zadeh, K.; Khoshmanesh, K., Modifying Dielectrophoretic Response of Nonviable Yeast Cells by Ionic Surfactant Treatment. *Anal. Chem.* **2013,** *85* (13), 6364-6371.

318. Strano, M. S.; Moore, V. C.; Miller, M. K.; Allen, M. J.; Haroz, E. H.; Kittrell, C.; Hauge, R. H.; Smalley, R. E., The role of surfactant adsorption during ultrasonication in the dispersion of single-walled carbon nanotubes. *J. Nanosci. Nanotechnol.* **2003,** *3* (1-2), 81-86.

319. Tan, Y. Q.; Resasco, D. E., Dispersion of single-walled carbon nanotubes of narrow diameter distribution. *J. Phys. Chem. B* **2005,** *109* (30), 14454-14460.

320. Kang, I.; Schulz, M. J.; Kim, J. H.; Shanov, V.; Shi, D., A carbon nanotube strain sensor for structural health monitoring. *Smart Mater. Struct.* **2006,** *15* (3), 737-748.

321. McEuen, P. L., Single-wall carbon nanotubes. *Phys. World* **2000,** *13* (6), 31-36.

322. Li, J.; Papadopoulos, C.; Xu, J. M.; Moskovits, M., Highly-ordered carbon nanotube arrays for electronics applications. *Appl. Phys. Lett.* **1999,** *75* (3), 367-369.

323. Boghossian , A. A.; Zhang , J.; Barone, P. W.; Reuel, N. F.; Kim, J.-H.; Heller, D. A.; Ahn, J.-H.; Hilmer, A. J.; Rwei, A.; Arkalgud, J. R.; Zhang, C. T.; Strano, M. S., Near-Infrared Fluorescent Sensors based on Single-Walled Carbon Nanotubes for Life Sciences Applications. *ChemSusChem* **2011,** *4* (7), 848-863.

324. Park, Y.; Yoo, J.; Lim, B.; Kwon, W.; Rhee, S. W., Improving the functionality of carbon nanodots: doping and surface functionalization. *J. Mater. Chem. A* **2016,** *4* (30), 11582-11603.

325. Cherukuri, P.; Bachilo, S. M.; Litovsky, S. H.; Weisman, R. B., Near-Infrared Fluorescence Microscopy of Single-Walled Carbon Nanotubes in Phagocytic Cells. *J. Am. Chem. Soc.* **2004,** *126* (48), 15638-15639.

326. O'Connell, M. J.; Bachilo, S. M.; Huffman, C. B.; Moore, V. C.; Strano, M. S.; Haroz, E. H.; Rialon, K. L.; Boul, P. J.; Noon, W. H.; Kittrell, C.; Ma, J.; Hauge, R. H.; Weisman, R. B.; Smalley, R. E., Band Gap Fluorescence from Individual Single-Walled Carbon Nanotubes. *Science* **2002,** *297* (5581), 593-596.

327. Falvo, M. R.; Clary, G. J.; Taylor, R. M.; Chi, V.; Brooks, F. P.; Washburn, S.; Superfine, R., Bending and buckling of carbon nanotubes under large strain. *Nature* **1997,** *389* (6651), 582-584.

328. Wong, E. W.; Sheehan, P. E.; Lieber, C. M., Nanobeam Mechanics: Elasticity, Strength, and Toughness of Nanorods and Nanotubes. *Science* **1997,** *277* (5334), 1971-1975.

329. Dai, H.; Hafner, J. H.; Rinzler, A. G.; Colbert, D. T.; Smalley, R. E., Nanotubes as nanoprobes in scanning probe microscopy. *Nature* **1996,** *384* (6605), 147-150.

330. Wang, X.; Jiang, Q.; Xu, W.; Cai, W.; Inoue, Y.; Zhu, Y., Effect of carbon nanotube length on thermal, electrical and mechanical properties of CNT/bismaleimide composites. *Carbon* **2013,** *53*, 145-152.

331. Franklin, A. D.; Chen, Z., Length scaling of carbon nanotube transistors. *Nat. Nanotechnol.* **2010,** *5*, 858.

332. Singh, B. P.; Saini, K.; Choudhary, V.; Teotia, S.; Pande, S.; Saini, P.; Mathur, R. B., Effect of length of carbon nanotubes on electromagnetic interference shielding and mechanical properties of their reinforced epoxy composites. *J. Nanopart. Res.* **2013,** *16* (1), 2161.

333. Wan, H.; Delale, F.; Shen, L., Effect of CNT length and CNT-matrix interphase in carbon nanotube (CNT) reinforced composites. *Mech. Res. Commun.* **2005,** *32* (5), 481-489.

334. Shokrieh, M. M.; Rafiee, R., Investigation of nanotube length effect on the reinforcement efficiency in carbon nanotube based composites. *Compos. Struct.* **2010,** *92* (10), 2415-2420.

335. Wang, X. X.; Wang, J. N.; Su, L. F., Preparation and electrochemical performance of ultra-short carbon nanotubes. *J. Power Sources* **2009,** *186* (1), 194-200.

336. Yang, S.; Huo, J.; Song, H.; Chen, X., A comparative study of electrochemical properties of two kinds of carbon nanotubes as anode materials for lithium ion batteries. *Electrochim. Acta* **2008,** *53* (5), 2238-2244.

337. Cheng, J.; Cheng, S. H., Influence of carbon nanotube length on toxicity to zebrafish embryos. *International journal of nanomedicine* **2012,** *7*, 3731-3739.

338. Sayes, C. M.; Liang, F.; Hudson, J. L.; Mendez, J.; Guo, W.; Beach, J. M.; Moore, V. C.; Doyle, C. D.; West, J. L.; Billups, W. E.; Ausman, K. D.; Colvin, V. L., Functionalization density dependence of single-walled carbon nanotubes cytotoxicity in vitro. *Toxicol. Lett.* **2006,** *161* (2), 135-142.

339. Chen, G.; Seki, Y.; Kimura, H.; Sakurai, S.; Yumura, M.; Hata, K.; Futaba, D. N., Diameter control of single-walled carbon nanotube forests from 1.3–3.0 nm by arc plasma deposition. *Scientific Reports* **2014,** *4*, 3804.

340. Tian, Y.; Timmermans, M. Y.; Kivistö, S.; Nasibulin, A. G.; Zhu, Z.; Jiang, H.; Okhotnikov, O. G.; Kauppinen, E. I., Tailoring the diameter of single-walled carbon nanotubes for optical applications. *Nano Research* **2011,** *4* (8), 807.

341. Zhou, W.; Ooi, Y. H.; Russo, R.; Papanek, P.; Luzzi, D. E.; Fischer, J. E.; Bronikowski, M. J.; Willis, P. A.; Smalley, R. E., Structural characterization and diameter-dependent oxidative stability of single wall carbon nanotubes synthesized by the catalytic decomposition of CO. *Chem. Phys. Lett.* **2001,** *350* (1), 6-14.

342. Stevie, F. A.; Griffis, D. P.; Russell, P. E., Focused Ion Beam Gases for Deposition and Enhanced Etch. In *Introduction to Focused Ion Beams: Instrumentation, Theory, Techniques and Practice*, Giannuzzi, L. A.; Stevie, F. A., Eds. Springer US: Boston, MA, 2005; pp 53-72.

343. Zheng, M.; Semke, E. D., Enrichment of Single Chirality Carbon Nanotubes. *J. Am. Chem. Soc.* **2007,** *129* (19), 6084-6085.

344. Tay, F. E. H.; Yu, L.; Iliescu, C., Particle Manipulation by Miniaturised Dielectrophoretic Devices. *Def. Sci. J.* **2009,** *59* (6), 595-604.

345. Zhang, Q.; Zhang, K., terative dipole moment method for the dielectrophoretic particle-particle interaction in a DC electric field. *J. Nanotechnol.* **2018**.

346. Camacho-Alanis, F.; Gan, L.; Ros, A., Transitioning streaming to trapping in DC insulator-based dielectrophoresis for biomolecules. *Sens. Actuators, B* **2012,** *173*, 668-675.

347. Gan, L.; Chao, T.-C.; Camacho-Alanis, F.; Ros, A., Six-Helix Bundle and Triangle DNA Origami Insulator-Based Dielectrophoresis. *Anal. Chem.* **2013,** *85* (23), 11427-11434.

348. Fiedler, S.; Shirley, S. G.; Schnelle, T.; Fuhr, G., Dielectrophoretic Sorting of Particles and Cells in a Microsystem. *Anal. Chem.* **1998,** *70* (9), 1909-1915.

349. Bhattacharya, S.; Chao, T.-C.; Ros, A., Insulator-based dielectrophoretic single particle and single cancer cell trapping. *Electrophoresis* **2011,** *32* (18), 2550-2558.

350. Jones, P. V.; Staton, S. J. R.; Hayes, M. A., Blood cell capture in a sawtooth dielectrophoretic microchannel. *Anal. Bioanal. Chem.* **2011,** *401* (7), 2103.

351. Jones, P. V.; DeMichele, A. F.; Kemp, L.; Hayes, M. A., Differentiation of Escherichia coli serotypes using DC gradient insulator dielectrophoresis. *Anal. Bioanal. Chem.* **2014,** *406* (1), 183-192.

352. Jones, P. V.; Huey, S.; Davis, P.; McLemore, R.; McLaren, A.; Hayes, M. A., Biophysical separation of Staphylococcus epidermidis strains based on antibiotic resistance. *Analyst* **2015,** *140* (15), 5152-5161.

353. Hilton, S. H.; Hayes, M. A., A mathematical model of dielectrophoretic data to connect measurements with cell properties. *Anal. Bioanal. Chem.* **2019,** *411* (10), 2223-2237.

354. Kim, D.; Sonker, M.; Ros, A., Dielectrophoresis: From Molecular to Micrometer-Scale Analytes. *Anal. Chem.* **2019,** *91* (1), 277-295.

355. Rabbani, M. T.; Schmidt, C. F.; Ros, A., Single-Walled Carbon Nanotubes Probed with Insulator-Based Dielectrophoresis. *Anal. Chem.* **2017,** *89* (24), 13235-13244.

356. Krupke, R.; Hennrich, F., Cover Picture: Separation Techniques for Carbon Nanotubes (Adv. Eng. Mater. 3/2005). *Adv. Eng. Mater.* **2005,** *7* (3).

357. Rabbani, M. T.; Sonker, M.; Ros, A., Carbon Nanotube Dielectrophoresis: Theory and Applications. *Electrophoresis (sumbitted)* **2020**.

358. Cummings, E. B.; Singh, A. K., Dielectrophoresis in Microchips Containing Arrays of Insulating Posts: Theoretical and Experimental Results. *Anal. Chem.* **2003,** *75* (18), 4724-4731.

359. Chou, C.-F.; Tegenfeldt, J. O.; Bakajin, O.; Chan, S. S.; Cox, E. C.; Darnton, N.; Duke, T.; Austin, R. H., Electrodeless Dielectrophoresis of Single- and Double-Stranded DNA. *Biophys. J.* **2002,** *83* (4), 2170-2179.

360. Hölzel, R.; Calander, N.; Chiragwandi, Z.; Willander, M.; Bier, F. F., Trapping Single Molecules by Dielectrophoresis. *Physical Review Letters* **2005,** *95* (12), 128102.

361. Nakano, A.; Chao, T.-C.; Camacho-Alanis, F.; Ros, A., Immunoglobulin G and bovine serum albumin streaming dielectrophoresis in a microfluidic device. *Electrophoresis* **2011,** *32* (17), 2314-2322.

362. Giddings, J. C., *Unified separation science*. Wiley New York etc: 1991.

363. Tunuguntla, R. H.; Chen, X.; Belliveau, A.; Allen, F. I.; Noy, A., High-Yield Synthesis and Optical Properties of Carbon Nanotube Porins. *J. Phys. Chem. C* **2017,** *121* (5), 3117-3125.

364. Sun, Z.; Nicolosi, V.; Rickard, D.; Bergin, S. D.; Aherne, D.; Coleman, J. N., Quantitative Evaluation of Surfactant-stabilized Single-walled Carbon Nanotubes: Dispersion Quality and Its Correlation with Zeta Potential. *J. Phys. Chem. C* **2008,** *112* (29), 10692-10699.

365. Fagan, J. A.; Becker, M. L.; Chun, J.; Nie, P.; Bauer, B. J.; Simpson, J. R.; Hight-Walker, A.; Hobbie, E. K., Centrifugal Length Separation of Carbon Nanotubes. *Langmuir* **2008,** *24* (24), 13880-13889.

366. Morgan, H.; Green, N. G., AC electrokinetics : colloids and nanoparticles. **2003**.

367. Abdallah, B. G.; Roy-Chowdhury, S.; Coe, J.; Fromme, P.; Ros, A., High Throughput Protein Nanocrystal Fractionation in a Microfluidic Sorter. *Anal. Chem.* **2015,** *87* (8), 4159-4167.

368. Abdallah, B. G.; Chao, T.-C.; Kupitz, C.; Fromme, P.; Ros, A., Dielectrophoretic Sorting of Membrane Protein Nanocrystals. *ACS Nano* **2013,** *7* (10), 9129-9137.

369. Luo, J.; Abdallah, B. G.; Wolken, G. G.; Arriaga, E. A.; Ros, A., Insulator-based dielectrophoresis of mitochondria. *Biomicrofluidics* **2014,** *8* (2), 021801.

370. Zhang, J.; Yan, S.; Yuan, D.; Alici, G.; Nguyen, N.-T.; Warkiani, M. E.; Li, W., Fundamentals and applications of inertial microfluidics: A review. *Lab on a Chip* **2016,** *16* (1), 10-34.

371. Henning, A.; Bier, F. F.; Hölzel, R., Dielectrophoresis of DNA: Quantification by impedance measurements. *Biomicrofluidics* **2010,** *4* (2), 022803.

372. Martinez-Duarte, R.; Camacho-Alanis, F.; Renaud, P.; Ros, A., Dielectrophoresis of lambda-DNA using 3D carbon electrodes. *Electrophoresis* **2013,** *34* (7), 1113-1122.

373. Liu, Y.; Hayes, M. A., Orders-of-Magnitude Larger Force Demonstrated for Dielectrophoresis of Proteins Enabling High-Resolution Separations Based on New Mechanisms. *Anal Chem* **2021,** *93* (3), 1352-1359.

374. Nakano, A.; Camacho-Alanis, F.; Ros, A., Insulator-based dielectrophoresis with beta-galactosidase in nanostructured devices. *Analyst* **2015,** *140* (3), 860-8.

375. Chiou, C.-H.; Chien, L.-J.; Kuo, J.-N., Nanoconstriction-based electrodeless dielectrophoresis chip for nanoparticle and protein preconcentration. *Applied Physics Express* **2015,** *8* (8), 085201.

376. Kovarik, M. L.; Jacobson, S. C., Integrated nanopore/microchannel devices for ac electrokinetic trapping of particles. *Analytical Chemistry* **2008,** *80* (3), 657-664.

377. Nielsen, A. V.; Beauchamp, M. J.; Nordin, G. P.; Woolley, A. T., 3D Printed Microfluidics. *Annu. Rev. Anal. Chem.* **2020,** *13* (1), null.

378. Nge, P. N.; Rogers, C. I.; Woolley, A. T., Advances in Microfluidic Materials, Functions, Integration, and Applications. *Chemical Reviews* **2013,** *113* (4), 2550-2583.

379. Knob, R.; Sahore, V.; Sonker, M.; Woolley, A. T., Advances in monoliths and related porous materials for microfluidics. *Biomicrofluidics* **2016,** *10* (3), 032901.

380. Sonker, M.; Sahore, V.; Woolley, A. T., Recent advances in microfluidic sample preparation and separation techniques for molecular biomarker analysis: A critical review. *Anal. Chim. Acta* **2017,** *986*, 1-11.

381. Sonker, M. Electrokinetically Operated Integrated Microfluidic Devices for Preterm Birth Biomarker Analysis. Ph.D., Brigham Young University, Provo UT, 2017.

382. Ge, Z.; Wang, W.; Yang, C., Rapid concentration of deoxyribonucleic acid via Joule heating induced temperature gradient focusing in poly-dimethylsiloxane microfluidic channel. *Analytica Chimica Acta* **2015,** *858*, 91-97.

383. Sahore, V.; Sonker, M.; Nielsen, A. V.; Knob, R.; Kumar, S.; Woolley, A. T., Automated microfluidic devices integrating solid-phase extraction, fluorescent labeling, and microchip electrophoresis for preterm birth biomarker analysis. *Anal. Bioanal. Chem.* **2018,** *410* (3), 933-941.

384. Raj M, K.; Chakraborty, S., PDMS microfluidics: A mini review. *Journal of Applied Polymer Science* **2020,** *137* (27), 48958.

385. Yeh, S.-H.; Chou, K.-H.; Yang, R.-J., Sample pre-concentration with high enrichment factors at a fixed location in paper-based microfluidic devices. *Lab on a Chip* **2016,** *16* (5), 925-931.

386. Gao, B.; Li, X.; Yang, Y.; Chu, J.; He, B., Emerging paper microfluidic devices. *Analyst* **2019,** *144* (22), 6497-6511.

387. Ortiz, R.; Koh, D.; Kim, D. H.; Rabbani, M. T.; Velasquez, C. A.; Sonker, M.; Arriaga, E.; Ros, A., Continuous organelle separation in an Insulator-based dielectrophoretic device. *Electrophoresis* **2021**.

388. He, Y.; Wu, Y.; Fu, J. z.; Gao, Q.; Qiu, J. j., Developments of 3D printing microfluidics and applications in chemistry and biology: a review. *Electroanalysis* **2016,** *28* (8), 1658-1678.

389. Ho, C. M. B.; Ng, S. H.; Li, K. H. H.; Yoon, Y.-J., 3D printed microfluidics for biological applications. *Lab on a Chip* **2015,** *15* (18), 3627-3637.

390. Yi, H.-G.; Lee, H.; Cho, D.-W., 3D printing of organs-on-chips. *Bioengineering* **2017,** *4* (1), 10.

391. Munoz-Abraham, A. S.; Rodriguez-Davalos, M. I.; Bertacco, A.; Wengerter, B.; Geibel, J. P.; Mulligan, D. C., 3D printing of organs for transplantation: where are we and where are we heading? *Current Transplantation Reports* **2016,** *3* (1), 93-99.

392. Parker, E. K.; Nielsen, A. V.; Beauchamp, M. J.; Almughamsi, H. M.; Nielsen, J. B.; Sonker, M.; Gong, H.; Nordin, G. P.; Woolley, A. T., 3D printed microfluidic devices with immunoaffinity monoliths for extraction of preterm birth biomarkers. *Anal. Bioanal. Chem.* **2018**.

393. Pham, D. T.; Gault, R. S., A comparison of rapid prototyping technologies. *International Journal of machine tools and manufacture* **1998,** *38* (10-11), 1257-1287.

394. Sood, A. K.; Ohdar, R.; Mahapatra, S. S., Improving dimensional accuracy of fused deposition modelling processed part using grey Taguchi method. *Materials & design* **2009,** *30* (10), 4243-4252.

395. Feygin, M., Apparatus and method for forming an integral object from laminations. Google Patents: 1988.

396. Choi, J.-W.; Wicker, R.; Lee, S.-H.; Choi, K.-H.; Ha, C.-S.; Chung, I., Fabrication of 3D biocompatible/biodegradable micro-scaffolds using dynamic mask projection microstereolithography. *J. Mater. Process. Technol.* **2009,** *209* (15-16), 5494-5503.

397. Bogue, R., 3D printing: the dawn of a new era in manufacturing? *Assembly Automation* **2013**.

398. Melchels, F. P.; Feijen, J.; Grijpma, D. W., A review on stereolithography and its applications in biomedical engineering. *Biomaterials* **2010,** *31* (24), 6121-6130.

399. Deckard, C. R., Method and apparatus for producing parts by selective sintering. Google Patents: 1989.

400. Tolochko, N. K.; Khlopkov, Y. V.; Mozzharov, S. E.; Ignatiev, M. B.; Laoui, T.; Titov, V. I., Absorptance of powder materials suitable for laser sintering. *Rapid Prototyping Journal* **2000**.

401. Pilipović, A.; Raos, P.; Šercer, M., Experimental analysis of properties of materials for rapid prototyping. *The International Journal of Advanced Manufacturing Technology* **2009,** *40* (1), 105-115.

402. Erbano, B. O.; Opolski, A. C.; Olandoski, M.; Foggiatto, J. A.; Kubrusly, L. F.; Dietz, U. A.; Zini, C.; Marinho, M. M. M. A.; Leal, A. G.; Ramina, R., Rapid prototyping of three-dimensional biomodels as an adjuvant in the surgical planning for intracranial aneurysms. *Acta Cirurgica Brasileira* **2013,** *28*, 756-761.

403. Lin, Y.; Xu, J., Microstructures Fabricated by Two-Photon Polymerization and Their Remote Manipulation Techniques: Toward 3D Printing of Micromachines. *Advanced Optical Materials* **2018,** *6* (8), 1701359.

404. Dottermusch, S.; Busko, D.; Langenhorst, M.; Paetzold, U. W.; Richards, B. S., Exposure-dependent refractive index of Nanoscribe IP-Dip photoresist layers. *Opt. Lett.* **2019,** *44* (1), 29-32.

405. Li, Y.; Park, S.; McLamb, M.; Lata, M.; Schöche, S.; Childers, D.; Aggarwal, I. D.; Poutous, M. K.; Boreman, G.; Hofmann, T., UV to NIR optical properties of IP-Dip, IP-L, and IP-S after two-photon polymerization determined by spectroscopic ellipsometry. *Opt. Mater. Express* **2019,** *9* (11), 4318-4328.

406. Schindelin, J.; Arganda-Carreras, I.; Frise, E.; Kaynig, V.; Longair, M.; Pietzsch, T.; Preibisch, S.; Rueden, C.; Saalfeld, S.; Schmid, B.; Tinevez, J. Y.; White, D. J.; Hartenstein, V.; Eliceiri, K.; Tomancak, P.; Cardona, A., Fiji: An Open-Source Platform for Biological-Image Analysis. *Nat. Methods* **2012,** *9* (7), 676-682.

407. Wolff, A.; Leiterer, C.; Csaki, A.; Fritzsche, W., Dielectrophoretic manipulation of DNA in microelectrode gaps for single-molecule constructs. *Frontiers in Bioscience-Landmark* **2008,** *13* (17), 6834-6840.

408. Dong, L.; Arai, F.; Fukuda, T. In *3D nanorobotic manipulation of nano-order objects inside SEM*, MHS2000. Proceedings of 2000 International Symposium on Micromechatronics and Human Science (Cat. No. 00TH8530), IEEE: 2000; pp 151-156.

409. Chen, Q.; Yuan, Y. J., A review of polystyrene bead manipulation by dielectrophoresis. *RSC advances* **2019,** *9* (9), 4963-4981.

410. Yokokawa, R.; Manta, Y.; Namura, M.; Takizawa, Y.; Le, N. C. H.; Sugiyama, S., Individual evaluation of DEP, EP and AC-EOF effects on λDNA molecules in a DNA concentrator. *Sensors and Actuators B: Chemical* **2010,** *143* (2), 769-775.

411. Otto, S.; Kaletta, U.; Bier, F. F.; Wenger, C.; Hölzel, R., Dielectrophoretic immobilisation of antibodies on microelectrode arrays. *Lab on a Chip* **2014,** *14* (5), 998-1004.

412. Rabbani, M. T.; Sonker, M.; Villarreal, J. C.; Ros, A. In *Manipulation of biomolecules using a 3d-printed insulator-based dielectrophoresis device*, 24th International Conference on Miniaturized Systems for Chemistry and Life Sciences, MicroTAS 2020, Chemical and Biological Microsystems Society: 2020; pp 651-652.

APPENDIX A

SUPPLEMENTAL MATERIAL FOR CHAPTER 4

This document contains supplementary information describing the numerical model employed in this study, the resulting movies and additional model results for 100 nm long SWNTs.

Numerical model for positive and negative dielectrophoresis trapping of SWNTs:

A numerical model was established with COMSOL 5.2a to study the trapping regions for the positive dielectrophoresis (pDEP) and the negative dielectrophoresis (nDEP) case. A 200 μm long channel with integrated post array was drawn to scale with post diameters of 10 μm and inter-post distances matching those of the experimental device (see main manuscript Figure 4.1).

The *Electric Current* module was used in a stationary study to compute the electric field distribution in the device. In this module, the electric field distribution was studied by solving the following Maxwell's equations:

$$\nabla . J = Q \tag{A.1}$$

$$J = \sigma E \tag{A.2}$$

$$E = -\nabla V \tag{A.3}$$

where, J is the current density, E is electric field, V is the potential and Q is the total charge. In the *Electric Currents* model, the posts walls and the side walls of the channel were selected as insulators. An applied potential of 13.3V (scaled according to 1000V applied across the 1.5 cm long microfluidic device) was applied to the inlet boundary and the outlet boundary was grounded.

Next, the *Particle Tracing* module was used with a time dependent solver to trace the trajectories of the particles. In this model, the drag force and Brownian force were computed with the following equations:

$$F_D = \frac{1}{\beta} m_p (u\text{-}v) \tag{A.4}$$

$$\beta = \frac{\rho_p {d_p}^2}{18\mu} \tag{A.5}$$

$$F_b = \alpha \sqrt{\frac{12\pi k_B \mu T r_p}{\Delta t}} \tag{A.6}$$

where F_D and F_b are the drag force and Brownian force, m_p, r_p, ρ_p and d_p are the mass, radius, density and diameter of the particle, β is the velocity response time, μ is the viscosity, T is temperature and k_B is the Boltzman constant. u and v are fluid velocity and particle velocity, respectively. Note that the fluid was considered stationary in this study. The dielectrophoretic force $\vec{F}_{dep}$ was also coupled with this model via equation A.9 and A.10 as described below. With the time dependent solver, the particle trajectories were computed with the following equation:

$$\frac{d(m_p v)}{dt} = F_t \tag{A.7}$$

where

$$F_t = F_{dep} + F_D + F_b \tag{A.8}$$

The DEP force for a spherical particle in a non-uniform electric field can be expressed as:

$$F_{dep\_sphere} = 2\pi r_s^3 \varepsilon_m \mathrm{Re(CM)} \nabla E^2 \tag{A.9}$$

where

$$\mathrm{Re(CM)} = \frac{\varepsilon_p - \varepsilon_m}{\varepsilon_p + 2\varepsilon_m} \tag{A.10}$$

Where r_s is the radius of the spherical particle, ε_m is the medium permittivity, ε_p is the particle permittivity and $\mathrm{Re(CM)}$ is the real part of the Clausius-Mossotti factor.

COMSOL only allows entries for spherical particles in the *Particle Tracing* module. Therefore, we used an equivalent radius r_{s_eq} for SWNTs assuming that a spherical particle experiences the same DEP force that acts on a rod like SWNT:

$$F_{dep\_SWNT} = F_{dep\_shpere} \tag{A.11}$$

where $\vec{F}_{dep\_SWNT}$ corresponds to equation 3.2 of the main manuscript. Solving for the radius of the sphere renders r_{s_eq}:

$$r_{s\_eq} = \sqrt[3]{\frac{1}{6}*(r_{SWNT}^2*l)} \tag{A.12}$$

where r_{SWNT} and l are the radius and length of SWNTs. We further assume that $\mathrm{Re(CM)}$ is the same for the SWNTs and the equivalent spherical particles used in the model and obtain:

$$\varepsilon_{p\_s} = \frac{\varepsilon_m*(1+2*\mathrm{Re(CM)})}{1-\mathrm{Re(CM)}} \tag{A.13}$$

where ε_{p_s} is the corrected equivalent particle permittivity, entered in the COMSOL model to compute $\vec{F}_{dep\_shpere}$ with the same $\mathrm{Re(CM)}$.

In addition, *E* was coupled via the result of the *Electric Current* module altering it with a sine wave function with a frequency of 1000 Hz and corresponding amplitude.

For the pDEP case, r_{SWNT} and l of the SWNTs was used as 0.76 nm and 1000 nm respectively, based on the values obtained through AFM measurements (see main manuscript). With equation A.12, r_{s_eq} was found as 7.5 nm. For the nDEP case, we assumed a r_{SWNT} of 0.76 nm and l of 10 µm considering the shorter sonication time, rendering longer SWNT species. A r_{s_eq} of 10 nm was found and used in the model.

According to equation A.13, for Re(CM)= 18.6 (pDEP) ε_{p_s} resulted in -174.07 and for nDEP, ε_p resulted in -130.25. These values were accordingly entered as model parameters. The model was solved time dependently for 1000 particles released at the vertical release lines at the middle positions between two rows of posts. Figure 4.2 of the main manuscript shows the end position after 3 seconds of migration. All parameters used for the numerical model are listed in the Table at the end of this document.

Numerical modeling results for non-trapping conditions

We also computed the numerical model for shorter lengths of SWNTs. We considered a length of 100 nm for the pDEP case and 1000 nm length for the nDEP case, which results in r_{s_eq} of 2 nm and 5 nm, respectively. From Figure A.1 it can be observed that DEP trapping did not occur in these two cases. The DEP force is not strong enough to trap the particles for these two cases, and characteristic trapping regions can not be observed.

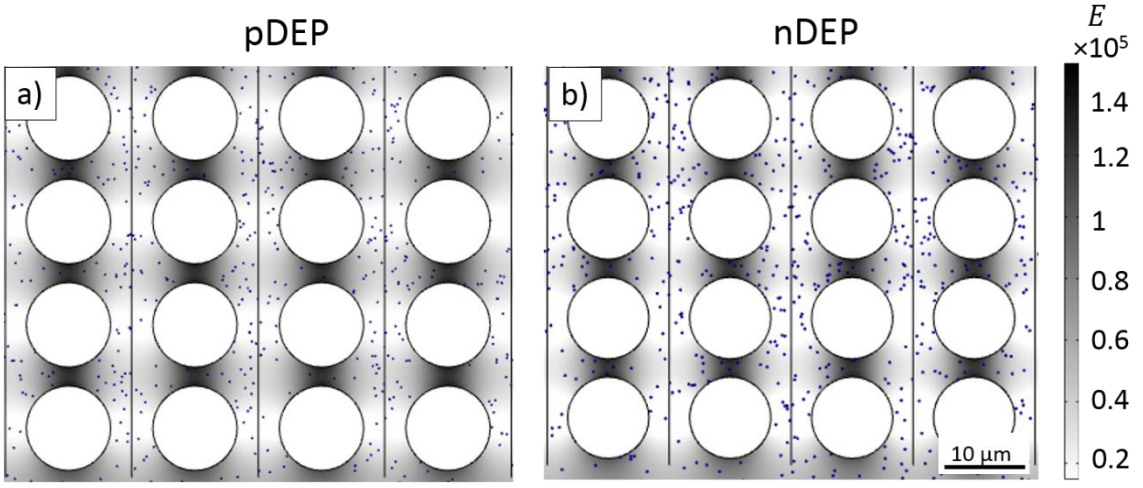

Figure A.1: a) Position of SWNT (shown as blue dots) with a length of 100 nm predicted with the numerical model for Re(CM) > 0. The image shows the end position of 1000 SWNTs released from each vertical line. SWNTs were not trapped by DEP in the post array. b) Similar to a) but for the nDEP case with Re(CM)<0. SWNTs of 100 nm length

did also not trap in the post array. The grey scale surface plot in a) and b) indicates electric field strength.

Numerical modeling results for trapping conditions (nDEP case only)

We further studied the nDEP case of the SWNTs with the numerical model inducing larger DEP forces. Longer SWNTs of l = 100 µm with r_{SWNT} = 0.76 nm were considered, and we obtained r_{s_eq} of 21 nm from equation A.12. From Figure A.2 it can be observed that SWNTs trapped closer to the circular posts compared to Figure 4.2a of the main manuscript.

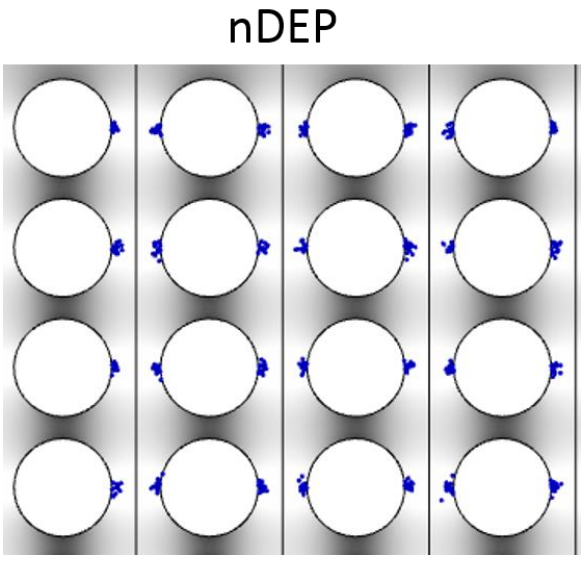

Figure A.2: a) SWNT (shown as blue dots) with length of 100 µm position predicted with the numerical model for Re(CM)< 0. The image shows the end position of 1000 SWNTs released from each vertical line. SWNTs were trapped by DEP in the post array.

Supplementary Table A1: Parameters used for numerical modeling

Variable	**Value**	**Unit**
Applied potential	13.3	V
Temperature	298	K
Density of water	997.0479	kg/m^3
Density of SWNT	1600	kg/m^3
Frequency	1000	Hz
Viscosity of water	0.00089	Pa s
Particle permittivity (ε_{p_s}), for pDEP	-174.07	n.a.
Particle permittivity (ε_{p_s}), for nDEP	-130.25	n.a.

APPENDIX B

SUPPLEMENTAL MATERIAL FOR CHAPTER 5

The supporting information document contains details on the numerical model, Table B.1 and Figure B.1.

Numerical Model

A numerical model was set up in COMSOL Multiphysics version 5.4. First, a 5.5 mm long channel matching the device dimensions including a 25 µm wide constriction was drawn in COMSOL, the potential was applied to the inlet and the center outlet was set to ground. The electric current module was used in a stationary study to compute the electric field distribution in the microdevice as described previously. The Creeping Flow Module was used to compute the velocity and pressure fields due to the laminar flow created by the pump. The Stokes equation for conservation of momentum and the continuity equation for conservation of mass were solved. Fluid density and viscosity for water were used and flow rates were set according to the experimental conditions (25 µL/h). The inlet and outlets were set to open boundaries with initial pressure set to zero.

The Particle Tracing and Fluid Flow Module was used to trace the sorting trajectories of the particles with a time-dependent solver. In this model, drag force and DEP force were computed as reported previously. Based on the Zeta potentials listed in Table 1 (main text), $\mathrm{Re(CM)}$ was calculated as 13.44 for sample A and -1.18 for sample B, similar to previous reports. Briefely, the Zeta potential was used to determine surface conductance, λ_s, by determining the diffuse layer conductance, $\lambda_{s,d}$, and the Stern layer conductance, $\lambda_{s,s}$,. Then, the particle conductivity was determined via $\sigma_P = 2\,\lambda_s a^{-1}$, as outlined in the main manuscript, which resulted in 2.12 S/m. The Clausius Mossotti factor resulted from the relation $\mathrm{Re(CM)} = -1 + \frac{\sigma_p}{\sigma_m}$, wich a measured medium conductivity of 0.15 S/m as outlined in the methods section of the main manuscript. The obtained $\mathrm{Re(CM)}$

was used to set up a user defined DEP force according to Equation 3.2 (main text). Furthermore, the stochastic motion due to the Brownian force, F_b, for SWNTs was also accounted for in the numerical model with :

$$F_b = G_{rand}\sqrt{\frac{2K_BT\beta}{\Delta T}} \quad \text{(B.1)}$$

where G_{rand} refers to the non-zero mean Gaussian random number, and ΔT to the mean distance. K_B ($1.38*10^{23}$ J/K) and T are the Boltzmann constant and temperature, respectively. The friction coefficient, β, for a small particle surrounded by fluidic medium can be expressed as:

$$\beta = \frac{K_BT}{D} \quad \text{(B.2)}$$

To obtain β, the diffusion coefficient of SWNTs was determined as previously reported by Nair *et al.*:

$$D = \frac{K_BT}{3\pi\eta L}(\ln(L/d) + 0.32) \quad \text{(B.3)}$$

where η is the viscosity of the medium (0.89 Pa s), L the SWNT length and d (=1 nm) denotes the diameter of SWNTs. Next, the drag force was computed with the following equation:

$$F_d = \frac{1}{\zeta}m_p\,(u\text{-}v) \quad \text{(B.4)}$$

$$\zeta = \frac{\rho_p {d_p}^2}{18\eta} \quad \text{(B.5)}$$

where m_p, and ρ_p are the mass and density of an individual SWNT. With the time dependent solver, the particle trajectories were computed with the following equation:

$$F_t = F_{dep} + F_b + F_d \quad \text{(B.6)}$$

where F_t is the total force acting on the SWNT. 1000 particles were released from the inlet and the recovery efficiency was calculated based on the number of particles present in each outlet at the end of the simulation using Equation 5.1 as described in the main text. Table B.1 summarizes the results of the numerical model for SWNT fractionation ranging from 50 – 2000 nm with a flow rate of 25μL/h and a potential of 350 V. The relevant particle parameters used in the model is listed in table B.1.

Table B.1: Sorting efficiencies (as defined in the main text) in different outlets from the numerical model.

	pDEP condition			nDEP condition		
Length (nm)	$\%E_{S1}$	$\%E_{S2}$	$\%E_C$	$\%E_{S1}$	$\%E_{S2}$	$\%E_C$
2000	26.2	9.5	64.3	70.6	22.3	7.1
1500	24.3	8.2	67.5	68.3	20.5	11.2
1000	22.2	7.5	70.3	64.1	19.8	16.1
750	19.9	6.3	73.8	57.7	17.9	24.4
500	14.6	5.7	79.7	53.8	16.1	30.1
400	12.4	5.3	82.3	51.6	15.3	33.1
300	12.2	4.7	83.1	50.3	14.5	35.2
250	10.8	4.4	84.8	48.6	14.1	37.3
200	10.5	3.9	85.6	46.9	13.2	39.9
100	8.2	3.5	88.3	43.7	12.1	44.2
50	6.6	3.2	90.2	40.6	11.5	47.9

Table B.2.

Relevant particle parameters used in the model.

Length (nm)	D (m^2/s)	β (kg/s)
2000	$2.07 * 10^{-15}$	$1.95 * 10^{-6}$
1500	$2.67 * 10^{-15}$	$1.51 * 10^{-6}$
1000	$3.81 * 10^{-15}$	$1.06 * 10^{-6}$
750	$4.90 * 10^{-15}$	$8.24 * 10^{-7}$
500	$6.96 * 10^{-15}$	$5.80 * 10^{-7}$
400	$8.43 * 10^{-15}$	$4.79 * 10^{-7}$
300	$1.08 * 10^{-15}$	$3.75 * 10^{-7}$
250	$1.26 * 10^{-15}$	$3.21 * 10^{-7}$
200	$1.52 * 10^{-14}$	$2.66 * 10^{-7}$
100	$2.71 * 10^{-14}$	$1.49 * 10^{-7}$
50	$4.74 * 10^{-14}$	$8.52 * 10^{-7}$

SWNT imaging in the constriction sorter without applied potential

Figure B.1 shows an image of the microfluidic chamber filled with NaDOC-wrapped SWNTs without an externally applied potential. Without an applied potential, SWNTs were evenly distributed in the sorter device.

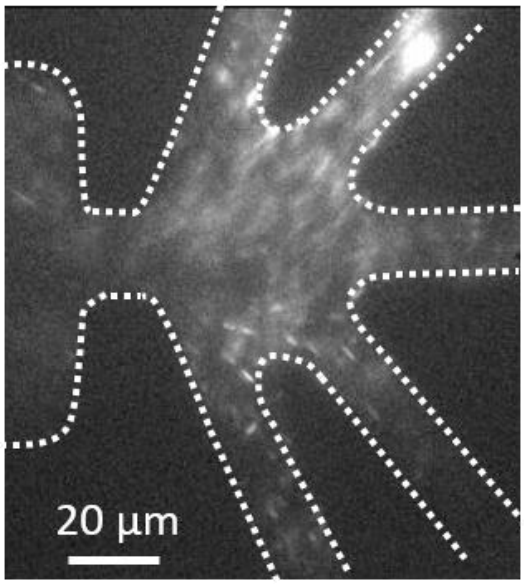

Figure B.1: NaDOC wrapped SWNTs in DEP fractionation device without electric field. IR fluorescence imaging of NaDOC wrapped SWNTs subject to pressure driven flow (left to right) without an applied potential. (Figure is adapted and reprinted with permission from Rabbani et al., copyright (2020), Anal. Chem.[266])

Experimental Observation of iDEP Separation of mixed SWNT

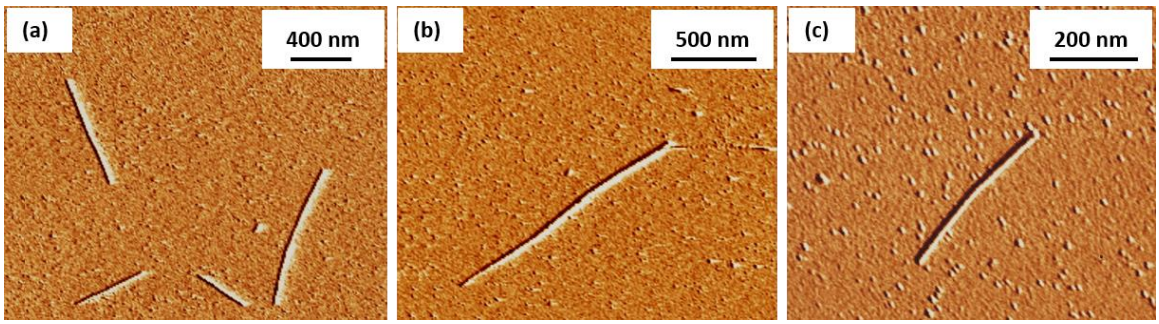

Figure B.2: AFM imaging of DEP fractionation of NaDOC wrapped SWNT. (a) Representative AFM image of NaDOC wrapped SWNT mixture of sample A and B introduced into the inlet. (b) Representative AFM image of fractionated NaDOC wrapped SWNTs collected from the side outlet after sorting of the mixed sample. (c) Representative AFM image of fractionated NaDOC wrapped SWNTs collected from the center outlet after sorting of the mixed sample. (Figure is adapted and reprinted with permission from Rabbani et al., copyright (2020), Anal. Chem.[266])

APPENDIX C

SUPPLEMENTAL MATERIAL FOR CHAPTER 6

The supporting document contains details on the trapping experiments of PS beads, Figure C.1.

nDEP trapping of PS beads

Figure C.1 shows an image of the 3D-printed elliptical post array device. The PS beads were trapped in the region of the lower electric field, showing nDEP with an application of an electric field of 700 V/cm with a frequency of 10 kHz

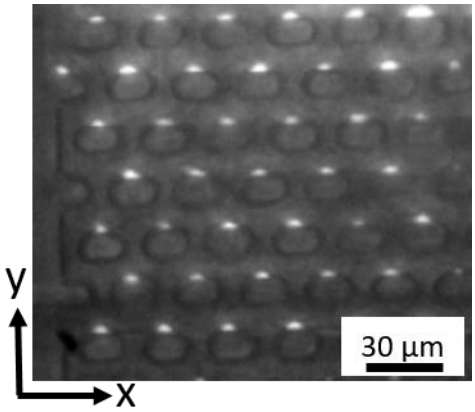

Figure C.1: nDEP trapping of PS beads. At 10 kHz (700V/cm), PS beads show nDEP corresponding to accumulation in the lowest electric field gradient regions in an elliptical post geometry.

APPENDIX D

CO-FLOW INJECTION FOR SERIAL CRYSTALLOGRAPHY AT X-RAY FREE-ELECTRON LASERS

JOURNAL OF APPLIED CRYSTALLOGRAPHY
ISSN 1600-5767

Co-flow injection for serial crystallography at X-ray free-electron lasers

Diandra Doppler,[a,b]‡ Mohammad T. Rabbani,[a,b]‡ Romain Letrun,[c] Jorvani Cruz Villarreal,[a,b] Dai Hyun Kim,[a,b] Sahir Gandhi,[a,b] Ana Egatz-Gomez,[a,b] Mukul Sonker,[a,b] Joe Chen,[d] Faisal H. M. Koua,[e] Jayhow Yang,[b] Mohamed Youssef,[e] Victoria Mazalova,[e] Saša Bajt,[f,g] Megan L. Shelby,[h] Matt A. Coleman,[h] Max O. Wiedorn,[e,f,i] Juraj Knoska,[e] Silvan Schön,[e] Tokushi Sato,[c] Mark S. Hunter,[j] Ahmad Hosseinizadeh,[k] Christopher Kuptiz,[j] Reza Nazari,[b,d] Roberto C. Alvarez,[b,d] Konstantinos Karpos,[b,d] Sahba Zaare,[b,d] Zachary Dobson,[a,b] Erin Discianno,[b] Shangji Zhang,[a,b] James D. Zook,[a,b] Johan Bielecki,[c] Raphael de Wijn,[c] Adam R. Round,[c,l] Patrik Vagovic,[c,e] Marco Kloos,[c] Mohammad Vakili,[c] Gihan K. Ketawala,[a,b] Natasha E. Stander,[a,b] Tien L. Olson,[a,b] Katherine Morin,[b] Jyotirmory Mondal,[m] Jonathan Nguyen,[a,b] José Domingo Meza-Aguilar,[b,c] Gerdenis Kodis,[a,b,d] Sara Vaiana,[d] Jose M. Martin-Garcia,[b,n] Valerio Mariani,[e] Peter Schwander,[k] Marius Schmidt,[k] Marc Messerschmidt,[a,b] Abbas Ourmazd,[k] Nadia Zatsepin,[b,d,o] Uwe Weierstall,[b,d] Barry D. Bruce,[m] Adrian P. Mancuso,[c,o] Thomas Grant,[p] Anton Barty,[e,q,q] Henry N. Chapman,[e,f,i] Matthias Frank,[h] Raimund Fromme,[a,b] John C. H. Spence,[b,d] Sabine Botha,[b,d] Petra Fromme,[a,b] Richard A. Kirian[b,d] and Alexandra Ros[a,b]*

[a]School of Molecular Sciences, Arizona State University, Tempe, Arizona, USA, [b]Center for Applied Structural Discovery, Biodesign Institute, Arizona State University, Tempe, Arizona, USA, [c]European XFEL, Schenefeld, Germany, [d]Department of Physics, Arizona State University, Tempe, Arizona, USA, [e]Center for Free-Electron Laser Science, Deutsches Elektronen-Synchrotron (DESY), Hamburg, Germany, [f]Hamburg Center for Ultrafast Imaging, Hamburg, Germany, [g]Deutsches Elektronen-Synchrotron (DESY), Hamburg, Germany, [h]Lawrence Livermore National Laboratory (LLNL), Livermore, California, USA, [i]Department of Physics, Universität Hamburg, Hamburg, Germany, [j]Linac Coherent Light Source, SLAC National Accelerator Laboratory, Menlo Park, California, USA, [k]Department of Physics, University of Wisconsin-Milwaukee, Milwaukee, Wisconsin, USA, [l]School of Chemical and Physical Sciences, Keele University, Staffordshire, UK, [m]Department of Biochemistry and Cellular and Molecular Biology, University of Tennessee, Knoxville, Tennessee, USA, [n]Department of Crystallography and Structural Biology, Institute of Physical Chemistry 'Rocasolano', CSIC, Madrid, Spain, [o]Department of Chemistry and Physics, La Trobe Institute for Molecular Science, La Trobe University, Melbourne, Australia, [p]Department of Structural Biology, Jacobs School of Medicine and Biomedical Sciences, SUNY University at Buffalo, Buffalo, New York, USA, and [q]Center for Data and Computing in Natural Science CDCS, Deutsches Elektronen-Synchrotron DESY, Hamburg, Germany. *Correspondence e-mail: alexandra.ros@asu.edu

Received 14 May 2021
Accepted 22 October 2021

Edited by S. Boutet, SLAC National Accelerator Laboratory, Menlo Park, USA

‡ These authors contributed equally.

Keywords: microfluidic devices; serial crystallography; 3D printing; X-ray free-electron lasers; XFELs; viscous media; sample consumption.

Supporting information: this article has supporting information at journals.iucr.org/j

Serial femtosecond crystallography (SFX) is a powerful technique that exploits X-ray free-electron lasers to determine the structure of macromolecules at room temperature. Despite the impressive exposition of structural details with this novel crystallographic approach, the methods currently available to introduce crystals into the path of the X-ray beam sometimes exhibit serious drawbacks. Samples requiring liquid injection of crystal slurries consume large quantities of crystals (at times up to a gram of protein per data set), may not be compatible with vacuum configurations on beamlines or provide a high background due to additional sheathing liquids present during the injection. Proposed and characterized here is the use of an immiscible inert oil phase to supplement the flow of sample in a hybrid microfluidic 3D-printed co-flow device. Co-flow generation is reported with sample and oil phases flowing in parallel, resulting in stable injection conditions for two different resin materials experimentally. A numerical model is presented that adequately predicts these flow-rate conditions. The co-flow generating devices reduce crystal clogging effects, have the potential to conserve protein crystal samples up to 95% and will allow degradation-free light-induced time-resolved SFX.

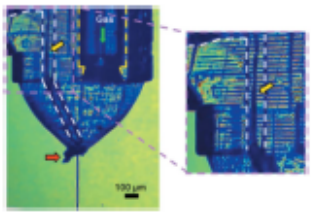

1. Introduction

Serial femtosecond crystallography (SFX) with X-ray free-electron lasers (XFELs) has shown impressive advances in the field of macromolecular structure determination in the past

decade (Martin-Garcia *et al.*, 2016; Chapman *et al.*, 2011; Boutet *et al.*, 2012; Orville, 2020). Examples include revealing structural details of membrane proteins with unprecedented resolution, such as G-protein coupled receptors (Zhang *et al.*, 2015; Kang *et al.*, 2015; Stauch & Cherezov, 2018; Gusach *et al.*, 2020) or photosystems (Kupitz *et al.*, 2014; Gisriel *et al.*, 2019). The recent demonstration of time-resolved (TR) imaging of enzyme catalysis under near-physiological conditions (Stagno *et al.*, 2016; Olmos *et al.*, 2018; Calvey *et al.*, 2016; Pandey *et al.*, 2021), made possible by XFEL crystallography using mixing injectors, further provides a tantalizing glimpse of the dawn of the new field of structural enzymology and its likely impact. This relates to all aspects of life controlled by enzymes and will improve our knowledge for the design of inhibitors to common diseases threatening our health.

Pump–probe TR-SFX with XFELs involves laser pulses triggering a reaction mechanism in light-activated proteins shortly before they are probed by an XFEL beam. This allows time resolution in the range of femtoseconds to microseconds (Neutze *et al.*, 2000; Chapman *et al.*, 2011). However, most biologically relevant processes, such as enzymatic reactions, are not light induced and instead require rapid mixing of the protein crystals with a ligand (*e.g.* a substrate or an antibiotic). Methods facilitating these mix-and-inject experiments are limited by the diffusion of the ligand into the crystals and this typically leads to time scales of the order of milliseconds to seconds, such as demonstrated with BlaC (Olmos *et al.*, 2018; Kupitz *et al.*, 2017), cytochrome c oxidase (Ishigami *et al.*, 2018) and the riboswitch (Stagno *et al.*, 2016).

Sample wastage remains a critical issue for SFX and TR-SFX studies with XFELs (Martin-Garcia *et al.*, 2016; Conrad *et al.*, 2015). Protein crystals are cumbersome to obtain in suspensions of adequate concentration in a sufficiently large volume (>10 ml with hundreds of milligrams of protein) for full data sets. Current XFELs operate at pulse frequencies up to 120 Hz at the LCLS (USA), 60 Hz at SACLA (Japan), 30 Hz at PAL-XFEL (South Korea), 100 Hz at SwissFEL (Switzerland) or megahertz pulse trains repeating at 10 Hz frequency at the EuXFEL (Germany). Thus, for all XFEL instruments, the vast majority of the sample is wasted if sample injection is carried out with any continuous liquid injection technique, such as delivery with a gas dynamic virtual nozzle (GDVN) (DePonte *et al.*, 2008). While this method is robust and has demonstrated great success in the past, it has several key limitations: (i) high flow rates in the tens of microlitres per minute are typically required, and (ii) clogging issues arise very often due to viscous samples, adsorption of crystals to the capillary and tubing during delivery, or agglomeration of larger protein crystals within the nozzles and delivery lines.

Several approaches to reduce sample consumption have been proposed. Viscous jet injectors slowly extruding crystals suspended in a viscous medium, such as lipidic cubic phase or agarose, have been successfully used to deliver samples into the path of the XFEL (Conrad *et al.*, 2015; Weierstall *et al.*, 2014). However, many proteins resist crystallization in viscous media, and the large diameter of the extrusion increases background scatter. Furthermore, these slowly focusing jets are not compatible with the higher-repetition-rate facilities in operation (Grünbein *et al.*, 2018) or under construction (LCLS-II, Menlo Park, California, USA).

Double flow-focusing injectors have been successful at injecting higher-viscosity samples at lower sample flow rates, but the samples may be significantly diluted by the sheath liquid required to achieve high enough flow rates to create a stable jet for data collection (Oberthuer *et al.*, 2017). Drop-on-demand systems have also been developed to synchronize the liquid droplets with the XFEL frequency (Mafuné *et al.*, 2016). Alternatively, pulsing the liquid jet of the GDVN by switching the liquid flow on and off has been proposed, but it produces large droplets and does not function *in vacuo* (James, 2015).

Acoustic injection of protein crystal suspensions can expose a high percentage of the crystals injected and exhibits a high hit rate, though it also suffers from a large background and requires large microcrystals (Roessler *et al.*, 2016). Fixed-target methods that raster an array of immobilized crystals with respect to the XFEL beam have been shown to give a vast reduction in sample consumption and improve hit rates (Hunter *et al.*, 2014). However, problems with preferential orientation of the crystal may prevent full sampling of reciprocal space, limitations arise with high-repetition XFELs and time-consuming array changing is often problematic with short beamtime allocations. Similar issues also apply for the recently developed methods that position droplets of a mixing reagent in a timed manner on fixed targets for TR studies (Mehrabi *et al.*, 2019). Furthermore, an approach combining acoustic droplet generation with a conveyor belt delivery has been shown to be suitable for SFX, but is limited by slow reaction time points for TR-SFX delivery in aqueous solutions (Fuller *et al.*, 2017). As for low-flow-rate viscous jet injectors, issues arise for the microfluidic electrokinetic sample holder (MESH) (Sierra *et al.*, 2012) and its updated version, the concentric MESH injector (coMESH) (Sierra *et al.*, 2016), for short millisecond time points as desired in mix-and-inject experiments and due to multiple crystal hits.

We have recently reported a new approach that encapsulates protein crystals in small droplets of mother liquor in an immiscible phase coupled with GDVN injection (Echelmeier *et al.*, 2019, 2020). The device has been successfully used at the LCLS (Echelmeier *et al.*, 2019), where diffraction from photosystem I was recorded, and more recently at the EuXFEL to determine the structure of the enzyme KDO8PS to 2.8 Å resolution at room temperature (Echelmeier *et al.*, 2020). This method has additional potential to synchronize the arrival of the droplet with the XFEL beam and further minimize sample loss, as demonstrated by the electrical triggering of the droplet release (Kim *et al.*, 2019). To synchronize the droplet generation with the XFEL, a feedback mechanism is required, which is linked to optical detection of the generated droplets. An advantage of this droplet approach to reduce sample waste lies in the small footprint of all necessary components and the fabrication of all elements through 3D-printing technology (Echelmeier *et al.*, 2019, 2020).

Apart from sample consumption issues, liquid jet injection for SFX with XFEL experiments also suffers from issues with

very high viscosity samples. Many proteins, including complex membrane proteins, require crystallization conditions in very high viscosity polyethylene glycol (PEG) solutions which often need to be maintained for injection to ensure crystal quality (Durbin & Feher, 2017; Middaugh *et al.*, 1979; Atha & Ingham, 1981; Conrad *et al.*, 2015; Pandey *et al.*, 2020). Overcoming this limitation could be a major breakthrough to allow more elaborate SFX studies of a larger variety of biologically important proteins.

Our development of the above-mentioned injection scheme based on interleaved immiscible phases, together with the issues arising for high-viscosity injection media, led us to the alternative scheme that we present here. During the characterization of droplet generation in our devices, we found regimes in which the sample and oil phases flowed in parallel towards the GDVN and then formed exceptionally long and stable liquid jets which are important for nozzle lifetime. This 'co-flow' phenomenon was characterized in this work both experimentally and with a theoretical model at various flow rates for the aqueous (Q_a) and oil (Q_o) phases. We further characterized two different materials for the 3D-printed co-flow generators, coupled in a hybrid fashion to a GDVN in one device. We also demonstrate the application of this injection method at the EuXFEL for a viscous sample of photosystem II (PSII) crystals embedded in mother liquor and the compatibility of the employed 3D-printed devices with light-induced TR-SFX.

2. Materials and methods

2.1. Materials

Pentaerythritol triacrylate (PETA), phenylbis(2,4,6-trimethylbenzoyl)phosphine oxide (BAPO), 2-morpholinoethanesulfonic acid (MES), sodium chloride (NaCl), calcium dichloride ($CaCl_2$), magnesium sulfate ($MgSO_4$), polyethylene glycol (PEG, MW 1450), polyethylene glycol methyl ether (MW 5000), perfluorodecalin (PFD) and 1*H*,1*H*,2*H*,2*H*-perfluoro-1-octanol (perfluorooctanol, PFO) were purchased from Sigma–Aldrich, USA. The detergents *n*-dodecyl *β*-maltoside and *n*-heptyl-*β*-D-thioglucopyranoside were purchased in crystallization grade from Glycon Biochemicals GmbH (Luckenwalde, Germany). SU-8 developer was obtained from Microchem, USA. The photoresist IP-S was purchased from Nanoscribe GmbH, Germany. Deionized water (18 MΩ) was supplied from an LA755 Elga purification system (Elga LabWater, USA), and propan-2-ol (isopropyl alcohol, IPA) and ethanol were obtained from VWR Analytical (USA) and Decon Labs (USA), respectively. Fused silica capillaries [360 µm outer diameter (OD), 100 µm inner diameter (ID)] were purchased from Molex, USA. Hardman extra-fast-setting epoxy was purchased from All-Spec, USA.

2.2. Co-flow device design and fabrication

Hybrid devices containing a co-flow junction prior to a GDVN (Fig. 1) were designed and fabricated as described

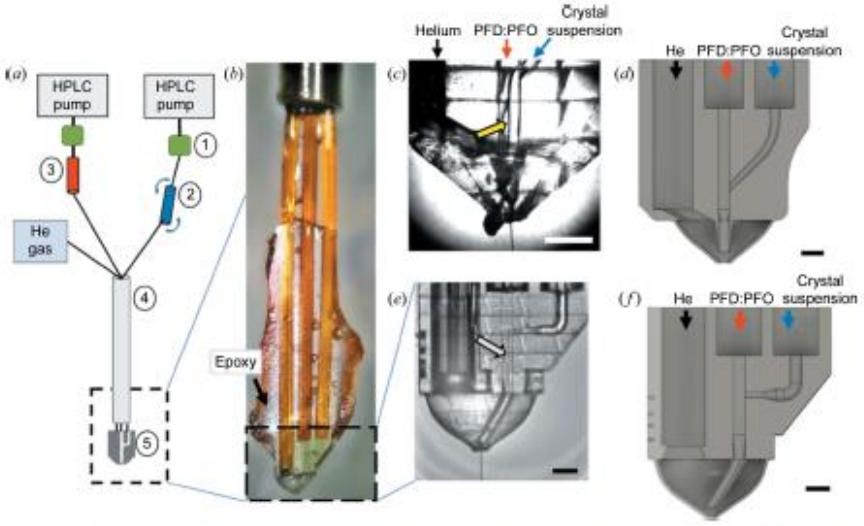

Figure 1
(*a*) The experimental setup of the co-flow generator at the EuXFEL (not to scale). (1) Flow-rate sensors, (2) crystal suspension reservoir mounted in the rotating anti-settler device, (3) oil reservoir, (4) nozzle rod and (5) hybrid device (3D-printed device with integrated co-flow generator and GDVN) mounted on the end of the nozzle rod. Black lines indicate capillary tubing or fused silica capillaries for fluid and gas transport. (*b*) The assembled hybrid device mounted in the nozzle rod. The co-flow/nozzle hybrid is located at the very end of the one gas and two fluidic lines connected to the fused silica capillaries through epoxy. (*c*) An image of the assembled Y-junction device. Co-flow is generated as indicated by the interface between the two phases (see yellow arrow). (*d*) A schematic drawing of the Y-junction device for co-flow formation designed in *Fusion 360*. (*e*) An image of the T-junction hybrid device, showing the oil–sample co-flow running (marked with a white arrow) and the jet leaving the nozzle. (*f*) A schematic drawing of the T-junction device for co-flow formation designed in *Fusion 360*. The scale bars represent 200 µm in panels (*c*)–(*f*).

previously (Echelmeier *et al.*, 2019). Briefly, devices were drawn in *Fusion 360* (AutoDesk, USA) and then 3D-printed with a Photonic Professional GT 3D printer (Nanoscribe GmbH, Germany) using either IP-S photoresist (Nanoscribe GmbH, Germany) or PETA with BAPO (1.2% *w*/*w* BAPO), termed PETA-B. Printing was accomplished in solid mode using dip-in laser lithography (Bückmann *et al.*, 2012) with two-photon polymerization. Once printed, devices were developed in SU-8 developer, or ethanol for PETA-B resin, and rinsed in IPA. Fused silica capillaries were inserted and fixed into the device inlets using epoxy. Their length depended on the experimental setup. At the EuXFEL, 2 m of capillary was attached to each inlet to traverse the length of the nozzle rod, and during preliminary testing in the home laboratory 60 cm of the capillary was used per inlet. The hybrid devices comprised a T-junction or a Y-junction for co-flow formation. The Y-junction is formed by an intersection of a rectangular channel section (100 × 100 µm) and a 75 µm diameter cylindrical channel at a 45° angle. The T-junction is, likewise, formed by a rectangular channel (75 × 100 µm) and a 75 µm diameter cylindrical channel at a 90° angle. These junctions can be seen in the computer-aided designs in Figs. 1(*d*) and 1(*f*). Two iterations of these devices were used for preliminary experiments and injection at the EuXFEL SPB/SFX instrument (Mancuso *et al.*, 2019). Devices containing only capillary inlets and junctions were used for preliminary experiments; experiments performed at the EuXFEL used junctions coupled to GDVNs (Nazari *et al.*, 2020).

2.3. Fluidic operation and setup

High-performance liquid chromatography (HPLC) pumps (LC20AD, Shimadzu Co., Japan) were connected to a custom or commercial stainless steel reservoir containing a plunger through which either crystal suspensions or the oil phase were dispensed (Oberthuer *et al.*, 2017; Wang *et al.*, 2014). Liquid-flow sensors SLI-0430 (Sensirion, Switzerland, accuracy of 5% of measured value, based on the flow rates used in this study up to 1.25 µl min^{-1}) and SLG-0075 (Sensirion, Switzerland, accuracy of 20% of measured flow velocity, based on the flow rates used in this study up to 3.8 µl min^{-1}) were used to monitor the flow rates before the reservoirs. Poly ethyl ether ketone tubing (Zeus, USA, 250 µm ID and 1/16 inch OD) with fittings and ferrules from IDEX Health & Science LLC (USA) was used to connect the HPLC pumps to the sensors and reservoirs. Fused silica capillaries were used to connect the reservoirs to the co-flow devices. During preliminary testing at the ASU laboratory, the device was mounted onto an Olympus IX71 microscope equipped with a Photron Fastcam Mini AX (Photron, USA). Helium gas pressures in the range of 150–600 psi (1 psi ≃ 6893 Pa) were used to operate the GDVNs and controlled manually via a gas regulator. For any flow-rate condition, the system was allowed to equilibrate for 5–10 min until the liquid pressures had stabilized. A schematic diagram of the experimental setup is provided in Fig. 1(*a*). The images obtained from microscopic observation of the co-flow generation were analysed by measuring the width of the aqueous flow using *ImageJ* (Abramoff *et al.*, 2004). The co-flow thickness was assessed at 150 µm from the junction as the width of the aqueous stream in replicates of three.

During experiments at the EuXFEL, the device was mounted in the nozzle rod and inserted through a load–lock system into the vacuum chamber at 1 mPa with the nozzle running (Mancuso *et al.*, 2019; Schulz *et al.*, 2019). Additionally, the reservoir containing the PSII crystals was mounted on a rotating anti-settling device (Lomb *et al.*, 2012) and a GP1 electronic pressure regulator (Equilibar, USA) was used to regulate the helium gas applied to the gas dynamic virtual nozzle. For imaging during the experiments, a Zyla 5.5 sCMOS (Andor, Northern Ireland) equipped with a Mitutoyo MY10X-80310× objective (Thorlabs, USA) was used, and the EuXFEL femtosecond pump–probe laser (800 nm) was employed as the illumination source (Palmer *et al.*, 2019).

2.4. Jet speed characterization

The jet produced by the hybrid co-flow device was illuminated with a double-pulsed fibre-coupled 633 nm 100 ns laser, as previously described (Nazari *et al.*, 2020). A Fastcam SA5 (Photron, USA) camera equipped with a Mitutoyo MY10X-80310× objective (Thorlabs, USA) and a 12× UltraZoom magnifying lens (Navitar, USA) was used to acquire the video needed for the speed analysis. When analysing the acquired video, the translation of the droplets created downstream of the jet where it breaks up is compared with the speed of acquisition. The speed of the jet can be deduced via particle-tracking velocimetry analysis procedures described previously (Adrian, 1991).

2.5. Photoresist laser testing

The 3D-printed structures made of the different photoresists were irradiated using a 532 nm Continuum Surelite Nd:YAG laser (Amplitude Technologies, France). The laser power used ranged from 50 to 360 mJ cm^{-2} at 10 Hz (pulse duration of 5 ns) with a circular (Gaussian profile) laser beam of 1 mm diameter for 10–15 min. The structure was then visually inspected and imaged under a stereomicroscope for damage.

2.6. Crystal sample preparation

The PSII samples were crystallized as described previously (Koua *et al.*, 2013) in the XBI laboratories of the EuXFEL facility (Han *et al.*, 2021). In brief, for homogenous microcrystal preparations, a detergent exchange from *n*-dodecyl *β*-maltoside to *n*-heptyl-*β*-D-thioglucopyranoside was conducted by precipitation of the PSII with PEG 1450 at a final concentration of 12%(*w*/*v*). The supernatant was discarded and the pellet resuspended in a buffer containing final concentrations of 20 m*M* MES pH 6.0, 20 m*M* NaCl, 5 m*M* $CaCl_2$ and 0.85%(*w*/*v*) *n*-heptyl-*β*-D-thioglucopyranoside. Crystallization was accomplished using 6–7% PEG 1450 as the precipitant at a chlorophyll concentration of 2–4 m*M*. The crystal growth was stopped by adding 2–3%(*w*/*v*) PEG 1450. Microcrystals grew within 1–2 h at 293 K to a range of

10–30 µm. The microcrystals were dehydrated by exchanging the mother liquor with stepwise increasing concentrations of a dehydration buffer to reach final concentrations of 20 m*M* MES pH 6.0, 20 m*M* NaCl, 5 m*M* $CaCl_2$, 22% dimethyl sulfoxide (DMSO), 9%(*w*/*v*) PEG 5000 and 9%(*w*/*v*) PEG 1450. All crystallization steps were performed under dim green light. The microcrystals were loaded in 3 ml aliquots into reservoirs for the injection.

2.7. Diffraction experiments

XFEL experiments were conducted on the SPB/SFX instrument at the EuXFEL (Schenefeld, Germany) (Mancuso *et al.*, 2019; Decking *et al.*, 2020) during beamtime P2326 (September 2019). The pulse structure of the XFEL was composed of 10 Hz bunch trains, with 125 pulses at 564 kHz per bunch train. The pulse duration as estimated from the electron bunch length was 50 fs with a photon energy of 9.31 keV. The beam was focused with Kirkpatrick–Baez mirrors to a beam diameter of about 2.8 × 4.2 µm (Bean *et al.*, 2016). The average pulse energy was ∼600 µJ. Diffraction data were collected using the AGIPD 1 Mpixel detector (Allahgholi *et al.*, 2019; Boukhelef *et al.*, 2013).

2.8. Numerical modelling

Numerical modelling was carried out with the finite-element software *COMSOL Multiphysics* (version 5.4a, COMSOL, Stockholm, Sweden) using the laminar two-phase flow and level set interface in the *Microfluidics* module. The laminar two-phase flow interface considers the Stokes equation in the steady state (Finlayson, 2006),

$$0 = -\nabla p + \mu \nabla^2 \mathbf{u}, \tag{1}$$

where p is the pressure, $\mathbf{u}$ is the velocity vector and μ is the dynamic viscosity. The density is assumed to be constant, representing an incompressible Newtonian fluid ($\nabla \cdot \mathbf{u} = 0$). The fluid velocity is specified at the inlet, and at the outlet the pressure is set as zero.

The level set method (LSM) applies a level set function $\phi(\mathbf{x}, t)$ to the space occupied by the interface, where $\mathbf{x}$ is the coordinate of a location within that space at a specific time t (Bashir *et al.*, 2011). In *COMSOL Multiphysics*, ϕ is a step function which is zero in one domain and one in the other. The function is initialized at time t_0 and then a numerical scheme defines the value of $\phi(\mathbf{x}, t)$ over time. Thus, the propagation of the interface can be traced in time. The fluid interface uses the following equation:

$$\frac{\partial \phi}{\partial t} + \mathbf{u} \cdot \nabla \phi = \gamma \nabla \cdot \left[\varepsilon \nabla \phi - \phi(1-\phi) \frac{\nabla \phi}{|\nabla \phi|} \right], \tag{2}$$

where γ is the reinitialization parameter and ε is the thickness of the interface. The terms on the right-hand side of equation (2) are necessary for numerical stability, while the terms on the left-hand side define the interface's correct motion. The thickness of the interface ε was adjusted to the largest value of the mesh size. The reinitialization parameter γ was adjusted to the maximum magnitude of the velocity field. Equation (1) was solved to obtain $\mathbf{u}$, which was then used in equation (2) (Deshpande & Zimmerman, 2006).

On the basis of this LSM method, the numerical simulation of the flow behaviour between two immiscible fluids, oil and aqueous buffer, was investigated in the T- and Y-junctions with a 2D (see example images in Fig. S1 in the supporting information) and a 3D model to display the curved interface between the immiscible phases (see example images in Fig. S2). Parameters (Tables S1 and S2) and further details are listed in the supporting information.

3. Results and discussion

Delivering samples in parallel co-flowing streams within a continuous sample-delivery device has the potential to reduce the amount of sample required for SFX experiments. A lubricant oil phase achieves an additional advantage by reducing clogging effects, since the aqueous sample experiences fewer interactions with the capillary walls, and it also facilitates the delivery of crystals in higher-viscosity buffer media. High-viscosity buffers are often encountered in protein crystallization, most frequently in membrane proteins such as PSII (Gisriel *et al.*, 2019; Nazari *et al.*, 2020) or in the case of photoactive yellow protein (Ananyev *et al.*, 2019; Gisriel *et al.*, 2019; Tenboer *et al.*, 2014). Here, we characterized a 3D-printed injection system that allows for co-flow to be generated and subsequently to deliver the sample through a coupled GDVN to the XFEL beam. The associated fluidic line schematic for sample delivery is shown in Fig. 1(*a*), and a photograph of a co-flow nozzle with capillaries attached to deliver liquids and gas is shown in Fig. 1(*b*). The co-flow generator exhibits an oil-phase inlet and an aqueous-phase inlet (for sample), meeting at a Y- or T-shaped intersection as shown in Figs. 1(*c*)–1(*d*) and 1(*e*)–1(*f*), respectively. The two liquids filling the reservoirs are pressurized through HPLC pumps and delivered through fused silica capillaries to the co-flow generator. The oil phase, a 10:1 mixture of PFD and PFO, was chosen because of its immiscibility with PEG-based and DMSO-containing aqueous buffers, as well as its chemical inertness with the protein crystals in the aqueous phase (Echelmeier *et al.*, 2019). The aqueous and oil phases meet at the intersection in the 3D-printed device, where interfacial and shear forces cause them to flow immiscibly in parallel streams. Figs. 1(*c*) and 1(*d*) show, respectively, a microscopic image of the assembled 3D-printed device generating a sample jet and a schematic of the hybrid device with a Y-intersection coupled to a 3D-printed GDVN injector, as recently described by Nazari *et al.* (2020). Figs. 1(*e*) and 1(*f*) show microscopic images of the fabricated 3D-printed device with the T-intersection. The co-flow in each of the two designs is generated shortly after the intersection of the two immiscible fluids and can be observed as a boundary in both Figs. 1(*c*) and 1(*e*).

The establishment of co-flow in these devices was investigated by varying the oil flow (Q_o) and the aqueous flow (Q_a) rates while maintaining a total flow rate Q_{tot} of 20 µl min^{-1}. These conditions were chosen because a total flow rate of

20 µl min^{-1} generated a fast enough jet for the X-ray repetition rate of 564 kHz used during the experiment (see more detail below on jet velocities) and since we found stable co-flow generation at sample flow rates below 10 µl min^{-1}. We explored two different types of resin for 3D-printing the high-resolution co-flow injectors. Figs. 2(*a*) and 2(*b*), respectively, show microscopy images of the T-junction and Y-junction geometries printed with IP-S photoresist. We further investigated two different configurations for generating co-flow with the sample and oil phases. In mode 1, the aqueous sample is delivered from the side channel (*i.e.* the channel connecting to the straight channel), and in mode 2, the aqueous sample is delivered from the continuous channel.

Fig. 2(*c*) shows a microscopy image of a Y-junction device printed in PETA-B. As the aqueous phase, we used either the mother liquor alone or the mother liquor containing PSII crystals. In these three images [Figs. 2(*a*)–2(*c*)], the interface between the two immiscible fluids can be clearly observed. To characterize the co-flow, the width of the aqueous stream (the distance measured from the 3D-printed capillary wall to the interface of the two co-flowing liquids) was determined at a defined position after the intersection, as outlined in the *Methods* section. Generally, the thickness of the aqueous flow stream decreases with increasing flow-rate ratio (Q_o/Q_a) for each of the geometries and resins, as one would expect from the corresponding volume fractions.

In Fig. 2(*d*), the thickness within the T-junction was investigated with PSII crystals, ranging from 5 to 25 µm, suspended in dehydration buffer (mother liquor) at varying flow-rate ratios. The same experiment was performed with just the dehydration buffer to identify any effects originating from the crystals in the solution. The two experiments show comparable results, indicating that the co-flow thickness is not disturbed by the presence of crystals in the crystal size range explored.

In addition, a numerical model was established (see *Methods* section) in which the parameters of the oil and aqueous phases were adapted to the liquids used and the properties of the device resin, as outlined in the supporting information, Table S1. The two phases were introduced from the inlets defined in the model with matching geometry of the T-junction and formed a well defined co-flow, as illustrated in Fig. S1, similarly to Figs. 2(*a*)–2(*c*). Variations in the co-flow widths were measured using the *ImageJ* software (Schneider *et al.*, 2012), similarly to the experimental case, and are plotted in Fig. 2(*d*) for the T-geometry and PSII dehydration buffer. The simulations are in excellent agreement with the experimental results obtained for the co-flow thickness.

The 90° angle in the T-junction geometry [Figs. 2(*a*) and 2(*d*)] proved to be challenging, with crystals building up during hours-long XFEL experiments and eventually leading to clogging. Therefore, a smoother transition design was created with a 45° angle between the two channels forming the intersection, termed a Y-junction. To alleviate clogging challenges further, the two different sample configuration modes were investigated. Figs. 2(*e*) and 2(*f*) show the comparison of these two modes in the Y-junction device. Note that data presented in Fig. 2(*e*) correspond to 3D-printed Y-junctions fabricated with IP-S photoresist and data in Fig. 2(*f*) were

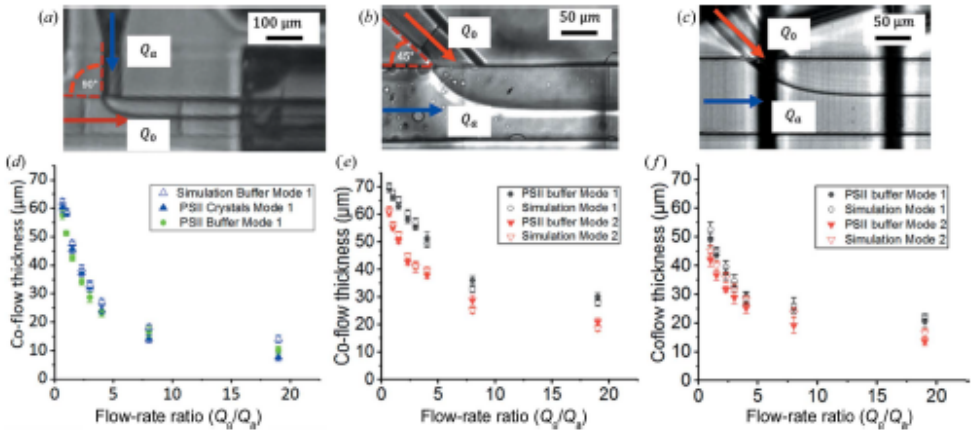

Figure 2
(*a*) Bright-field microscopy image of the T-junction geometry 3D-printed with IP-S photoresist in mode 1 with a flow-rate ratio of 1. (*b*) Bright-field microscopy image of the Y-junction geometry 3D-printed with IP-S photoresist in mode 2 with a flow-rate ratio of 4. (*c*) Bright-field microscopy image of the Y-junction geometry 3D-printed with PETA-B photoresist in mode 2 with a flow-rate ratio of 1. (*d*) Co-flow thickness of the T-junction device with PSII crystal in the buffer (filled green circles), PSII buffer only (filled blue triangles) and simulation (open blue triangles). The error bars indicate the standard deviation of the co-flow thickness. The devices used to test these conditions were made of IP-S photoresist. (*e*) The co-flow thickness of the Y-junction with PSII buffer in mode 1 (filled black circles) and mode 2 (filled red triangles) compared with the numerical simulation in mode 1 (open black circles) and simulation mode 2 (open red triangles). The error bars indicate the standard deviation of the co-flow thickness. The devices used to test these conditions were made of IP-S photoresist. (*f*) The co-flow thickness of the Y-junction with PSII buffer in mode 1 (filled black circles) and mode 2 (filled red triangles) compared with simulation mode 1 (open black circles) and simulation mode 2 (open red triangles). The error bars indicate the standard deviation of the co-flow thickness. The devices used to test these conditions were made of PETA-B photoresist.

obtained with a device made of PETA-B. As for the T-junction geometry, the thickness of the aqueous flow decreases with increasing flow-rate ratio for both device resins.

The co-flow thickness in the IP-S device differs considerably in the two modes, as a smaller co-flow thickness (width of the aqueous phase) is apparent over all probed flow-rate ratios. This trend was also confirmed in the numerical model data. This phenomenon could be caused by the aqueous sample entering the continuous channel at a larger diameter (100 µm) in mode 2 than in mode 1 (75 µm). Overall, a similar trend to the IP-S co-flow characterization was observed by the Y-junction fabricated with PETA-B photoresist. No significant differences were observed between the two design modes, either experimentally or in the simulation.

Since co-flow conditions were observed up to a flow-rate ratio of 19, for the devices tested in Fig. 3 we conclude that the sample consumption can be reduced by about 95% with this method.

While the crystals employed in this work, with sizes of the order of tens of micrometres, required flow-rate ratios of 3 or lower to be fully encapsulated in their mother liquor, it is hypothesized that nanocrystalline slurries and such with crystal sizes up to 5 µm would be comfortably suspended in their injection solution when the ratios meet the explored limit of 19 as this ratio leads to a co-flow thickness of 10 µm [see Figs. 2(*d*)–2(*f*)]. However, limitations for SFX experiments need to be taken into account, such as clogging, which is enhanced at very low sample flow rates, and decreased hit rates, which may occur given high dilution with the oil phase in the extreme-flow-rate-ratio cases. In addition, the viscosity of the sample medium poses further limitations in jetting samples with GDVNs, although these can be overcome with co-flow injection, as indicated below.

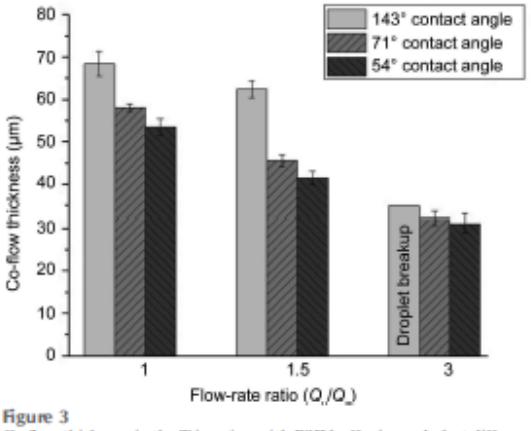

Figure 3
Co-flow thickness in the T-junction with PSII buffer in mode 1 at different flow rates and contact angles. Co-flow thickness was estimated for contact angles of 143, 71 and 54°. The co-flow thickness decreases with decreasing contact angle. For a flow-rate ratio of 3, instead of co-flow, droplet generation was observed for a hydrophobic condition (contact angle of 143°). The error bars indicate the standard deviation of the co-flow thickness.

The co-flow thickness depends not only on the device geometry and mode but also on the surface properties of the devices, most notably the wetting properties. When two immiscible fluids and a solid interface are in contact with each other, there is an inward-directed force that attempts to minimize the contact with the surface by pulling one of the liquids into the shape of a sphere. The resultant angle between the interface of the two fluids and the solid layer is a function of the specific free energy of the interface, where the interfacial tension forces between all three phases can be related to the contact angle (θ) of the surface (Tiab & Donaldson, 2012; Rowlinson & Windom, 1982). This contact angle depends on the two liquids used and the characteristics of the surface of the solid.

In our case, we observed that surfaces printed with IP-S photoresist showed significant changes in the contact angle and thus in the wetting properties over time. A shift from hydrophobic to hydrophilic surface properties over time was observed for both the IP-S and PETA-B surfaces. As demonstrated in Fig. S5, the contact angle drops significantly for IP-S surfaces over a period of two weeks from hydrophobic (~140°) to hydrophilic (below 80°), as assessed with the sessile drop method. Over a similar time scale, the PETA-B surfaces showed a comparable trend, although the contact angle change due to to wetting properties is less pronounced. Since devices are usually fabricated days or weeks in advance of XFEL experiments, we therefore repeated the numerical simulations with three different resin contact angles for three Q_o and Q_a while maintaining Q_{tot} at 20 µl min^{-1}. Fig. 3 displays the obtained co-flow width for mode 1 in a T-junction device. For each tested flow-rate ratio, the thickness of the aqueous flow stream decreases when the contact angle decreases (*i.e.* when the material becomes increasingly hydrophilic). For a flow-rate ratio of 3 (Q_o of 15 µl min^{-1} and Q_a of 5 µl min^{-1}) on the most hydrophilic surface with a contact angle of 54°, the co-flow began to break up into droplets. Fig. S3 demonstrates the co-flow formation for the lower flow-rate ratios and droplet breakup at the largest flow-rate ratio as obtained from the numerical model. Thus, the variation in surface properties of the co-flow device material determines to a great extent when stable co-flow conditions prevail. In addition, we note that the experiments carried out at the EuXFEL were performed with devices that were produced and assembled several weeks in advance of the experiment, thus exhibiting hydrophilic surface properties, which generated stable co-flow in the SPB/SFX chamber, as shown next. The most extreme case with a contact angle of 54° may be avoided when devices are prepared less than two weeks in advance.

The co-flow devices were utilized at the EuXFEL during beamtime P2326. Fig. 4(*a*) shows the T-junction hybrid device coupled with a GDVN in the vacuum chamber of the SPB/SFX instrument with co-flow established (yellow arrow) and a jet that was approximately 600 µm in length, which is twice the length of a water jet at the same flow rate (Nazari *et al.*, 2020). Having a sufficiently fast jet is imperative because the sample must be replenished after being vaporized by the destructive

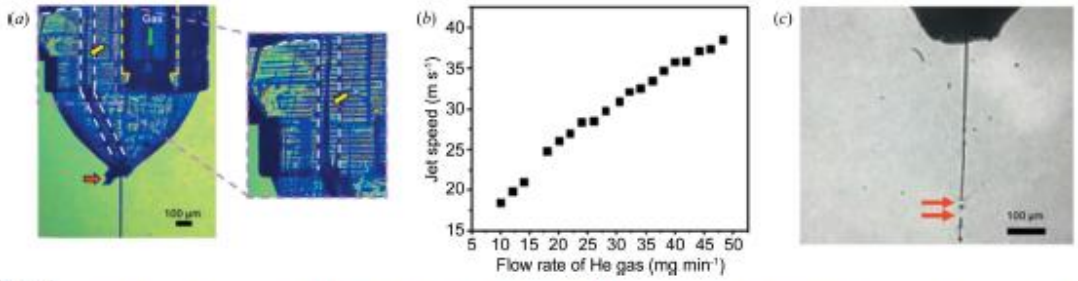

Figure 4
(*a*) An image of an IP-S co-flow device installed in the SPB/SFX chamber at the EuXFEL. The enlarged image shows the boundary of the two immiscible phases indicated by the yellow arrow. (*b*) Jet speed versus flow rate of He gas as investigated for PSII buffer obtained from a PETA-B co-flow hybrid. (*c*) Optical microscopy image of a jet containing protein crystals recorded in the SPB/SFX chamber (Q_o of 15 µl min^{-1}, Q_a of 5 µl min^{-1} and He flow rate of 20 mg min^{-1}). Jet imaging was performed by optical laser illumination after the second X-ray pulse in the bunch train to achieve this image. Highlighted with red arrows are the positions of where consecutive XFEL pulses impact the jet.

femtosecond X-ray pulses delivered at a megahertz repetition rate. Prior to the XFEL experiments, the jet speed was measured using methods published previously (Nazari *et al.*, 2020), based on the He mass flow applied to the GDVN, as shown in Fig. 4(*b*). The jet speed was analysed while exhibiting co-flow at a total liquid flow rate of 20 µl min^{-1} (Q_o = 15 µl min^{-1} and Q_a = 5 µl min^{-1}), which was the flow rate typically used when injecting with a GDVN-style nozzle.

In the SPB/SFX chamber, Q_{tot} = 20 µl min^{-1} and 20 mg min^{-1} of He were employed, and thus the jet speed was approximately 25.5 m s^{-1}. At this gas flow rate, two jet dissections caused by two X-ray pulses can be observed [Fig. 4(*c*)], indicating that the jet is fast enough to replenish the sample between X-ray pulses (spaced by 1.77 µs). This image relates to a co-flowing sample originating from a Y-junction device extruding a stable jet of the sample from the nozzle tip of the hybrid device. The upper red arrow in the image points to the location where the X-rays dissect the jet; the bottom arrow points to a spot just downstream where the 'hole' from the previous X-ray interaction point is clearly visible. This result is significant because a previous report (Wiedorn *et al.*, 2018) suggested that a minimum jet speed of 50 m s^{-1} was needed to replenish the sample between X-ray pulses at 1.1 MHz. With a repetition rate of 564 kHz, our results indicate that sample replenishing was achieved at about half that speed under co-flow injection conditions.

Due to the tremendous success in elucidating light-driven reactions with serial crystallography (Orville, 2020) it is also important to investigate whether new injection devices are compatible with the laser power and the typical wavelength ranges used for these experiments. We therefore tested both 3D-printed device materials for stability with a 532 nm nanosecond pump laser, which corresponds to the wavelength used to excite PSII to initiate the light-induced water oxidation reaction in the photosynthesis process (Kupitz *et al.*, 2014). To mimic the laser intensities used on the SPB/SFX instrument at the EuXFEL for TR experiments with PSII crystals, we subjected the 3D-printed devices to various laser powers and illumination times at a frequency of 10 Hz, corresponding to the pump laser frequency employed at the EuXFEL. As an example, Fig. 5 compares PETA-B devices before and after laser illumination in air at the highest power tested. No visible damage has occurred after 10 min of exposure at 360 mJ cm^{-2}. In contrast, the IP-S device showed

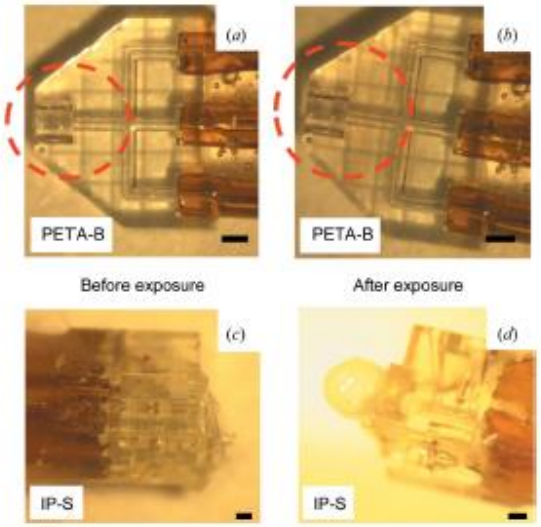

Figure 5
(*a*), (*b*) An exposure test of a 3D-printed PETA-B device (for demonstration purposes, a microfluidic mixer with similar device thickness and channel cross section to the co-flow hybrid devices) with a nanosecond 532 nm laser at 360 mJ cm^{-2} fluence in air for 10 min. The beam diameter was 1 mm and it was aligned over the device, as indicated by the red dashed circle corresponding approximately to the overlap spot in the EuXFEL experiment (with a distance of 800 µm from the nozzle tip into the device overlapping with the circular laser spot). (*b*) No visible damage was observed after laser illumination. (*c*), (*d*) A 3D-printed IP-S injection device (for demonstration purposes, a microfluidic droplet generator with similar device thickness and channel cross section to the co-flow hybrid devices) was employed for testing. Representative images are shown of IP-S devices (*c*) before and (*d*) after laser exposure (200 mJ cm^{-2} for 15 min). The IP-S devices show bubble formation at the nozzle exit of the device, indicating damage after laser illumination. Scale bars represent 200 µm in panels (*a*)–(*d*).

considerable degradation after 200 mJ cm^{-2} for 15 min, which could be attributed to heating effects and/or photochemical effects.

The robustness of the 3D-printed PETA-B co-flow hybrid devices was further substantiated through their use at the EuXFEL. They could be used for hours of operation in the SPB/SFX chamber in vacuum with the pump laser illuminating them for TR-SFX studies. Furthermore, diffraction was recorded for PSII crystals injected in co-flow mode at Q_o of 15 µl min^{-1} and Q_s of 5 µl min^{-1}. A representative diffraction pattern of PSII to a resolution above 5 Å is shown in Fig. 6.

Finally, we discuss the injection of highly viscous samples using the co-flow/GDVN hybrid devices during XFEL serial crystallography experiments in comparison with traditional GDVNs, which are still a highly attractive injection method in serial crystallography. Traditional nozzle life is strongly dependent on the samples injected, since highly viscous or concentrated samples tend to clog them within hours. This was also observed in our experiments. Employing 3D-printed GDVNs injecting crystals in dehydration buffer, jets could be run on average for 1 h before clogging effects became apparent (data not shown). In contrast, the 3D-printed hybrid co-flow devices lasted about 3.5 h (on average), which can be attributed to the addition of fluorinated oils to the system. The oil phase serves as a lubricant inside the microfluidic device, preventing crystals from agglomerating on the channel walls and clogging, and preventing the formation of irregularly shaped deposits of salt or polymer precipitations at the nozzle tip. Creating co-flow, however, dilutes the total volume of sample for injection, reducing the crystal concentration in the jet. This disadvantage is counteracted by the above-discussed improvements in injector lifetime, reducing the need to change injectors during beamtime and thus saving valuable experimentation time at XFEL instruments. Diluted crystal concentrations due to co-flow injection can also be counteracted with higher crystal densities.

An additional advantage of injection using co-flow is the ability to inject very high viscosity buffers, which would otherwise require extremely high pressures during the injection. For the PSII dehydration buffer employed in this study, a viscosity of 16.4 cP was determined (as a comparison, room-temperature water has a viscosity of 1 cP). At this viscosity, and with 2 m capillaries connecting from the reservoir to the nozzle, the pressure required to drive the sample to the nozzle within our devices ranged from 100 to 600 psi, dependent on the set flow rate. This is much lower than viscous injection with GDVNs without a co-flow injector, where typically pressures above 1000 psi are required.

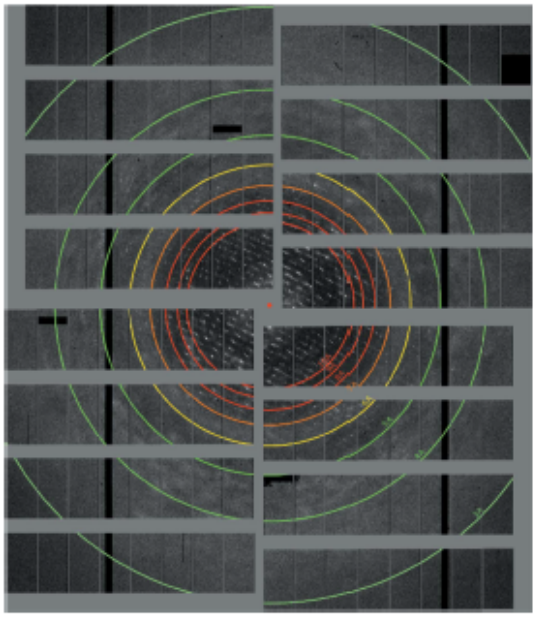

Figure 6
A representative diffraction pattern of PSII crystals delivered with the 3D-printed PETA-B co-flow hybrid device with a resolution better than 5 Å.

4. Conclusions

We have developed and characterized novel 3D-printed co-flow injection devices for serial crystallography experiments at XFELs. These devices are robust and can be readily fabricated as hybrid devices coupled to GDVNs with high-resolution 3D-printing technology. Both the commercial resin IP-S and the triacrylate resin PETA-B reliably generated co-flow, allowing a reduction in sample flow rates of a highly viscous sample buffer for SFX experiments at XFELs to 1 µl min^{-1}, which translates to about 95% less sample slurry injected. The devices can jet highly viscous buffers and co-flowing oil phase, generating long jets which are advantageous for positioning the XFEL interaction region far from the nozzle tip to reduce degradation. The devices also show lubricating effects, similar to droplet devices using the same oils (Echelmeier *et al.*, 2019, 2020; Pandey *et al.*, 2020), and could be operated on average three to four times longer than regular GDVNs with the same buffers, sometimes lasting full shifts (12 h) at the EuXFEL without severe clogging. This leads to a more effective use of available beamtime, as nozzle exchange times where no data can be collected are avoided. This advantage can offset potential disadvantages due to dilution effects with the co-flowing oil. In addition, the PETA-B devices exhibit minimal light absorbance in the visible wavelength range and are therefore suited for TR-SFX when light-induced reactions are studied at XFELs. This was verified in device fatigue measurements with conditions mimicking laser illumination during SFX experiments and during TR-SFX at the EuXFEL with PSII crystals. Finally, the co-flow injectors presented here were fabricated with high-resolution 3D-printing technology, which will further allow the integration of microfluidic mixers upstream from the co-flow generation region through fairly simple design adaptations similar to the 3D-printed mixers used in TR-SFX experiments in the past (Ishigami *et al.*, 2018).

These co-flow injectors could therefore play an important role in TR-SFX experiments with XFELs in the future.

Acknowledgements

We acknowledge the European XFEL in Schenefeld, Germany, for provision of X-ray free-electron laser beamtime on Scientific Instrument SPB/SFX (Single Particles, Clusters and Biomolecules and Serial Femtosecond Crystallography) and would like to thank the instrument group and facility staff for their assistance. Dr Don Seo is gratefully acknowledged for providing access to the viscometer. Author contributions are as follows. Conceived experiment: AR, PF; planned experiments: AR, PF, NZ, RAK, TG, DD, MTR, SG; developed co-flow injector: AR, JCV, DD, DHK, SG, RN, RAK, SZa, MSo; executed SFX experiment: RL, AR, PF, RF, FHMK, NZ, BDB, DD, MOW, VMaz, JB, RdW, PV, ARR, MK, MV, MF, RCA, KK, JM, MM, MSc, TS; responsible SPB/SFX instrument scientist: RL; led development of SPB/SFX instrument: APM; contributed to SPB/SFX instrument development: MOW, JK, SBa, MY, HNC, APM, RL, JB, RdW, ARR, PV, TS; prepared crystal sample: FHMK, JM, JDMA, PF, RF, JMMG, JY, MLS, MAC, TLO, KM, ED, ZD, JDZ, BDB, JN, JDMA, MSc, CK; set up and tested optical laser: RL, SV, GK, TS; contributed to experiment preparation: DHK, JCV, AEG, MS, UW, JCHS, SS, MY, MSH, RN, SZh, MSo; analysed diffraction data: SBo, NZ, RAK, NES, PS, AO, AH; developed numerical model: MTR, AR; analysed co-flow data: DD, MTR, SG, AR; contributed to online data processing: AB, TG, JC, VMar, RAK, NZ, GKK, NES, SBo; wrote manuscript: AR, DD, MTR with input from all other co-authors.

Funding information

Financial support from the STC Program of the US National Science Foundation through BioXFEL (agreement No. 1231306), NSF ABI Innovations (award No. 1565180), NSF CAREER (award No. 1943448) and NSF MCB (award No. 1817862), and from the National Institutes of Health (award No. R01GM095583 and award No. S10OD021816-01 entitled '3D Nanoprinter') is gratefully acknowledged. The development of the underlying algorithms was supported by the US Department of Energy, Office of Science, Basic Energy Sciences (award No. DE-SC0002164; underlying dynamic techniques), and by the NSF (award No. 1231306; underlying data analytical techniques). The work was also supported by the Biodesign Center for Applied Structural Discovery at Arizona State University and by the Cluster of Excellence 'CUI: Advanced Imaging of Matter' of the Deutsche Forschungsgemeinschaft (DFG) (EXC 2056, project No. 390715994). GK and SMV were partially supported by the National Institutes of Health (grant No. R01GM120537).

References

Abramoff, M. D., Magalhaes, P. J. & Ram, S. J. (2004). *Biophoton. Int.* **11**, 36–42.

Adrian, R. (1991). *Annu. Rev. Fluid Mech.* **23**, 261–304.

Allahgholi, A., Becker, J., Delfs, A., Dinapoli, R., Goettlicher, P., Greiffenberg, D., Henrich, B., Hirsemann, H., Kuhn, M., Klanner, R., Klyuev, A., Krueger, H., Lange, S., Laurus, T., Marras, A., Mezza, D., Mozzanica, A., Niemann, M., Poehlsen, J., Schwandt, J., Sheviakov, I., Shi, X., Smoljanin, S., Steffen, L., Sztuk-Dambietz, J., Trunk, U., Xia, Q., Zeribi, M., Zhang, J., Zimmer, M., Schmitt, B. & Graafsma, H. (2019). *J. Synchrotron Rad.* **26**, 74–82.

Ananyev, G., Roy-Chowdhury, S., Gates, C., Fromme, P. & Dismukes, G. C. (2019). *ACS Catal.* **9**, 1396–1407.

Atha, D. H. & Ingham, K. C. (1981). *J. Biol. Chem.* **256**, 12108–12117.

Bashir, S., Rees, J. M. & Zimmerman, W. B. (2011). *Chem. Eng. Sci.* **66**, 4733–4741.

Bean, R. J., Aquila, A., Samoylova, L. & Mancuso, A. P. (2016). *J. Opt.* **18**, 074011.

Boukhelef, D., Szuba, J., Wrona, K. & Youngman, C. (2013). *Proceedings of ICALEPCS 2013*, San Francisco, 6–11 October 2013, Abstract No. TUPPC045, pp. 665–668. Geneva: JACoW.

Boutet, S., Lomb, L., Williams, G. J., Barends, T. R. M., Aquila, A., Doak, R. B., Weierstall, U., DePonte, D. P., Steinbrener, J., Shoeman, R. L., Messerschmidt, M., Barty, A., White, T. A., Kassemeyer, S., Kirian, R. A., Seibert, M. M., Montanez, P. A., Kenney, C., Herbst, R., Hart, P., Pines, J., Haller, G., Gruner, S. M., Philipp, H. T., Tate, M. W., Hromalik, M., Koerner, L. J., van Bakel, N., Morse, J., Ghonsalves, W., Arnlund, D., Bogan, M. J., Caleman, C., Fromme, R., Hampton, C. Y., Hunter, M. S., Johansson, L. C., Katona, G., Kupitz, C., Liang, M. N., Martin, A. V., Nass, K., Redecke, L., Stellato, F., Timneanu, N., Wang, D. J., Zatsepin, N. A., Schafer, D., Defever, J., Neutze, R., Fromme, P., Spence, J. C. H., Chapman, H. N. & Schlichting, I. (2012). *Science*, **337**, 362–364.

Bückmann, T., Stenger, N., Kadic, M., Kaschke, J., Frölich, A., Kennerknecht, T., Eberl, C., Thiel, M. & Wegener, M. (2012). *Adv. Mater.* **24**, 2710–2714.

Calvey, G. D., Katz, A. M., Schaffer, C. B. & Pollack, L. (2016). *Struct. Dyn.* **3**, 054301.

Chapman, H. N., Fromme, P., Barty, A., White, T. A., Kirian, R. A., Aquila, A., Hunter, M. S., Schulz, J., DePonte, D. P., Weierstall, U., Doak, R. B., Maia, F., Martin, A. V., Schlichting, I., Lomb, L., Coppola, N., Shoeman, R. L., Epp, S. W., Hartmann, R., Rolles, D., Rudenko, A., Foucar, L., Kimmel, N., Weidenspointner, G., Holl, P., Liang, M. N., Barthelmess, M., Caleman, C., Boutet, S., Bogan, M. J., Krzywinski, J., Bostedt, C., Bajt, S., Gumprecht, L., Rudek, B., Erk, B., Schmidt, C., Hömke, A., Reich, C., Pietschner, D., Strüder, L., Hauser, G., Gorke, H., Ullrich, J., Herrmann, S., Schaller, G., Schopper, F., Soltau, H., Kühnel, K. U., Messerschmidt, M., Bozek, J. D., Hau-Riege, S. P., Frank, M., Hampton, C. Y., Sierra, R. G., Starodub, D., Williams, G. J., Hajdu, J., Timneanu, N., Seibert, M. M., Andreasson, J., Rocker, A., Jönsson, O., Svenda, M., Stern, S., Nass, K., Andritschke, R., Schröter, C. D., Krasniqi, F., Bott, M., Schmidt, K. E., Wang, X. Y., Grotjohann, I., Holton, J. M., Barends, T. R. M., Neutze, R., Marchesini, S., Fromme, R., Schorb, S., Rupp, D., Adolph, M., Gorkhover, T., Andersson, I., Hirsemann, H., Potdevin, G., Graafsma, H., Nilsson, B. & Spence, J. C. H. (2011). *Nature*, **470**, 73–77.

Conrad, C. E., Basu, S., James, D., Wang, D., Schaffer, A., Roy-Chowdhury, S., Zatsepin, N. A., Aquila, A., Coe, J., Gati, C., Hunter, M. S., Koglin, J. E., Kupitz, C., Nelson, G., Subramanian, G., White, T. A., Zhao, Y., Zook, J., Boutet, S., Cherezov, V., Spence, J. C. H., Fromme, R., Weierstall, U. & Fromme, P. (2015). *IUCrJ*, **2**, 421–430.

Decking, W., Abeghyan, S., Abramian, P., Abramsky, A., Aguirre, A., Albrecht, C., Alou, P., Altarelli, M., Altmann, P., Amyan, K., Anashin, V., Apostolov, E., Appel, K., Auguste, D., Ayvazyan, V., Baark, S., Babies, F., Baboi, N., Bak, P., Balandin, V., Baldinger, R., Baranasic, B., Barbanotti, S., Belikov, O., Belokurov, V., Belova, L., Belyakov, V., Berry, S., Bertucci, M., Beutner, B., Block, A., Blöcher, M., Böckmann, T., Bohm, C., Böhnert, M., Bondar, V., Bondarchuk, E., Bonezzi, M., Borowiec, P., Bösch, C., Bösenberg, U., Bosotti, A., Böspflug, R., Bousonville, M., Boyd, E., Bozhko, Y.,

Brand, A., Branlard, J., Briechle, S., Brinker, F., Brinker, S., Brinkmann, R., Brockhauser, S., Brovko, O., Brück, H., Brüdgam, A., Butkowski, L., Büttner, T., Calero, J., Castro-Carballo, E., Cattalanotto, G., Charrier, J., Chen, J., Cherepenko, A., Cheskidov, V., Chiodini, M., Chong, A., Choroba, S., Chorowski, M., Churanov, D., Cichalewski, W., Clausen, M., Clement, W., Cloué, C., Cobos, J. A., Coppola, N., Cunis, S., Czuba, K., Czwalinna, M., D'Almagne, B., Dammann, J., Danared, H., de Zubiaurre Wagner, A., Delfs, A., Delfs, T., Dietrich, F., Dietrich, T., Dohlus, M., Dommach, M., Donat, A., Dong, X., Doynikov, N., Dressel, M., Duda, M., Duda, P., Eckoldt, H., Ehsan, W., Eidam, J., Eints, F., Engling, C., Englisch, U., Ermakov, A., Escherich, K., Eschke, J., Saldin, E., Faesing, M., Fallou, A., Felber, M., Fenner, M., Fernandes, B., Fernández, J. M., Feuker, S., Filippakopoulos, K., Floettmann, K., Fogel, V., Fontaine, M., Francés, A., Martin, I. F., Freund, W., Freyermuth, T., Friedland, M., Fröhlich, L., Fusetti, M., Fydrych, J., Gallas, A., García, O., Garcia-Tabares, L., Geloni, G., Gerasimova, N., Gerth, C., Geßler, P., Gharibyan, V., Gloor, M., Głowinkowski, J., Goessel, A., Gołębiewski, Z., Golubeva, N., Grabowski, W., Graeff, W., Grebentsov, A., Grecki, M., Grevsmuehl, T., Gross, M., Grosse-Wortmann, U., Grünert, J., Grunewald, S., Grzegory, P., Feng, G., Guler, H., Gusev, G., Gutierrez, J. L., Hagge, L., Hamberg, M., Hanneken, R., Harms, E., Hartl, I., Hauberg, A., Hauf, S., Hauschildt, J., Hauser, J., Havlicek, J., Hedqvist, A., Heidbrook, N., Hellberg, F., Henning, D., Hensler, O., Hermann, T., Hidvégi, A., Hierholzer, M., Hintz, H., Hoffmann, F., Hoffmann, M., Hoffmann, M., Holler, Y., Hüning, M., Ignatenko, A., Ilchen, M., Iluk, A., Iversen, J., Iversen, J., Izquierdo, M., Jachmann, L., Jardon, N., Jastrow, U., Jensch, K., Jensen, J., Ježabek, M., Jidda, M., Jin, H., Johansson, N., Jonas, R., Kaabi, W., Kaefer, D., Kammering, R., Kapitza, H., Karabekyan, S., Karstensen, S., Kasprzak, K., Katalev, V., Keese, D., Keil, B., Kholopov, M., Killenberger, M., Kitaev, B., Klimchenko, Y., Klos, R., Knebel, L., Koch, A., Koepke, M., Köhler, S., Köhler, W., Kohlstrunk, N., Konopkova, Z., Konstantinov, A., Kook, W., Koprek, W., Körfer, M., Korth, O., Kosarev, A., Kosiński, K., Kostin, D., Kot, Y., Kotarba, A., Kozak, T., Kozak, V., Kramert, R., Krasilnikov, M., Krasnov, A., Krause, B., Kravchuk, L., Krebs, O., Kretschmer, R., Kreutzkamp, J., Kröplin, O., Krzysik, K., Kube, G., Kuehn, H., Kujala, N., Kulikov, V., Kuzminych, V., La Civita, D., Lacroix, M., Lamb, T., Lancetov, A., Larsson, M., Le Pinvidic, D., Lederer, S., Lensch, T., Lenz, D., Leuschner, A., Levenhagen, F., Li, Y., Liebing, J., Lilje, L., Limberg, T., Lipka, D., List, B., Liu, J., Liu, S., Lorbeer, B., Lorkiewicz, J., Lu, H. H., Ludwig, F., Machau, K., Maciocha, W., Madec, C., Magueur, C., Maiano, C., Maksimova, I., Malcher, K., Maltezopoulos, T., Mamoshkina, E., Manschwetus, B., Marcellini, F., Marinkovic, G., Martinez, T., Martirosyan, H., Maschmann, W., Maslov, M., Matheisen, A., Mavric, U., Meißner, J., Meissner, K., Messerschmidt, M., Meyners, N., Michalski, G., Michelato, P., Mildner, N., Moe, M., Moglia, F., Mohr, C., Mohr, S., Möller, W., Mommerz, M., Monaco, L., Montiel, C., Moretti, M., Morozov, I., Morozov, P., Mross, D., Mueller, J., Müller, C., Müller, J., Müller, K., Munilla, J., Münnich, A., Muratov, V., Napoly, O., Näser, B., Nefedov, N., Neumann, R., Neumann, R., Ngada, N., Noelle, D., Obier, F., Okunev, I., Oliver, J. A., Omet, M., Oppelt, A., Ottmar, A., Oublaid, M., Pagani, C., Paparella, R., Paramonov, V., Peitzmann, C., Penning, J., Perus, A., Peters, F., Petersen, B., Petrov, A., Petrov, I., Pfeiffer, S., Pflüger, J., Philipp, S., Pienaud, Y., Pierini, P., Pivovarov, S., Planas, M., Plawski, E., Pohl, M., Polinski, J., Popov, V., Prat, S., Prenting, J., Priebe, G., Pryschelski, H., Przygoda, K., Pyata, E., Racky, B., Rathjen, A., Ratuschni, W., Regnaud-Campderros, S., Rehlich, K., Reschke, D., Robson, C., Roever, J., Roggli, M., Rothenburg, J., Rusiński, E., Rybaniec, R., Sahling, H., Salmani, M., Samoylova, L., Sanzone, D., Saretzki, F., Sawlanski, O., Schaffran, J., Schlarb, H., Schlösser, M., Schlott, V., Schmidt, C., Schmidt-Foehre, F., Schmitz, M., Schmökel, M., Schnautz, T., Schneidmiller, E., Scholz, M., Schöneburg, B., Schultze, J., Schulz, C., Schwarz, A., Sekutowicz, J., Sellmann, D., Semenov, E., Serkez, S., Sertore, D., Shehzad, N., Shemarykin, P., Shi, L., Sienkiewicz, M., Sikora, D., Sikorski, M., Silenzi, A., Simon, C., Singer, W., Singer, X., Sinn, H., Sinram, K., Skvorodnev, N., Smirnow, P., Sommer, T., Sorokin, A., Stadler, M., Steckel, M., Steffen, B., Steinhau-Kühl, N., Stephan, F., Stodulski, M., Stolper, M., Sulimov, A., Susen, R., Świerblewski, J., Sydlo, C., Syresin, E., Sytchev, V., Szuba, J., Tesch, N., Thie, J., Thiebault, A., Tiedtke, K., Tischhauser, D., Tolkiehn, J., Tomin, S., Tonisch, F., Toral, F., Torbin, I., Trapp, A., Treyer, D., Trowitzsch, G., Trublet, T., Tschentscher, T., Ullrich, F., Vannoni, M., Varela, P., Varghese, G., Vashchenko, G., Vasic, M., Vazquez-Velez, C., Verguet, A., Vilcins-Czvitkovits, S., Villanueva, R., Visentin, B., Viti, M., Vogel, E., Volobuev, E., Wagner, R., Walker, N., Wamsat, T., Weddig, H., Weichert, G., Weise, H., Wenndorf, R., Werner, M., Wichmann, R., Wiebers, C., Wiencek, M., Wilksen, T., Will, I., Winkelmann, L., Winkowski, M., Wittenburg, K., Witzig, A., Wlk, P., Wohlenberg, T., Wojciechowski, M., Wolff-Fabris, F., Wrochna, G., Wrona, K., Yakopov, M., Yang, B., Yang, F., Yurkov, M., Zagorodnov, I., Zalden, P., Zavadtsev, A., Zavadtsev, D., Zhirnov, A., Zhukov, A., Ziemann, V., Zolotov, A., Zolotukhina, N., Zummack, F. & Zybin, D. (2020). *Nat. Photon.* **14**, 391–397.

DePonte, D. P., Weierstall, U., Schmidt, K., Warner, J., Starodub, D., Spence, J. C. H. & Doak, R. B. (2008). *J. Phys. D Appl. Phys.* **41**, 195505.

Deshpande, K. B. & Zimmerman, W. B. (2006). *Chem. Eng. Sci.* **61**, 6486–6498.

Durbin, S. D. & Feher, G. (2017). *Methods Mol. Biol.* **1607**, 17–50.

Echelmeier, A., Cruz Villarreal, J., Messerschmidt, M., Kim, D., Coe, J. D., Thifault, D., Botha, S., Egatz-Gomez, A., Gandhi, S., Brehm, G., Conrad, C. E., Hansen, D. T., Madsen, C., Bajt, S., Meza-Aguilar, J. D., Oberthür, D., Wiedorn, M. O., Fleckenstein, H., Mendez, D., Knoška, J., Martin-Garcia, J. M., Hu, H., Lisova, S., Allahgholi, A., Gevorkov, Y., Ayyer, K., Aplin, S., Ginn, H. M., Graafsma, H., Morgan, A. J., Greiffenberg, D., Klujev, A., Laurus, T., Poehlsen, J., Trunk, U., Mezza, D., Schmidt, B., Kuhn, M., Fromme, R., Sztuk-Dambietz, J., Raab, N., Hauf, S., Silenzi, A., Michelat, T., Xu, C., Danilevski, C., Parenti, A., Mekinda, L., Weinhausen, B., Mills, G., Vagovic, P., Kim, Y., Kirkwood, H., Bean, R., Bielecki, J., Stern, S., Giewekemeyer, K., Round, A. R., Schulz, J., Dörner, K., Grant, T. D., Mariani, V., Barty, A., Mancuso, A. P., Weierstall, U., Spence, J. C. H., Chapman, H. N., Zatsepin, N., Fromme, P., Kirian, R. A. & Ros, A. (2020). *Nat. Commun.* **11**, 4511.

Echelmeier, A., Kim, D., Cruz Villarreal, J., Coe, J., Quintana, S., Brehm, G., Egatz-Gomez, A., Nazari, R., Sierra, R. G., Koglin, J. E., Batyuk, A., Hunter, M. S., Boutet, S., Zatsepin, N., Kirian, R. A., Grant, T. D., Fromme, P. & Ros, A. (2019). *J. Appl. Cryst.* **52**, 997–1008.

Finlayson, B. A. (2006). *Introduction to Chemical Engineering Computing*, pp. 176–179. Hoboken: Wiley.

Fuller, F. D., Gul, S., Chatterjee, R., Burgie, E. S., Young, I. D., Lebrette, H., Srinivas, V., Brewster, A. S., Michels-Clark, T., Clinger, J. A., Andi, B., Ibrahim, M., Pastor, E., de Lichtenberg, C., Hussein, R., Pollock, C. J., Zhang, M., Stan, C. A., Kroll, T., Fransson, T., Weninger, C., Kubin, M., Aller, P., Lassalle, L., Bräuer, P., Miller, M. D., Amin, M., Koroidov, S., Roessler, C. G., Allaire, M., Sierra, R. G., Docker, P. T., Glownia, J. M., Nelson, S., Koglin, J. E., Zhu, D., Chollet, M., Song, S., Lemke, H., Liang, M., Sokaras, D., Alonso-Mori, R., Zouni, A., Messinger, J., Bergmann, U., Boal, A. K., Bollinger, J. M. Jr, Krebs, C., Högbom, M., Phillips, G. N. Jr, Vierstra, R. D., Sauter, N. K., Orville, A. M., Kern, J., Yachandra, V. K. & Yano, J. (2017). *Nat. Methods*, **14**, 443–449.

Gisriel, C., Coe, J., Letrun, R., Yefanov, O. M., Luna-Chavez, C., Stander, N. E., Lisova, S., Mariani, V., Kuhn, M., Aplin, S., Grant, T. D., Dörner, K., Sato, T., Echelmeier, A., Cruz Villarreal, J., Hunter, M. S., Wiedorn, M. O., Knoska, J., Mazalova, V., Roy-Chowdhury, S., Yang, J.-H., Jones, A., Bean, R., Bielecki, J., Kim, Y., Mills, G., Weinhausen, B., Meza, J. D., Al-Qudami, N., Bajt, S., Brehm, G., Botha, S., Boukhelef, D., Brockhauser, S., Bruce, B. D., Coleman, M. A., Danilevski, C., Discianno, E., Dobson, Z.,

Fangohr, H., Martin-Garcia, J. M., Gevorkov, Y., Hauf, S., Hosseinizadeh, A., Januschek, F., Ketawala, G. K., Kupitz, C., Maia, L., Manetti, M., Messerschmidt, M., Michelat, T., Mondal, J., Ourmazd, A., Previtali, G., Sarrou, I., Schön, S., Schwander, P., Shelby, M. L., Silenzi, A., Sztuk-Dambietz, J., Szuba, J., Turcato, M., White, T. A., Wrona, K., Xu, C., Abdellatif, M. H., Zook, J. D., Spence, J. C. H., Chapman, H. N., Barty, A., Kirian, R. A., Frank, M., Ros, A., Schmidt, M., Fromme, R., Mancuso, A. P., Fromme, P. & Zatsepin, N. A. (2019). *Nat. Commun.* **10**, 5021.

Grünbein, M. L., Bielecki, J., Gorel, A., Stricker, M., Bean, R., Cammarata, M., Dörner, K., Fröhlich, L., Hartmann, E., Hauf, S., Hilpert, M., Kim, Y., Kloos, M., Letrun, R., Messerschmidt, M., Mills, G., Nass Kovacs, G., Ramilli, M., Roome, C. M., Sato, T., Scholz, M., Sliwa, M., Sztuk-Dambietz, J., Weik, M., Weinhausen, B., Al-Qudami, N., Boukhelef, D., Brockhauser, S., Ehsan, W., Emons, M., Esenov, S., Fangohr, H., Kaukher, A., Kluyver, T., Lederer, M., Maia, L., Manetti, M., Michelat, T., Münnich, A., Pallas, F., Palmer, G., Previtali, G., Raab, N., Silenzi, A., Szuba, J., Venkatesan, S., Wrona, K., Zhu, J., Doak, R. B., Shoeman, R. L., Foucar, L., Colletier, J. P., Mancuso, A. P., Barends, T. R. M., Stan, C. A. & Schlichting, I. (2018). *Nat. Commun.* **9**, 3487.

Gusach, A., Maslov, I., Luginina, A., Borshchevskiy, V., Mishin, A. & Cherezov, V. (2020). *Curr. Opin. Struct. Biol.* **63**, 18–25.

Han, H., Round, E., Schubert, R., Gül, Y., Makroczyová, J., Meza, D., Heuser, P., Aepfelbacher, M., Barák, I., Betzel, C., Fromme, P., Kursula, I., Nissen, P., Tereschenko, E., Schulz, J., Uetrecht, C., Ulický, J., Wilmanns, M., Hajdu, J., Lamzin, V. S. & Lorenzen, K. (2021). *J. Appl. Cryst.* **54**, 7–21.

Hunter, M. S., Segelke, B., Messerschmidt, M., Williams, G. J., Zatsepin, N. A., Barty, A., Benner, W. H., Carlson, D. B., Coleman, M., Graf, A., Hau-Riege, S. P., Pardini, T., Seibert, M. M., Evans, J., Boutet, S. & Frank, M. (2014). *Sci. Rep.* **4**, 6026.

Ishigami, I., Lewis-Ballester, A., Echelmeier, A., Brehm, G., Zatsepin, N., Grant, T., Coe, J., Lisova, S., Nelson, G., Zhang, S., Dobson, Z., Boutet, S. R. S., Batyuk, A., Fromme, P., Fromme, R. J. S., Ros, A., Yeh, S.-R. & Rousseau, D. (2018). *Proc. Natl Acad. Sci. USA*, **116**, 572–577.

James, D. (2015). Dissertation, Arizona State University, USA.

Kang, Y. Y., Zhou, X. E., Gao, X., He, Y. Z., Liu, W., Ishchenko, A., Barty, A., White, T. A., Yefanov, O., Han, G. W., Xu, Q. P., de Waal, P. W., Ke, J. Y., Tan, M. H. E., Zhang, C. H., Moeller, A., West, G. M., Pascal, B. D., Van Eps, N., Caro, L. N., Vishnivetskiy, S. A., Lee, R. J., Suino-Powell, K. M., Gu, X., Pal, K., Ma, J. M., Zhi, X. Y., Boutet, S., Williams, G. J., Messerschmidt, M., Gati, C., Zatsepin, N. A., Wang, D. J., James, D., Basu, S., Roy-Chowdhury, S., Conrad, C. E., Coe, J., Liu, H. G., Lisova, S., Kupitz, C., Grotjohann, I., Fromme, R., Jiang, Y., Tan, M. J., Yang, H. Y., Li, J., Wang, M. T., Zheng, Z., Li, D. F., Howe, N., Zhao, Y. M., Standfuss, J., Diederichs, K., Dong, Y. H., Potter, C. S., Carragher, B., Caffrey, M., Jiang, H. L., Chapman, H. N., Spence, J. C. H., Fromme, P., Weierstall, U., Ernst, O. P., Katritch, V., Gurevich, V. V., Griffin, P. R., Hubbell, W. L., Stevens, R. C., Cherezov, V., Melcher, K. & Xu, H. E. (2015). *Nature*, **523**, 561–567.

Kim, D., Echelmeier, A., Cruz Villarreal, J., Gandhi, S., Quintana, S., Egatz-Gomez, A. & Ros, A. (2019). *Anal. Chem.* **91**, 9792–9799.

Koua, F. H., Umena, Y., Kawakami, K. & Shen, J. R. (2013). *Proc. Natl Acad. Sci. USA*, **110**, 3889–3894.

Kupitz, C., Basu, S., Grotjohann, I., Fromme, R., Zatsepin, N. A., Rendek, K. N., Hunter, M. S., Shoeman, R. L., White, T. A., Wang, D., James, D., Yang, J.-H., Cobb, D. E., Reeder, B., Sierra, R. G., Liu, H., Barty, A., Aquila, A. L., Deponte, D., Kirian, R. A., Bari, S., Bergkamp, J. J., Beyerlein, K. R., Bogan, M. J., Caleman, C., Chao, T.-C., Conrad, C. E., Davis, K. M., Fleckenstein, H., Galli, L., Hau-Riege, S. P., Kassemeyer, S., Laksmono, H., Liang, M., Lomb, L., Marchesini, S., Martin, A. V., Messerschmidt, M., Milathianaki, D., Nass, K., Ros, A., Roy-Chowdhury, S., Schmidt, K., Seibert, M., Steinbrener, J., Stellato, F., Yan, L., Yoon, C., Moore, T. A., Moore, A. L., Pushkar, Y., Williams, G. J., Boutet, S., Doak, R. B., Weierstall, U., Frank, M., Chapman, H. N., Spence, J. C. H. & Fromme, P. (2014). *Nature*, **513**, 261–265.

Kupitz, C., Olmos, J. L. Jr, Holl, M., Tremblay, L., Pande, K., Pandey, S., Oberthür, D., Hunter, M., Liang, M., Aquila, A., Tenboer, J., Calvey, G., Katz, A., Chen, Y., Wiedorn, M. O., Knoska, J., Meents, A., Majriani, V., Norwood, T., Poudyal, I., Grant, T., Miller, M. D., Xu, W., Tolstikova, A., Morgan, A., Metz, M., Martin-Garcia, J. M., Zook, J. D., Roy-Chowdhury, S., Coe, J., Nagaratnam, N., Meza, D., Fromme, R., Basu, S., Frank, M., White, T., Barty, A., Bajt, S., Yefanov, O., Chapman, H. N., Zatsepin, N., Nelson, G., Weierstall, U., Spence, J., Schwander, P., Pollack, L., Fromme, P., Ourmazd, A., Phillips, G. N. Jr & Schmidt, M. (2017). *Struct. Dyn.* **4**, 044003.

Lomb, L., Steinbrener, J., Bari, S., Beisel, D., Berndt, D., Kieser, C., Lukat, M., Neef, N. & Shoeman, R. L. (2012). *J. Appl. Cryst.* **45**, 674–678.

Mafuné, F., Miyajima, K., Tono, K., Takeda, Y., Kohno, J., Miyauchi, N., Kobayashi, J., Joti, Y., Nango, E., Iwata, S. & Yabashi, M. (2016). *Acta Cryst.* D**72**, 520–523.

Mancuso, A. P., Aquila, A., Batchelor, L., Bean, R. J., Bielecki, J., Borchers, G., Doerner, K., Giewekemeyer, K., Graceffa, R., Kelsey, O. D., Kim, Y., Kirkwood, H. J., Legrand, A., Letrun, R., Manning, B., Lopez Morillo, L., Messerschmidt, M., Mills, G., Raabe, S., Reimers, N., Round, A., Sato, T., Schulz, J., Signe Takem, C., Sikorski, M., Stern, S., Thute, P., Vagovič, P., Weinhausen, B. & Tschentscher, T. (2019). *J. Synchrotron Rad.* **26**, 660–676.

Martin-Garcia, J. M., Conrad, C. E., Coe, J., Roy-Chowdhury, S. & Fromme, P. (2016). *Arch. Biochem. Biophys.* **602**, 32–47.

Mehrabi, P., Schulz, E. C., Agthe, M., Horrell, S., Bourenkov, G., von Stetten, D., Leimkohl, J.-P., Schikora, H., Schneider, T. R., Pearson, A. R., Tellkamp, F. & Miller, R. J. D. (2019). *Nat. Methods*, **16**, 979–982.

Middaugh, C. R., Tisel, W. A., Haire, R. N. & Rosenberg, A. (1979). *J. Biol. Chem.* **254**, 367–370.

Nazari, R., Zaare, S., Alvarez, R. C., Karpos, K., Engelman, T., Madsen, C., Nelson, G., Spence, J. C. H., Weierstall, U., Adrian, R. J. & Kirian, R. A. (2020). *Opt. Express*, **28**, 21749–21765.

Neutze, R., Wouts, R., van der Spoel, D., Weckert, E. & Hajdu, J. (2000). *Nature*, **406**, 752–757.

Oberthuer, D., Knoška, J., Wiedorn, M. O., Beyerlein, K. R., Bushnell, D. A., Kovaleva, E. G., Heymann, M., Gumprecht, L., Kirian, R. A., Barty, A., Mariani, V., Tolstikova, A., Adriano, L., Awel, S., Barthelmess, M., Dörner, K., Xavier, P. L., Yefanov, O., James, D. R., Nelson, G., Wang, D. J., Calvey, G., Chen, Y., Schmidt, A., Szczepek, M., Frielingsdorf, S., Lenz, O., Snell, E., Robinson, P. J., Šarler, B., Belšak, G., Maček, M., Wilde, F., Aquila, A., Boutet, S., Liang, M., Hunter, M. S., Scheerer, P., Lipscomb, J. D., Weierstall, U., Kornberg, R. D., Spence, J. C., Pollack, L., Chapman, H. N. & Bajt, S. (2017). *Sci. Rep.* **7**, 44628.

Olmos, J. L., Pandey, S., Martin-Garcia, J. M., Calvey, G., Katz, A., Knoska, J., Kupitz, C., Hunter, M. S., Liang, M., Oberthuer, D., Yefanov, O., Wiedorn, M., Heyman, M., Holl, M., Pande, K., Barty, A., Miller, M. D., Stern, S., Roy-Chowdhury, S., Coe, J., Nagaratnam, N., Zook, J., Verburgt, J., Norwood, T., Poudyal, I., Xu, D., Koglin, J., Seaberg, M. H., Zhao, Y., Bajt, S., Grant, T., Mariani, V., Nelson, G., Subramanian, G., Bae, E., Fromme, R., Fung, R., Schwander, P., Frank, M., White, T. A., Weierstall, U., Zatsepin, N., Spence, J., Fromme, P., Chapman, H. N., Pollack, L., Tremblay, L., Ourmazd, A., Phillips, G. N. & Schmidt, M. (2018). *BMC Biol.* **16**, 59.

Orville, A. M. (2020). *Curr. Opin. Struct. Biol.* **65**, 193–208.

Palmer, G., Kellert, M., Wang, J., Emons, M., Wegner, U., Kane, D., Pallas, F., Jezynski, T., Venkatesan, S., Rompotis, D., Brambrink, E., Monoszlai, B., Jiang, M., Meier, J., Kruse, K., Pergament, M. & Lederer, M. J. (2019). *J. Synchrotron Rad.* **26**, 328–332.

Pandey, S., Bean, R., Sato, T., Poudyal, I., Bielecki, J., Cruz Villarreal, J., Yefanov, O., Mariani, V., White, T. A., Kupitz, C., Hunter, M., Abdellatif, M. H., Bajt, S., Bondar, V., Echelmeier, A., Doppler, D., Emons, M., Frank, M., Fromme, R., Gevorkov, Y., Giovanetti, G.,

Jiang, M., Kim, D., Kim, Y., Kirkwood, H., Klimovskaia, A., Knoska, J., Koua, F. H. M., Letrun, R., Lisova, S., Maia, L., Mazalova, V., Meza, D., Michelat, T., Ourmazd, A., Palmer, G., Ramilli, M., Schubert, R., Schwander, P., Silenzi, A., Sztuk-Dambietz, J., Tolstikova, A., Chapman, H. N., Ros, A., Barty, A., Fromme, P., Mancuso, A. P. & Schmidt, M. (2020). *Nat. Methods*, **17**, 73–78.

Pandey, S., Calvey, G., Katz, A. M., Malla, T. N., Koua, F. H. M., Martin-Garcia, J. M., Poudyal, I., Yang, J.-H., Vakili, M., Yefanov, O., Zielinski, K. A., Bajt, S., Awel, S., Doerner, K., Frank, M., Gelisio, L., Jernigan, R., Kirkwood, H., Kloos, M., Koliyadu, J., Mariani, V., Miller, M. D., Mills, G., Nelson, G., Olmos, J. L., Sadri, A., Sato, T., Tolstikova, A., Xu, W., Ourmazd, A., Spence, J. H. C., Schwander, P., Barty, A., Chapman, H. N., Fromme, P., Mancuso, A. P., Phillips, G. N., Bean, R., Pollack, L. & Schmidt, M. (2021). *IUCrJ*, **8**, 878–895.

Roessler, C. G., Agarwal, R., Allaire, M., Alonso-Mori, R., Andi, B., Bachega, J. F. R., Bommer, M., Brewster, A. S., Browne, M. C., Chatterjee, R., Cho, E., Cohen, A. E., Cowan, M., Datwani, S., Davidson, V. L., Defever, J., Eaton, B., Ellson, R., Feng, Y. P., Ghislain, L. P., Glownia, J. M., Han, G. Y., Hattne, J., Hellmich, J., Héroux, A., Ibrahim, M., Kern, J., Kuczewski, A., Lemke, H. T., Liu, P. H., Majlof, L., McClintock, W. M., Myers, S., Nelsen, S., Olechno, J., Orville, A. M., Sauter, N. K., Soares, A. S., Soltis, S. M., Song, H., Stearns, R. G., Tran, R., Tsai, Y., Uervirojnangkoorn, M., Wilmot, C. M., Yachandra, V., Yano, J., Yukl, E. T., Zhu, D. L. & Zouni, A. (2016). *Structure*, **24**, 631–640.

Rowlinson, J. S. & Windom, B. (1982). *Molecular Theory of Capillarity*. Mineola: Dover Publication.

Schneider, C. A., Rasband, W. S. & Eliceiri, K. W. (2012). *Nat. Methods*, **9**, 671–675.

Schulz, J., Bielecki, J., Doak, R. B., Dörner, K., Graceffa, R., Shoeman, R. L., Sikorski, M., Thute, P., Westphal, D. & Mancuso, A. P. (2019). *J. Synchrotron Rad.* **26**, 339–345.

Sierra, R. G., Gati, C., Laksmono, H., Dao, E. H., Gul, S., Fuller, F., Kern, J., Chatterjee, R., Ibrahim, M., Brewster, A. S., Young, I. D., Michels-Clark, T., Aquila, A., Liang, M., Hunter, M. S., Koglin, J. E., Boutet, S., Junco, E. A., Hayes, B., Bogan, M. J., Hampton, C. Y., Puglisi, E. V., Sauter, N. K., Stan, C. A., Zouni, A., Yano, J., Yachandra, V. K., Soltis, S. M., Puglisi, J. D. & DeMirci, H. (2016). *Nat. Methods*, **13**, 59–62.

Sierra, R. G., Laksmono, H., Kern, J., Tran, R., Hattne, J., Alonso-Mori, R., Lassalle-Kaiser, B., Glöckner, C., Hellmich, J., Schafer, D. W., Echols, N., Gildea, R. J., Grosse-Kunstleve, R. W., Sellberg, J., McQueen, T. A., Fry, A. R., Messerschmidt, M. M., Miahnahri, A., Seibert, M. M., Hampton, C. Y., Starodub, D., Loh, N. D., Sokaras, D., Weng, T.-C., Zwart, P. H., Glatzel, P., Milathianaki, D., White, W. E., Adams, P. D., Williams, G. J., Boutet, S., Zouni, A., Messinger, J., Sauter, N. K., Bergmann, U., Yano, J., Yachandra, V. K. & Bogan, M. J. (2012). *Acta Cryst.* D**68**, 1584–1587.

Stagno, J. R., Liu, Y., Bhandari, Y. R., Conrad, C. E., Panja, S., Swain, M., Fan, L., Nelson, G., Li, C., Wendel, D. R., White, T. A., Coe, J. D., Wiedorn, M. O., Knoska, J., Oberthuer, D., Tuckey, R. A., Yu, P., Dyba, M., Tarasov, S. G., Weierstall, U., Grant, T. D., Schwieters, C. D., Zhang, J., Ferré-D'Amaré, A. R., Fromme, P., Draper, D. E., Liang, M., Hunter, M. S., Boutet, S., Tan, K., Zuo, X., Ji, X., Barty, A., Zatsepin, N. A., Chapman, H. N., Spence, J. C. H., Woodson, S. A. & Wang, Y. X. (2016). *Nature*, **541**, 242–246.

Stauch, B. & Cherezov, V. (2018). *Annu. Rev. Biophys.* **47**, 377–397.

Tenboer, J., Basu, S., Zatsepin, N., Pande, K., Milathianaki, D., Frank, M., Hunter, M., Boutet, S., Williams, G. J., Koglin, J. E., Oberthuer, D., Heymann, M., Kupitz, C., Conrad, C., Coe, J., Roy-Chowdhury, S., Weierstall, U., James, D., Wang, D., Grant, T., Barty, A., Yefanov, O., Scales, J., Gati, C., Seuring, C., Srajer, V., Henning, R., Schwander, P., Fromme, R., Ourmazd, A., Moffat, K., Van Thor, J. J., Spence, J. C. H., Fromme, P., Chapman, H. N. & Schmidt, M. (2014). *Science*, **346**, 1242–1246.

Tiab, D. & Donaldson, E. C. (2012). *Petrophysics*, pp. 371–418. Oxford: Gulf Professional Publishing.

Wang, D., Weierstall, U., Pollack, L. & Spence, J. (2014). *J. Synchrotron Rad.* **21**, 1364–1366.

Weierstall, U., James, D., Wang, C., White, T. A., Wang, D. J., Liu, W., Spence, J. C. H., Bruce Doak, R., Nelson, G., Fromme, P., Fromme, R., Grotjohann, I., Kupitz, C., Zatsepin, N. A., Liu, H. G., Basu, S., Wacker, D., Won Han, G., Katritch, V., Boutet, S., Messerschmidt, M., Williams, G. J., Koglin, J. E., Marvin Seibert, M., Klinker, M., Gati, C., Shoeman, R. L., Barty, A., Chapman, H. N., Kirian, R. A., Beyerlein, K. R., Stevens, R. C., Li, D. F., Shah, S. T. A., Howe, N., Caffrey, M. & Cherezov, V. (2014). *Nat. Commun.* **5**, 3309.

Wiedorn, M. O., Oberthür, D., Bean, R., Schubert, R., Werner, N., Abbey, B., Aepfelbacher, M., Adriano, L., Allahgholi, A., Al-Qudami, N., Andreasson, J., Aplin, S., Awel, S., Ayyer, K., Bajt, S., Barák, I., Bari, S., Bielecki, J., Botha, S., Boukhelef, D., Brehm, W., Brockhauser, S., Cheviakov, I., Coleman, M. A., Cruz-Mazo, F., Danilevski, C., Darmanin, C., Doak, R. B., Domaracky, M., Dörner, K., Du, Y., Fangohr, H., Fleckenstein, H., Frank, M., Fromme, P., Gañán-Calvo, A. M., Gevorkov, Y., Giewekemeyer, K., Ginn, H. M., Graafsma, H., Graceffa, R., Greiffenberg, D., Gumprecht, L., Göttlicher, P., Hajdu, J., Hauf, S., Heymann, M., Holmes, S., Horke, D. A., Hunter, M. S., Imlau, S., Kaukher, A., Kim, Y., Klyuev, A., Knoška, J., Kobe, B., Kuhn, M., Kupitz, C., Küpper, J., Lahey-Rudolph, J. M., Laurus, T., Le Cong, K., Letrun, R., Xavier, P. L., Maia, L., Maia, F., Mariani, V., Messerschmidt, M., Metz, M., Mezza, D., Michelat, T., Mills, G., Monteiro, D. C. F., Morgan, A., Mühlig, K., Munke, A., Münnich, A., Nette, J., Nugent, K. A., Nuguid, T., Orville, A. M., Pandey, S., Pena, G., Villanueva-Perez, P., Poehlsen, J., Previtali, G., Redecke, L., Riekehr, W. M., Rohde, H., Round, A., Safenreiter, T., Sarrou, I., Sato, T., Schmidt, M., Schmitt, B., Schönherr, R., Schulz, J., Sellberg, J. A., Seibert, M. M., Seuring, C., Shelby, M. L., Shoeman, R. L., Sikorski, M., Silenzi, A., Stan, C. A., Shi, X., Stern, S., Sztuk-Dambietz, J., Szuba, J., Tolstikova, A., Trebbin, M., Trunk, U., Vagovic, P., Ve, T., Weinhausen, B., White, T. A., Wrona, K., Xu, C., Yefanov, O., Zatsepin, N., Zhang, J., Perbandt, M., Mancuso, A. P., Betzel, C., Chapman, H. & Barty, A. (2018). *Nat. Commun.* **9**, 4025.

Zhang, H. T., Unal, H., Gati, C., Han, G. W., Liu, W., Zatsepin, N. A., James, D., Wang, D. J., Nelson, G., Weierstall, U., Sawaya, M. R., Xu, Q. P., Messerschmidt, M., Williams, G. J., Boutet, S., Yefanov, O. M., White, T. A., Wang, C., Ishchenko, A., Tirupula, K. C., Desnoyer, R., Coe, J., Conrad, C. E., Fromme, P., Stevens, R. C., Katritch, V., Karnik, S. S. & Cherezov, V. (2015). *Cell*, **161**, 833–844.

JOURNAL OF APPLIED CRYSTALLOGRAPHY

Volume 55 (2022)

Supporting information for article:

Co-flow injection for serial crystallography at X-ray free-electron lasers

Diandra Doppler, Mohammad T. Rabbani, Romain Letrun, Jorvani Cruz Villarreal, Dai Hyun Kim, Sahir Gandhi, Ana Egatz-Gomez, Mukul Sonker, Joe Chen, Faisal H. M. Koua, Jayhow Yang, Mohamed Youssef, Victoria Mazalova, Saša Bajt, Megan L. Shelby, Matt A. Coleman, Max O. Wiedorn, Juraj Knoska, Silvan Schön, Tokushi Sato, Mark S. Hunter, Ahmad Hosseinizadeh, Christopher Kuptiz, Reza Nazari, Roberto C. Alvarez, Konstantinos Karpos, Sahba Zaare, Zachary Dobson, Erin Discianno, Shangji Zhang, James D. Zook, Johan Bielecki, Raphael de Wijn, Adam R. Round, Patrik Vagovic, Marco Kloos, Mohammad Vakili, Gihan K. Ketawala, Natasha E. Stander, Tien L. Olson, Katherine Morin, Jyotirmory Mondal, Jonathan Nguyen, José Domingo Meza-Aguilar, Gerdenis Kodis, Sara Vaiana, Jose M. Martin-Garcia, Valerio Mariani, Peter Schwander, Marius Schmidt, Marc Messerschmidt, Abbas Ourmazd, Nadia Zatsepin, Uwe Weierstall, Barry D. Bruce, Adrian P. Mancuso, Thomas Grant, Anton Barty, Henry N. Chapman, Matthias Frank, Raimund Fromme, John C. H. Spence, Sabine Botha, Petra Fromme, Richard A. Kirian and Alexandra Ros

1. Numerical Modeling.

To simulate the co-flow width, the laminar two-phase flow and Level Set Method (LSM) are used. "Fine" meshing was selected during the simulation, which created a domain of 696196 triangular elements, 24102 boundaries, and 792 edges, respectively. Walls are considered as wetted and impermeable. More detailed boundary conditions, their relevant equations, and nomenclature used in the two-phase flow and level set method are described in Table S1. The parameters used in the model are listed in Table S2.

2D Model.

A 2D model matching the cross-section of the co-flow devices in the experimental observation plane was set up first. The result of numerical modeling is shown for co-flow in three different flow conditions in the T-junction and Y-junction in Figure S1.

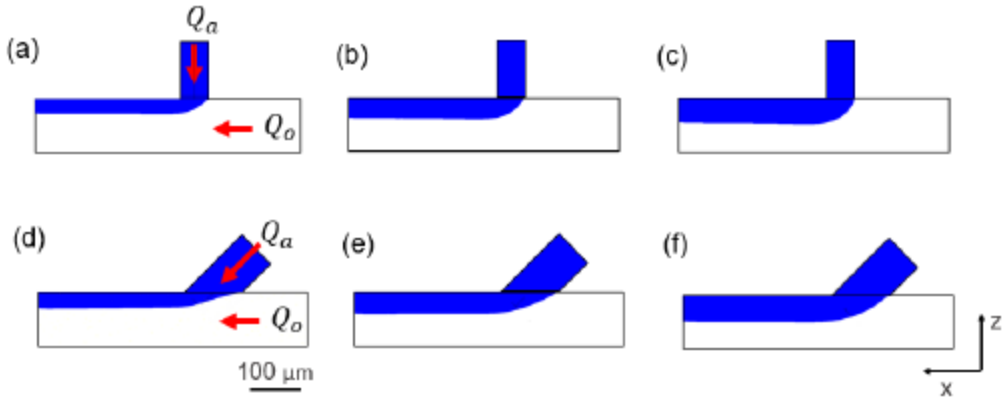

Figure S-1. *Result of numerical modeling for co-flow of different flow conditions in T- and Y-junction for Mode 1: The flow rates are a) Q_o = 18 µL/min and Q_a = 2 µL/min, b) Q_o = 16 µL/min and Q_a = 4 µL/min, c) Q_o = 14 µL/min and Q_a = 6 µL/min, d) Q_o = 18 µL/min and Q_a = 2 µL/min, e) Q_o = 16 µL/min and Q_a = 4 µL/min, and f) Q_o = 14 µL/min and Q_a = 6 µL/min. The average co-flow thickness of each conditions are a) 18.12 ± 0.65 µm, b) 27.16 ± 0.89 µm, c) 38.66 ± 1.31 µm, d) 32.88 ± 0.56, e) 49.35 ± 0.89, and f) 52.31 ± 1.36 respectively. The blue color represents the aqueous sample phase. The oil phase is presented in white in the continuous channel.*

3D Model.

To illustrate the curved nature of the water/oil interface, a 3D model was established. Briefly, a 3D model of the T-junction was established to reflect the 3D-printed device investigated in this work, as shown in Figure S-2. The T-junction design consists of a cylindrical tube with an inner diameter of 75 µm, connected to the rectangular fluidic channel. The height, width, and length of the rectangular channel are 100, 100, and 500 µm, respectively. To simulate the co-flow, laminar two-phase incompressible flow and the Level Set Method (LSM) were used. Meshing was chosen as "fine," and walls are considered wetted and impermeable. More detailed boundary conditions, other relevant equations, and nomenclature used in the two-phase flow and level set method are described below in Table S-1.

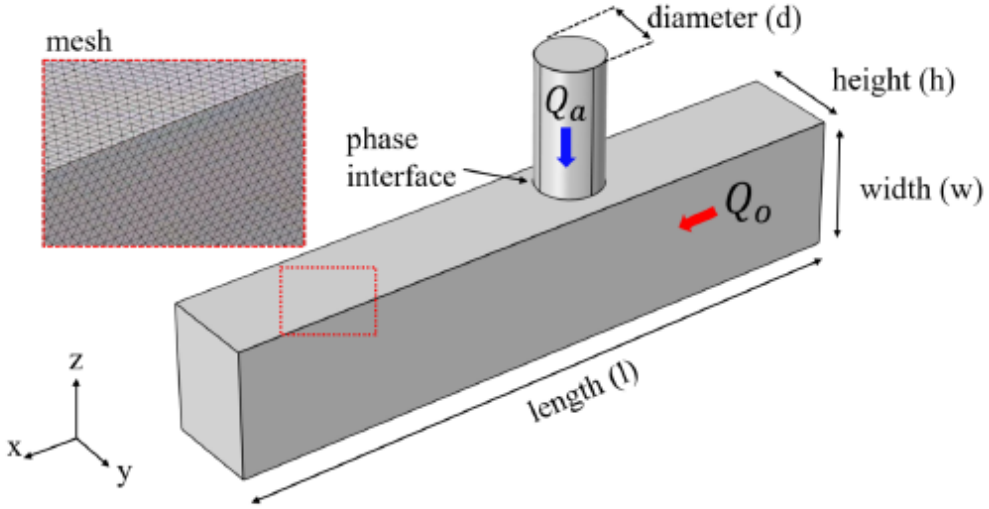

Figure S-2. *Schematic of the T- junction microchannel in the numerical study. The main horizontal channel contains the continuous phase (Q_o, oil). The perpendicular inlet channel contains the aqueous phase (Q_a, buffer).*

The 3D numerical modeling was carried out for co-flow in three different contact angle conditions is described in Figure S3 from the T-junction 3D model. The numerical simulation was performed at different oil flow (Q_o) and aqueous flow (Q_a) rates while maintaining a total flowrate, Q_{tot}, of 20 µL/min. We explored the simulation for a hydrophobic condition (θ = 143°) and a hydrophilic condition (θ = 71°). Figure S-3a) represents the oil/aqueous interface for the hydrophilic condition at a flow rate ratio of 1. The oil/interface is curved due to its hydrophilicity and is represented in figure S-3b). Figure S-3c) represents the oil/aqueous interface for the hydrophobic condition at a flow rate ratio of 1. Figure S-3-d) shows the curvature of this interface through the channel. For a flow rate ratio of 1.5 and higher, no co-flow was observed for the hydrophobic condition, and instead of the co-flow droplet generation was observed. Figure S-3e) represents the generation of droplets for θ = 143° and a flow rate ratio of 1.5.

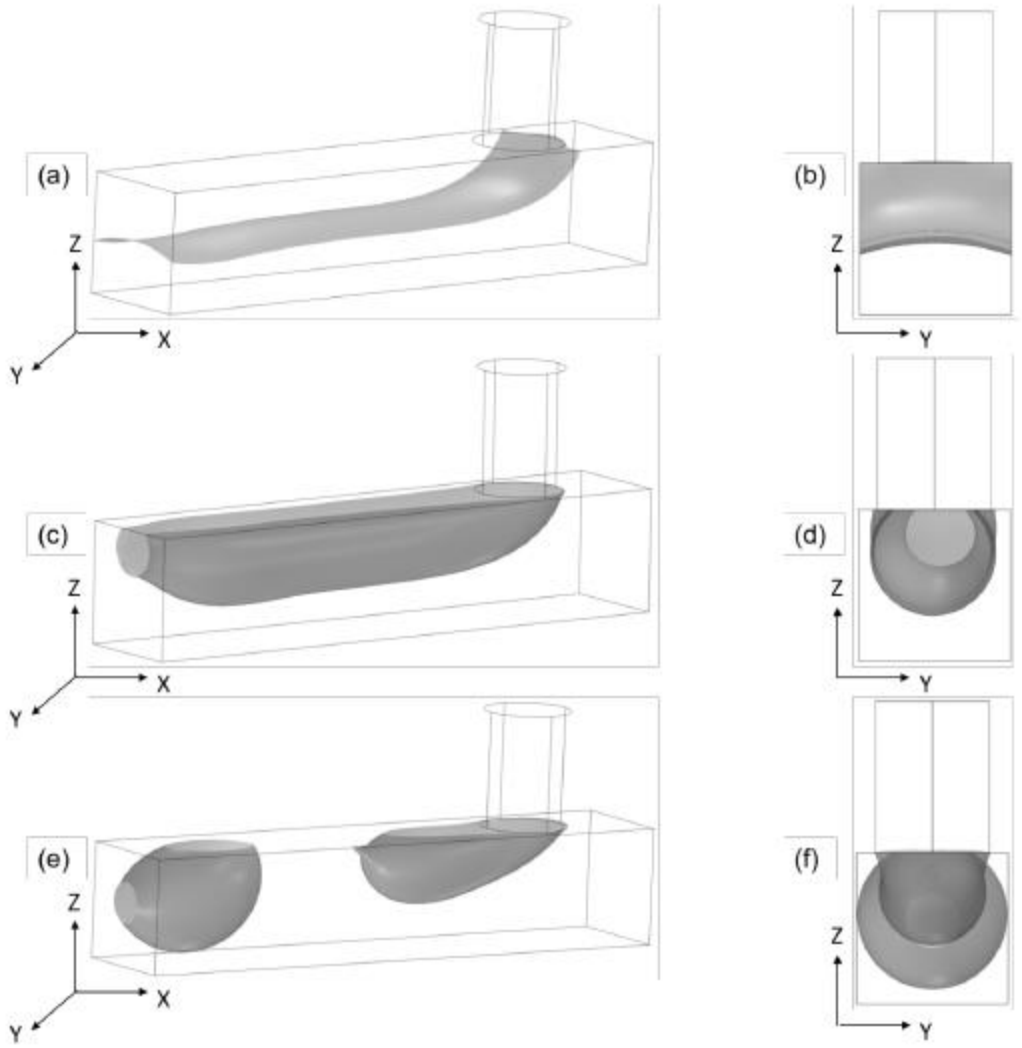

Figure S-3. *Result of the oil/aqueous interface for a hydrophobic and hydrophilic condition at different flow rate ratios in a T- junction microchannel from the 3D numerical model. a) 3D-view of the oil/aqueous interface for (θ = 71°) with a flow rate ratio of 1. b) The view of the oil/aqueous interface when observed along the channel axis for conditions similar to a). c) The 3D-view of the oil/aqueous interface for (θ = 143°) with a flow rate ratio of 1. d) The view of the oil/aqueous interface along the channel axis for conditions similar to c). e) The generation of the droplet is observed for (θ = 143°) with a flow rate ratio of 3. f) The view of the oil/aqueous interface along the channel axis for conditions similar to e). Note that under this condition, the co-flow breaks into droplets.*

Physics	Boundary conditions
Laminar Flow	Surface domain: $0 = -\nabla p + \mu\nabla^2 \boldsymbol{u}$ $\rho\nabla \cdot (\boldsymbol{u}) = 0$ Wall : $u = 0$ (No slip condition) Inlets : Boundary condition = Laminar inflow (flow rate) Entrance thickness: L_{entrt} = 100 µm Outlet : $p_0 = 0$
Level Set	Surface domain (Phase initialization) : $\frac{\partial \phi}{\partial t} + \boldsymbol{u} \cdot \nabla\phi = \gamma\nabla \cdot \left(\varepsilon\nabla\phi - \phi(1-\phi)\frac{\partial \phi}{\lvert\nabla\phi\rvert}\right)$ Initial Value and Inlet for the oil phase: ϕ = 0 Initial Value and Inlet for the aqueous phase: ϕ = 1 γ: 0.0236 [N/m] * η_{oil} : 13.3 cP** η_{buffer} : 16.4 cP*** ρ_{oil}: density of oil: 1.8 [g/cm^3] ρ_{buffer} : density of the buffer : 1.01 [g/cm^3] Wetted wall: θ : 1.23 [rad] for the IP-S and 1.06 [rad] for the PETA-B-based resist
Nomenclature	ϕ = level set function γ = surface tension [mN/m] n = normal unit vector $\boldsymbol{u}$ = medium or fluid velocity vector ρ_{oil}: density of PFD: PFO 10/1 v/v [g/cm^3] ρ_{buffer} = density of the buffer [g/cm^3] η_{oil} = viscosity of a PFD: PFO 10/1 v/v [cP] η_{buffer} = viscosity of buffer [cP] t = time [s] p = pressure [Pa] T = the absolute fluid temperature [K] u = fluid velocity [m/s] μ = dynamic fluid viscosity [Pa·s] θ = contact angle [rad]

Table S-1. *The boundary conditions for the simulation, relevant equations, and nomenclature. * from Echelmeier, A., Sample Delivery Enabled by 3D Printing for Reduced Sample Consumption and Mix-and-Inject Serial Crystallography at X-ray Free Electron Lasers, Thesis, Arizona State University, 2019. ** from Echelmeier et al. Segmented Flow Generator for Serial Crystallography at X-Ray Free Electron Lasers,*

*Nature Communications, (2020) 11, 4511. *** Determined with the PSII buffer as defined in the main manuscript with a viscosimeter (DV1 Digital Viscometer, Brookfield Metek, USA)*

Flow rate (Q_o: Q_a) µl/min	ε (interface thickness) µm	γ (reinitialization parameter) m/s
19:1	0.73	0.032
18:2	0.73	0.030
16:4	0.73	0.028
15:5	0.73	0.025
14:6	0.73	0.030
12:8	0.73	0.037
10:10	0.73	0.047

Table S-2. Relevant simulation parameters used in the model.

2. Contact Angle Variation of 3D-printed Devices.

The sessile drop method was employed to measure the contact angle, θ, for the oil, water, 3D-printed surface system. The solid interface was made by 3D-printing a 5.0 mm x 5.0 mm x 0.1 mm block of either IP-S or PETA-B on a slide. A 5 µL droplet of water was placed on the polymer surface and the two were inverted and placed on top of a plastic cuvette overfilled with oil. A Jiusion USB Digital Microscope (Amazon, USA) connected to a laptop was used to capture the interface which was illuminated by a cell phone flash-light. The image of the interface (see Figure S-4 as an example) was analyzed in ImageJ[1] with the contact angle plug-in (https://imagej.nih.gov/ij/plugins/contact-angle.html) using the manual points procedure. Various times were assessed as shown in Figure S-5 and each timepoint was repeated in triplicate.

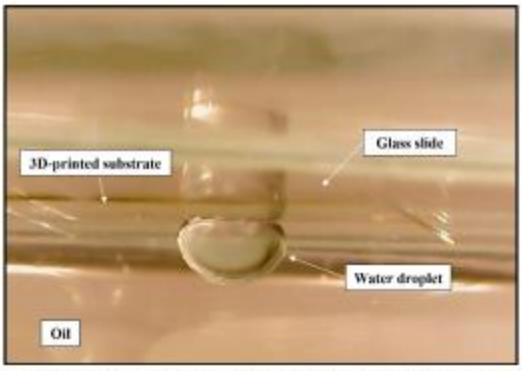

Figure S-4: *Microscopic image of a 5 uL water droplet surrounded by oil on a 1- day old 3D-printed IP-S surface.*

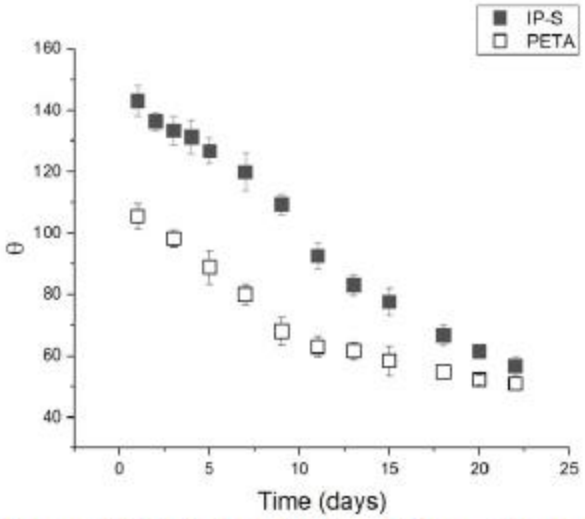

Figure S-5. *Contact angle (θ) variation over time after device fabrication through 3D-printing both for resin IP-S and PETA-B.*

3. Photosystem II crystals.

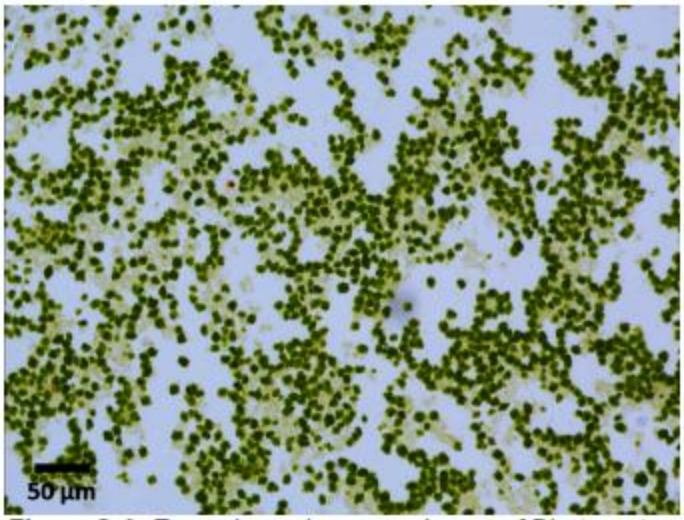

Figure S-6: *Exemplary microscopy image of Photosystem II crystals grown in dehydration buffer.*

References

1. Schneider, C. A.; Rasband, W. S.; Eliceiri, K. W., NIH Image to ImageJ: 25 years of image analysis. *Nat Methods* **2012,** *9* (7), 671-5.

APPENDIX E

COPYRIGHT PERMISSION

The following chapters of this dissertation have been published and are used with permission from the publishers:

Chapter 2: Reprinted with permission from Rabbani, MT.; Sonker, M., A. Ros., Carbon Nanotube Dielectrophoresis: Theory and Applications, Electrophoresis 2020, 41(21-22): 13235-44.

Chapter 3: Reprinted with permission from Rabbani, MT.; Sonker, M., A. Ros., Carbon Nanotube Dielectrophoresis: Theory and Applications, Electrophoresis 2020, 41(21-22): 13235-44.

Chapter 4: Reprinted with permission from Rabbani, MT.; Schmidt, CF.; A. Ros., Single-walled Carbon Nanotube Probed with Insulator-based Dielectrophoresis, Analytical Chemistry 2017, 89(24):13235-44, Copyright (2017), American Chemical Society.

Chapter 5: Reprinted with permission from Rabbani, MT.; Schmidt, CF.; A. Ros., Length-Selective Dielectrophoretic Manipulation of Single-Walled Carbon Nanotubes, Analytical Chemistry 2020, 92(13):8901-8, Copyright (2020), American Chemical Society.

Appendix D: Reprinted with permission from Doppler, D.; Rabbani, MT., Leturn, R., Cruz Villarreal, J., Kim, DH., Gandhi, S., Egatz Gomez, A., Sonker, M., Chen, J., Koua, FHM., Yang, J., Youssef, M., Mazalova, V., Bajt, S., Shelby, ML., Coleman, MA., Wiedorn, MO., Knoska, J., Schon, S., Sato, T., Hunter, MS., Hosseinizadeh, A., Kupitz, C., Nazari, R., Alvarez, RC., Krapos, K., Zaare, S., Dobson, Z., Discianno, E., Zhang, S., Zook, JD., Bielecki, J., De Wijn, R., Round, AR., Vagovic, P., Kloos, M., Vakili, M., Ketawala, GK., Stander, NE., Olson, TL., Morin, K., Mondal, J., Ngyuen, J., Meza-Aguilar, JD., Kodis, G., Viana, S., Martin-Garcia, JM., Mariani, V., Schwander, P., Schmidt, M., Messerschmidt, M., Ourmazad, A., Zatesoin, N., Weierstall, U., Bruce, BD., Mancuso, AP., Grant, T., Barty, A., Chapman, HN., Frank, M., Fromme, R., Spence, JCH., Botha, S., Fromme, P., Kirian, RA., Ros, A., Co-Flow Injection for Serial Crystallography at X-ray Free-electro Laser. J Appl Crystallography 2022, 55 (1).